Environmental change, trilobite extinction and massive volcanism at the Cambrian Series 2 – Series 3 boundary

Luke Edward Faggetter

Submitted in accordance with the requirements for the degree of
Doctor of Philosophy

The University of Leeds
School of Earth and Environment
Earth Surface Science Institute

November 2017

The candidate confirms that the work submitted is their own, except where work which has formed part of jointly-authored publications has been included. The contribution of the candidate and the other authors to this work has been explicitly indicated below. The candidate confirms that appropriate credit has been given within the thesis where reference has been made to the work of others.

In the case of each data chapters outlined below, the candidate was the primary and corresponding author of material written for publication. Additional edits, extensive discussions, and reviews were provided by all co-authors at all stages during the PhD.

Chapter 2: Sequence stratigraphy, chemostratigraphy and facies analysis of Cambrian Series 2 – Series 3 boundary strata in north-western Scotland

This chapter is published as:

Luke E. Faggetter, Paul B. Wignall, Sara B. Pruss, Yadong Sun, Robert J. Raine, Robert J. Newton, Mike Widdowson, Michael M. Joachimski & Paul M. Smith (2016). Sequence stratigraphy, chemostratigraphy and facies analysis of Cambrian Series 2–Series 3 boundary strata in north-western Scotland. *Geological Magazine*, 1-13.

The candidate is the lead author and takes responsibility for all data analysis, interpretation and for writing the manuscript. Major editorial contributions were made by all co-authors on the manuscript. Field data collection was led by the candidate, and supported by Wignall, Pruss and Widdowson.

Chapter 3: Trilobite extinctions, facies changes and the ROECE carbon isotope excursion at the Cambrian Series 2 – 3 boundary, Great Basin, western USA.

This chapter is published as:

Faggetter, L. E., Wignall, P. B., Pruss, S. B., Newton, R. J., Sun, Y., & Crowley, S. F. (2017). Trilobite extinctions, facies changes and the ROECE carbon isotope excursion at the Cambrian Series 2– Series 3 boundary, Great Basin, western USA. *Palaeogeography, Palaeoclimatology, Palaeoecology*, *478*, 53-66.

The candidate is the lead author and takes responsibility for all data analysis, interpretation and for writing the manuscript. Major editorial contributions were made by all co-authors on the manuscript. Field data collection was led by the candidate, and supported by Wignall, Pruss and Newton.

Chapter 4: The search for mercury anomalies at the Cambrian Series 2 – Series 3 boundary: evidence for increased volcanic activity coincident with extinction?

Faggetter, L.E., Wignall, P.B., Pruss, S.B., Jones, D.S., Grasby, S., Widdowson, M. Newton, R.J. The search for mercury anomalies at the Cambrian Series 2 – Series 3 boundary: evidence for increased volcanic activity coincident with extinction?

This chapter is formatted for submission to *Chemical Geology.*

The candidate is the lead author and takes responsibility for all data analysis, interpretation and for writing the manuscript. Major editorial contributions were made by all co-authors on the manuscript. Field data collection was led by the candidate, and supported by Wignall, Pruss and Newton.

Chapter 5: Carbon isotope chemostratigraphy and Hg concentrations across the Cambrian Series 2 – 3 boundary, south Georgina Basin, Australia.

Faggetter, L.E., Wignall, P.B., Poulton, S.W., Jones, D. S., Sun, Y., Newton, R.J.

The candidate is the lead author and takes responsibility for all data analysis, interpretation and for writing the manuscript. Field data collection was led by the candidate, and supported by additional samples contributed by Poulton.

Acknowledgements

First and foremost, I would like to acknowledge three people as instrumental in the process of writing this thesis; Paul Wignall, Rob Newton and Mike Widdowson. It goes without saying that producing a thesis without supervision would be near impossible, this is undeniably the case for the pages that follow.

It's probably accurate to reflect that it all started going downhill seven years ago when Paul agreed to supervise my undergraduate thesis. I approached him as a lowly Bsc. student trying to find an advisor that would allow a dissertation topic that I actually *wanted* to do; safe to say at that point I didn't imagine myself ending up as one of the Wignall PhD cohort. His guidance and teaching has been fundamental in forming the foundation of my scientific approach, something that I will hold onto going forward. He has been endlessly patient through countless iterations of my work, providing some stellar feedback (you should ask me about this) and honing my skill as a young geoscientist. His name has got me through doors, but, I'd like to think what I've learned from him justified me being there. It really has been great.

Rob, he may not understand the full scope of his damage, is responsible for instilling in me the scientific aspiration that I intend to take beyond my doctorate. I knew v*ery* little about geochemistry before I started this (*what is* an isotope?!) but now consider the expertise he shared as key in shaping how I approach questions about Earth history. At times it might have seemed like I wasn't taking everything in, that's because I really do have to go away and do my homework. From the get-go it was a challenge, but one that rewarded me with breakthrough moments in my understanding, and one that has equipped me with the tools to progress as a scientist. Rob also taught me that the best geochemists wash their hands before AND after they use the toilet, but that isn't the only gem that stuck with me.

Sometime during my attempt at getting a NERC funded PhD, Paul suggested I meet Mike, a co-supervisor on a prospective project with its roots set in Australia. I met Mike, and, approximately 45 minutes later we agreed that I would head to Oz with him and his PhD student. This was my first introduction to real field geology, and it lit me up. The ~4 months spent there was not only the conceptual genesis of my PhD, but was also some of the most rewarding fieldwork, it really did leave a lasting imprint. I will always

want to be in the field and Mike granted me a principal opportunity which affirmed that, and put me on track to get to here.

Beyond the professional context I feel very fortunate to have formed great personal relationships with my supervisors. I guess when you're on your own in the outback, or (lost?) on disused Nevadan mining roads, or being battered by Scottish highland elements, it really helps to get on with them. What was particularly pertinent was that this was never forced, and that I'm pretty thankful for.

Amongst the Leeds SoEE group there are people that have been formative in my progression through this PhD. Those who I've shared office space with, fieldwork, data, beer, confusion and understanding are really important people. I'd like to thank: Allie T, Andy B, Autumn P, Hollie R, James W, Kathy D, Katie F, Laura G, Rhian R-O, Sarah S, Tianchen H and Tom F. I've alphabetised the order because they are all equally important.

Outside of Leeds I have been supported by a number of people who I want to mention. Sara P for sharing the joy of fieldwork (all over Laurentia!), for challenging, progressing and improving my science, and also for putting me forward for "real life" things such as a job. Yadong Sun because he makes measuring isotopes seem easy and is top company. Also my co-authors on the following papers, collaboration should be at the heart of science and I'm very grateful for their input and hard work.

I also want to thank my Mum, Dad, Sister and Joanne. The dawn of my interest in natural sciences probably starts with a semi-feral childhood spent between Kent and Scotland. Those who know me know I *have* to get outside, from a young age this was fostered and as I grew up my parents afforded me the opportunity to answer questions about what is outside! They are unconditionally supportive and that goes a long way. Without the companionship shared with Joanne I would likely be a lot more frayed at the edges, this has been really important to me.

Thanks for reading my reflections, PTO for the good stuff.

Abstract

The Cambrian Series 2 – Series 3 boundary (~509 Ma) was a dynamic interval marked by a major perturbation to the global carbon cycle; widespread sea level fall (Sauk Supersequences); the eruption of the Kalkarindji large igneous province and the extinction of the dominant trilobites- the olenellids of Laurentia and the redlichiids of Gondwana. This thesis investigates the relative timing of these phenomena from field sites across the Laurentian and Gondwanan palaeocontinents, assessing the severity of environmental change coinciding with extinction. We report that the Redlichiid-Olenellid Extinction Carbon isotope Excursion (ROECE) coincides with the Series 2 – Series 3 boundary in Laurentian sections (NW Scotland, SW USA), though only in the SW USA does ROECE co-occur with the trilobite extinction. Scottish successions of this age are hindered by a lack of fossils, and as such the exact timing of ROECE relative to the extinction is unclear. New evidence presented in this thesis shows a variable record of anoxia at the extinction horizon, the most severe manifestation indicates euxinic conditions during the extinction at Ruin Wash, Pioche Formation, Nevada. Elsewhere in the SW USA and NW Scotland, there is evidence for periodic dysoxia (e.g. basal Ghrudaidh Formation, Durness Group, Scotland and Carrara Formation, SW USA) at the Series 2 – Series 3 boundary and extinction interval. Facies analysis reveals that on Laurentia, ROECE and the extinction horizon occur during the transgressive phase of the Sauk II supersequence. To investigate the temporal relationship between the Series 2 – Series 3 boundary, ROECE, extinction and Kalkarindji eruptions, this thesis presents new Hg data as a proxy for volcanism. On Laurentia the data show an inconsistent relationship between these phenomena, whilst on Gondwana a new preliminary study shows evidence for Hg enrichments at this interval, establishing it as a site to further investigate the sedimentary trace of volcanism.

Contents

List of Tables

List of Figures

Abbreviations

$^{40}Ar/^{39}Ar$: $^{40}Argon$ / $^{39}Argon$

BTE: Botomian – Toyonian extinction

CIR: Cambrian Information Revolution

CS: Centralian Superbasin

CSR: Cambrian Substrate Revolution

FAD: First appearance datum

GOBE: Great Ordovician Biodiversity Event

HBRE: Hawke Bay Regression Event

Hg: Mercury

LIP: Large Igneous Province

m: Metres

Ma: Million years ago

Myr: Million years

ORB: Oxygen restricted biofacies

ROECE: Redlichiid Olenellid Extinction Carbon isotope Event

SCS: Sub-commission on Cambrian Stratigraphy

SSF: Small shelly fossils

TGSF: Transgondwanan Super-fan

TGSM: Transgondwanan Supermountain

U-Pb: Uranium-Lead

VPDB: Vienna Pee-Dee Belemnite

1   Chapter One: Introduction

1.1   Rationale

The advent of macroscopic life is rooted in the Ediacaran (Droser and Gehling, 2015; Smith et al., 2016b; Zhu et al., 2017) though it is the Cambrian Period that has traditionally taken the stage as the crucible of modern animals. Global diversity in the early Palaeozoic radiated in two distinct pulses: during the first 20 million years of the Cambrian, known as the "Cambrian Explosion", and during the Great Ordovician Biodiversification Event (GOBE; Sepkoski, 1979; 1981; Zhu et al., 2006; Bambach et al., 2007; Servais et al., 2008). The Cambrian Explosion saw the radiation of Phanerozoic mineralised animals initially beginning with the appearance of small shelly fossils, followed by diverse groups including arthropods, archaeocyaths, radiocyaths and a diversity of soft bodied organisms (Matthews and Missarzhevsky, 1975; Zhuravlev, 1986; Wood, 1998; Riding, 2001; Rowland, 2001; Zhu et al., 2006; Braun et al., 2007). This radiation is understood to have occurred in a two-phase fashion over ~20 million years (myr; Maloof et al., 2010) framing the Cambrian Explosion not as a rapid, enigmatic increase in diversity but as an exploration of diverse new body plans and ecological niches. This evolutionary success was interrupted close the Cambrian Series 2 – Series 3 boundary (~ 509 Ma; Ogg et al., 2016) when the first mass extinction of the Phanerozoic struck (Newell, 1972; Debrenne, 1991; Zhuravlev and Wood, 1996). At this time, early Cambrian reef taxa went extinct to be followed in quick succession by the dominant trilobites, the olenellids of Laurentia and the redlichiids of Gondwana (Rowland, 1988; 2001; Palmer, 1998). There is clear evidence for environmental instability in Cambrian oceans, involving disruption to the carbon cycle and periods of anoxia (e.g. Zhuravlev and Wood, 1996; Gill et al., 2011). It is apparent that this instability also occurred at the Series 2 – Series 3 boundary (e.g. Hough et al., 2006). This thesis therefore aims to assess evidence for palaeoenvironmental change at the Series 2 – Series 3 boundary and evaluate potential causal mechanisms behind extinction. More broadly, we assess the notion that, at the Series 2 – Series 3 boundary, the Cambrian Explosion was punctuated by an interval of exogenous
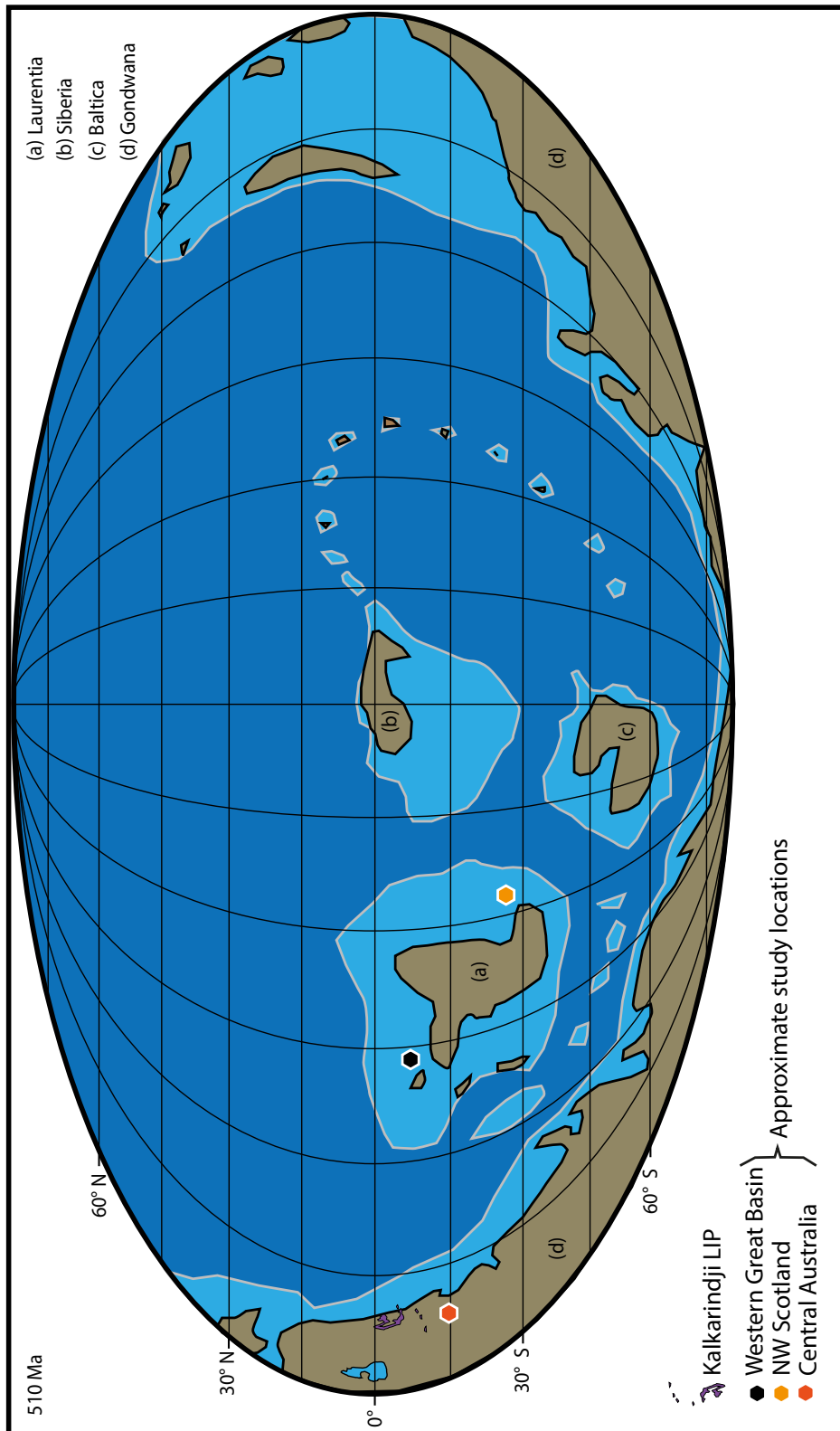
Figure 1.1: Global palaeogeography at 510 Ma from Scotese (2016) showing approximate position of study locations and the Kalkarindji LIP modified from Marshall et al. (2016).

environmental stress, and, in the midst of a global diversity boom, Cambrian biota suffered a severe loss.

Contemporaneous events at the Series 2 – Series 3 boundary purportedly include major sea-level oscillations, the spread of anoxic bottom waters to shallow marine shelves and the emplacement of a large igneous province (LIP; the Kalkarindji Province in northern Australia; Fig. 1.1). The temporal coincidence of these phenomena invites the suggestion that they are inter-related (Sloss, 1963; Jourdan et al., 2014). As well as this, significant changes to the carbon cycle drove a large negative carbon isotope excursion in the carbonate carbon isotope record (the Redlichiid Olenellid Extinction isotope Excursion; ROECE) at the Series 2 – Series 3 boundary (Zhu et al., 2006; Faggetter et al, 2017).

Large igneous province volcanism, ocean anoxia and sea level change have been implicated in driving both the extinction of the olenellid trilobites and the ROECE event (Palmer, 1998; Montañez et al. 2000). However, the lack of robust dating of these phenomena confounds the understanding of a cause-effect relationship. For example, studies of the Kalkarindji LIP suggest an eruption age close to the Series 2 – Series 3 boundary, leading to the implication that it played a role in driving major environmental change (Glass and Phillips, 2006; Jourdan et al., 2014) but there has been no direct evidence linking volcanism, ocean anoxia and the ROECE in the same section. The detailed temporal relationship is therefore unclear. Attempts to establish an age framework for the Kalkarindji are ongoing and the best available age, from a single zircon U-Pb radiometric date, is 510.7 ± 0.6 Ma (Fig. 1.2.; Jourdan et al., 2014). This date is close to that of the Series 2 – Series 3 boundary which, although currently unratified by the Subcommission on Cambrian Stratigraphy (SCS), is placed at 509 Ma. However, this close temporal relationship provides no empirical evidence that regions experiencing extinction and environmental stress were also affected by volcanism. This presents two problems when correlating these events. Firstly, the lack of a ratified radiometric age for the Cambrian Series 2 – Series 3 boundary means comparative studies are based on undefined ages and, secondly, inherent error from radiometric methods makes precise correlation between the Kalkarindji LIP and extinction challenging to pin

down. A temporal coincidence is not proof enough that the Kalkarindji coincided with, or was a driver behind environmental change and extinction. Whilst ongoing geochronological studies are essential, establishing a sedimentary proxy for volcanism in strata recording these phenomena could provide the "smoking gun" that volcanism occurred simultaneously with extinction, as such this thesis explores the use of Hg as a proxy for volcanism.
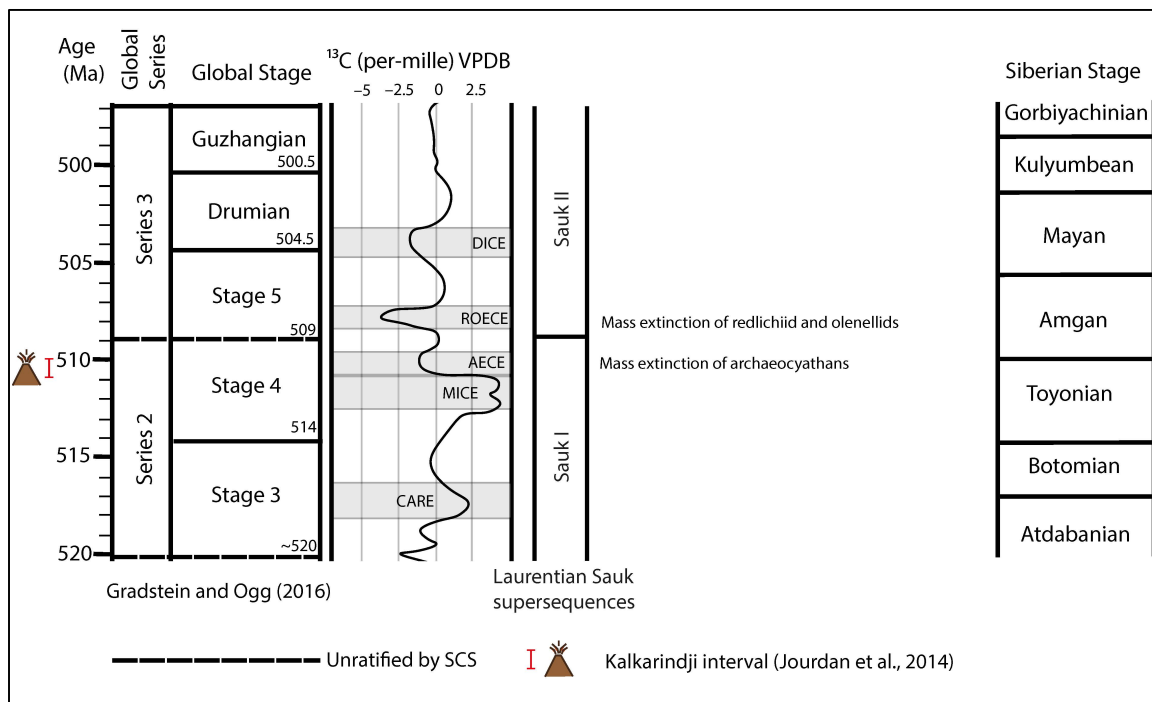
Figure 1.2: Global Cambrian chronostratigraphy, inorganic carbon isotope curve (from Zhu et al., 2006), Sauk supersequences correlated to the global stage framework (Raine and Smith, 2012) and position of Cambrian extinction events alongside Siberian stages (modified from Ogg et al., 2016).

1.2 Aims and objectives

Long standing dating and correlation issues mean that cause-effect links between sea-level change, ocean anoxia, environmental change, extinction and volcanism have remained elusive. Compared with other mass extinction events, there have been relatively few studies of this interval. Investigating the nature and timing of events at the Cambrian Series 2 – Series 3 boundary requires an integrated approach examining multiple sections from

across the Cambrian globe. This thesis utilises geological fieldwork and chemostratigraphic analysis of Series 2 – Series 3 boundary strata in Australia, Scotland and the western USA to elucidate the timing and nature of marine environmental change, ocean anoxia, extinction and LIP volcanism. The overall objective of this work is to reconstruct a detailed timeline of events at the Series 2 – Series 3 boundary and to assess whether these phenomena reflect local, regional, or global environmental signals. Sedimentological facies analysis is used to elucidate palaeoenvironmental change in the boundary strata, carbonate carbon isotope chemostratigraphy provides an insight into the carbon cycle and is used to correlate by comparison with the global δ^{13}C curve, and mercury (Hg) chemostratigraphy is used as a tracer for volcanism in sedimentary sections.

The specific research questions this thesis aims to answer are:
1. What environmental change is seen in marine strata recording the Series 2 – Series 3 boundary? What was the severity and does it coincide with trilobite extinction?
2. What role did the eruption of the Kalkarindji large igneous province play in trilobite extinctions and can evidence for these eruptions be detected using mercury concentrations in far-field sedimentary successions?
3. What is the temporal relationship between carbon cycle perturbations and trilobite extinction?
4. Does sea level fall coincide with the ROECE and/or extinction?

1.3   Thesis structure and publication chapters

In order to address these research questions, this thesis is comprised of six chapters, two of which are published peer-reviewed publications, one is a manuscript in submission and one is a manuscript formatted for submission. Following the thesis rationale, research aims and objectives outlined here**,** chapters **2 – 5** present data chapters comprising original case studies designed to answer the broad research questions detailed previously.

Chapter 2: Faggetter, L.E., Wignall, P.B., Pruss, S.B., Sun, Y., Raine, R.J., Newton, R.J., Widdowson, M., Joachimski, M.M., Smith., P.M. (2016). Sequence stratigraphy, chemostratigraphy and facies analysis of Cambrian Series 2–Series 3 boundary strata in northwestern Scotland. **Published** online 4/11/16 - *Geological Magazine*, 1-13.

This chapter examines the sequence stratigraphy, sedimentology and carbon isotope record of Series 2 – Series 3 boundary rocks from the Durness Group, northwest Scotland. Specifically, it presents new details of the nature of the Sauk I/ Sauk II supersequence boundary in the Ghrudaidh and Eilean Dubh formations (lower Durness Group) and elucidates the temporal relationship between sea-level change and the ROECE event. The Durness Group is an expansive Cambro- Ordovician carbonate sequence which, in the Cambrian succession, lacks a robust age framework. This publication provides the first chemostratigraphic scheme for these rocks enabling global correlation of the lower Durness Group. As well as aiming to constrain the age of these rocks, pyrite framboid petrography is used to assess redox and sequence stratigraphic analysis during sea-level fluctuations. Specifically, this publication aims to answer the question: *What is the relationship between ROECE, the Series 2 – Series 3 boundary and the Sauk I – II supersequence boundary in the Durness Group, NW Scotland?*

Chapter 3: Faggetter, L. E., Wignall, P. B., Pruss, S. B., Newton, R. J., Sun, Y., Crowley, S. F. (2017). Trilobite extinctions, facies changes and the ROECE carbon isotope excursion at the Cambrian Series 2–3 boundary, Great Basin, western USA. **Published** - *Palaeogeography, Palaeoclimatology, Palaeoecology*, *478,* 53-66.

Chapter 2 establishes the ROECE and Series 2 – Series 3 boundary as coincident, but rocks in Scotland are not sufficiently fossiliferous to assess the temporal association between these two events and the extinction of the olenellid trilobites. Chapter 3 examines facies changes, sequence stratigraphy, pyrite framboid petrography and carbon isotope stratigraphy of boundary rocks in the western Great Basin, USA. Sections are investigated in Death Valley, California and Nevada. An abrupt olenellid extinction

horizon in Nevada is correlated, using carbon isotope stratigraphy with the Death Valley sections. The relationship between the Sauk I – II supersequence boundary, anoxia, carbon cycle disruption and extinction is evaluated. The ROECE, extinction horizon and the traditional level of the Series 2 – Series 3 boundary, are shown to be coincident. Specifically, **Chapter 3** aims to answer the question:

What is the temporal relationship between the ROECE event and the olenellid extinction in western US Series 2 – Series 3 boundary strata and what were the environmental changes?

Chapter 4: Faggetter, L.E., Wignall, P.B., Pruss, S.B., Jones, D.S., Grasby, S., Widdowson, M. Newton, R.J. The search for mercury anomalies at the Cambrian Series 2 – Series 3 boundary: evidence for increased volcanic activity coincident with extinction? **Submitted,** *Chemical Geology***.**

Building on the conclusions of Chapter 3, this chapter is the first attempt to show the coincidence of LIP volcanism and extinction at the Series 2 – Series 3 boundary. This chapter presents a mercury record from rocks studied in Chapter 3. Based on the principle that periods of intensive volcanic activity are marked by high concentrations of Hg in the sedimentary record, this paper establishes a Hg chemostratigraphy from the Series 2 – Series 3 boundary sections in the western USA which contain a record of the olenellid extinction and asks the question:

During the extinction of the olenellid trilobites, what is the evidence for coeval volcanism and does sedimentary Hg track the activity of the Kalkarindji LIP?

Chapter 5: Faggetter, L.E., Wignall, P.B., Poulton, S.W., Jones, D. S., Sun, Y., Newton, R.J. Carbon isotope chemostratigraphy and Hg concentrations across the Cambrian Series 2 – 3 boundary, south Georgina Basin, Australia. **In prep.**

The previous three data chapters have focussed on sites located on the Cambrian continent of Laurentia. To gain a global perspective on environmental change, carbon cycle disruptions and the effects of volcanism, this final chapter focuses on rocks from the eastern equatorial

margin of Gondwana. The Series 2 – Series 3 boundary rocks of the South Georgina Basin, central Australia are investigated (Fig. 1.1.). The sedimentary record of this region represents deposition proximal to the Kalkarindji LIP, and is therefore a "ground zero" site at which to investigate the environment imprint of the province. The succession includes a thick carbonate sequence overlain unconformably by black shale (Creveling et al., 2014). The chapter is a preliminary attempt to establish a carbon isotope stratigraphy enabling global chemostratigraphic correlation, Hg chemostratigraphy to explore a "local" signal of Hg deposition proximal to the Kalkarindji LIP and a redox reconstruction to verify the hypothesis that during the Series 2 – Series 3 boundary, Cambrian oceans were oxygen poor. **Chapter 5** builds on the conclusions of all three previous data chapters, presents preliminary data and asks:

In constraining the timing of the Kalkarindji LIP relative to the Series 2 – Series 3 boundary and the global $\delta^{13}C$ chemostratigraphic framework, do proximal sedimentary records preserve Hg enrichments indicative of volcanic activity and what is the temporal relationship to the ROECE event? What is the evidence for ocean anoxia during this interval and does it coincide with the emplacement of Kalkarindji, the ROECE event and by extrapolation, the olenellid extinction interval?

This thesis is designed as a multidisciplinary, global study of palaeoenvironmental change at the Cambrian Series 2 – Series 3 boundary, and an attempt to correlate the relative timing of each of the pre-discussed phenomena. As such we present four regional studies, which when presented in concert, collate an evaluation of events in a global framework. **Chapter 6** synthesizes the findings of the previous four data chapters and discusses the implications before offering further research questions.

1.4   Evolution of the Cambrian System: Biotic changes

The early Cambrian is an extraordinary period of macro-evolutionary divergence among morphologically distinctive bilaterians in the fossil record, which includes the appearance of many representatives of the major modern animal groups. It is essential to contextualise the research questions posed

in this thesis within the broader development of the Cambrian system. Many abiotic and biotic changes rooted in the Proterozoic – Phanerozoic transition played a part in driving the biological expansion witnessed in the Cambrian Explosion and are relevant to the Series 2 – Series 3 boundary; here a summation of developments is presented.

The Cambrian Explosion commenced in the Fortunian Stage, or Nemakit-Daldynian of the Siberian nomenclature. It has long been heralded as perhaps the most significant evolutionary transition in Earth History; marking the appearance of many of the stem groups of modern animals (Valentine, 2002) and the widespread appearance of mineralising animals, a thorough review of which is provided by Kouchinsky et al. (2012) and depicted in Fig. 1.3. Although both soft-tissue and skeletonised macrofossils are present in the latest Ediacaran, their relationship to Cambrian faunas is in debate (e.g. Smith et al., 2016b and Zhu et al., 2017). Despite this, it was during the Cambrian Fortunian that an early increase in global generic abundance initiated, and, by the Cambrian Series 3, 80% of modern skeletal morphotypes were present (Thomas et al., 2000). The divergence of major bilaterian animal clades occurred in a two-phase episodic manner, as exemplified by the diversification of lophotrochozoans in the Fortunian; and, following this, ecdysozoans and deuterostomes in Stage 3 (Fig. 1.3; Erwin et al., 2011; Kouchinsky et al., 2012; Zhang et al., 2014). This step-by-step appearance includes two main clustered sets of geochonronologically distinct intervals of high-rank phylogenies and represents two successive phases of bilaterian diversification (Kouchinsky et al., 2012). The pulsed nature of diversification accompanies a general increase in generic diversity through the Cambrian Terreneuvian and into the Series 2, punctuated by the Botomian – Toyonian biotic crisis heralding ~45% global generic diversity loss (Sepkoski, 1996; Zhuravlev and Wood, 1996).

The first phase of the Cambrian Explosion, marked by the appearance of biomineralised fossils in the Terreneuvian (~ 541 – 521 Ma), is dominated by an array of plates, spines, shells and other skeletal remains of bilaterian affinity (Erwin et al., 2011). Fossil assemblages of the Fortunian depict a pulse of origination in large dominated by disarticulated elements of a
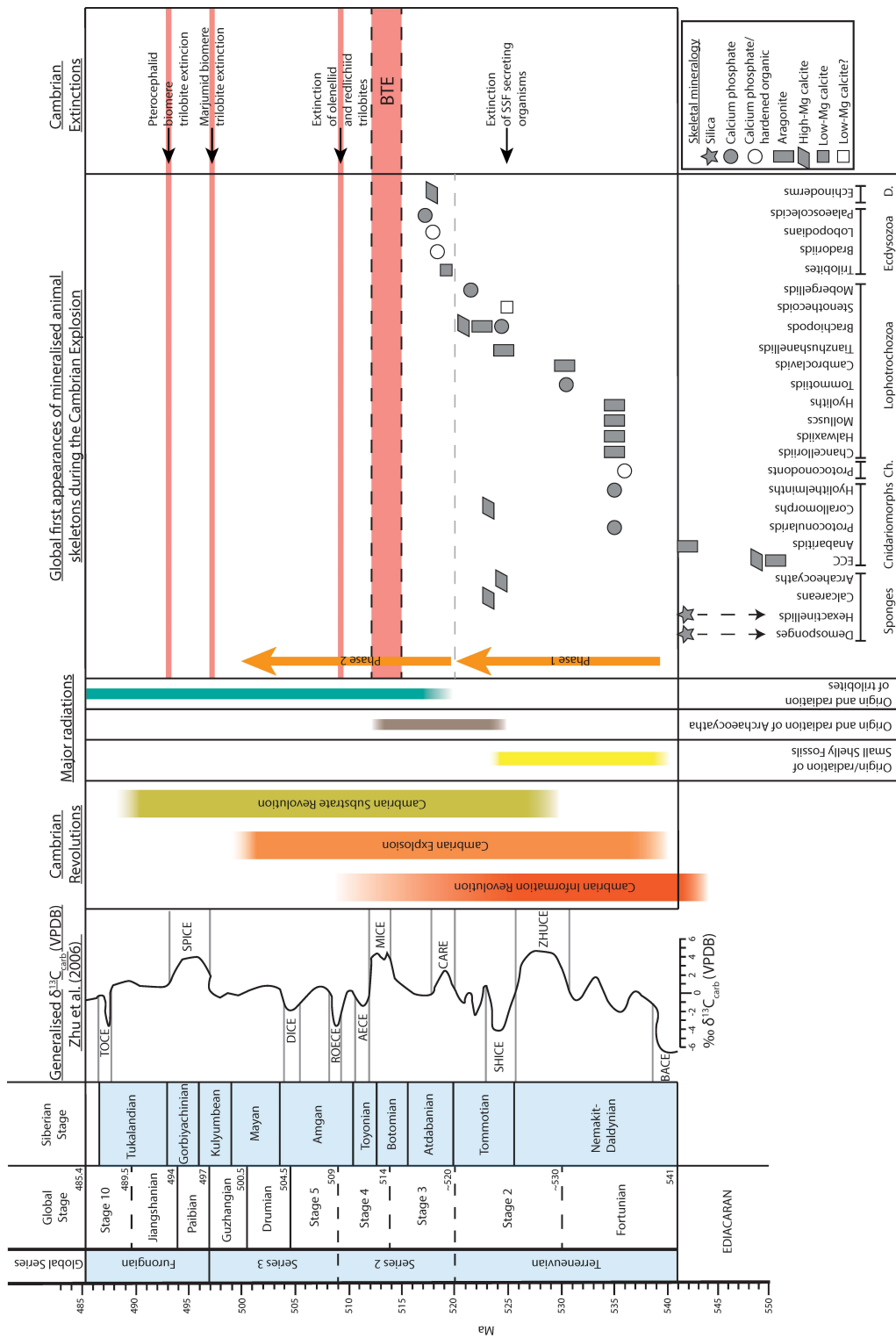
Figure 1.3: Overview of major events during the Cambrian Explosion. Cambrian timescale from Ogg et al. (2016); generalised inorganic carbon isotope curve and Cambrian extinctions from Zhu et al. (2006); SSF range from Maloof et al. (2010); CIR range from Plotnick et al. (2010); CSR range from Bottjer et al. (2010); global first appearances of mineralised animal skeletons from Kouchinsky et al. (2012) where ECC - Ediacaran calcified cnidariomorphs; Ch - Chaetognatha; D - Deuterostomia.

considerably diverse (both morphologically and phylogenetically) collective known as the "Small Shelly Fossils", or "SSFs" (Maloof et al., 2010; Erwin et al., 2011). As an example of their diversity, the SSF group encompassed many animals including anabaratiids, protoconodonts, hyoliths, tommotids, molluscs, conularids, halkieriids, chancelloriids, cambroclaves and other cap-shaped fossils (Maloof et al., 2010). Porter (2004) provides a pertinent observation that many SSF elements are preserved as phosphate minerals, and their diversity peaks coincide with phosphate deposits. Although phosphate deposits are common in the Ediacaran, these deposits lack SSFs, suggesting the acquisition of skeletons in the bilaterian clade can be linked to changing seawater chemistry in the Cambrian (Porter, 2004). In Stage 2 (Tommotian), other, larger, metazoan body fossils appear, exemplified by appearance of the archaeocyaths (Fig. 1.3; Maloof et al., 2010). Although once problematic, archaeocyaths are now considered to be filter-feeding sponge-grade metazoans and, in symbiosis with calcifying microbes, were important bioherm framework builders during the Tommotian (Rowland, 2001). Often in association with archaeocyaths, other large calcifying metazoans also appeared in the Tommotian, including radiocyaths and corallomorphs (Zhuravlev, 1986; Debrenne et al., 1990; Kruse et al., 1995; Kouchinsky et al., 2012), marking another distinct pulse in origination.

Following this, in the Cambrian Stage 3 (Atdabanian), phase two of bilaterian radiation is marked by the first appearances of biomineralisation in the superphylum Ecdysozoa. Body fossils appear that are recognisable as belonging to broader Phanerozoic taxa such as the appearance of the phylum Echinodermata and the phylum Arthropoda; containing perhaps one of the most recognisable class of animals often associated with the Cambrian Explosion- trilobites (Zhuravlev and Riding, 2001). The order Redlichiida (family Archaeospididae, including the redlichiid and olenellid trilobites) are the earliest trilobites and the earliest fossils of which are observed on the Siberian Platform. Widespread evidence for biomineralisation among this second radiation phase is exemplified by the appearance of calcification (low-magnesium calcite) in trilobite carapaces found fossilised in Stage 3 (Atdabanian) deposits in Siberia and Laurentia (Kouchinsky et al., 2012). Following this, calcium phosphate carapaces of

lobopodians and palaeoscolecids appeared in the middle part of Stage 3 (Fig. 1.3; Kouchinsky et al., 2012).

Aside from mineralised skeletons, enormously important in tracking the Cambrian Explosion is the trace fossil record. Also known as the ichnofossil record, these sedimentary imprints provide an insight into biotic expansion beyond the fossilisation of skeletal remains or soft-bodied organisms in Lagerstätte. The Cambrian Terreneuvian and Series 2 displays a dramatic increase in the amount of ichnodiversity (ichnotaxonomic richness) and ichnodisparity (the variability of morphologic plans) in line with the explosion of body fossils during the Cambrian Explosion (Mángano and Buatois, 2016). Across the Ediacaran – Cambrian boundary and into the Cambrian Terreneuvian, the number of ichnogenera rose from 11 in the Ediacaran to 42 in the Cambrian Fortunian. Again, demonstrating the rise in ichnodisparity during the Cambrian Explosion was the increase of trace fossil architectural designs, rising from a maximum of seven in the Ediacaran, to 21 in the Fortunian (Mángano and Buatois, 2016).

While metazoan body plans were evolving during the Cambrian Terreneuvian and Series 2, the marine biotic environment was also undergoing dramatic changes, leaving a lasting ecological imprint upon Cambrian sea-floor sediments upon which benthic organisms lived. Ediacaran and late Neoproterozoic seafloors were characterised by well-developed microbial mats (Bottjer and Hagadorn, 1999) and poorly homogenised sediment (Droser et al., 1999) resulting in a sharp sediment-water interface with very little mixing between the two (Bottjer et al., 2000). Across the Ediacaran – Cambrian transition and into the Cambrian Terreneuvian and Series 2, shallow marine substrates became less dominated by microbial mats and were increasingly subject to vertical burrowing- signalling the shift toward a more typical Phanerozoic style substrate with a greater water content in seafloor sediments and a blurred water-sediment interface (Bottjer et al., 2000). The diminution of widespread microbial mat coverage and the increase in vertical burrowing of shallow marine sediments drove an agronomic revolution which shifted the source of microbial or mat-related food sources away from a more layered structure on the surface to well homogenised within the sediment (Seilacher, 1994).

Bottjer et al. (2000) named this transition of seafloor sediments and substrates, and it's evolutionary and ecological effects, the Cambrian Substrate Revolution (CSR) and provided several lines of evidence of the enduring effect this substrate revolution had upon evolution. In the early Cambrian, the extinction of immobile or sessile echinoderms (for example, helicoplacoid echinoderms) that were previously adapted to live on Ediacaran-style microbial or hard substrates, was evidence that the short-term impact of the switch from hard, well consolidated substrate to looser, mixed substrate (Bottjer et al., 2000), drove the selective extinction of fauna adapted to the pre-substrate revolution seafloor. The opposite is recorded for edrioasteroid and eocrinoid echinoderms, which flourished as they adapted to the change in substrates by first living unattached on the seafloor in the early Cambrian, then developing stems and attaching to hard substrates- thereby avoiding the effects of substrate instability resulting from increased bioturbation (Bottjer et al., 2000). The change from Ediacaran mat-dominated to Cambrian softer, water saturated sediments and the agronomic revolution which homogenised food within the substrate also drove an environmental restriction to some animals in the post-CSR world. Metazoans such as molluscs, which would have previously thrived on mat-dominated sediments, were negatively affected by the disruption to a microbial-mat food source by the increasing prevalence of vertical burrows- essentially limiting their habitat to deeper water settings free from burrowing animals (Bottjer et al., 2000).

With the biotic radiation of the Cambrian Explosion, and alongside the CSR, came a broad diversification of sedimentary fabrics. Cambrian biofabrics are a direct product of metazoan appearance and include ichnofabrics, shell beds and constructional frameworks (e.g. archaeocyathan reefs; Droser and Li, 2001). Following the Ediacaran – Cambrian transition, marine sedimentary fabrics were irreversibly changed (except for recovery periods following large mass extinction events). The advent of skeletonised metazoans resulted in sediments composed of skeletal particles and shells; diversifying life modes partially or completely mixed sediments and entirely new sedimentary structures were built through calcifying metazoans (e.g. archaeocyathan reefs; Droser and Li, 2001). Throughout the Cambrian

Explosion there is a clear increase in the extent, tiering depth and complexity of bioturbation, and the sudden appearance of shell beds occur with the earliest skeletonised metazoans (Droser and Li, 2001). Droser and Li (2001) ascribe three important fabric producing process during the Cambrian Explosion: 1) preserved structures that are organised and built by animals- such as reefs, stromatolites and thrombolites; 2) the formation of sedimentary deposits formed of biogenic grains (e.g. skeletal material or oncoids) which are either primary sedimentary deposits or the result of erosion and/or transportation (e.g. shell beds, oncolite beds or oozes); and 3) bioturbated sediments formed from post-depositional processes. The distribution and abundance of biofabrics serve as an important insight into the relative importance or abundance of the organisms that form biofabrics, and as such have been used to evidence the environmental and ecological niches that new Cambrian metazoans inhabited during the Cambrian Explosion. Although trace fossils are present in the Ediacaran, there have been no reported ichnofabrics resulting from this Precambrian activity; the earliest ichnofabrics are described in sections containing the first appearance of *Treptichnus pedum*, the sinuous, looping burrow, which both defines the base of the Cambrian and represents the development of preservable infaunal activity (Droser and Li, 2001). Droser and Li (2001) outline several important Cambrian ichnofabrics and shell concentrations: *Skolithos* piperock, *Teichichnus* burrows, "mottled" limestone and shell beds (described by the organism dominating the composition, e.g. a trilobite shell bed). The *Skolithos* piperock first appears in the Series 2 and is perhaps the best-known Cambrian ichnofabric, composed of vertical burrows, often densely distributed and widespread amongst high-energy shallow marine sandstones. Piperock is most commonly associated with *Skolithos*, but is also produced by *Monocraterion* and *Diplocraterion* (Droser and Li, 2001). The ichnofabric *Teichichnus* is widespread and common throughout the Cambrian and is formed by the *Teichichnus* burrow that will typically partially or totally disrupt sedimentary fabrics and dominate the ichnofabric exhibiting bioturbation up to 6cm deep (Droser and Li, 2001). Finally, "mottled" ichnofabrics in the Cambrian are common and are typically found in shallow marine carbonates which have been bioturbated by *Thalassinoides*,

Planolites and *Bergaureria*. While early Cambrian mottled limestones retain bedding and sedimentary structures, it is not uncommon for all sedimentary fabrics to be destroyed by bioturbation later in the Cambrian (Droser and Li, 2001).

The CSR, concomitant diversification and increased disparity of biofabrics and trace fossils alludes to a further sophistication amongst the biotic realm during the Cambrian radiation. This depicts an environment that is characterised by more complicated relationships between predators, prey, primary producers and their surrounding environment (Plotnick et al., 2010). To describe this within a framework that accounts for increasing sensory interaction (or "sensory ecology"), Plotnick et al. (2010) proposed the Cambrian Information Revolution (CIR). This conceptualises an information landscape or distribution of environmental signals, where a signal is generated, transmitted, detected, processed and potentially responded to- essentially describing cognition amongst the organisms of the Cambrian Explosion. The concept of this information landscape details the navigational capacities of the organism and the sensory information about the external environmental that is received and processed whilst determining how and why to move around in their environment (Plotnick et al., 2010). The information landscape is described by Plotnick et al. (2010) in three ways: 1) the object or source landscape describes the location in space of the object of interest (e.g. a mate, predator, prey or food) that could generate a signal potentially reaching an organism. 2) the signal landscape is the spatial distribution of all the signals, the spatial distribution results from the interaction of the processes of signal propagation with the pattern of signal sources. 3) the information landscape is the distribution of the signals as they are sensed by the organism, this is fundamentally determined by the ability of the animal to detect and process the information landscape. The CIR is grounded in the theory of "movement ecology" proposed by Nathan et al. (2008); which addresses new behaviours exhibited by bilaterians radiating during the Cambrian Explosion, such as the internal state (why move?), biomechanical functionality (how to move?), navigation capabilities (when and where to move?) and the influence of exogenous factors (e.g. food resources, predator-prey relationships). Movement ecology places a

strong emphasis on the importance of the external environment, and environmental signals as a key facet driving behavioural responses (Nathan, 2008). The CIR underscores the notion that the Cambrian Explosion is characterised by increasing complexity and heterogeneity of marine ecosystems and that this complexity results in further evolutionary change (Plotnick et al., 2010). Plotnick (2007) notes that there is a paucity of evidence that macroscopic sensory organs existed during the Ediacaran, though maintains that it is likely that Ediacaran organisms were photosensitive. In the Cambrian Terreneuvian, there is little evidence that SSFs had developed sensory organs, the earliest preserved visual organs are trilobite eyes from the base of Cambrian Stage 3 (Clarkson et al., 2006). The key facets of the CIR depict the coevolution of an increasingly spatially complex marine environment and complex sensory systems, evolving as a root consequence of the Cambrian Explosion, rapid diversification and increasing disparity of mobile bilaterian taxa (Plotnick, 2010). Plotnick et al. (2010) proposes that information landscapes evolved rapidly from the Ediacaran into the Cambrian and became widespread and heterogeneous, maintaining a causal link to the widespread biological and environmental changes of the Cambrian Explosion, CSR and major bilaterian radiations.

Despite the evident proliferation of life and the environment during the Cambrian Explosion, there were critical intervals characterised by severe biological crises and major turnover at generic levels; the first of which occurring in the late Series 2 (Fig. 1.3). During the Cambrian Series 2, the engineering and widespread construction of archaeocyathan reefs represents the acme of Cambrian sponge morphologies, diversity and habitability which supported a diversity of fauna (Zhuravlev and Wood, 1996). Archaeocyathan reefs radiated from the Siberian platform to every other continent of the Cambrian globe. Physically, these structures were very large (up to 80m tall, e.g. Rowland, 2004), ecologically diverse habitats that supported a variety of life and were a critical source of organic carbon, nutrients and oxygen to early Cambrian environments (Wood, 1999). Just 15 million years into the Cambrian Explosion, metazoan animal evolution reached a pinnacle in family-level diversity, then dropped precipitously,

marking the onset of the Botomian – Toyonian extinction (BTE). The remarkable diversification witnessed in the Cambrian Fortunian and Stage 2 was abruptly halted by the Sinsk Event - a decline in global generic diversity in archaeocyathan reefs and in the off-reef Tommotian fauna, which badly affected trilobites and hyoliths (Brasier, 1996). The Sinsk Event is linked to the widespread encroachment of deep water marine anoxia onto the shallow-marine shelves, where archaeocyathan reefs proliferated, this platform drowning is best evidenced by the deposition of black shales of the Siberian Sinsk Formation, (Gondwanan palaeocontinent; Zhuravlev and Wood, 1996; Ivantsov et al., 2005). The cause of this widespread anoxic event is still elusive. Theories pertain to persistent eutrophication and corresponding phytoplankton blooms driving extensive anoxia and to dramatic climate change following the eruption of the Kalkarindji large igneous province (LIP; Zhuravlev and Wood, 1996; Jourdan et al., 2014); but also to the reduction in suitable mid-shelf carbonate habitats severely affecting highly provincialized faunas (Brasier, 1996). Throughout geological history the emplacement of LIPs has been directly correlated to mass extinction events (Wignall, 2001). Not only is the Kalkarindji LIP the first known Phanerozoic LIP, but its age also closely corresponds to the BTE, evoking a temporal association similar to other LIP – extinction events. There is only one reliable U-Pb zircon date for the Kalkarindji (Jourdan et al., 2014) and therefore the age framework for the Kalkarindji is in its early stages of development.

Following the Sinsk Event and the apparent de-oxygenation of Botomian – Toyonian oceans, the Hawke Bay Regression Event (HBRE) sea level fall/regression bracketed the BTE. The Hawk Bay Regression Event is observable on several Cambrian continents (Hallam and Wignall, 1999; Rowland and Shapiro, 2002) and heralded the final extinction event, killing off the remaining archaeocyath populations, severely affecting hyoliths as well as some endemic, shallow marine trilobites (Brasier, 1996; Zhuravlev and Wood, 1996). In the case of marine anoxia and sea-level change, it is hypothesised that archaeocyaths were vulnerable due to their benthic, sessile, filter feeding life mode. They are reliant upon healthy ecosystems to feed and proliferate, and were unable to migrate from shallow continental

shelves and escape rapid environmental change and intensifying anoxia (Zhuravlev, 2001).

Despite trilobites undergoing widespread radiation from the Cambrian Series 2 onward, there is also significant replacement of large trilobite faunas from the Cambrian Series 3 through to the upper Furongian (Fig. 1.3). These faunal divisions are known as a "biomeres" and are characterised by Palmer (1965) as "a regional biostratigraphic unit bounded by abrupt non-evolutionary changes in the dominant elements of a single phylum" and asserts that the changes between biomere faunas (i.e. extinction of faunas) are not necessarily due to sedimentary hiatus and they are, or may be, diachronous. Typically, biomere boundaries exhibit a pattern of abrupt diversity drop and the taxonomic turnover of all, or nearly all, of the trilobites at generic level, of which there are at least three clear examples from the Laurentian of North America (Fig. 1.3; Palmer, 1984). The first such example of this occurs at the top of the Olenellid biomere, marked by the top of the *Olenellus* zone, at the Cambrian Series 2 – Series 3 boundary (e.g. Palmer, 1998; Webster et al., 2008; Faggetter et al., 2017). This event is best recorded in Series 2 – Series 3 boundary strata from the Pioche Formation, eastern Nevada (Palmer, 1998; Webster et al., 2008). Preceding their disappearance, Olenelloid trilobite species are found abundantly in non-archaeocyathan bearing limestone and siliciclastic rocks, however, approaching the top of the *Olenellus* zone in Nevada (Ruin Wash, see Chapter 3), a diverse assemblage of 8 olenellid species abruptly disappear with no evidence of declining populations or facies control (Palmer, 1998; Webster et al., 2008). Though no rigorous attempts to fit multiple sections recording the olenellid extinction within a sequence stratigraphic framework exists, preliminary evidence suggests that the last appearance of the olenellids displays a close temporal association with sea level fall, namely the Sauk I/ Sauk II boundary; this thesis therefore investigates the link between extinction and sea-level change. It is also noted that a close temporal relationship exists between a large negative (globally reproducible to ~ -4‰) $\delta^{13}C_{carb}$ excursion named ROECE. Previous suggestions by Brasier (1996) suggests a close correspondence between olenellid trilobite extinction and BTE, this thesis also addresses the temporal distinction

between the two events, based on new $\delta^{13}C$ chemostratigraphies and the distinction between ROECE and the BTE associated MICE/AECE events (Figs. 1.2; 1.3). Finally, as aforementioned, the close temporal association between the ROECE, olenellid and redlichiid (of Gondwana) trilobite extinction and the emplacement of the Kalkarindji LIP has invoked an LIP-volcanism style link between these events (e.g. Jourdan et al., 2014). However, very little evidence exists beyond the temporal coincidence, as such this thesis sets out to investigate a sedimentological trace of volcanism coincident with extinction and ROECE.

In the Furongian, there are significant trilobite turnover events associated with the top of the Marjumid and Pterocephalid biomeres, essentially bracketing the base and top of the Paibian Stage (Fig. 1.3; Brasier et al., 1996; Saltzman et al., 2000; Taylor, 2006; Zhu et al., 2006; Gill et al., 2011; Gerhardt and Gill, 2016). These two trilobite turnover events bookend a significant positive (globally reproducible to ~+5‰) $\delta^{13}C_{carb}$ excursion named Steptoean PositIve Carbon isotope Excursion (SPICE; Fig. 1.3), the peak of which corresponds with a period of maximum regression in Laurentia (the Sauk II/Sauk III boundary; Saltzman et al., 2000). The initial end-Marjumid extinction close to the base of the Paibian (regionally the Marjuman-Steptoean of Laurentia, hence the "Marjumid" extinction), is in fact made of up a two-phase extinction event in the base of the Paibian (Gerhardt et al., 2016). The first extinction occurring at the top of the Marjumid biomere (corresponding to the Guzhangian – Paibian boundary) and the second event in the base of the Pterocephaliid biomere (in the basal Paibian; see Gerhardt et al., 2016 for in depth description). The first extinction of this two-phase event shows little evidence that it coincides with any significant disruption to the carbon cycle, and as such its relationship with the SPICE excursion appears temporal, until further trends are elucidated (Gerhardt, 2016). However, the onset of SPICE corresponds well with the second-phase extinction in the basal Pterocephaliid biomere in the lower Paibian (Gerhardt et al., 2016). There is also abundant geochemical evidence that the onset of SPICE marks the spread of anoxic/euxinic conditions in subsurface ocean waters (Saltzman et al., 2000; Gill et al., 2011), and therefore Gerhardt et al. (2016) suggest the possibility that anoxia may be a

driving mechanism behind this second phase of extinction within the basal Paibian Pterocephaliid biomere. Bracketing the end of SPICE is another extinction event in the base of the Ptychaspid biomere (Brasier, 1996; Palmer, 1979). Again, occurring in the two-step fashion, the first stage recording the decline of shallow-shelf genera and families coincident with the deposition of phosphatic limestones and the appearance of exotic olenid trilobites; followed by the complete disappearance of shallow-shelf trilobites as replaced by a diverse fauna of olenid trilobites (Taylor, 1985). Taylor (1985) and Brasier (1996) note that the coincidence of phosphatic limestones in association with a shift from heavier to lighter carbon isotopes during the end of the SPICE interval suggests the plausibility that oxygen-depleted, possibly cooler water, may have accompanied the migration of olenid trilobites may have driven out the preceding more endemic shallow-water faunas.

1.5   Abiotic changes: changing seawater chemistry over the Proterozoic – Phanerozoic transition

As discussed, the Proterozoic – Phanerozoic transition is most famously defined by the dramatic diversification of multicellular animals and their newly acquiesced mineralised skeletons in the late Ediacaran (Droser and Gehling, 2015). More recently, considerable efforts have been made to correlate biotic patterns during this interval with tectono-physiographic regimes of enhanced continental weathering; anomalous rates of sedimentation; significant expansion of the marine reservoir of weathering products; increased ocean alkalinity and nutrient flux; and the widespread formation of shallow and epicontinental seas (Squire et al., 2006; Peters and Gaines, 2012). This is recorded by the influx of continental weathering products to the global ocean, the changing ocean chemistry during the early Cambrian and also stable isotope systems of $^{87}Sr/^{86}Sr$ and ^{13}C, and framed within a sequence stratigraphic framework (e.g. Keller et al., 2012). Discussed here are the precursor changes that occurred across the Proterozoic – Phanerozoic transition that have been widely accredited as laying the foundational abiotic conditions that allowed the dramatic biotic proliferation of the Cambrian Explosion.

1.5.1 Continental denudation and later transgression: the Great Unconformity and the Sauk Supersequence, insights from the Laurentian continent

The Great Unconformity is a geomorphic surface separating Neoproterozoic and Phanerozoic rocks – first described from Laurentia in the Grand Canyon, SW USA, and later reported globally from Gondwana, Baltica, Avalonia and Siberia (Brasier, 1980; Sears and Price, 2003; Avigad et al., 2005; Peters and Gaines, 2012). Typically, this nonconformity represents a widespread erosive surface exposing crystalline continental basement rocks which are overlain by marine deposits of Cambrian age. This globally recognisable stratigraphic surface marks the termination of a protracted period of continental denudation through the Neoproterozoic, during which extensive areas of igneous and metamorphic rocks were exhumed, physically and chemically weathered, mobilised and deposited overlying the Great Unconformity (Peters and Gaines, 2012). The ensuing enhanced physical and chemical weathering of silica-rich continental crust resulted in anomalously high rates of sedimentation and is represented by the deposition of thick marine transgressive sedimentary packages in the Cambrian, e.g. the Sauk Sequence (Keller et al., 2012; Peters and Gaines, 2012).

Unlike other first order Phanerozoic sequence stratigraphic boundaries, the Great Unconformity is unique in that the sediments overlying exposed basement rocks preserve the first appearance of mineralising crown-group animals (Marshall, 2006). As such, it has garnered much attention as a contributor to the precursor ocean geochemical conditions fostering early metazoan animal radiation and initiating the appearance of mineralising metazoans (e.g. Porter, 2004; Squire et al., 2006; Peters and Gaines, 2012). Overlying the Great Unconformity on the Laurentian continent is the first craton-wide depositional package of the Phanerozoic; the Sauk Sequence (Fig. 1.4 A; Keller et al., 2012; Peters and Gaines, 2012). This time-transgressive, Cambro – Ordovician Sauk Sequence is the basal package of a long-term sinusoidal trend elucidating 56 myr (~3 myr) cycles of oscillating sedimentation through the Phanerozoic (Meyers and
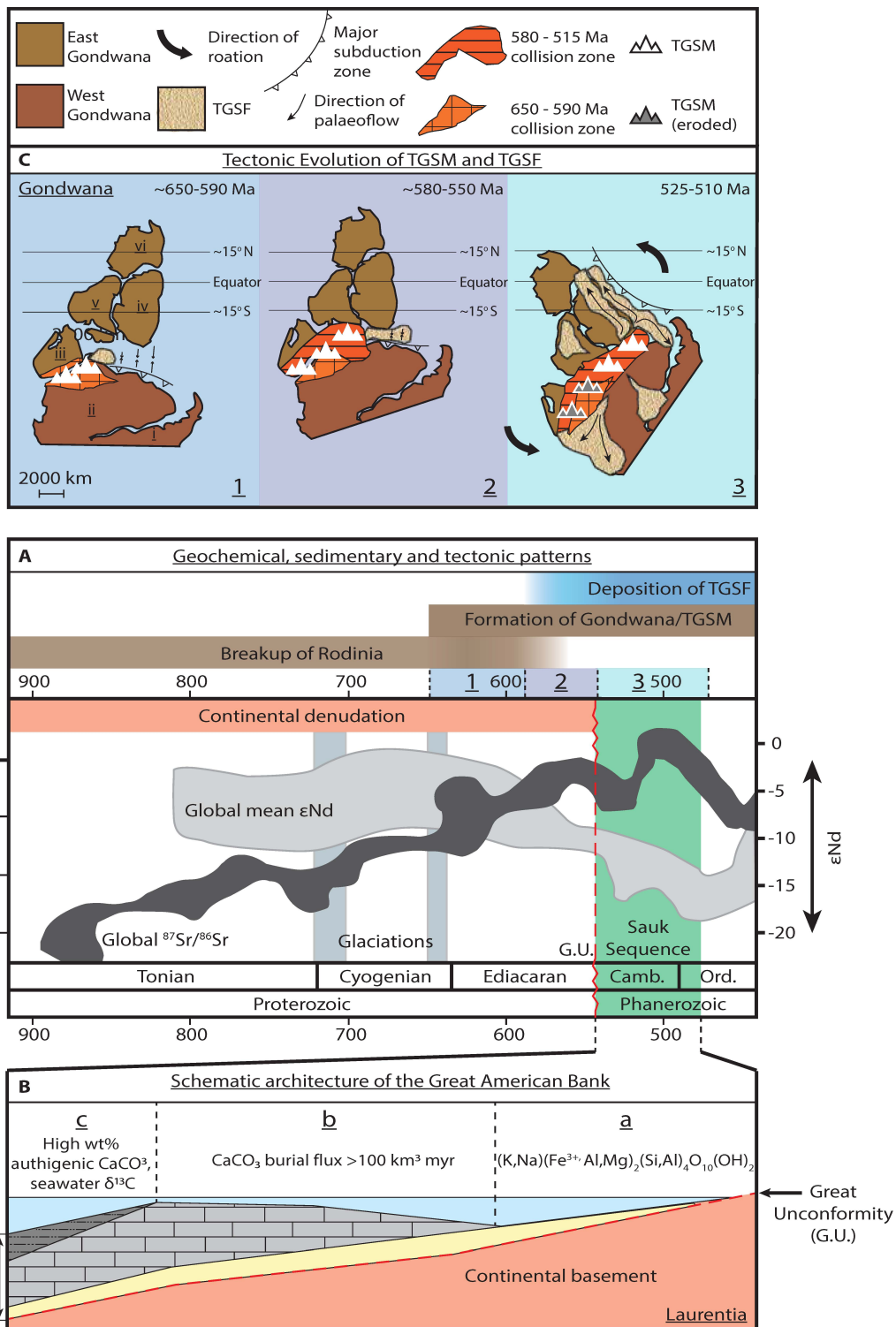
Figure 1.4: Overview of Proterozoic - Phanerozoic transition. A: Geochemical, sedimentary and tectonic patterns modified from Peters and Gaines (2012) and Keller et al. (2012). B: Schematic architecture of the Great American Bank and Sauk Sequences,   modified from Peters and Gaines 2012. C: Amalgamation history of Gondwana modified from Squire et al. (2006).

Peters, 2011) and exhibits the highest sedimentation rates of the past 900 myr (Peters and Gaines, 2012). During the Sauk Sequence transgression, the landward shift of erosive shoreface, backshore, aeolian and fluvial zones accentuated physical and chemical weathering rates on the Great Unconformity (Peters and Gaines, 2012). The passage of this transgression efficiently stripped and remobilised low continental interiors of soil and regolith, vastly increasing the spatial extent of silicate mineral weathering and transport (Peters and Gaines, 2012). This is pertinent because freshly exposed soil and regolith chemically weathers faster than undisturbed rock (more than three times faster; Millot et al., 2002; Mortatti and Probst, 2003), and the chemical weathering of basement-rock silicate minerals is enhanced by physical reworking during the passage of transgression (Millot et al., 2002). The sharp transition between Proterozoic basement rocks and the dominant quartz and feldspar marine deposits overlying the Great Unconformity is evidence of the efficacy of transgressive shoreface systems to remove and remobilise continental regolith (Peters and Gaines, 2012) and represents an intense and prolonged period of increased weathering flux to early Cambrian oceans.

This prolonged period of denudation, subsequent enhanced physical and chemical weathering, and reworking of material during transgression impacted directly on critical changes in seawater chemistry and subsequent global biogeochemical cycling (Peters and Gaines, 2012). Enhanced continental silicate weathering resulted in dramatically increased consumption of atmospheric CO_2, amplifying the flux of HCO_3^-, Ca^{2+}, $H_3SiO_4^-$, SO_4^{2-}, Cl^-, Na^+, Mg^{2+}, K^+, Fe^{3+} ions to the oceans (Millot et al., 2002; Mortatti and Probst, 2003; Peters and Gaines, 2012) thereby increasing the ocean reservoir size of continental weathering products. Peters and Gaines (2012) posit that the establishment of Sauk carbonate deposits is evidence that earliest Cambrian oceans stored a large pre-existing reservoir of continental weathering products and experienced enhanced weathering fluxes originating from the formation, and subsequent transgression over, the Great Unconformity. As sedimentological evidence for this, they define a continent-wide (Laurentian) sedimentary architecture encompassing three facies belts (Fig. 1.4 B): a generally coarse grained,

near shore, inner detrital belt; a broad, thick, middle carbonate belt; and an outer, fine grain detrital belt; and investigate the sedimentological and geochemical evidence for a large marine reservoir of continental weathering products.

The broad, thick, and time-extensive middle belt carbonate platform most parsimoniously evidences enhanced continental crust weathering. On Laurentia, the deposition of the Cambro – Ordovician carbonate belt known as the "Great American Bank" represents the peak in Phanerozoic carbonate shelf burial (Ronov et al., 1980; Ginsburg, 1983; Walker et al., 2002), driven in large by seawater chemistry following the Great Unconformity and transgressive reworking (Peters and Gaines, 2012). In the Cambrian Terreneuvian, conditions aligned to enable the formation of the Sauk carbonate deposition on Laurentia (and elsewhere globally e.g. Maloof et al., 2010; Schopf et al., 2015; Smith et al., 2016a; Schmid, 2017). The continent was positioned in an equatorial low-latitude setting encouraging of carbonate formation, evidenced by anomalously high rates of carbon throughput (e.g. large reflexive carbon isotope excursions, see Maloof et al., 2010). Coupled with an absence of a deep-sea carbonate sink (established in the Mesozoic by the appearance of calcareous plankton; Ginsburg, 1982; Walker et al., 2002), this meant that Cambrian carbonate burial rates were only constrained by the accommodation space created by rising sea level during the Sauk transgression, and by the rapid subsidence of the Laurentian passive margin (Levy and Christie-Blick, 1991; Keller et al., 2012; Peters and Gaines, 2012). This resulted in the highest burial flux of shelf carbonates in the Phanerozoic (Fig. 1.5; Peters and Gaines, 2012). This is supported by trends exhibited through the Phanerozoic, illustrating that the area of continental basement rock exposed before sedimentation predicts changes in carbonate burial rates (Fig. 1.5; Peters and Gaines, 2012).

Further evidence supporting the link between enhanced weathering of continental crust during the Sauk transgression comes from outer detrital belt mudstone facies. Coupled petrographic and geochemical analysis demonstrates a corresponding increase in authigenic carbonate precipitation in carbonate cemented mudstones of the Sauk Sequence (Gaines et al., 2012). Carbonate cemented mudstones are abundant throughout the
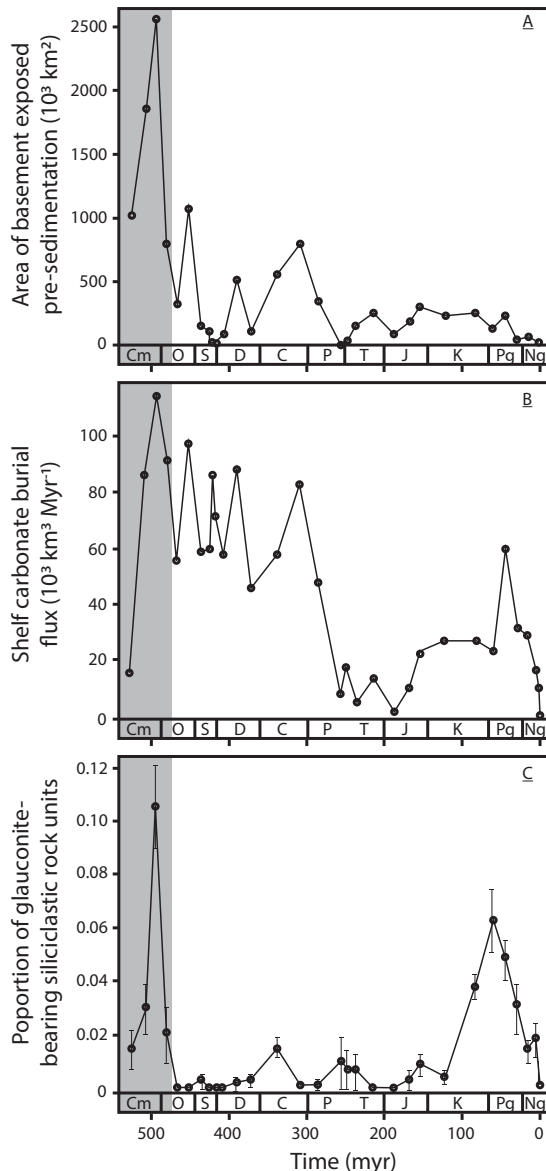
Figure 1.5: Phanerozoic sedimentation patterns from North America, including Sauk Sequence, from Peters and Gaines (2012).

Phanerozoic; however, a significant amount form through microbially mediated remineralisation of organic matter, and therefore do not exhibit an authigenic $\delta^{13}C$ value, rather they are depleted relative to seawater values (Coleman, 1985). Carbonate cements found in the outer detrital belt exhibit three supporting characteristics indicative of authigenic carbonate formation; 1) a greater wt% carbonate than composite shale standards, 2) $\delta^{13}C$ values consistent with precipitation from seawater, and, 3) petrographic textures indicating rapid, displacive growth at the sediment – water interface (Fig. 1.4 B; Gaines, 2012; Peters and Gaines, 2012). Additionally, detrital micrite is absent or rare, and concretions and mud-mounds exhibit $\delta^{13}C$ indicating precipitation from sea-water derived bicarbonate (Elrick and Snider, 2002).

Finally, the signal of enhanced weathering of continental basement-rock is preserved in the inner detrital belt by a peak in glauconite-rich

siliciclastic rocks (Fig. 1.5; Peters and Gaines, 2012). Chafetz and Reid (2000) state that the conditions necessary to foster the formation and accumulation of glauconite-rich facies in the Cambrian must differ drastically from modern marine shelves. In the modern, glauconite authigenesis occurs in areas where sedimentation rates are low, and pore-water exchange with seawater is sustained over long periods of time (Odin and Matter, 1981). However, Chafetz and Reid (2000) predicate that unusually frequent and widespread deposition of glauconite rich facies requires rapid authigenesis in seawater containing high concentrations of weathering products, particularly K^+, Fe^{3+} and $H_3SiO_4^-$, which Peters and Gaines (2012) argue is fostered in the inner detrital belt by restricted circulation and low sedimentation rates. Unusual ocean chemistry in the early Cambrian has long been recognised, in particular, an anomalous abundance of glauconite and phosphate (e.g. Brasier, 1980; 1990) associated with nutrient rich waters (Brasier, 1992) and transgression (Brasier, 1980; Peters and Gaines; 2012), often iterated as a driving factor behind the explosion of mineralising animals in the Cambrian (e.g. Porter 2004). Pertinently, the Sauk Sequence represents the peak in the proportion of glauconite-bearing siliciclastic rocks during the Phanerozoic and a dramatic pulse in Ca^{2+} concentrations measured in evaporite fluid inclusions; both peaks are attributed to a large dissolved marine reservoir of weathering products following the Sauk transgression (Fig. 1.5; Lowenstein et al., 2001, Peters and Gaines, 2012). Importantly, the deposition of massive swathes of shallow marine carbonate platforms in an ocean saturated in weathering products available for biomineralisation is widely suggested to have created the ecospace (e.g. archaeocyath reefs, trilobite biomeres) and ocean precursor conditions that would harbour many of the faunas of the Cambrian Explosion (Porter, 2004; Squire et al., 2006; Keller et al., 2012; Peters and Gaines, 2012).

1.5.2 Transgondwanan Supermountain erosion and the formation of the Gondwana Super-fan system

Tectonic activity in the Proterozoic led to dramatic continental rearrangement, collisional orogenesis and convergent-margin orogenesis across the Proterozoic – Phanerozoic transition (Squire et al., 2006). Following the breakup of Rodinia between ~900-650 Ma (Hoffman, 1991)

the fragments of the supercontinent (Africa, Antarctica, Arabia, Australia, India) began to collide and amalgamate forming a large proto-Gondwanan terrane and a collision zone between the existing East and West Gondwanan blocks (Fig. 1.4 C; Squire et al., 2006). During the early Cambrian, the collision occurred between the main continental blocks comprising East Gondwana (composed of Arabia, Australia, Antarctica, India) and West Gondwana (Africa and South America), driving uplift which would form the East African – Antarctic Orogen (also known as the Pan African Orogeny) across central Gondwana (Fig. 1.4 C; Squire et al., 2006; Meinhold et al., 2013). Squire et al. (2006) analysed and compiled detrital-zircon U-Pb age patterns from across Africa, Antarctica, Arabia, Australia and India to trace the detrital provenance, and reconstruct the orogenic history of ~100km^3, of quartz rich, early Palaeozoic sedimentary units. This immense depositional system, known as the Transgondwanan Super-fan (TGSF), formed in response to the erosion of the Transgondwanan Supermountain (TGSM), an >8000 km long and ~>1000 km wide mountain chain along the East African – Antarctic Orogen (Fig. 4 C; Burke and Kraus, 2000; Squire et al., 2006). River systems drained and transported vast volumes of detritus from the TGSM to giant sedimentary fans forming the TGSF, depositing sediments in proximal foreland basins and eventually in distal parts of the system in intracontinental basins (e.g. the Mozambique basin; Boger and Miller, 2004; Squire et al., 2006, Meinhold et al., 2013). Early Cambrian quartz-rich sedimentary units of the TGSF are found in modern day India, Israel, Africa, Australia, New Zealand, South America and Antarctica (Squire et al., 2006). Reconstructing accurate estimates for the total sediment volume deposited by the TGSF is inherently problematic. However, estimates have been made by calculating volumes of component fan systems from Australia, Arabia and north Africa (constituting less than half of the total fan system) and infer that the original areal extent of the fan system was close to 3.5 times larger than the modern-day Bengal Fan, making the original volume of the TGSF plausibly greater than >100 Mkm^3 (Curray, 1991; Fergusson and Coney, 1992; Burke and Kraus, 2000). Composite detrital-zircon U-Pb analysis display a dominant ~650-550 Ma peak and secondary ~1200-900 Ma from the early Cambrian deposits of the

TGSF, exhibiting the close temporal relationship between continent-continent collisional orogeny (East and West Gondwana), erosion, and massive sediment deposition (Squire et al., 2006; Meinhold et al., 2013). The shutdown of the TGSF system is evidenced by the sudden diminution in the extent of quartz-rich sedimentary rocks in the late Ordovician (Squire et al., 2006). However, late Silurian and late early Devonian (~390 Ma) quartz-rich turbidites likely represent the final deposition stage of the TGSF.

The dating of the TGSF and its extensive quartz-rich sedimentary deposits establishes an episodic nature for the tectonic evolution of Gondwana. This is critical when considering the influence of uplift, exhumation of deep metamorphosed basement rocks, sustained continental weathering, sediment flux and subsequent reworking upon evolving ocean chemistry during this interval. The initial phase of mountain building associated with the TGSM formation occurred between ~650-590 Ma, resulting from the oblique collision of eastern Africa and the Arabian – Nubian Shield, (Fig. 1.4 C; Abdelsalam et al., 2003). Following this, the most extensive phase of development of the mountain chain ensued during continued oblique convergence between East and West Gondwana, ~580 Ma and coincided with extensive drowning of craton margins in northern Africa and Arabia (Fig. 1.4 C; Brasier and Lindsay, 2001; Boger and Miller, 2004; Squire et al., 2006). A final phase of continental suturing occurred ~525-510 Ma, and represents the collision of Antarctica and Australia with India, Africa and South America (Fig 1.4 C), a zone known as the Kuunga intracratonic zone (previously Kuunga intracratonic zone, see Squire et al. 2006 for discussion). This three-phase framework for the amalgamation of Gondwana (northeast Africa, eastern Africa and the Kuunga intracratonic zone) occurred in rapid succession with the latter two collision events (eastern Africa and the Kuunga suturing) occurring in anomalously short periods (~30 and 15 Ma respectively) given the great length and highly irregular margin shape (Squire et al., 2006). This extensive period of continental amalgamation, uplift and erosion drove deposition and reworking of the TGSF for at least 260 myr (650-390 Ma), liberating and transporting enormous volumes (>100km^3) of detritus rich in continental weathering products eroded from the TGSM (e.g. P, Fe, Sr, Ca, HCO$_3$) to marine

sedimentary basins in the early Palaeozoic, delivering more ions to shallow marine environments, fuelling widespread biomineralisation during the Cambrian Explosion (Squire et al., 2006).

1.5.3 Continental weathering history of the Proterozoic – Phanerozoic transition traced by increasing stable ^{87}Sr/^{86}Sr isotopes values

In modern seawater, Strontium (Sr), is derived from two major sources; submarine alteration of ocean crust (due to increased seafloor spreading rates) and the subaerial chemical weathering of continental crust and regolith, producing a range of ^{87}Sr/^{86}Sr values spanning 0.703-0.712 (ocean crust – continental crust respectively) (Hoffman, 1997; Puecker-Ehrenbrink and Miller, 2006; Shields, 2007). Once normalised to account for the isotopic evolution of Sr sources to the ocean, the ^{87}Sr/^{86}Sr composition of seawater is strongly influenced by changes in the flux of continental weathering relative to ocean crust weathering on geological timescales (Shields, 2007). Seawater ^{87}Sr/^{86}Sr values show a progressive increase from ~0.7055 to 0.7090 between ~800 Ma to ~500 Ma (Fig. 1.4 A; Jacobsen and Kaufman, 1999), exhibiting the highest ^{87}Sr/^{86}Sr values in the past 900 myr close to the Cambrian Series 2 – Series 3 boundary (Fig 1.6; Montañez et al, 2000; Peters and Gaines, 2012). Peters and Gaines (2012) recognised the long-term rise in seawater ^{87}Sr/^{86}Sr during the Neoproterozoic and attributed this trend to the progressive decay of ^{87}Rb in the continental crust and to the long-term erosion and exposure of ^{87}Sr rich granitic rocks required the form the Great Unconformity. In the late Proterozoic, Squire et al. (2006) ascertains that increasing seawater ^{87}Sr/^{86}Sr values are accentuated by topographic and biotic conditions during the uplift and erosion of the TGSM. After ~700 Ma, Squire et al. (2006) places emphasis of the role of the steep topography of the TGSM and the advent of primitive soil biota in continental regolith in accelerating continental erosion and the flux of weathering products from the TGSM to the oceans.

In the Cambrian Terreneuvian, seawater ^{87}Sr/^{86}Sr values in carbonate rocks from Morocco, Siberia, Mongolia and China exhibit a monotonic decline by ~0.0006 (Fig. 1.6; Maloof et al., 2010). A major control thought to underlie changing seawater mineralogy is the Mg/Ca ratio of seawater; ratios of ~2.0 favouring aragonite production and lower values favouring calcite

(Lowenstein et al., 2001). Such shifts in seawater chemistry are therefore thought to have driven switches between ocean states that favour aragonite (aragonite seas) and those that favour calcite (calcite seas) production, and are reflected in the mineralogy of biomineralising metazoans during the Cambrian Explosion (Porter, 2004; Maloof et al., 2010). Mechanisms explaining declining seawater $^{87}Sr/^{86}Sr$ values in the Terreneuvian are discussed in detail by Maloof et al., (2010), in which several model scenarios of changing seawater chemistry are offered to explain the decreasing seawater $^{87}Sr/^{86}Sr$ trend. They proffer that changes to carbonate and silicate weathering fluxes, high temperature hydrothermal alteration of ocean crust, fluctuating burial of aragonite/calcite carbonate minerals and dolomitisation could all be potential controls on declining seawater $^{87}Sr/^{86}Sr$ values. The most parsimonious model for decreasing seawater $^{87}Sr/^{86}Sr$ values presented by Maloof et al. (2010) depicts a change in the rate of hydrothermal alteration of oceanic crust. This scenario explains a 0.0006 decline in seawater $^{87}Sr/^{86}Sr$ values, if only driven by changing rates of hydrothermal alteration of ocean crust, through a 2.25 x increase in the flux of seawater through high-temperature hydrothermal systems at mid-ocean ridges. This significant increase of mid-ocean ridge hydrothermal alteration on seawater $^{87}Sr/^{86}Sr$ must fit within the complex tectonic rearrangement underway across the Proterozoic – Phanerozoic transition. Much has been made here of Gondwanan continental amalgamation, however, a 2.25 x increase in mid-ocean ridge hydrothermal alteration of $^{87}Sr/^{86}Sr$ is most simply explained by a 2.25 x increase in the length of mid ocean ridges (over a 20 myr time scale), requiring a dramatic episode of continent dispersal and major mid-ocean ridge activity. Following the final dispersal of the northern Rodinian continent (also known as Pannotia or the Pan-African supercontinent) into Laurentia, Baltica, Siberia and west Gondwana in the latest Ediacaran, a period of major mid-ocean rift activity drove the formation of the Iapetus Ocean (Bond et al., 1988; Hartz and Torsvick, 2002). In the
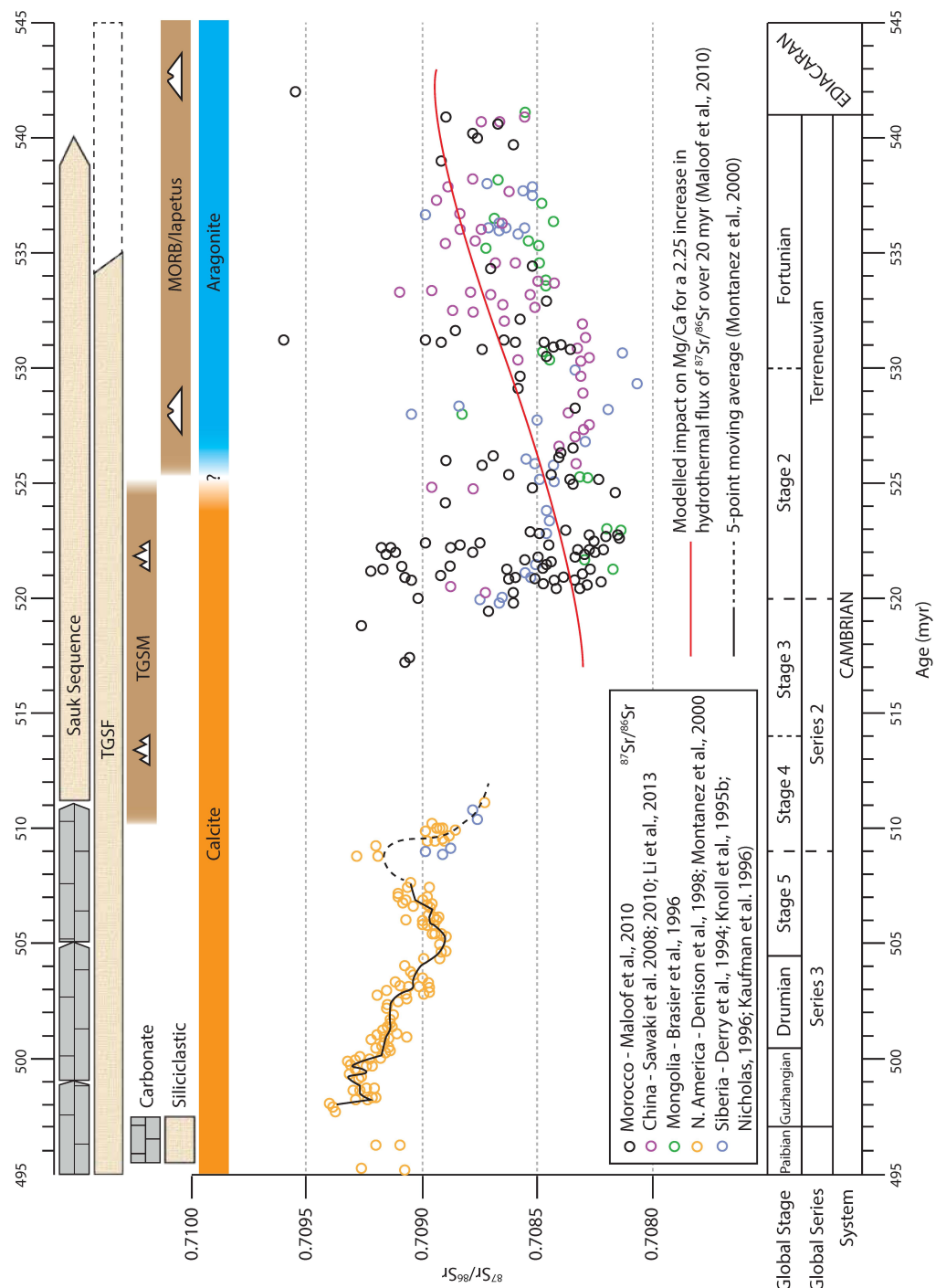
Figure 1.6: Compilation of 87Sr/86Sr stable isotope ratios in the Cambrian and comparison with major sedimentary and tectonic regimes, modified from Squire et al. (2006); Keller et al. (2012) and Peters and Gaines (2012). Cambrian timescale from Ogg et al. (2016).

Terreneuvian, a well-developed rift-to-drift period heralding the break-up of the northern Rodinian continent, drove the separation of Laurentia, West Gondwana and Baltica (Bond et al., 1988). The subsequent opening of the Iapetus is proposed to account for the more-than-doubled total mid-ocean ridge length proposed by Maloof et al., 2010 and resultant seawater $^{87}Sr/^{86}Sr$ values declining until around ~525-520 Ma. Porter (2007; 2010) supports this and illustrates a shift from aragonite seas to calcite seas ~525 Ma as evidenced by skeletal mineralogy and fluid inclusions. This concomitant evidence for diminished Mg/Ca ratios of seawater in the late Terreneuvian (~525 Ma) is consistent with removal of Mg by increased mid-ocean ridge hydrothermal activity which in turn can explain decreasing seawater $^{87}Sr/^{86}Sr$ values up to ~521 Ma (Maloof et al., 2010; Porter, 2007, 2010). Following this ~20 myr negative trend across the Proterozoic – Phanerozoic boundary and into the late Terreneuvian (Figs. 1.4, 1.6), seawater $^{87}Sr/^{86}Sr$ values begin a rapid (1-5myr) increase which culminated during the Cambrian Series 3, recording the highest Phanerozoic $^{87}Sr/^{86}Sr$ values (Figs. 1.4, 1.5; Shields, 2007). Both Peters and Gaines (2012) and Squire et al. (2006) recognise the temporal coincidence between the peak in seawater $^{87}Sr/^{86}Sr$ values with transgressive reworking of Sauk Sequence carbonate rocks, the uplift and erosion of the TGSM during the collision of Antarctica and Australia, and subsequent high sedimentation rates during the deposition of the TGSM.

Montañez et al. (2000) define a high-resolution seawater $^{87}Sr/^{86}Sr$ curve for the Cambrian Series 2 – Series 3 boundary (traditionally Early – Middle) from carbonate rocks in the southwestern USA and Canadian Rocky Mountains. Superimposed upon long-term variations of $^{87}Sr/^{86}Sr$ from continental/oceanic weathering fluxes are relatively short-term (1-5myr) fluctuations showing an initial tentative (supported by only 3 data points) increase in $^{87}Sr/^{86}Sr$ values directly across the Series 2 – Series 3 boundary; followed by a steady incease during the Series 3 (Montañez et al., 2000). This peak at the boundary is interpreted to record both the culmination of TGSM

weathering fluxes in the Cambrian (Montañez et al., 2000; Squire et al., 2006) and transgressive reworking of detritus deposited during the Sauk Sequence (Peters and Gaines, 2012). Immediately following this, an abrupt, short-term low point at the base of the Series 3 is hypothesised as the result of an episode of widespread rifting of the palaeo-Pacific margin (Weddell Sea-South African margin of Gondwana) during which continental rifting, increased weathering of mantle-derived mafic rocks and an increased hydrothermal Sr influx from mid-ocean ridge basalts drove a decrease in seawater $^{87}Sr/^{86}Sr$ values (Montañez et al., 2000).

1.5.4 Carbon isotope variation in the Cambrian

Fig. 1.7 shows a compilation of carbon chemostratigraphic studies and a generalised carbon isotope curve for the Cambrian, showing ten major carbon isotope excursions; four positive and six negative (Zhu et al., 2006). In the Cambrian, generally synchronous $\delta^{13}C_{carb}$ oscillations, with a periodicity of ~1-2 Myr (and less) and magnitude changes varying between ~2‰ - ~7‰, depicts a carbon cycle reflexing to changes derived from several possible factors. The onset or early phases of many of these excursions appear to coincide with important biotic events- evolutionary radiation, turnover and extinction, and thus a temporal association has long been noted (e.g. Montañez et al., 2000; Zhu et al., 2006). Facing the issues of disparate or highly provincialized fossil data and other problematic and incomplete correlative tools (e.g. magnetostratigraphy, sequence stratigraphy), Zhu et al. (2006) recognised the importance of a $\delta^{13}C$ chemostratigraphic framework for the Cambrian, compiling a generalised $\delta^{13}C_{carb}$ curve and delineating positive and negative excursions. Defined here are the ten major $\delta^{13}C_{carb}$ excursions (Zhu et al., 2006), many of which are named from locations in China, to be followed by a discussion of the hypothetical drivers behind carbon isotopic variation in the Cambrian.

The base of the Cambrian system is marked by the first appearance datum (FAD) of *Treptichnus pedum*, however, due to the often-problematic correlation of trace fossils across palaeocontinents, the *T. pedum* horizon can also be identified by the Basal Cambrian Carbon isotope Excursion- BACE. This is a large negative excursion associated with the base of the Cambrian system, exhibiting the reversal from positive $\delta^{13}C$ values in the

late Ediacaran to negative $\delta^{13}C$ values in the basal Cambrian Terreneuvian Series. This negative isotope shift shows a temporal correspondence with acritarch extinction and disappearance of some Ediacaran fauna (Corsetti and Hagadorn, 2000; Armthor et al., 2003; Zhu et al., 2006).

The ZHUjiaqing Carbon isotope Excursion (ZHUCE), named after the basal Cambrian Zhujiaging Formation in eastern Yunnan, China, is a large positive excursion in the lower Cambrian Stage 2. This excursion corresponds with the radiation of the third major assemblage of the small shelly fossils (SSFs); an early mineralised metazoan assemblage on the Yangtze Platform (Zhu et al, 2006).

The SHIyantou Carbon isotope Excursion (SHICE), after the Shiyantau Formation in Yunnan, China, is a large negative excursion immediately proceeding the ZHUCE in the middle part of the Cambrian Stage 2. Following a radiation in the early Stage 2, the ZHUCE corresponds to the disappearance of many SSF secreting metazoans (Zhu et al., 2006).

Again, showing a temporal correspondence with metazoan radiation, the Cambrian Arthropod Radiation isotope Excursion (CARE) is defined as a positive excursion close to the base of the currently unratified Series 2. This is associated with the appearance of a broad variety of arthropods, thought to be accentuated by the close correspondence with periods of exceptional preservation, e.g. the Chengjiang, Sirius Passet, Poleta, Guinashan, Balang and Emu Bay Lagerstättens (Zhu et al., 2006).

The MIngzinsi Carbon Isotope Excursion (MICE) is named after the Mingxinsi Formation of Guizhou, China. This is a large positive isotope excursion in the lower part of Stage 4 and is associated with later Lagerstätten deposits (e.g. Sinsk Formation, Russia and Kinzers Formation, USA) as well as a major archaeocyathan radiation.

Following this, in mid Stage 4, is the Archaeocyathan Extinction Carbon isotope Excursion (AECE), a large negative excursion. Again, exhibiting the innate relationship between carbon cycling and biotic events in the Cambrian; the AECE excursion shows a close temporal association with the disappearance of archaeocyaths on several Cambrian continents (Zhu et al., 2006; Ishikawa et al., 2014).
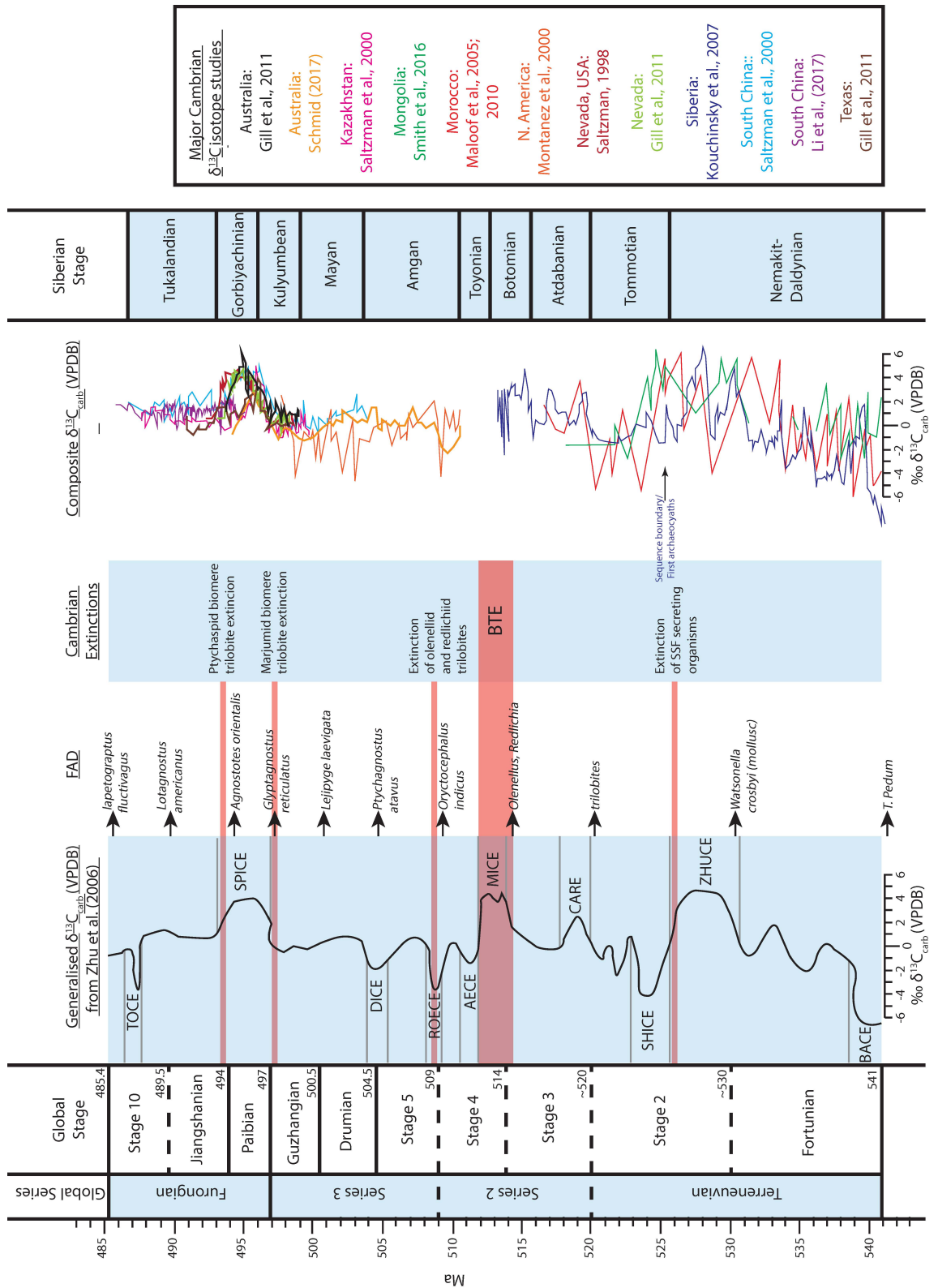
Figure 1.7: Compilation of ^{13}C stable isotope ratios against generalised Cambrian excursions, FAD (first appearance datum) and extinction events, from Zhu et al. (2006). Timescale from Ogg et al. (2016).

35

At the Cambrian Series 2 – Series 3 boundary is the Redlichiid Olenellid Extinction Carbon isotope Excursion (ROECE). This large negative excursion coincides with the extinction of the redlichiid trilobites of Gondwana, and the olenellids of Laurentia, as well as exceptional preservation conditions of the Kaili Lagerstätte, Guizhou, China (Zhu et al., 2006).

The DrumIan Carbon isotope Excursion (DICE) is a negative inflexion coinciding with the Drumian Stage of the Great Basin, USA and coincides with the FAD of the agnostid trilobite order marked by *Ptychagnostus atavus*. Again, illustrating close temporal relationships between carbon isotope excursions and formations displaying exception preservation; the DICE interval corresponds to the Spence, Wheeler, Marjum (Utah, USA), Conasuaga (Georgia, USA) and Burgess Shale (British Columbia, Canada) Lagerstätten (Zhu et al., 2006).

The Steptoean PosItive Carbon isotope Excursion (SPICE) occurs synchronously across deposits at the base of the Furongian Series and Paibian Stage. The onset of the significant positive shift in $\delta^{13}C$ values is marked by the extinction of trilobites of the Pterocephaliid Biomere on (Saltzman et al., 2000) and transgression, while peak positive values coincide with regression and lowstand at the Sauk II/ Sauk III hiatus (Saltzman et al., 2000; Gill et al., 2011).

The final excursion within the Cambrian is termed the Top Of Cambrian Excursion (TOCE) or Sunwaptan Negative carbon Isotope Excursion (SNICE), and is a large negative $\delta^{13}C$ excursion in the upper most Stage 10. Although it is yet to be well constrained globally, Sial et al. (2013) suggest that the period between peak positive SPICE values and peak negative SNICE values reflects a period of global cooling.

In the early Cambrian, the mechanisms explaining large-amplitude, high frequency excursions of inorganic carbon ($\delta^{13}C_{carb}$) have long puzzled workers; a number of ideas have been suggested to control this large variation. Across the Ediacaran – Cambrian transition, Brasier and Lindsay (2001) note first and second order $\delta^{13}C_{carb}$ cycles shaping distinct trends on 10s of myrs (first order) and 1-5 myr trends (second order). They note that between the post-Sturtian interval to the Cambrian (~730-500 Ma) $\delta^{13}C_{carb}$

values fall from ~+11 ‰ to ~+8 ‰ in the Ediacaran and ~+5 ‰ in the Cambrian; Cambrian values, however, exhibit frequent second order variability. Brasier and Lindsay (2001) note that during period, increased sedimentation rates (e.g. Squire et al., 2006; Peters and Gaines, 2012) would have expected to increase the amount of carbon buried globally. They postulate that this period of high sediment accumulation must have been offset by rates of organic carbon oxidation in order account for the first order fall in $\delta^{13}C_{carb}$ values across the Proterozoic – Phanerozoic transition. As for the high frequency second order $\delta^{13}C_{carb}$ fluctuations in the Cambrian (e.g. during the Terreneuvian, Fig. 1.7), Brasier and Lindsay (2001) again propose that this is due to changing rates between organic burial and oxidation, however on this shorter time scale, they suggest it is modulated by subsidence and sea level change. Their hypothesis assumes that positive $\delta^{13}C$ excursions record an increase in the burial flux of organic matter, due to the increased extent of marine depositional basins during transgression (sea-level rise); and that negative $\delta^{13}C$ excursions record reduced rates of carbon burial and an increase in organic carbon oxidation rates during periods of regression (sea-level fall). Brasier and Lindsay (2001) note initial evidence that peak $\delta^{13}C$ maxima coincide with transgressive maxima as the end Botomian (Fig. 1.7) maxima (described by Zhu et al., 2006 as MICE), and that negative $\delta^{13}C$ values at the top of the Nemakit-Daldynian coincides with the end Yudoma regression. They also note that negative excursions can in some cases be correlated with evidence for hiatus, erosion and exposure.

Kirschvink and Raub (2003) suggest an alternative hypothesis for carbon isotope variability during the Cambrian. Their argument is complex, rooted in true polar wander during the Neoproterozoic. They contend that extensive shelf-slopes and continental margins, formed after the break-up of Rodinia, accumulated and stored vast amounts of isotopically light carbon in the late Neoproterozoic. Following this, they hypothesise that an initial phase of true polar wander moved organic rich shelf-slope and margin deposits to higher latitudes, thereby favouring conditions which would trap biogenic methane as gas hydrates and possibly in permafrost. Continued sedimentation in the late Neoproterozoic buried biogenic methane and increased the storage

volume in hydrates, eventually forming deep reservoirs of methane under high pressure. Kirschvink and Raub (2003) then invoke a sudden pulse of true polar wander, moving deep, pressurised methane deposits back to tropical latitudes where they warmed and were subject to ocean thermohaline changes, as well as sea-level changes, which altered sedimentation regimes. Due to this, the separate methane reservoirs independently reached a point of critical failure (seismically induced, or sediment failure or erosion), releasing independent pulses of methane clathrates to Cambrian oceans subjecting broad regions to geologically sudden warming events whilst simultaneously liberating isotopically light carbon into the global ocean. Kirschvink and Raub (2003) posit that second order effects such as differential weathering and climate change may have perturbed riverine carbon fluxes to ocean basins thus further altering the carbon cycle. Maloof et al. (2005) also support this hypothesis of methane or organic carbon release on <100,000-year time scales, and invoke a similarity to the Paleocene – Eocene thermal maximum. The mechanism of repeated "bursts" of methane into the ocean would have driven global temperatures up in a series of thermal-cycling events during the Cambrian Terreneuvian, and demonstrates a close temporal relationship with the rapid biodiversification of the Cambrian explosion. This hypothesis supports the strong correlation between temperature parameters and biological diversity and species richness (Currie, 1991), thus Kirschvink and Raub (2003) invoke a "methane fuse" as key driver behind the broader phenomenon of the Cambrian Explosion. Squire et al. (2006) builds on the hypothesis of Kirschvink and Raub (2003) and Maloof et al. (2005) by suggesting that the geologically rapid uplift and erosion of the TGSM could potentially have exhumed and consequentially oxidised, large reserves of hydrocarbons. Squire et al. (2006) suggests that the isotopically light C released during the erosion of the TGSM comes from oxidation of Neoproterozoic fossil fuels, and offer the 7 trillion feet[3] trapped in the New Guinea Highlands as a modern analogue for such reserves that would be susceptible to exhumation by erosion. Maloof et al. (2010) later modified their hypothesis to argue that the high frequency, high magnitude Cambrian $\delta^{13}C$ excursions would require volcanic outgassing up to an order of magnitude higher than any modern-

day fluxes, and invoked a 2.25 times increase in the seafloor spreading rates during the early Cambrian. Investigation into Cambrian isotope variation is ongoing, and this thesis suggests further work in Chapter 6.

1.5.5 Sea-level, hiatus and evidence for redox oscillation

Haq and Schutter, (2008) provide an overview of first order eustatic trends and third-order cycles, which, when in conjunction with second order sequences from Laurentia and China (e.g. Sauk sequence, Keller et al, 2012; Mei et al., 2007, respectively), exhibit a long-term rising sea level trend throughout the Cambrian (Fig 1.8). Haq and Schutter (2008) resolve sea-level changes at third-order resolution, in some instances particularly well-documented strata enable fourth-order cycles to be determined, such as in the Cambrian Series 2 and Series 3 (Fig 1.8). They also reveal that the Cambrian Terreneuvian (in particular Stage 2) and Furongian are characterised by longer, 2-5 myr cycles. Haq and Schutter (2008) implicate many major (>75 m) magnitude shifts throughout the Cambrian, though resolving these using sequence stratigraphic correlation across Cambrian continents is problematic, either due to incomplete records or stifled by complex epeirogenic and tectonic regimes (e.g. Mei et al., 2007; Keller et al., 2012; Nielson et al., 2015). It is therefore difficult to resolve true eustatic changes, and thus sea-level records for the Cambrian are taken from specific continents, and correlated where possible.

Sequence stratigraphic assessment of Cambrian sedimentary cycles of the Great Basin, SW USA, have provided a historically important archive for studying sea-level variations. Sloss' (1963) initial subdivision of unconformity bound Phanerozoic sedimentary sequences begins with the aforementioned Sauk sequence, which was later subdivided into second and third-order sequences (e.g. Palmer, 1981, Keller et al., 2012). Palmer (1981) subdivided these craton-wide sedimentary packages into the Sauk I, Sauk II and Sauk III supersequences based on individual trilobite biozones. Although this designation is purely biostratigraphic and unrelated to significant accommodation events (Keller et al., 2012), it is consistent with observations that throughout the Cambrian, major trilobite faunal zones (e.g. appearance of agnostid trilobite groups in the Series 3 and Furongian) closely correlate to small-scale (third or fourth-order) eustatic sea-level rises, often the lower

boundaries of which are placed at the base of transgressive systems tracts (Peng et al., 2012 and references therein). Keller et al., (2012) revisit the Sauk sequence and subdivide it into five supersequences (α through ε; Fig. 1.8) spanning the Cambrian into the Ordovician, tracing craton-wide depositional sequences and building a high-resolution sequence stratigraphic framework that deciphers second-order accommodation events.

On the Chinese craton, an extensive sequence stratigraphic summary is compiled by Mei et al. (2007) (Fig. 1.8). Two second order sequences correspond to the Terreneuvian – Series 2 and the Series 3 – Furongian. Within the first second-order package there are five third-order sequences, the basal two of which are long-term ~10^6 myrs sequences. In the Series 3 and Furongian, a further five third-order sequences are identified, of which a sequence boundary close to the Guzhangian – Paibian boundary also correlates with the Sauk II/ Sauk III (Sauk γ – δ boundary) on Laurentia.

The first major hiatus of the Cambrian is the sub-Tommotian unconformity on the Siberian platform (Knoll et al., 1995). During the first phase of the Cambrian Explosion, in the Tommotian (upper stage two in of Global nomenclature), fossils recording rapid biological diversification are preserved in sedimentary successions across Siberia. The stratotype area for the Tommotian in south-eastern Siberia was initially defined to within the Ust'-Yudoma Formation along the Aldan River, above this, separated by a regional unconformity marked by karst formation, is the sudden appearance of over 100 SSF species and the first archaeocyaths, initially regarded as recording the initiation of the Cambrian Explosion (Rozanov, 1984; Landing, 1994; Knoll et al., 1995). This sub-Tommotian unconformity was first treated as a minor regional hiatus (Rozanov and Landing, 1995) in an otherwise complete section, which portrayed this succession as an accurate record of animal proliferation. However, after reassessment based on chemostratigraphic and sedimentological data, Knoll et al., (1995) establish the sub-Tommotian unconformity as a major hiatal surface, recording an estimated 3-6 myr gap. This significantly altered the interpretation that the Cambrian Explosion commenced in the Tommotian, essentially pushing the initiation back several million years into the Nemakit-Daldynian (Knoll et al.,
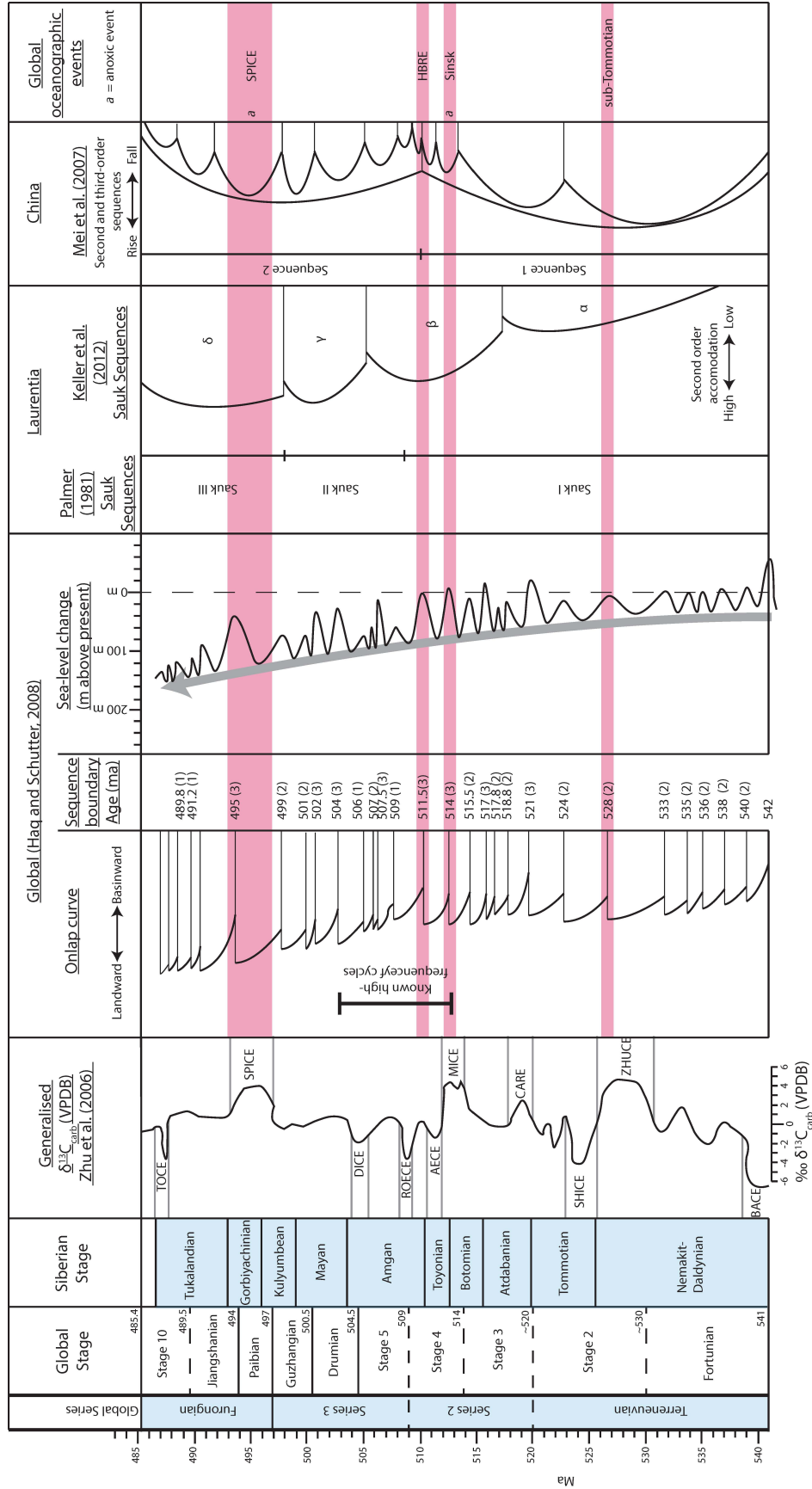
Figure 1.8: Schematic compilation of sea-level changes, major periods of hiatus and evidence for redox oscillations. Sea-level and onlap curve are taken from Haq and Schutter (2008), where onlap curve represents the measure of relative landward or basinward movement of the regional baseline. Biochronological ages of the sequence boundaries are estimated in the next column. In parenthesis, next to these ages is a semi-quantitative measure of the relative magnitude of each short-term event [minor, 1 (<25m); medium, 2 (25-75m); major, 3(>75m)]. The sea-level curve shows long-term trend with grey arrow and short-term (third-order) sea-level fluctuations calibrated to present day sea-level. Laurentian Sauk sequences are derived from the divisions derived from Palmer (1981) and Keller et al. (2012). Second and third-order curves from China are taken from Mei et al. (2007). Global oceanographic events are described in Chapter 1.5.5.

41

1995). While this is well documented on the Siberian craton, is it problematic to reconcile with broader-resolution global sea-level changes, though it potentially represents a sea-level change ~528 as recorded by Haq and Schutter (2008).

Following this, in the Botomian (upper Stage 3), the Cambrian Explosion was again set-back by a coupled transgression-regression event, beginning with the Sinsk Event (Zhuravlev and Wood, 1996). Zhuravlev and Wood report several lines of evidence to support the scenario that anoxic bottom-water encroached onto shelves during sea-level rise: prominent phosphate deposition indicating nutrient-rich upwelling; rhythmic laminations in the Sinsk formation suggesting seasonal algal blooms related to upwelling; and, the deposition of a widespread black shale unit recording starved-basin conditions on the outer shelf (Zhuravlev and Wood, 1996; Brasier and Sukhov, 1996). Whilst expressions of the Sinsk Event are largely limited to the Siberian Platform, the following Hawke Bay Regression Event (HBRE) is more prominently developed on other Cambrian continents (e.g. Palmer and James, 1980; Zhuravlev and Wood, 1996; Álvaro and Vennin, 1998; Nielson et al., 2015; Lasemi and Amin-Rasouli, 2016). Palmer and James (1980) first defined the HBRE as a major unconformity at, or close to, the traditional early-middle Cambrian boundary (Series 2 – Series 3 boundary). They also observed that in eastern Laurentia, the HBRE was out of phase with simultaneous transgression on western Laurentia (the Sauk sequences; Fig. 1.8). Like many Cambrian expressions of sea-level change, the HBRE is complex to correlate across continents, as it relates to regional epeirogenic uplift events as well as to eustatic sea-level fall (e.g. Nielson et al., 2015). However, within the scope of the Cambrian Explosion it was an important event. The resultant reduction of shallow shelf environments had a lasting detrimental effect on archaeocyathan and reef communities, ultimately resulting in their extinction (Brasier, 1996). Together this transgression-regression, and accompanying faunal extinctions and resultant diversification (Zhuravlev and Wood, 1996) is known at the Botomian-Toyonian Extinction (BTE), and plausibly constitutes the first Phanerozoic ocean anoxic event.

In the upper Cambrian Series 3 and Furongian another major oceanographic event is linked to sea-level change, anoxia, disruption to the carbon cycle and extinction (Saltzman et al., 2000). The SPICE event marks a global oceanographic event during which anoxic (and anoxic-euxinic) bottoms waters shoaled onto shallow marine shelves during an initial interval of sea-level rise. Coupled $\delta^{13}C$ and $\delta^{34}S$ cycles support the idea that this event is inherently linked to redox conditions (through their respective redox sensitive reservoirs; Gill et al., 2011), the resultant coupled sea-level rise/anoxic event implicated as driving trilobite extinctions within the Pterocephaliid biomere (Gerhardt et al., 2016), and demonstrate the innate link between biotic radiation, extinction, redox oscillations and sea-level change in the Cambrian.

1.6 Methods

An outline of the methods applied in this thesis is supplied here. This provides a rationale behind the techniques explored, whilst specific methods are detailed in each respective chapter.

1.6.1 Carbonate sedimentology

Where possible, this thesis utilises carbonate sedimentology to elucidate shifts in relative sea level, changes in redox regimes (e.g. fossiliferous vs fissile or laminated strata) and to characterise depositional units within sequence stratigraphy. In the interest of consistency, the description and characterisation of carbonate rocks are made in the classification of Dunham (1962). Dunham (1962) outlines three main textural features of carbonate rocks that have retained their depositional features, and builds a descriptive framework around them: 1) the presence or absence of carbonate mud, differentiating carbonate mud from grainstone; 2) the type and abundance of grains, which allows muddy carbonates to be subdivided into mudstone, wackestone and packstone; and 3) any evidence of binding during deposition, which characterises boundstone. For textures that contain mud, the differentiation of being either "mud-supported" (<10% grains is carbonate mudstone, >10 % grains is wackestone) or "grain-supported" (packstone) is invoked. Grainstone lacks mud and boundstone exhibits original

components bound together. Carbonate rocks that retain too little of their original depositional textures or features are classified as crystalline carbonates. For each individual study within this thesis where the Dunham classification is used, descriptive specifics are outlined respective to the samples characterised.

1.6.2 Pyrite framboid petrography

This thesis follows the procedure set out by Wilkin et al. (1996) and Wignall and Newton (1998) who calibrate the size distribution of pyrite framboid populations against an oxygen restricted biofacies (ORB), and establish the use of the size distribution of pyrite framboid populations as a proxy indicator of changing redox regimes. The abundance of authigenic pyrite in ancient sediments, and the two redox sensitive traits (degree of pyritisation of iron and sulphur:organic carbon ratios) established the potential of authigenic pyrite to elucidate oxygen-poor deposition; yet could not distinguish between oxygen-poor, anoxic (oxygen free, H_2S free) or euxinic (oxygen free, H_2S bearing) (Canfield et al., 1996). Significant attention is often paid to bulk chemical and stable isotope analysis of porewaters and solids which are frequently used to trace chemical processes that are redox controlled and occur during diagenesis (Wilkin et al., 1996). However, Wilkin et al. (1996) formed a quantitative framework measuring the size distribution of pyrite framboids in different modern environments and theorised that this could be applied to the ancient. Pyrite framboids form as a spherical or sub-spherical aggregate of numerous closely packed pyrite microcrysts which are equant and equidimensional (Butler and Rickard, 2000). Wilkin and Barnes (1997) describe their formation through four consecutive process: 1) nucleation and growth of initial iron monosulfide microcrysts; 2) the reaction of these microcrysts to greigite (Fe_3S_4) (although this is in debate, see Schoonen, 2005 for discussion); 3) aggregation of uniformly sized greigite microcrysts (i.e. framboidal growth); and 4) the replacement of greigite by pyrite. In modern environments pyrite framboid populations form in the narrow iron-reduction zone developed at the redox boundary, as aggregates of iron monosulfide microcrysts. In the more intensely anoxic environment immediately underlying this boundary, characterised by active sulfate-reduction, pyrite

framboids cease to form, instead these conditions favour the growth of crystalline and/or amorphous grains on pyrite (Wilkin et al., 1996; Suits and Wilkin, 1998). If euxinia is developed in bottom waters (i.e. free H_2S is present in the water column), then framboids can develop in the water column (Wilkin et al., 1996). However, formation in the water column restricts their growth to no larger than 5-6 µm in diameter before they sink below the iron reduction zone and stop growing (Wilkin et al., 1996). Therefore, euxinic conditions will produce a distinct size distribution characterised by a small range of very small (<5-6 µm diameter) pyrite framboids (Wilkin et al., 1996). However, it is worth highlighting that a drawback of this proxy is the plausible inability to distinguish between a euxinic (O_2 free, H_2S excess) or ferruginous (O_2 free, Fe^{2+} excess) water column, as the factor controlling pyrite formation and size growth is its ambient buoyancy which is crossed once it reaches a diameter of ~5-6 µm, therefore euxinic size distributions could potentially accumulate under a ferruginous water column (e.g. Hammarlund et al., 2012). Despite this, there remains a strong contrast between euxinic size distributions and dysoxic populations. In weakly oxygenated settings where seafloor conditions are dysoxic, pyrite framboids are observed growing in the surficial sediments where their size is limited by the local availability of reactants, and not limited by their neutral buoyancy; this results in potentially larger framboids and a wider range of sizes (Wilkin et al, 1996). When in conjunction with sedimentological evidence (e.g. evidence for bioturbation or lamination), the disparity between euxinic, dysoxic framboid size distributions and oxic conditions (no framboids, rare pyrite crystals) validates their use as a redox proxy and has been widely utilised (e.g. Wignall and Newton, 1998; Nielsen and Shen, 2004; Wignall et al., 2005, 2010; Shen et al., 2007; Chang et al., 2009; Zhou and Jiang, 2009; Bond et al., 2010; Liao et al., 2010; Hammarlund et al., 2012; Wang et al., 2012 and more).

1.6.3 Carbon isotope analysis

Carbon isotope analysis within this thesis is primarily used as a chemostratigraphic tool for elucidating the temporal coincidence between trilobite extinctions, the Cambrian Series 2 – Series 3 boundary, and the ROECE event, which hitherto have not been recorded in a single section.

Due to the individual nature of the Chapters in this thesis, Chapters 2 to 5 have separate methodologies which are detailed respectively.

1.6.4 Sedimentary mercury concentrations

Volcanism represents a primary source of gaseous Hg^0 and, unlike other volcanic trace metals, its long atmospheric residence time (1-2 years) permits hemispheric circulation and establishes its potential as a tracer for volcanism (Pyle and Mather, 2003; Percival et al., 2015, 2017). Oxidation of Hg^0 by halogens, ozone and radicals forms reactive Hg^{2+}, a soluble ion which is deposited during precipitation. Horowitz et al. (2017) found that, during its residence in the troposphere, Hg is most effectively oxidised by bromine (Br), forming atmospheric HgBr complexes. As the largest source of atmospheric Br is organobromines - which are produced as a by-product of phytoplankton photosynthesis - the most effective oxidation and deposition of Hg^{2+} occurs above and, subsequently to, the marine realm (Horowitz et al., 2017). In modern oceans ~49% of marine Hg deposition occurs in tropical oceans due to the greater availability of productivity-driven organobromines and other oxidising radicals at these latitudes (Horowitz et al., 2017). Once in the marine realm Hg^{2+} forms complexes with clay minerals (Kongchum et al., 2011), organic matter (Benoit et al., 2001), and, in anoxic/euxinic conditions, it is scavenged from seawater as sulphide complexes (Benoit et al., 1999). Persistent anoxic conditions optimise bacterial Hg methylation in the water column, resulting in increased Hg drawdown from the water column to sediments and enhancement of methylmercury (MeHg) burial (Mason et al., 1993; Monperrus et al., 2007; Emili et al., 2011; Yin et al., 2017). This process can also operate in transition from oxic to anoxic conditions; where Hg and MeHg were previously scavenged during oxic conditions and sequestered into a solid phase in sediments, the re-mobilisation of Hg during an upward shift of the anoxic zone to the sediment – water interface can enhance the release of Hg and MeHg back into the water column (Emili et al., 2011). Due to the affinity between Hg and bacterial methylation, Hg and total organic carbon (TOC) typically show a positive correlation in marine sediments (Outridge et al., 2007), and, crucially for this study, during intervals of intense environmental loading Hg can become enriched in marine sediments. This

provides valuable evidence for exogenous environmental sources of Hg and has been used to trace LIP eruptions in locations far removed from the site of eruption.

Mercury anomalies have been detected at several mass extinction levels known to coincide with LIP eruptions, but no examples are older than the Permian (Sanei et al., 2012; Percival et al., 2015; Thibodeau et al., 2016; Font et al., 2016; Grasby et al., 2016). Prior to the Permian, there are few known LIPs, and, whilst a connection between mass extinction and massive volcanism has been strongly implicated (e.g. Jones et al., 2017), the Kalkarindji remains the oldest Phanerozoic province to coincide with extinction and the zircon age returned by Jourdan et al. (2014) suggests a strong temporal relationship to the Series 2 – Series 3 boundary. To assess this coincidence between the Kalkarindji and the BTE, we examine marine sedimentary Hg concentrations from our target field locations in Chapters 5 and 6.

1.7   Hypotheses

Beyond the specific research questions posed in 1.2, this thesis tests the following broad hypotheses, fixed in the abiotic and biotic evolution of the Cambrian.

Extinction at the Series 2 – Series 3 boundary is a severe punctuation of the dramatic biologic proliferation of the Cambrian Explosion.

The early Cambrian (Terreneuvian – Series 2) is defined as a period of innovative biological radiation; the appearance of mineralising bilaterians; a diversity of soft-bodied trace fossils; revolutionised seafloor substrates; the advent of biologically derived sediments and biofabrics and increasingly complex sensory adaptions. By mid-Series 2, the second phase of Cambrian radiation was well established, and almost 80% of modern skeletal morphotypes were present; however, the Cambrian Explosion suffered a set-back which halted the biological expansion of the previous ~35 myr. The BTE was lethal for archaeocyathan fauna, a coupled sea-level fall and ocean anoxic event has long been implicated as the mechanism, though this event would benefit from further scrutiny. Immediately following this, at the Series

2 – Series 3 boundary, trilobites underwent dramatic and prolific diversification, however, at this time the dominant trilobite of the order Redlichiida and suborder Olenellina disappeared. This would be the first example of the disappearance of dominant trilobite faunas at biomere boundaries throughout the Cambrian Series 3 and Furongian, to what extent is this event linked to the BTE, and is it a severe mass extinction or faunal turover?

Trilobite extinction, ROECE and facies changes reflect dynamic abiotic changes across the Cambrian Series 2 – Series 3 boundary, inherently linked to sea-level variation, continental arrangement and weathering regimes.

Following a protracted period of globally diversity decline (BTE and olenellid extinction), Series 2 – Series 3 interval facies exhibit evidence for changing climate, disruption to biotic regimes, sea-level fall and microbially dominated intervals. These are inherently linked to the long-term evolution of continental rearrangement (e.g. the formation of Gondwana), the establishment of habitable continental shelves (e.g. Sauk sequences, TGSF), the effect of second and third-order sea-level changes and longer term variations to organic carbon burial. At the Series 2 – Series 3 boundary, anoxia, transgression, extinction and carbon isotope variation coincide; does this interval reflect repeating wider Cambrian trends and does evidence from this thesis confirm previous work that this reflects a period of widespread environmental instability?

The Kalkarindji Large Igneous Province (LIP) was emplaced during the interval of the ROECE event and olenellid trilobite extinctions, thus implying the first Phanerozoic LIP-extinction event.

LIP-mass extinction links are well known from the Phanerozoic (e.g. Wignall, 2001) and increasingly, new studies imply that there may yet be other examples in geologic history that have not yet been established (e.g. Gong et al., 2017; Jones et al., 2017). The Cambrian Series 2 – Series 3 boundary interval n has long been recognised as coincident with biotic crisis (Brasier, 1996; Zhuravlev and Wood, 1996), and, after the establishment of

a suite of geochemically related volcanics in modern-day Australia (Hanley and Wingate, 2000), the emerging temporal association has led to the idea that this is the first Phanerozoic LIP-extinction event (Glass and Phillips, 2006; Evins et al., 2009; Jourdan et al., 2014). Various mechanisms have been proposed for these extinctions including encroaching anoxia on to the shelf, the sudden replacement of endemic trilobite species with more pandemic species, and dramatic environmental change following the emplacement of the Kalkarindji LIP, however, to date no study exhibits these phenomena in-situ. This thesis uses the novel Hg proxy as a sedimentary geochemical tracer of volcanism, and assessed evidence for increased volcanism at the Series 2 – Series 3 boundary.

1.8   References:

Abdelsalam, M. G., Abdel-Rahman, E. S. M., El-Faki, E. F. M., Al-Hur, B., El-Bashier, F. R. M., Stern, R. J., Thurmond, A. K. (2003). Neoproterozoic deformation in the northeastern part of the Saharan Metacraton, northern Sudan. *Precambrian Research*, *123*(2-4), 203-221.

Álvaro, J. J., Vennin, E. (1998). Stratigraphic signature of a terminal Early Cambrian regressive event in the Iberian Peninsula. *Canadian Journal of Earth Sciences*, *35*(4), 402-411.

Amthor, J. E., Grotzinger, J. P., Schröder, S., Bowring, S. A., Ramezani, J., Martin, M. W., Matter, A. (2003). Extinction of Cloudina and Namacalathus at the Precambrian-Cambrian boundary in Oman. *Geology*, *31*(5), 431-434.

Avigad, D., Sandler, A., Kolodner, K., Stern, R. J., McWilliams, M., Miller, N., Beyth, M. (2005). Mass-production of Cambro–Ordovician quartz-rich sandstone as a consequence of chemical weathering of Pan-African terranes: Environmental implications. *Earth and Planetary Science Letters*, *240*(3-4), 818-826.

Bambach, R. K., Bush, A. M., Erwin, D. H. (2007). Autecology and the filling of ecospace: key metazoan radiations. *Palaeontology*, *50*(1), 1-22.

Benoit, J. M., Gilmour, C. C., Mason, R. P., Heyes, A. (1999). Sulfide controls on mercury speciation and bioavailability to methylating

bacteria in sediment pore waters. *Environmental Science & Technology*, *33*(6), 951-957.

Benoit, J. M., Mason, R. P., Gilmour, C. C., Aiken, G. R. (2001). Constants for mercury binding by dissolved organic matter isolates from the Florida Everglades. *Geochimica et cosmochimica acta*, *65*(24), 4445-4451.

Boger, S. D., Miller, J. M. (2004). Terminal suturing of Gondwana and the onset of the Ross–Delamerian Orogeny: the cause and effect of an Early Cambrian reconfiguration of plate motions. *Earth and Planetary Science Letters*, *219*(1-2), 35-48.

Bond, G. C., Kominz, M. A., Grotzinger, J. P. (1988). Cambro-Ordovician eustasy: Evidence from geophysical modelling of subsidence in Cordilleran and Appalachian passive margins. In *New perspectives in basin analysis* (pp. 129-160). Springer, New York, NY.

Bond, D. P., Wignall, P. B. (2010). Pyrite framboid study of marine Permian–Triassic boundary sections: a complex anoxic event and its relationship to contemporaneous mass extinction. *Bulletin*, *122*(7-8), 1265-1279.

Bottjer, D. J., Hagadorn, J. W. (1999). The Cambrian substrate revolution and evolutionary paleoecology of the Mollusca. In *Geological Society of America Abstracts with Programs* (Vol. 31, No. 7, p. 335).

Bottjer, D. J., Hagadorn, J. W., Dornbos, S. Q. (2000). The Cambrian substrate revolution. *GSA today*, *10*(9), 1-7.

Brasier, M. D. (1980). The Lower Cambrian transgression and glauconite-phosphate facies in western Europe. *Journal of the Geological Society*, *137*(6), 695-703.

Brasier, M. D. (1990). Phosphogenic events and skeletal preservation across the Precambrian-Cambrian boundary interval. *Geological Society, London, Special Publications*, *52*(1), 289-303.

Brasier, M. D. (1992). Nutrient-enriched waters and the early skeletal fossil record. *Journal of the Geological Society*, *149*(4), 621-629.

Brasier, M. D. (1996). The basal Cambrian transition and Cambrian bio-events (from terminal Proterozoic extinctions to Cambrian biomeres).

In *Global events and event stratigraphy in the Phanerozoic* (pp. 113-138). Springer, Berlin, Heidelberg.

Brasier, M. D., Lindsay, J. F. (2001). Did supercontinental amalgamation trigger the "Cambrian Explosion". *The Ecology of the Cambrian Radiation. Columbia University Press, New York*, 69-89.

Brasier, M. D., Sukhov, S. S. (1998). The falling amplitude of carbon isotopic oscillations through the Lower to Middle Cambrian: northern Siberia data. *Canadian Journal of Earth Sciences*, *35*(4), 353-373.

Braun, A., Chen, J., Waloszek, D., Maas, A. (2007) First Early Cambrian Radiolaria, in Vickers-Rich, P., and Komarower, P., eds., The Rise and Fall of the Ediacaran Biota: Geological Society of London Special Publication 286, p. 143–149.

Briggs, D. E. (2015). The Cambrian Explosion. *Current Biology*, *25*(19), R864- R868.

Burke, K., Kraus, J. U. (2000). Deposition of immense Cambro–Ordovician sandstone bodies, now exposed mainly in N. *Africa and Arabia, during the aftermath of the final assembly of Gondwana: Geological Society of America Abstracts with Program*, *32*(7), 249.

Butler, I. B., Rickard, D. (2000). Framboidal pyrite formation via the oxidation of iron (II) monosulfide by hydrogen sulphide. *Geochimica et Cosmochimica Acta*, *64*(15), 2665-2672.

Canfield, D. E., Lyons, T. W., Raiswell, R. (1996). A model for iron deposition to euxinic Black Sea sediments. *American Journal of Science*, *296*(7), 818-834.

Chafetz, H. S., Reid, A. (2000). Syndepositional shallow-water precipitation of glauconitic minerals. *Sedimentary Geology*, *136*(1-2), 29-42.

Clarkson, E., Levi-Setti, R., Horváth, G. (2006). The eyes of trilobites: the oldest preserved visual system. *Arthropod structure & development*, *35*(4), 247-259.

Coleman, M. L. (1985). Geochemistry of diagenetic non-silicate minerals: kinetic considerations. *Phil. Trans. R. Soc. Lond. A*, *315*(1531), 39-56.

Corsetti, F. A., Hagadorn, J. W. (2003). The Precambrian-Cambrian transition in the southern Great Basin, USA. *The Sedimentary Record*, *1*(1), 4-8.

Creveling, J. R., Johnston, D. T., Poulton, S. W., Kotrc, B., März, C., Schrag, D. P., Knoll, A. H. (2014). Phosphorus sources for phosphatic Cambrian carbonates. *Geological Society of America Bulletin*, *126*(1-2), 145-163.

Curray, J. R. (1991). Possible greenschist metamorphism at the base of a 22-km sedimentary section, Bay of Bengal. *Geology*, *19*(11), 1097-1100.

Currie, D. J. (1991). Energy and large-scale patterns of animal-and plant-species richness. *The American Naturalist*, *137*(1), 27-49.

Debrenne, F., Lafuste, J., Zhuravlev, A. (1990). Coralomorphes et spongiomorphes à l'aube du Cambrien. *Bulletin du Muséum national d'histoire naturelle. Section C, Sciences de la terre, paléontologie, géologie, minéralogie*, *12*(1), 17-39.

Debrenne, F. (1991). Extinction of the Archaeocyatha. *Historical Biology*, *5*(2-4),95-106.

Denison, R. E., Koepnick, R. B., Burke, W. H., Hetherington, E. A. (1998). Construction of the Cambrian and Ordovician seawater 87Sr/86Sr curve. *Chemical Geology*, *152*(3-4), 325-340.

Derry, L. A., Brasier, M. D., Corfield, R. E. A., Rozanov, A. Y., Zhuravlev, A. Y. (1994). Sr and C isotopes in Lower Cambrian carbonates from the Siberian craton: a paleoenvironmental record during the 'Cambrian explosion'. *Earth and Planetary Science Letters*, *128*(3-4), 671-681.

Droser, M. L., Gehling, J. G., Jensen, S. (1999). When the worm turned: Concordance of Early Cambrian ichnofabric and trace-fossil record in siliciclastic rocks of South Australia. *Geology*, *27*(7), 625-628.

Droser, M. L., Li, X. (2001). The Cambrian radiation and the diversification of sedimentary fabrics. *The ecology of the Cambrian radiation*, 137-169.

Droser, M. L., Gehling, J. G. (2015). The advent of animals: The view from the Ediacaran. *Proceedings of the National Academy of Sciences*, *112*(16), 4865-4870.

Dunham, R. J. (1962). Classification of carbonate rocks according to depositional textures, in HAM, W. E., ed., *Classification of Carbonate Rocks: American Association of Petroleum Geologists Memoir*, v. 1, p. 108-121

Dzik, J. (2005). Behavioral and anatomical unity of the earliest burrowing animals and the cause of the "Cambrian explosion". *Paleobiology*, *31*(3), 503-521.

Elrick, M., Snider, A. C. (2002). Deep-water stratigraphic cyclicity and carbonate mud mound development in the Middle Cambrian Marjum Formation, House Range, Utah, USA. *Sedimentology*, *49*(5), 1021-1047.

Emili, A., Koron, N., Covelli, S., Faganeli, J., Acquavita, A., Predonzani, S., De Vittor, C. (2011). Does anoxia affect mercury cycling at the sediment–water interface in the Gulf of Trieste (northern Adriatic Sea)? Incubation experiments using benthic flux chambers. *Applied geochemistry*, *26*(2), 194-204.

Erwin, D. H., Laflamme, M., Tweedt, S. M., Sperling, E. A., Pisani, D., Peterson, K. J. (2011). The Cambrian conundrum: early divergence and later ecological success in the early history of animals. *science*, *334*(6059), 1091-1097.

Evins, L. Z., Jourdan, F., Phillips, D. (2009). The Cambrian Kalkarindji Large Igneous Province: extent and characteristics based on new 40 Ar/39 Ar and geochemical data. *Lithos*, *110*(1), 294-304.

Faggetter, L. E., Wignall, P.B., Pruss, S.B., Sun, Y., Raine, R.J., Newton, R.J., Widdowson, M., Joachimski, M.M., Smith, P.M. (2016). Sequence stratigraphy, chemostratigraphy and facies analysis of Cambrian Series 2– Series 3 boundary strata in northwestern Scotland. *Geological Magazine*, 1-13.

Faggetter, L. E., Wignall, P. B., Pruss, S. B., Newton, R. J., Sun, Y., Crowley, S. F. (2017). Trilobite extinctions, facies changes and the ROECE carbon isotope excursion at the Cambrian Series 2–3 boundary, Great Basin, western USA. *Palaeogeography, Palaeoclimatology, Palaeoecology*, *478*, 53-66.

Fergusson, C. L., Coney, P. J. (1992). Implications of a Bengal Fan-type deposit in the Paleozoic Lachlan fold belt of southeastern Australia. *Geology*, *20*(11), 1047-1049.

Font, E., Adatte, T., Sial, A. N., Drude de Lacerda, L., Keller, G., Punekar, J. (2016). Mercury anomaly, Deccan volcanism, and the end-Cretaceous mass extinction. *Geology*, *44*(2), 171-174.

Gaines, R. R., Hammarlund, E. U., Hou, X., Qi, C., Gabbott, S. E., Zhao, Y., Canfield, D. E. (2012). Mechanism for Burgess Shale-type preservation. *Proceedings of the National Academy of Sciences*, *109*(14), 5180-5184.

Gerhardt, A. M., Gill, B. C. (2016). Elucidating the relationship between the later Cambrian end-Marjuman extinctions and SPICE Event. *Palaeogeography, palaeoclimatology, palaeoecology*, *461*, 362-373.

Gill, B. C., Lyons, T. W., Young, S. A., Kump, L. R., Knoll, A. H., Saltzman, M. R. (2011). Geochemical evidence for widespread euxinia in the Later Cambrian ocean. *Nature*, *469*(7328), 80-83.

Ginsburg, R. N. (1982). Actualistic depositional models for the Great American Bank (Cambro-Ordovician). In *International Congress on Sedimentology*, *11*, 114

Glass, L. M., Phillips, D. (2006). The Kalkarindji continental flood basalt province: A new Cambrian large igneous province in Australia with possible links to faunal extinctions. *Geology*, *34*(6), 461-464.

Grasby, S. E., Beauchamp, B., Bond, D. P., Wignall, P. B., Sanei, H. (2016). Mercury anomalies associated with three extinction events (Capitanian crisis, latest Permian extinction and the Smithian/Spathian extinction) in NW Pangea. *Geological magazine*, *153*(2), 285-297.

Hammarlund, E. U., Dahl, T. W., Harper, D. A., Bond, D. P., Nielsen, A. T., Bjerrum, C. J., Canfield, D. E. (2012). A sulfidic driver for the end-Ordovician mass extinction. *Earth and Planetary Science Letters*, *331*, 128-139.

Hanley, L. M., Wingate, M. T. D. (2000). SHRIMP zircon age for an Early Cambrian dolerite dyke: an intrusive phase of the Antrim Plateau Volcanics of northern Australia. *Australian Journal of Earth Sciences*, *47*(6), 1029-1040.

Hartz, E. H., Torsvik, T. H. (2002). Baltica upside down: a new plate tectonic model for Rodinia and the Iapetus Ocean. *Geology*, *30*(3), 255-258.

Haq, B. U., Schutter, S. R. (2008). A chronology of Paleozoic sea-level changes. *Science*, *322*(5898), 64-68.

Hoffman, P. F. (1991). Did the breakout of Laurentia turn Gondwanaland inside-out? *Science*, *252*(5011), 1409-1412.

Hofmann, A. W. (1997). Mantle geochemistry: the message from oceanic volcanism. *Nature*, *385*(6613), 219.

Hough, M. L., Shields, G. A., Evins, L. Z., Strauss, H., Henderson, R. A., Mackenzie, S. (2006). A major sulphur isotope event at c. 510 Ma: a possible anoxia–extinction–volcanism connection during the Early–Middle Cambrian transition? *Terra Nova*, *18*(4), 257-263.

Horowitz, H. M., Jacob, D. J., Zhang, Y., Dibble, T. S., Slemr, F., Amos, H. M., Sunderland, E. M. (2017). A new mechanism for atmospheric mercury redox chemistry: implications for the global mercury budget. *Atmospheric Chemistry and Physics*, *17*(10), 6353-6371.

Huajin, C., Xuelei, C., Lianjun, F., Jing, H. (2009). Framboidal pyrites in cherts of the Laobao Formation, South China: Evidence for anoxic deep ocean in the terminal Ediacaran. *Acta Petrologica Sinica*, *25*(4), 1001-1007.

Ishikawa, T., Ueno, Y., Shu, D., Li, Y., Han, J., Guo, J., Komiya, T. (2014). The δ13C excursions spanning the Cambrian explosion to the Canglangpuian mass extinction in the Three Gorges area, South China. *Gondwana Research*, *25*(3), 1045-1056.

Ivantsov, A. Y., Zhuravlev, A. Y., Leguta, A. V., Krassilov, V. A., Melnikova, L. M., Ushatinskaya, G. T. (2005). Palaeoecology of the early Cambrian Sinsk biota from the Siberian platform. *Palaeogeography, Palaeoclimatology, Palaeoecology*, *220*(1-2), 69-88.

Jacobsen, S. B., Kaufman, A. J. (1999). The Sr, C and O isotopic evolution of Neoproterozoic seawater. *Chemical Geology*, *161*(1-3), 37-57.

Jones, D. S., Martini, A. M., Fike, D. A., Kaiho, K. (2017). A volcanic trigger for the Late Ordovician mass extinction? Mercury data from south China and Laurentia. *Geology*, *45*(7), 631-634.

Jourdan, F., Hodges, K., Sell, B., Schaltegger, U., Wingate, M. T. D., Evins, L. Z., Blenkinsop, T. (2014). High-precision dating of the Kalkarindji large igneous province, Australia, and synchrony with the Early–Middle Cambrian (Stage 4–5) extinction. *Geology*, *42*(6), 543-546.

Keller, M., Cooper, J. D., Lehnert, O. (2012). Sauk megasequence supersequences, southern Great Basin: second-order accommodation events on the southwestern Cordilleran margin platform.

Kaufman, A. J., Knoll, A. H., Semikhatov, M. A., Grotzinger, J. P., Jacobsen, S. B., Adams, W. (1996). Integrated chronostratigraphy of Proterozoic–Cambrian boundary beds in the western Anabar region, northern Siberia. *Geological Magazine*, *133*(5), 509-533.

Kiessling, W., Aberhan, M., Villier, L. (2008). Phanerozoic trends in skeletal mineralogy driven by mass extinctions. *Nature Geoscience*, *1*(8), 527.

Knoll, A. H., Kaufman, A. J., Semikhatov, M. A., Grotzinger, J. P., Adams, W. (1995). Sizing up the sub-Tommotian unconformity in Siberia. *Geology*, *23*(12), 1139-1143.

Kongchum, M., Hudnall, W. H., Delaune, R. D. (2011). Relationship between sediment clay minerals and total mercury. *Journal of Environmental Science and Health, Part A*, *46*(5), 534-539.

Kouchinsky, A., Bengtson, S., Runnegar, B., Skovsted, C., Steiner, M., Vendrasco, M. (2012). Chronology of early Cambrian biomineralization. *Geological Magazine*, *149*(2), 221-251.

Kruse, P. D., Zhuravlev, A. Y., James, N. P. (1995). Primordial metazoan-calcimicrobial reefs: Tommotian (early Cambrian) of the Siberian platform. *Palaios*, 291-321.

Landing, E. (1994). Precambrian-Cambrian boundary global stratotype ratified and a new perspective of Cambrian time. *Geology*, *22*(2), 179-182.

Lasemi, Y., Amin-Rasouli, H. (2016). The lower–middle Cambrian transition and the Sauk I-II unconformable boundary in Iran, a record of late early Cambrian global Hawke Bay regression. *Geological Society of America Special Papers*, *525*, SPE525-10.

Levy, M., Christie-Blick, N. (1991). Tectonic subsidence of the early Paleozoic passive continental margin in eastern California and southern Nevada. *Geological Society of America Bulletin*, *103*(12), 1590-1606.

Li, D., Ling, H. F., Shields-Zhou, G. A., Chen, X., Cremonese, L., Och, L., Manning, C. J. (2013). Carbon and strontium isotope evolution of seawater across the Ediacaran–Cambrian transition: evidence from the Xiaotan section, NE Yunnan, South China. *Precambrian Research*, *225*, 128-147.

Li, D., Zhang, X., Chen, K., Zhang, G., Chen, X., Huang, W., Shen, Y. (2017). High-resolution C-isotope chemostratigraphy of the uppermost Cambrian stage (Stage 10) in South China: implications for defining the base of Stage 10 and palaeoenvironmental change. *Geological Magazine*, *154*(6), 1232-1243.

Lowenstein, T. K., Timofeeff, M. N., Brennan, S. T., Hardie, L. A., Demicco, R. V. (2001). Oscillations in Phanerozoic seawater chemistry: Evidence from fluid inclusions. *Science*, *294*(5544), 1086-1088.

Liao, W., Wang, Y., Kershaw, S., Weng, Z., Yang, H. (2010). Shallow-marine dysoxia across the Permian–Triassic boundary: evidence from pyrite framboids in the microbialite in South China. *Sedimentary Geology*, *232*(1-2), 77-83.

Mac Niocaill, C., Smethurst, M. A. (1994). Palaeozoic palaeogeography of Laurentia and its margins: a reassessment of palaeomagnetic data. *Geophysical Journal International*, *116*(3), 715-725.

Maloof, A. C., Schrag, D. P., Crowley, J. L., Bowring, S. A. (2005). An expanded record of Early Cambrian carbon cycling from the Anti-Atlas Margin, Morocco. *Canadian Journal of Earth Sciences*, *42*(12), 2195-2216.

Maloof, A. C., Porter, S. M., Moore, J. L., Dudás, F. Ö., Bowring, S. A., Higgins, J. A., Eddy, M. P. (2010). The earliest Cambrian record of animals and ocean geochemical change. *Geological Society of America Bulletin*, *122*(11-12), 1731-1774.

Mángano, M. G., Buatois, L. A. (2016). The Cambrian explosion. In *The Trace-Fossil Record of Major Evolutionary Events* (pp. 73-126). Springer, Dordrecht.

Marshall, C. R. (2006). Explaining the Cambrian "explosion" of animals. *Annu. Rev. Earth Planet. Sci.*, *34*, 355-384.

Marshall, P. E., Widdowson, M., Murphy, D. T. (2016). The Giant Lavas of Kalkarindji: rubbly pāhoehoe lava in an ancient continental flood basalt province. *Palaeogeography, Palaeoclimatology, Palaeoecology*, *441*, 22-   37.

Mason, R. P., Fitzgerald, W. F., Hurley, J., Hanson, A. K., Donaghay, P. L., Sieburth, J. M. (1993). Mercury biogeochemical cycling in a stratified estuary. *Limnology and Oceanography*, *38*(6), 1227-1241.

Matthews, S. T., Missarzhevsky, V. V. (1975). Small shelly fossils of late Precambrian and early Cambrian age: a review of recent work. *Journal of the Geological Society*, *131*(3), 289-303.

Mei, M. X., Ma, Y. S., Zhang, H., Meng, X. Q., Chen, Y. H. (2007). Sequence-stratigraphic frameworks for the Cambrian of the upper-Yangtze region: ponder on the sequence stratigraphic background of the Cambrian biological diversity events. *Journal of Stratigraphy*, *31*(1), 68-78.

Meinhold, G., Morton, A. C., Avigad, D. (2013). New insights into peri-Gondwana paleogeography and the Gondwana super-fan system from detrital zircon U–Pb ages. *Gondwana Research*, *23*(2), 661-665.

Meyers, S. R., Peters, S. E. (2011). A 56 million year rhythm in North American sedimentation during the Phanerozoic. *Earth and Planetary Science Letters*, *303*(3-4), 174-180.

Millot, R., Gaillardet, J., Dupré, B., Allègre, C. J. (2002). The global control of silicate weathering rates and the coupling with physical erosion: new insights from rivers of the Canadian Shield. *Earth and Planetary Science Letters*, *196*(1-2), 83-98.

Monperrus, M., Tessier, E., Amouroux, D., Leynaert, A., Huonnic, P., Donard, O. F. X. (2007). Mercury methylation, demethylation and reduction rates in coastal and marine surface waters of the Mediterranean Sea. *Marine Chemistry*, *107*(1), 49-63.

Montañez, I. P., Banner, J. L., Osleger, D. A., Borg, L. E., Bosserman, P. J. (1996). Integrated Sr isotope variations and sea-level history of Middle to Upper Cambrian platform carbonates: Implications for the evolution of Cambrian seawater 87Sr/86Sr. *Geology*, *24*(10), 917-920.

Montañez, I. P., Osleger, D. A., Banner, J. L., Mack, L. E., Musgrove, M. (2000). Evolution of the Sr and C isotope composition of Cambrian oceans. *GSA today*, *10*(5), 1-7.

Mortatti, J., Probst, J. L. (2003). Silicate rock weathering and atmospheric/soil CO2 uptake in the Amazon basin estimated from river water geochemistry: seasonal and spatial variations. *Chemical geology*, *197*(1-4), 177-196.

Nathan, R., Getz, W. M., Revilla, E., Holyoak, M., Kadmon, R., Saltz, D., Smouse, P. E. (2008). A movement ecology paradigm for unifying organismal movement research. *Proceedings of the National Academy of Sciences*, *105*(49), 19052-19059.

Newell, N. D. (1972). The evolution of reefs. *Scientific American*, *226*, 54-65.

Nicholas, C. J. (1996). The Sr isotopic evolution of the oceans during the 'Cambrian Explosion'. *Journal of the Geological Society*, *153*(2), 243-254.

Nielsen, J. K., Shen, Y. (2004). Evidence for sulfidic deep water during the Late Permian in the East Greenland Basin. *Geology, 32*(12), 1037-1040.

Odin, G. S., Matter, A. (1981). De glauconiarum origine. *Sedimentology*, *28*(5), 611-641.

Ogg, J. G., Ogg, G., Gradstein, F. M. (2016). *A Concise Geologic Time Scale: 2016*. Elsevier.

Outridge, P. M., Sanei, H., Stern, G. A., Hamilton, P. B., Goodarzi, F. (2007). Evidence for control of mercury accumulation in sediments by variations of aquatic primary productivity in Canadian High Arctic lakes. *Environmental Science & Technology*, *41*, 5259-65.

Palmer, A. R. (1965). Biomere: A new kind of biostratigraphic unit. *Journal of Paleontology*, 149-153.

Palmer, A. R. (1984). The biomere problem: evolution of an idea. *Journal of Paleontology*, 599-611.

Palmer, A. R. (1998). Terminal early Cambrian extinction of the Olenellina: documentation from the Pioche Formation, Nevada. *Journal of Paleontology*, *72*(04), 650-672.

Palmer, A. R., James, N. P. (1980). The Hawke Bay event: a circum-Iapetus regression near the Lower–Middle Cambrian boundary. In *The Caledonides in the USA* (Vol. 2, pp. 15-18). Dept. of Geological Sciences, Virginia Polytechnic Institute and State University.

Palmer, A. R., Taylor, M. E. (1981). Subdivision of the Sauk sequence. In *Short Papers for the Second International Symposium on the Cambrian System: US Geological Survey, Open-File Report* (pp. 81-743).

Peng, S., Babcock, L., Robison, R., Lin, H., Rees, M., Saltzman, M. (2004). Global Standard Stratotype-section and Point (GSSP) of the Furongian Series and Paibian Stage (Cambrian). *Lethaia*, *37*(4), 365-379.

Peng, S., Babcock, L. E., Cooper, R. A. (2012). The Cambrian Period. In *The geologic time scale* (pp. 437-488).

Peucker-Ehrenbrink, B., Miller, M. W. (2006). Marine 87Sr/86 Sr record mirrors the evolving upper continental crust. *Geochimica et Cosmochimica Acta*, *70*(18), A487.

Percival, L. M. E., Witt, M. L. I., Mather, T. A., Hermoso, M., Jenkyns, H. C., Hesselbo, S. P., Ruhl, M. (2015). Globally enhanced mercury deposition during the end-Pliensbachian extinction and Toarcian OAE: A link to the Karoo–Ferrar Large Igneous Province. *Earth and Planetary Science Letters*, *428*, 267-280.

Percival, L. M., Ruhl, M., Hesselbo, S. P., Jenkyns, H. C., Mather, T. A., Whiteside, J. H. (2017). Mercury evidence for pulsed volcanism during the end-Triassic mass extinction. *Proceedings of the National Academy of Sciences*, *114*(30), 7929-7934.

Peters, S. E., Gaines, R. R. (2012). Formation of the 'Great Unconformity as a trigger for the Cambrian explosion. *Nature*, *484*(7394), 363.

Plotnick, R. E. (2007). Chemoreception, odor landscapes, and foraging in ancient marine landscapes. *Palaeontologia Electronica*, *10*(1), 1-11.

Plotnick, R. E., Dornbos, S. Q., Chen, J. (2010). Information landscapes and sensory ecology of the Cambrian Radiation. *Paleobiology*, *36*(2), 303-317.

Porter, S. M. (2004). Closing the phosphatization window: testing for the influence of taphonomic megabias on the pattern of small shelly fossil decline. *Palaios*, *19*(2), 178-183.

Porter, S. M. (2007). Seawater chemistry and early carbonate biomineralization. *Science*, *316*(5829), 1302-1302.

Porter, S. M. (2010). Calcite and aragonite seas and the de novo acquisition of carbonate skeletons. *Geobiology*, *8*(4), 256-277.

Pyle, D. M., Mather, T. A. (2003). The importance of volcanic emissions for the global atmospheric mercury cycle. *Atmospheric Environment*, *37*(36), 5115-5124.

Riding, R. (2001). Calcified algae and bacteria, in Zhuravlev, A.Yu., and Riding, R., eds., The Ecology of the Cambrian Radiation: New York, Columbia University Press, p. 445–473.

Ronov, A. B., Khain, V. E., Balukhovsky, A. N., Seslavinsky, K. B. (1980). Quantitative analysis of Phanerozoic sedimentation. *Sedimentary Geology*, *25*(4), 311-325.

Rowland, S. M., Gangloff, R. A. (1988). Structure and paleoecology of Lower Cambrian reefs. *Palaios*, 111-135.

Rowland, S. M. (2001). Archaeocyaths—a history of phylogenetic interpretation. *Journal of Paleontology*, *75*(6), 1065-1078.

Rowland, S. M., R. S. Shapiro. (2002). Reef patterns and environmental influences in the Cambrian and earliest Ordovician. In W. Kiessling, E. Flugel, and J. Golonka, eds. Phanerozoic reef patterns. *SEPM Special Publication. 72,95–128.*

Rozanov, A. Y. (1984). The Precambrian Cambrian boundary in Siberia. *Episodes*, *7*(1), 20-24.

Rozanov, A. Y., Landing, E. (1995). Precambrian-Cambrian boundary global stratotype ratified and a new perspective of Cambrian time: Comment and Reply. *Geology, 23*(3), 285-286.

Saltzman, M. R., Runnegar, B., Lohmann, K. C. (1998). Carbon isotope stratigraphy of Upper Cambrian (Steptoean Stage) sequences of the

eastern Great Basin: Record of a global oceanographic event. *Geological Society of America Bulletin*, *110*(3), 285-297.

Saltzman, M. R., Ripperdan, R. L., Brasier, M. D., Lohmann, K. C., Robison, R. A., Chang, W. T., Runnegar, B. (2000). A global carbon isotope excursion (SPICE) during the Late Cambrian: relation to trilobite extinctions, organic-matter burial and sea level. *Palaeogeography, Palaeoclimatology, Palaeoecology*, *162*(3-4), 211-223.

Sanei, H., Grasby, S. E., Beauchamp, B. (2012). Latest Permian mercury anomalies. *Geology*, *40*(1), 63-66.

Sawaki, Y., Ohno, T., Fukushi, Y., Komiya, T., Ishikawa, T., Hirata, T., Maruyama, S. (2008). Sr isotope excursion across the Precambrian– Cambrian boundary in the Three Gorges area, South China. *Gondwana Research*, *14*(1-2), 134-147.

Schmid, S. (2017). Chemostratigraphy and palaeo-environmental characterisation of the Cambrian stratigraphy in the Amadeus Basin, Australia. *Chemical Geology*, *451*, 169-182.

Schoonen, M. A. (2004). Mechanisms of sedimentary pyrite formation. *Special Papers – Geological Society of America*, 117-134.

Schopf, J. W., Sergeev, V. N., Kudryavtsev, A. B. (2015). A new approach to ancient microorganisms: taxonomy, paleoecology, and biostratigraphy of the Lower Cambrian Berkuta and Chulaktau microbiotas of South Kazakhstan. *Paleontological Research*, *89*(5), 695-729.

Scotese, C.R. (2016). PALEOMAP PaleoAtlas for GPlates and the PaleoData Plotter Program,PALEOMAP Project, http://www.earthbyte.org/paleomappaleoatlas-for-gplates/

Sears, J. W., Price, R. A. (2003). Tightening the Siberian connection to western Laurentia. *Geological Society of America Bulletin*, *115*(8), 943-953.

Seilacher, A. (1994). From biomats to benthic agriculture: a biohistoric revolution. *Biostabilization of sediments*, 97-105.

Sepkoski, J. J. (1979). A kinetic model of Phanerozoic taxonomic diversity II. Early Phanerozoic families and multiple equilibria. *Paleobiology*, *5*(03), 222-251.

Sepkoski, J. J. (1981). A factor analytic description of the Phanerozoic marine fossil record. *Paleobiology*, *7*(01), 36-53.

Sepkoski, J. J. (1996). Patterns of Phanerozoic extinction: a perspective from global data bases. In *Global events and event stratigraphy in the Phanerozoic* (pp. 35-51). Springer, Berlin, Heidelberg.

Servais, T., Lehnert, O., Li, J. U. N., Mullins, G. L., Munnecke, A., Nuetzel, A., Vecoli, M. (2008). The Ordovician Biodiversification: revolution in the oceanic trophic chain. *Lethaia*, *41*(2), 99-109.

Shen, W., Lin, Y., Xu, L., Li, J., Wu, Y., Sun, Y. (2007). Pyrite framboids in the Permian–Triassic boundary section at Meishan, China: evidence for dysoxic deposition. *Palaeogeography, Palaeoclimatology, Palaeoecology*, *253*(3-4), 323-331.

Shields, G. A. (2007). A normalised seawater strontium isotope curve: Possible implications for Neoproterozoic-Cambrian weathering rates and the further oxygenation of the Earth. *Earth*, *2*(2), 35-42.

Sial, A. N., Peralta, S., Gaucher, C., Toselli, A. J., Ferreira, V. P., Frei, R., Pereira, N. S. (2013). High-resolution stable isotope stratigraphy of the upper Cambrian and Ordovician in the Argentine Precordillera: carbon isotope excursions and correlations. *Gondwana Research*, *24*(1), 330-348.

Sloss, L. L. (1963). Sequences in the cratonic interior of North America. *Geological Society of America Bulletin*, *74*(2), 93-114.

Smith, E. F., Macdonald, F. A., Petach, T. A., Bold, U., Schrag, D. P. (2016a). Integrated stratigraphic, geochemical, and paleontological late Ediacaran to early Cambrian records from southwestern Mongolia. *Bulletin*, *128*(3-4), 442-468.

Smith, E. F., Nelson, L. L., Strange, M. A., Eyster, A. E., Rowland, S. M., Schrag, D. P., Macdonald, F. A. (2016b). The end of the Ediacaran: Two new exceptionally preserved body fossil assemblages from Mount Dunfee, Nevada, USA. *Geology*, *44*(11), 911-914.

Squire, R. J., Campbell, I. H., Allen, C. M., Wilson, C. J. (2006). Did the Transgondwanan Supermountain trigger the explosive radiation of animals on Earth? *Earth and Planetary Science Letters*, *250*(1-2), 116-133.

Suits, N. S., Wilkin, R. T. (1998). Pyrite formation in the water column and sediments of a meromictic lake. *Geology*, *26*(12), 1099-1102.

Taylor, M.E. (1985). Late Cambrian trilobite mass extinction coincident with oxygen depletion of outer shelf benthic habitats in central Nevada. *SEPM Mid-year meeting (Golden, CO), Abstracts, 2*, 88-89.

Taylor, J. F. (2006). History and status of the biomere concept. *Memoir-Association of Australian Palaeontologists*, *32*, 247.

Thibodeau, A. M., Ritterbush, K., Yager, J. A., West, A. J., Ibarra, Y., Bottjer, D. J., Corsetti, F. A. (2016). Mercury anomalies and the timing of biotic recovery following the end-Triassic mass extinction. *Nature communications*, *7*, 11147.

Thomas, R. D. K., Shearman, R. M., Stewart, G. W. (2000). Evolutionary exploitation of design options by the first animals with hard skeletons. *Science*, *288*(5469), 1239-1242.

Valentine, J. W. (2002). Prelude to the Cambrian explosion. *Annual Review of Earth and Planetary Sciences*, *30*(1), 285-306.

Walker, L. J., Wilkinson, B. H., Ivany, L. C. (2002). Continental drift and Phanerozoic carbonate accumulation in shallow-shelf and deep-marine settings. *The Journal of Geology*, *110*(1), 75-87.

Wang, L., Shi, X., Jiang, G. (2012). Pyrite morphology and redox fluctuations recorded in the Ediacaran Doushantuo Formation. *Palaeogeography, Palaeoclimatology, Palaeoecology*, *333*, 218-227.

Webster, M., Gaines, R. R., Hughes, N. C. (2008). Microstratigraphy, trilobite biostratinomy, and depositional environment of the "lower Cambrian" Ruin Wash Lagerstätte, Pioche Formation, Nevada. *Palaeogeography, Palaeoclimatology, Palaeoecology*, *264*(1-2), 100-122.

Wignall, P. B., Newton, R. (1998). Pyrite framboid diameter as a measure of oxygen deficiency in ancient mudrocks. *American Journal of Science*, *298*(7), 537-552.

Wignall, P. B., Newton, R., Brookfield, M. E. (2005). Pyrite framboid evidence for oxygen-poor deposition during the Permian–Triassic

crisis in Kashmir. *Palaeogeography, Palaeoclimatology, Palaeoecology*, *216*(3-4), 183-188.

Wignall, P. B., Bond, D. P., Kuwahara, K., Kakuwa, Y., Newton, R. J., Poulton, S. W. (2010). An 80 million year oceanic redox history from Permian to Jurassic pelagic sediments of the Mino-Tamba terrane, SW Japan, and the origin of four mass extinctions. *Global and Planetary Change*, *71*(1-2), 109-123.

Wilkin, R. T., Barnes, H. L., Brantley, S. L. (1996). The size distribution of framboidal pyrite in modern sediments: an indicator of redox conditions. *Geochimica et cosmochimica acta*, *60*(20), 3897-3912.

Wilkin, R. T., Barnes, H. L. (1997). Formation processes of framboidal pyrite. *Geochimica et Cosmochimica Acta*, *61*(2), 323-339.

Wood, R. (1998). The ecological evolution of reefs. *Annual Review of Ecology and Systematics*, *29*(1), 179-206.

Yin, R., Xu, L., Lehmann, B., Lepak, R. F., Hurley, J. P., Mao, J., Hu, R. (2017). Anomalous mercury enrichment in Early Cambrian black shales of South China: Mercury isotopes indicate a seawater source. *Chemical Geology*, *467*, 159-167.

Zhang, X., Shu, D., Han, J., Zhang, Z., Liu, J., Fu, D. (2014). Triggers for the Cambrian explosion: hypotheses and problems. *Gondwana Research*, *25*(3), 896-909.

Zhou, C., Jiang, S. Y. (2009). Palaeoceanographic redox environments for the lower Cambrian Hetang Formation in South China: Evidence from pyrite framboids, redox sensitive trace elements, and sponge biota occurrence. *Palaeogeography, Palaeoclimatology, Palaeoecology*, *271*(3-4), 279-286.

Zhu, M. Y., Babcock, L. E., Peng, S. C. (2006). Advances in Cambrian stratigraphy and paleontology: integrating correlation techniques, paleobiology, taphonomy and paleoenvironmental reconstruction. *Palaeoworld*, *15*(3), 217-222.

Zhu, M., Zhuravlev, A. Y., Wood, R. A., Zhao, F. Sukhov, S. S. (2017). A deep root for the Cambrian explosion: Implications of new bio-and chemostratigraphy from the Siberian Platform. *Geology*, *45*(5), 459-462.

Zhuravlev, A.Yu. (1986). Radiocyathids, in Hoffman, A., and Nitecki, M.H., eds., *Problematic Fossil Taxa*, Oxford, Oxford University Press, p. 35–44.

Zhuravlev, A. Y., Hoffman, A., Nitecki, M.H. (1986). Radiocyathids. *Problematic fossil taxa*, 35-44

Zhuravlev, A. Y. (2001). Paleoecology of Cambrian reef ecosystems. In *The history and sedimentology of ancient reef systems* (pp. 121-157). Springer, Boston, MA.

Zhuravlev, A. I., Riding, R. (Eds.). (2001). *The ecology of the Cambrian radiation*. Columbia University Press.

Zhuravlev, A., Y. Wood, R. A. (1996). Anoxia as the cause of the mid-Early Cambrian (Botomian) extinction event. *Geology*, *24*(4), 311-314.

2. Chapter Two: Sequence stratigraphy, chemostratigraphy and facies analysis of Cambrian Series 2 – Series 3 boundary strata in north-western Scotland

This chapter is published as:

2.1 Abstract

Globally, the Series 2 – Series 3 boundary of the Cambrian coincides with a major carbon isotope excursion, sea-level changes and trilobite extinctions. Here we examine the sedimentology, sequence stratigraphy and carbon isotope record of this interval in the Cambrian strata (Durness Group) of NW Scotland. Carbonate carbon isotope data from the lower part of the Durness Group (Ghrudaidh Formation) show that the shallow-marine, Laurentian margin carbonates record two linked sea-level and carbon isotopic events. Whilst the carbon isotope excursions are not as pronounced as those expressed elsewhere, correlation with global records (Sauk I/ Sauk II boundary and *Olenellus* biostratigraphic constraint) identifies them as representing the local expression of ROECE and DICE. The upper part of the ROECE is recorded in the basal Ghrudaidh Formation whilst DICE is seen around 30 m above the base of this unit. Both carbon isotope excursions co-occur with surfaces interpreted to record regressive-transgressive events that produced amalgamated sequence boundaries and ravinement/flooding surfaces overlain by conglomerates of reworked intraclasts. The ROECE has been linked with redlichiid and olenellid trilobite extinctions but in NW Scotland, *Olenellus* is found after the negative peak of the carbon isotope excursion but before sequence boundary formation.

Keywords: Durness Group, ROECE, DICE, trilobite extinction, Scotland

2.2 Introduction

The Series 2 – Series 3 transition in the Cambrian Period coincides with the first biotic crisis of the Phanerozoic, which saw major losses amongst the archaeocyathid sponges and two major trilobite groups, the redlichiids and olenellids (Palmer, 1998; Zhu et al., 2004; Zhu, Babcock and Peng, 2006; Guo et al., 2010; Fan, Deng and Zhang, 2011; Wang et al., 2011; Zhang et al., 2013; Ishikawa et al., 2014). Around the same time, a series of major carbon isotope oscillations have been recorded including a major negative $\delta^{13}C$ excursion thought to coincide with the trilobite extinctions (Montañez et al., 2000; Zhu et al., 2004; Zhu, Babcock and Peng, 2006; Wang et al., 2011; Peng, Babcock and Cooper, 2012). The event has therefore been termed the Redlichiid-Olenellid Extinction Carbon isotope Excursion (ROECE) (Zhu et al., 2004; Zhu, Babcock and Peng, 2006; Alvaro et al., 2008; Guo et al., 2010; Fan, Deng and Zhang, 2011; Wang et al., 2011).

The ROECE is also contemporaneous with a major regression-transgression couplet responsible for the boundary between the Sauk I and Sauk II supersequences of the Laurentian continent (Sloss, 1963; Palmer and James, 1980; Mckie, 1993; Raine and Smith, 2012). However, this sea-level change does not have an expression outside of Laurentia and, thus, has no apparent effect in Gondwana (Pratt and Bordonaro, 2014) or South China (Zhu et al., 2004). In contrast, its Laurentian expression is a major hiatus in shelf locations whilst down-dip a thick lowstand package is seen, such as the Hawke Bay Formation of Newfoundland – the regression has therefore been referred to as the 'Hawke Bay event' (Palmer and James, 1980).

The relationship between extinctions, sea-level change and C isotope excursions is a common theme in studies of environmental crises, but their interplay at this time in the Cambrian is unclear. Originally it was suggested that there were two crises: the Sinsk event (Zhuravlev and Wood, 1996), named after the widespread development of black shales in Siberia, which especially affected archaeocyathans; and a later, severe extinction of redlichiid and olenellid trilobites coinciding with the regressive Hawke Bay event (Palmer and James, 1980; Zhuravlev and Wood, 1996). However, others have also related this second crisis to the spread of anoxic waters and a negative shift of carbon isotope values (Zhu et al., 2004).

The Cambrian carbonate carbon isotope record experienced multiple oscillations, and correlating these excursions provides potentially the best approach for intercontinental correlation (e.g. Maloof et al., 2010; Peng, Babcock and Cooper, 2012; Smith et al., 2015). At least two negative excursions occur in latest Cambrian Series 2, the Archaeocyathan Extinction Carbon isotope Excursion (AECE) (Brasier et al., 1994; Zhu, Babcock and Peng, 2006) and the ROECE. What remains unclear about both of these isotopic events is their relationship to the extinction events. For example, while it is well established that archaeocyathans suffer a major decline at the Sinsk event (Zhuravlev and Wood 1996), their final disappearance remains unconstrained. In some instances, archaeocyathans are thought to extend closer to the Series 2 – Series 3 boundary (Perejn et al., 2012), with a few putative occurrences even known from Series 3 Cambrian (Debrenne et al., 1984). If the archaeocyathans persisted to the Series 2 – Series 3 boundary, the ROECE event may well be coeval with the last occurrence of the archaeocyathans as well as that of the redlichiid and olenellid trilobites.

In Series 3, the base of the Drumian Stage is defined by the first appearance datum (FAD) of the agnostid trilobite *Ptychagnostus atavus* which, in the Great Basin (USA), is associated with transgression and the Drumian negative carbon isotope excursion (DICE) (Babcock et al., 2004; 2007; Zhu et al., 2006; Howley and Jiang, 2010). The onset of the excursion commonly coincides with the FAD of *P.atavus* (Montañez et al., 2000; Babcock et al., 2007) and has an amplitude of around -3 ‰ in the Great Basin and Canadian Rockies (Montañez et al., 2000; Howley and Jiang, 2010). Elsewhere, however, the excursion is substantially less pronounced. Thus, in the carbonate record of South China (Wang et al., 2011) and the organic carbon record of Sweden DICE is only ~1 ‰ (Ahlberg et al., 2009).

In order to further evaluate events around the Series 2 – Series 3 boundary we have conducted a facies and sequence stratigraphical analysis of the transition between the An t-Sm and Ghrudaidh formations in northwest Scotland (Fig. 2.1). Facies analysis of the Scottish strata shows a major lithological change at this level and recent sequence stratigraphic study has suggested that the formational boundary also correlates with the Sauk I/Sauk II supersequence boundary of North America (Raine and Smith,

2012). To further aid correlation, and in an attempt to identify the $\delta^{13}C$ changes associated with ROECE and DICE, carbonate and organic carbon isotope results are presented here.
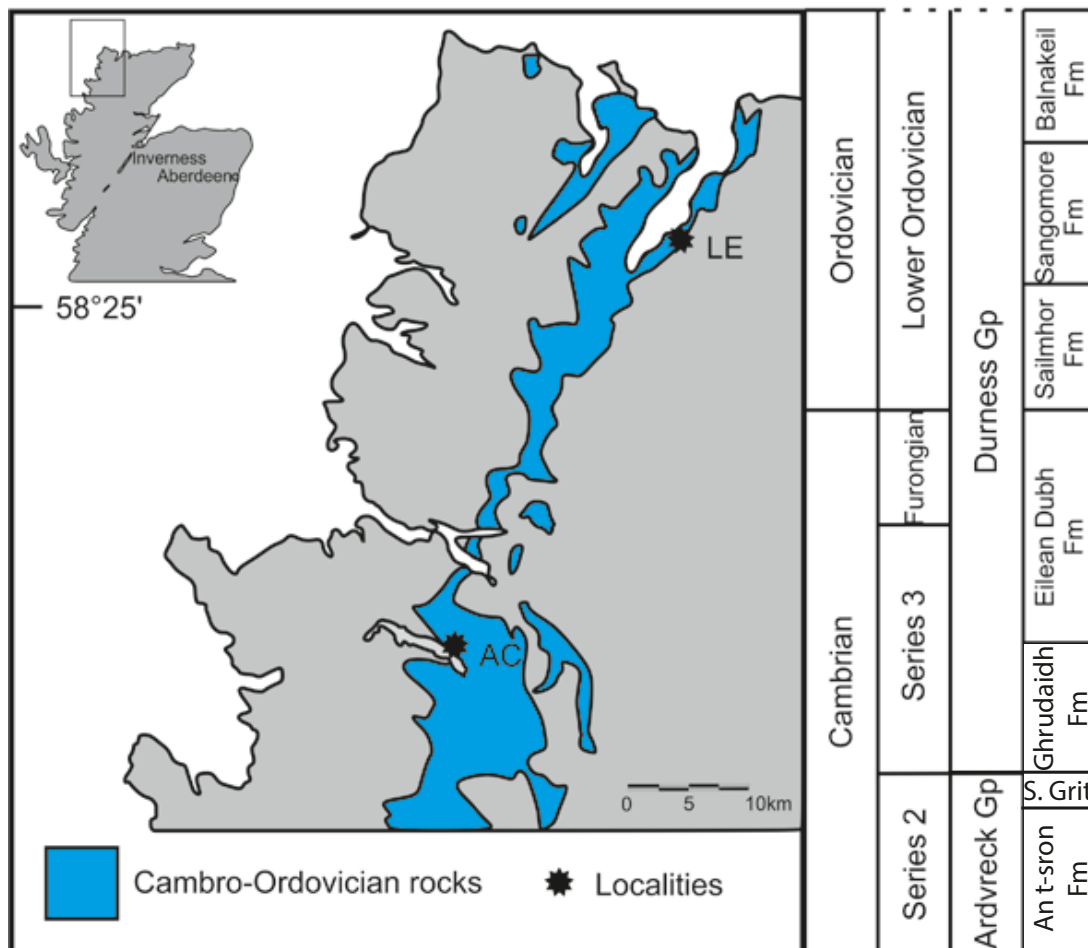

Figure 2.1: Locality map of the study locations (LE- Loch Eriboll, AC- Ardvreck Castle) in northwest Scotland, modified from Raine and Smith (2012), and summary of Lower-Middle Cambrian stratigraphic units in the region.

2.3 Geological setting and study locations

An almost continuous belt of Cambro-Ordovician rocks crop out along the Caledonian foreland within the Moine Thrust Zone of northwestern Scotland, from Loch Eriboll in the north to the Isle of Skye in the southwest (Fig. 2.1; Raine and Smith, 2012). These strata record deposition on the south-eastern Laurentian margin and are characterised by the predominance of marine sandstone of the Ardvreck Group and limestone and dolostone of the Durness Group. The Salterella Grit Member of the An t-Sròn Formation forms the uppermost part of the Ardvreck Group and consists of *Skolithos*-bioturbated cross-stratified, quartz arenitic sandstone (McKie, 1989, 1990). The transition to the Ghrudaidh Formation of the Durness Group marks the establishment of a thick succession of dolostone and limestone beds that formed in a range of supratidal, peritidal and shallow marine carbonate platform deposits (Raine and Smith, 2012). Quartz sand grains persist for a few metres in the basal Ghrudaidh Formation but their disappearance at higher levels has been attributed to an abrupt transgression causing the sediment hinterland to become far distant (Raine & Smith, 2012).

2.3.1 Loch Eriboll (58°28'56.64" N, 4°40'01.01" W)

A promontory on the western shore of Loch Eriboll is one of the few localities in NW Scotland in which the An t-Sròn, Ghrudaidh and the lower portion of the Eilean Dubh formations are well exposed without a significant tectonic break (Raine and Smith, 2012). The outcrop spans the upper Pipe Rock Member of the Eriboll Formation through the Fucoid and Salterella Grit members, and the Ghrudaidh Formation to a level above its boundary with the Eilean Dubh Formation.

2.3.2 Ardvreck Castle (58°10'12.51" N, 4°59'55.00" W)

A road cutting along the eastern shore of Loch Assynt exposes the upper sections of the Salterella Grit Member, and the transition into the lowest beds of the Ghrudaidh Formation.

2.4 Methods

Detailed sedimentary logging and sample collection was conducted at Loch Eriboll through a 52 m-thick section of siliciclastic and carbonate rocks of the Ardvreck and Durness groups. At Ardvreck Castle, a 10 m section

spanning the same boundary was also logged. Bed numbers were allocated, and field observations and petrographical analyses were used for lithofacies and fossil identification. SEM analysis (secondary and backscattered imaging and EDX elemental mapping) was undertaken to examine more detailed petrographic features including the nature of the pyrite content.

The $\delta^{13}C_{carb}$ and $\delta^{18}O_{carb}$ were analysed at the GeoZentrum Nordbayern of the FAU Erlangen-Nürnberg, Germany. Carbonate powders were reacted with 100% phosphoric acid at 70°C using a Gasbench II connected to a ThermoFisher Delta V Plus mass spectrometer. All values are reported in per mil relative to V-PDB by assigning $\delta^{13}C$ and $\delta^{18}O$ values of +1.95 and -2.20‰ to international standard NBS19 and -46.6 and -26.4‰ to international standard LSVEC, respectively. Reproducibility monitored by replicate analyses of laboratory standards calibrated to NBS19 and LSVEC was ±0.07 (1 sd) for $\delta^{13}C$ and ± 0.05 (1 sd) for $\delta^{18}O$.

2.5 Facies Analysis

2.5.1 Loch Eriboll

Salterella Grit Member

The 11 m-thick Salterella Grit Member consists of beds of medium-grained, cross-bedded and planar and parallel laminated quartz arenite together with strongly bioturbated quartz arenite ('pipe rock') with abundant *Skolithos* burrows (Fig. 2.2). The cross-sets are stacked on low-angle bounding surfaces and in some beds the intensity of *Skolithos* burrows is sufficient to obliterate the bedding especially in uppermost levels where the abundance of Salterella also increases. Petrographic examination shows the original quartz grains are well sorted and range from well-rounded to sub-rounded (Fig. 2.3 G, H). Also present are thin interbeds of laminated mudstones and fine siltstones that display a cleavage. The contact between these finer beds and overlying sandstone beds commonly display small gutter casts.

Ghrudaidh Formation

The Ghrudaidh Formation consists of massive, burrow-mottled and well-bedded dolomite beds that frequently display small vugs. The vugs have been interpreted to record the former presence of gypsum and anhydrite

(Raine and Smith, 2012), although they are now partly-filled with dolomite rhombs. In the absence of evaporitic pseudomorphs in the vugs, it is also feasible that these features are a remnant of volume reduction during dolomitization. Finely laminated white and dark grey dolomite is also present notably around 27 m above the base of the formation. Toward the top of the section is a ~1 m-thick (bed LE23), oolitic grainstone bed, a rare coarse-grained horizon. In thin section the majority of the dolomite beds consist of a mosaic of interlocking dolomite rhombs of silt to sand grade, which have mostly obliterated primary depositional fabrics. Thus, even apparently fine-grained, laminated dolomites seen in the field are found to be dolosparites when seen in thin section.

Salterella is the only identifiable fossil in this section of the Ghrudaidh Formation although other shell hash is also present (e.g. in LE9). The common burrows are mostly *Planolites* but there are also some branching *Thalassinoides*-like trace fossils.

The base of the Ghrudaidh Formation is taken at the sharp base of bed LE6 that marks the first appearance of carbonate. It is a dark, pyritic dolomite bed containing carbonate nodules, which in turn is succeeded by cleaved, pyritic, vuggy dolomite with Salterella and echinoderm fragments. SEM analysis of samples from LE6 reveals common pyrite microcrystal agglomerations (≤10 µm), scattered microcrystals and rare pyrite framboids that range in size from 5 µm to 25 µm diameter. A sample from the uppermost 8 cm of LE6 also revealed the presence of abundant tiny halite cubes, around 10 µm in diameter (Fig. 2.3, E, F; Fig. 2.4).
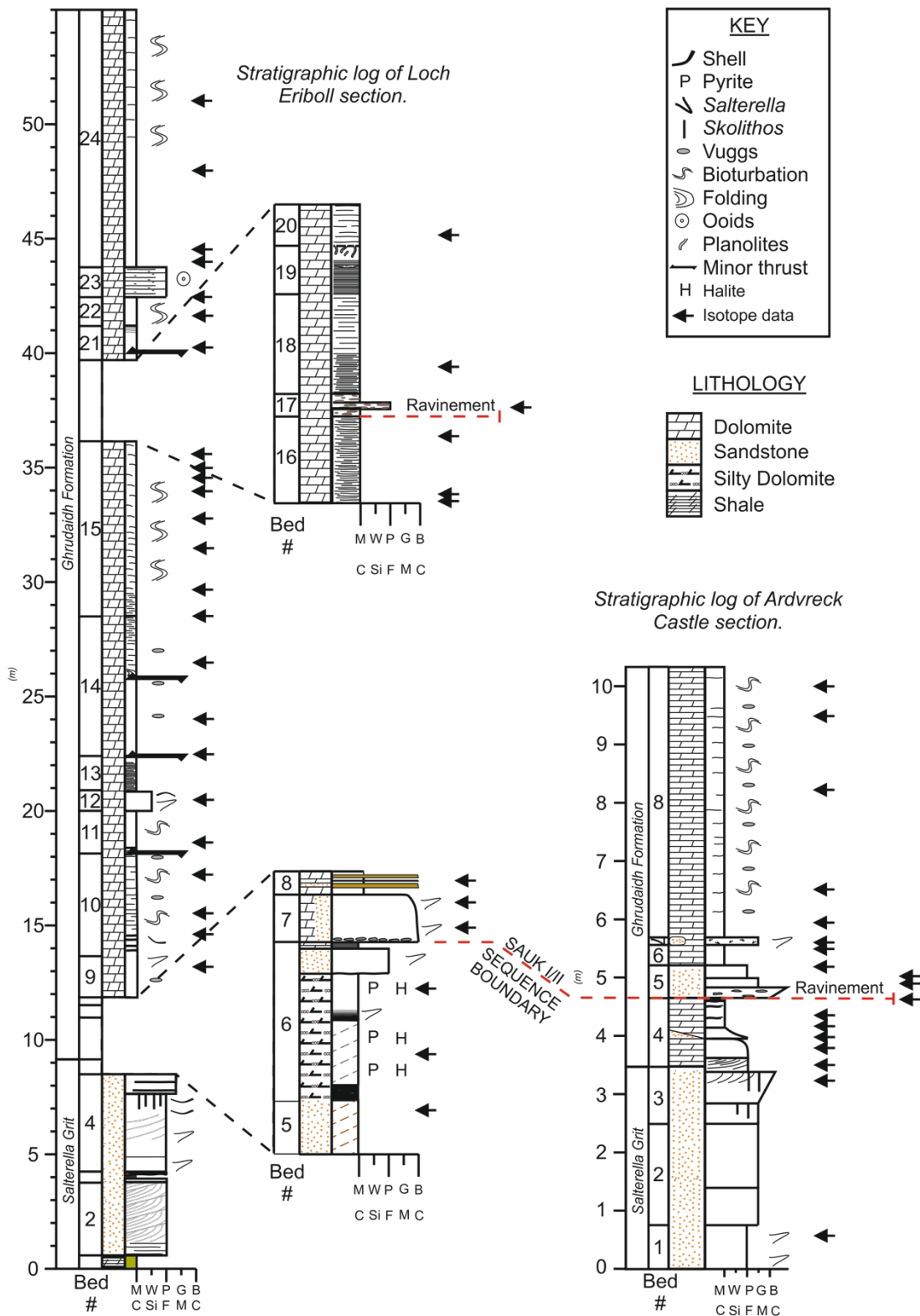
Figure 2.2: Sedimentary logs of the Loch Eriboll and Ardvreck Castle sections showing the correlation of a ravinement surface near the base of the Ghrudaidh Formation, and a second surface ~27m above the base of the Formation at Loch Eriboll.

Bed LE7 is a microconglomerate bed that sits on a sharp, slightly erosive base. It grades upwards into a dolomite with common well-rounded, quartz sand grains. The well-rounded lithoclasts are up to 1 cm in diameter and consist of dolosparite. Another rudaceous horizon occurs ~25 m above the base of the Ghrudaidh Formation (LE17) where three thin (<10 cm-thick) erosive-based microconglomerates occur. The well-rounded equant pebbles are up to 1 cm in diameter and are composed of biomicrite (Fig. 2.3 B). This clast lithology is not seen in the underlying beds, which are recrystallized dolostone (although they appear finer-grained and laminated in the field).

2.5.2 Ardvreck Castle

Salterella Grit Member

Like the strata in the Loch Eriboll section, the upper Salterella Grit Member at Ardvreck Castle is dominated by quartz arenite beds with trough cross sets and abundant *Skolithos* burrows.

Ghrudaidh Formation:

The contact between the Salterella Grit and Ghrudaidh Formation is sharp and is overlain by a bed (AC3) consisting in equal amounts of well-rounded quartz grains and sparry dolomite that grades upward into less quartz-rich dolomite (AC4). This basal 1 m of the Ghrudaidh Formation is a transitional lithology that sees a decline in siliciclastic content and a transition to the pure dolomites that form the remainder of the formation. SEM examination reveals no halite crystals in these beds. The quartz-sand-bearing dolomite beds are sharply truncated by a thin microconglomerate (bed AC5) composed of small (~ 5 mm), well-rounded pebbles of dolomite in a matrix dominated by well-rounded quartz grains. The succeeding Ghrudaidh strata are dominated by beds of vuggy, burrowed, massive dolomite that dominate the remainder of the Formation.
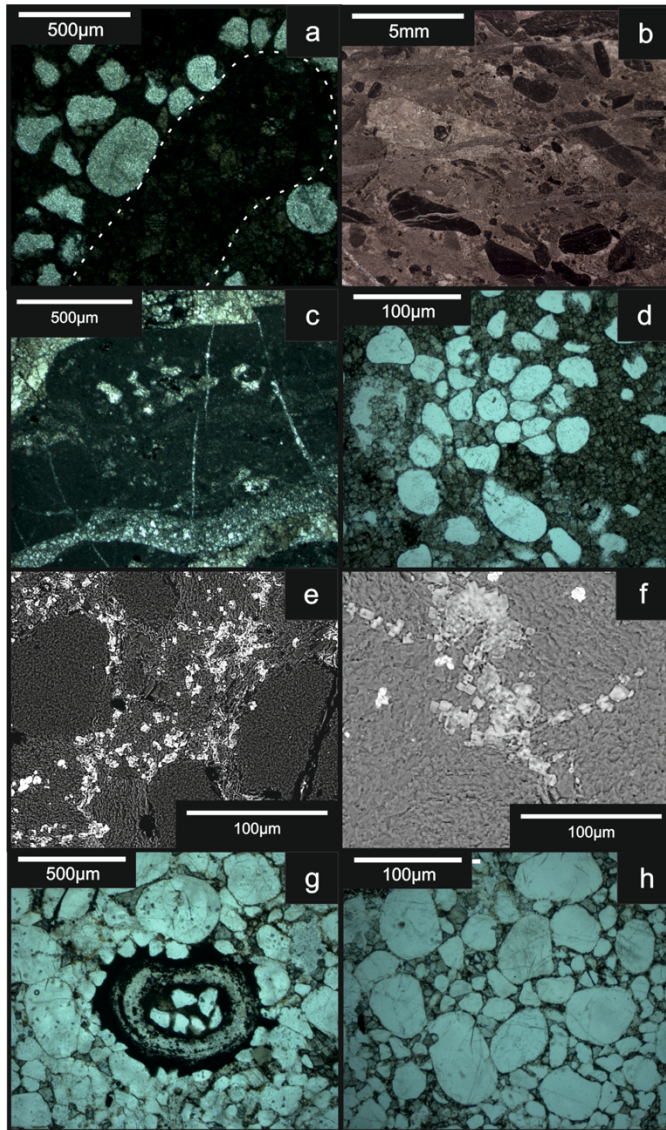
Figure 2.3: Photomicrographs of Ghrudaidh Formation facies. A: dolosparite pebble (highlighted with dotted line) in a sandy dolomicrite matrix, LE 17. B: Scan of slide of rudaceous limestone, exhibiting well-rounded, micrite clasts in a dolosparite matrix. C: Rudaceous limestone of bed LE17 showing irregularly shaped, sparry bioclasts in an intraclast. D: Photomicrograph of sandy/silty dolomite from the base of the Ghrudaidh Formation at Ardvreck Castle consisting of equal portions of rounded (aeolian) quartz grains and dolomite microspar (AC 3). E, F: Backscatter SEM images of LE 6 lagoonal facies. Bright white cubes are halite, mid grey is a fine dolomite matrix and the largest, dull grey grains in E are aeolian quartz silt and fine sand. G: Photomicrographs from Ardvreck Section. *Salterella* shell amongst well rounded quartz grains of the Salterella Grit, (Bed AC 1). H: Rounded silt and fine sand grains, a relatively poorly sorted lithology from Bed AC 1.

2.5.3 Interpretation

The Salterella Grit Member has been interpreted to be a tidal sandbank facies formed during a shallowing phase of deposition (McKie 1990, 1993). Conditions alternated between periods influenced by strong tidal currents and more quiescent intervals when intense burrowing occurred. The subsequent sharp transition to the fine-grained strata at the base of the Ghrudaidh Formation at Loch Eriboll indicates a considerable decrease in depositional energy. This observation, combined with the abundant occurrence of halite and small pyrite framboids at Loch Eriboll, suggests a restricted, evaporitic lagoonal setting and low oxygen conditions. The persistence of the well-rounded quartz grains that dominate the Salterella Grit Member, in these basal beds of the Ghrudaidh Formation, shows that the source terrain (probably aeolian dunes on the adjacent Laurentian craton) was still nearby.

The basal Ghrudaidh strata at Ardvreck Castle differs from that at Loch Eriboll because it has a higher proportion of quartz grains and lacks evidence (such as pyrite framboids and halite) for lagoonal deposition. It is possible that this is an intertidal facies developed immediately adjacent to aeolian dunes. However, contrasting facies are seen 0.9 km to the north of the Ardvreck locality at Lochan Feòir (NC 2367 2520), where very thinly bedded, black dolomitic mudstones containing abundant Salterella and articulated *Olenellus* aff. *reticulatus* Peach occur in the basal Ghrudaidh Formation (Huselbee and Thomas, 1998). The Lochan Feòir strata are similar to those found at Loch Eriboll suggesting that high energy and low energy strata show rapid lateral changes.

The sharp truncation of the basal Ghrudaidh lagoonal/intertidal facies by a microconglomerate at both study locations is interpreted to record the passage of a zone of erosion (see sequence stratigraphic discussion below) and heralded the establishment of persistently well-oxygenated conditions, as shown by the bioturbation and shelly fossils in the overlying fine-grained dolostone (now mostly recrystallized). The gradual loss of rounded quartz grains up section indicates an increasingly more distant source terrain (Raine and Smith, 2012). The low-energy conditions were occasionally punctuated by much higher energy conditions recorded by the rare oolitic

strata. The frequent vuggy appearance of the strata suggests replacement of secondary evaporites as a result of concentrated pore-fluid brines. The elevated salinity is interpreted to have occurred late in deposition of the Ghrudaidh Formation.

The bedset LE16-18 records a shift in conditions as the intensely burrowed strata is replaced by laminated dolomites and then a thin, erosive-based microconglomerate. This succession is similar to the strata that are seen at the base of the Ghrudaidh Formation where lagoonal beds were truncated during transgression.

2.6   Chemostratigraphy

This study presents the first $\delta^{13}C$ and $\delta^{18}O$ chemostratigraphic data for the Durness Group. A total of 20 samples from Ardvreck Castle were analysed, of which two samples from the Salterella Grit had insufficient carbonate content to yield a signal. In addition 40 samples from Loch Eriboll were analysed, and three were found to be too carbonate poor to yield a reliable value.

At Loch Eriboll, the lowest $\delta^{13}C_{carb}$ value is returned from the Salterella Grit Member, sample AS46 with a TIC of 4.5 wt % returned from Salterella shells. Although this is found in a sandstone we interpret the organic source of the carbonate to represent an original environmental signal. Above this $\delta^{13}C_{carb}$ values of -3.0 ‰ occur in the silty dolomites immediately above at the base of the Ghrudaidh Formation (Fig. 2.5). These were followed by an increase in the overlying 10 m culminating in peak positive values of -0.4 ‰ before a decline to a broad lowpoint of -2 ‰ around 30 m above the base of the formation. The curve then swings to heavier values of -0.6‰ and then falls to -1.6‰ at the top of the Loch Eriboll section. The shorter Ardvreck Castle $\delta^{13}C_{carb}$ record (Fig. 2.5) shows a rapid increase across the Salterella Grit/Ghrudaidh boundary to a positive peak 2 m above before declining. The two lowest values measured from the Salterella Grit Member at the base of the section come from sandstone in which the main carbonate content is the shells of Salterella (carbonate content ranges from 1 to 7 wt %, see Table 2.1). The positive hump of $\delta^{13}C_{carb}$ values seen at both location and is considered to record the same chemostratigraphic event. However, at

Ardvreck Castle this excursion occurs over a shorter interval (Fig. 2.5), an observation we attribute to a more condensed section at this location.

The $\delta^{18}O_{carb}$ values at both the Loch Eriboll and Ardvreck Castle locations show slight covariance with $\delta^{13}C_{carb}$ values only in samples taken from the Salterella Grit Member (Fig. 2.5 inset). The two lightest $\delta^{18}O_{carb}$ values that also correspond with the lightest $\delta^{13}C_{carb}$ values (Fig. 2.3) are from the sandstone of the Salterella Grit at Ardvreck Castle (see Table 2.1). In this member the main source of carbonate are the shells of Salterella and the carbonate content is significant enough (1-8 wt% TIC) to measure a carbonate carbon isotope signal. Whilst it is possible that this slight covariation is a reflection of an early diagenetic signal, at Loch Eriboll the strong similarity between Salterella Grit $\delta^{13}C_{carb}$ values (-2.98‰) and basal Ghrudaidh Formation values (-2.84‰) suggests that the Salterella Grit lowest data point at Loch Eriboll is in accordance with a reliable primary isotopic signal from the Ghrudiadh Formation. This observation suggests that $\delta^{13}C_{carb}$ values have not been affected by significant diagenesis and that the returning limb of ROECE recorded within the Salterella Grit and immediately above in the Ghrudaidh Formation is a primary record of oceanic carbon isotope fluctuations.

The $\delta^{13}C_{org}$ record we obtained (Table 2.1) shows frequent oscillations with no consistent trends between the sections nor any similarity with the $\delta^{13}C_{carb}$ curve. This variability probably relates to the extremely low total organic carbon values (mostly < 0.5 %) and the likelihood that values are influenced by factors such as reworked, detrital organic carbon.

Interpretation

Global oscillations in the Cambrian $\delta^{13}C_{carb}$ record include the ROECE, a major negative excursion developed around the Series 2 – Series 3 boundary during which values drop to -4‰ followed by a rapid recovery to heavier values (Montañez et al., 2000; Guo et al., 2010). From the Scottish data, we interpret the abrupt rise of $\delta^{13}C_{carb}$ at the base of the Ghrudaidh Formation to record this recovery phase. The amplitude of ROECE varies considerably between regions. Laurentian values are around 4.5 ‰, in China it can reach 7 ‰ but in Siberia it is only 1.5 ‰ (Wang et al., 2011). In
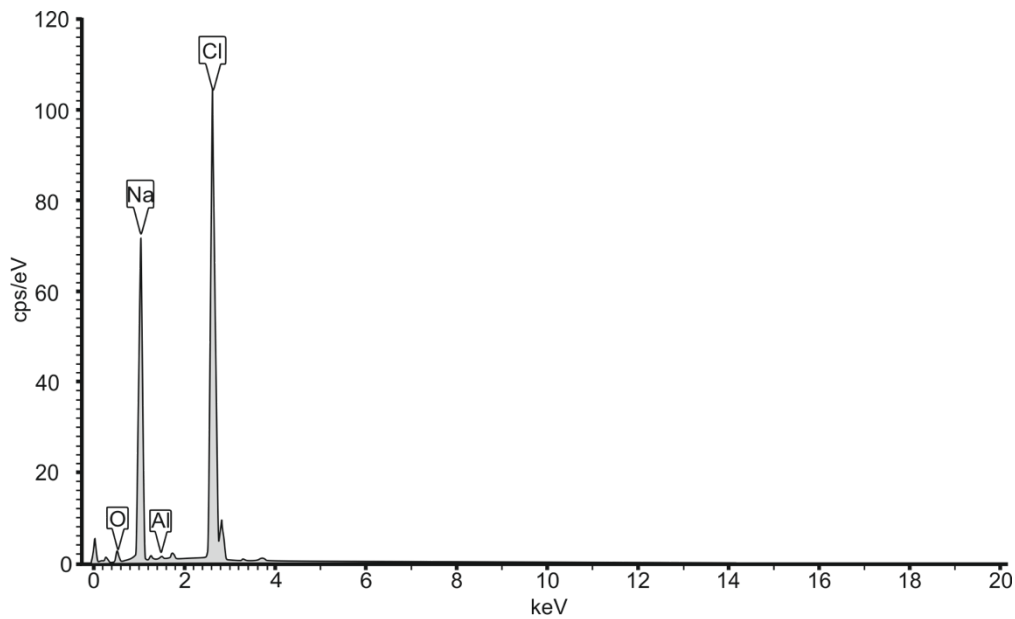
Figure 2.4: Representative EDS spectra taken from a halite cube in bed LE 6.

Scotland the excursion is 3 ‰ but this is likely not the full amplitude because the lowpoint of the curve is not recorded in the carbonate-free clastic sediments of the lower Salterella Grit.

The oscillations of $\delta^{13}C_{carb}$ values within the higher levels of the Ghrudaidh Formation (only studied at Loch Eriboll) can be closely matched with the global curve (Fig. 2.6) and they suggest that the prolonged lowpoint of values ~30 m above the base of the Ghrudaidh Formation (beds LE 16-18) could be DICE, an excursion that marks the Stage 5-Drumian stage age. As with ROECE, DICE varies considerably in magnitude. In South China it ranges from 1.0 to 2.5 ‰ but in the Great Basin of the western United States it is present as a 3.5 ‰ negative excursion (Zhu et al., 2004; Howley and Jiang 2010). The larger values in the USA may reflect the exacerbation of the excursion by regional factors such as upwelling of deep oceanic waters and/or erosion from newly uplifted mountains (Howley and Jiang, 2010). The amplitude of DICE in Scotland is towards the lower end of this reported range, with a magnitude of ~1 ‰.

Our chemostratigraphic age assignment for the Ghrudaidh Formation is also supported by the modest biostratigraphic data that is available. The single *Olenellus* reported from basal beds of the Ghrudaidh Formation (Huselbee and Thomas 1998), indicates a late Series 2 age. The presence of Salterella up to 10 m above the base of the formation also indicates a Series
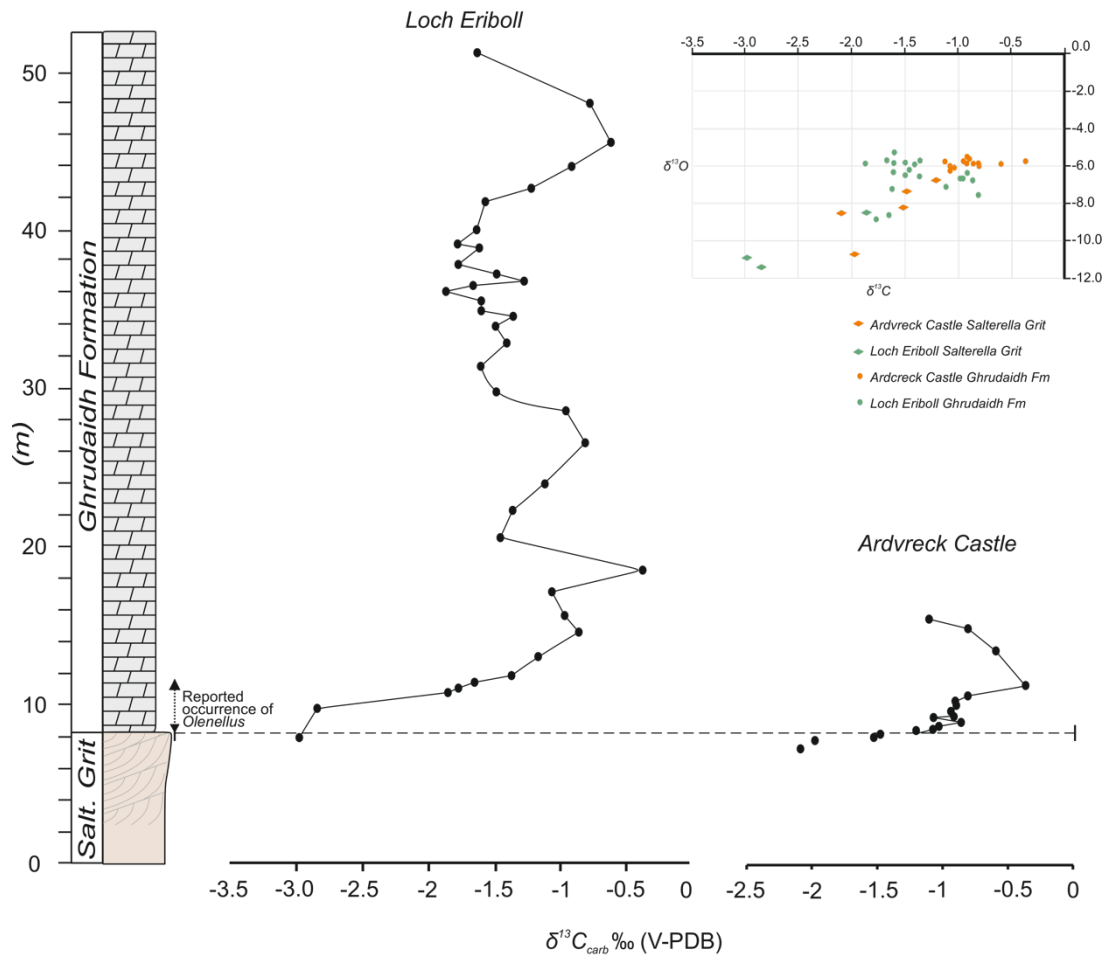
Figure 2.5: δ¹³C$_{carb}$ chemostratigraphic curve from Loch Eriboll and Arvreck sections. Top right inset is a cross-plot of C and O data with samples from the Salterella Grit Member and Ghrudaidh Fm from each location delineated by respective symbols. The reported occurrence of *Olenellus* is from Huselbee and Thomas, 1998, the precise location of the specimen is unknown but is indicated by the arrow interval.

2 age (Fritz and Yochelson, 1988; Wright and Knight, 1995). No other biostratigraphically useful fossils occur but Wright and Knight (1995) argued that the higher levels of the Ghrudaidh Formation correlated with the Bridge Cove Member of the March Point Formation in western Newfoundland. This age assignment places the Scottish strata above the 10 m level in our logs within the early part of Series 3. This is in agreement with our recognition of DICE 30 m above the base of the Ghrudaidh Formation at Loch Eriboll.

2.7   Sequence stratigraphy

The sequence stratigraphy of the Cambro-Ordovician succession of northwest Scotland was discussed by Raine and Smith (2012) who placed the boundary between Sloss's (1963) Sauk I and Sauk II supersequences at the An t-Sròn/Ghrudaidh formational boundary. In North America, this supersequence boundary is a major hiatal surface that formed during the Hawke Bay Event (Wright and Knight, 1995), but it is not clearly manifested outside of Laurentia (e.g. Alvaro and Debrenne, 2010; Pratt and Bordonaro, 2014). Northwest Scotland lay on the Laurentian margin and so this shallow-water setting might be expected to show a well-developed sequence boundary. However, the effect of the Hawke Bay event was surprisingly subdued. The formational boundary marks the culmination of prolonged shallowing and sees the transition from open, inner shelf conditions of the uppermost Salterella Grit to the restricted, lagoonal and intertidal facies of the basal Ghrudaidh Formation. This base level shift, from inner shelf to lagoon, is probably no more than 10 m. A few metres higher a ravinement surface marks the onset of flooding and modest deepening: again base-level changes are only of the order of a few metres. There are two options for the placement of a sequence boundary in this succession. The first would place it at the formational contact. This would imply that the overlying lagoonal/intertidal facies are a thin development of a lowstand systems tract with its top boundary being an initial flooding (ravinement) surface. The second option would consider the ravinement surface to be amalgamated with a sequence boundary and with the formational boundary only recording a facies change. Given the overall inner platform setting of the Scottish outcrops it is perhaps unlikely that any lowstand strata would be developed, because such sediment packages are typically found distally in offshore/shelf margin locations. Therefore we consider the second option to be the most probable. Thus the sequence boundary is developed low in the Ghrudaidh Formation and not at its base. It is likely to record a major hiatus. The halite crystals developed immediately below the surface at Loch Eriboll may have grown during this non-depositional episode in a supratidal setting. The succeeding 20 m-thick succession of dolomicrites do not record major

facies changes but the significant up-section decline of terrigenous material suggests continued transgression and flooding of the hinterland.
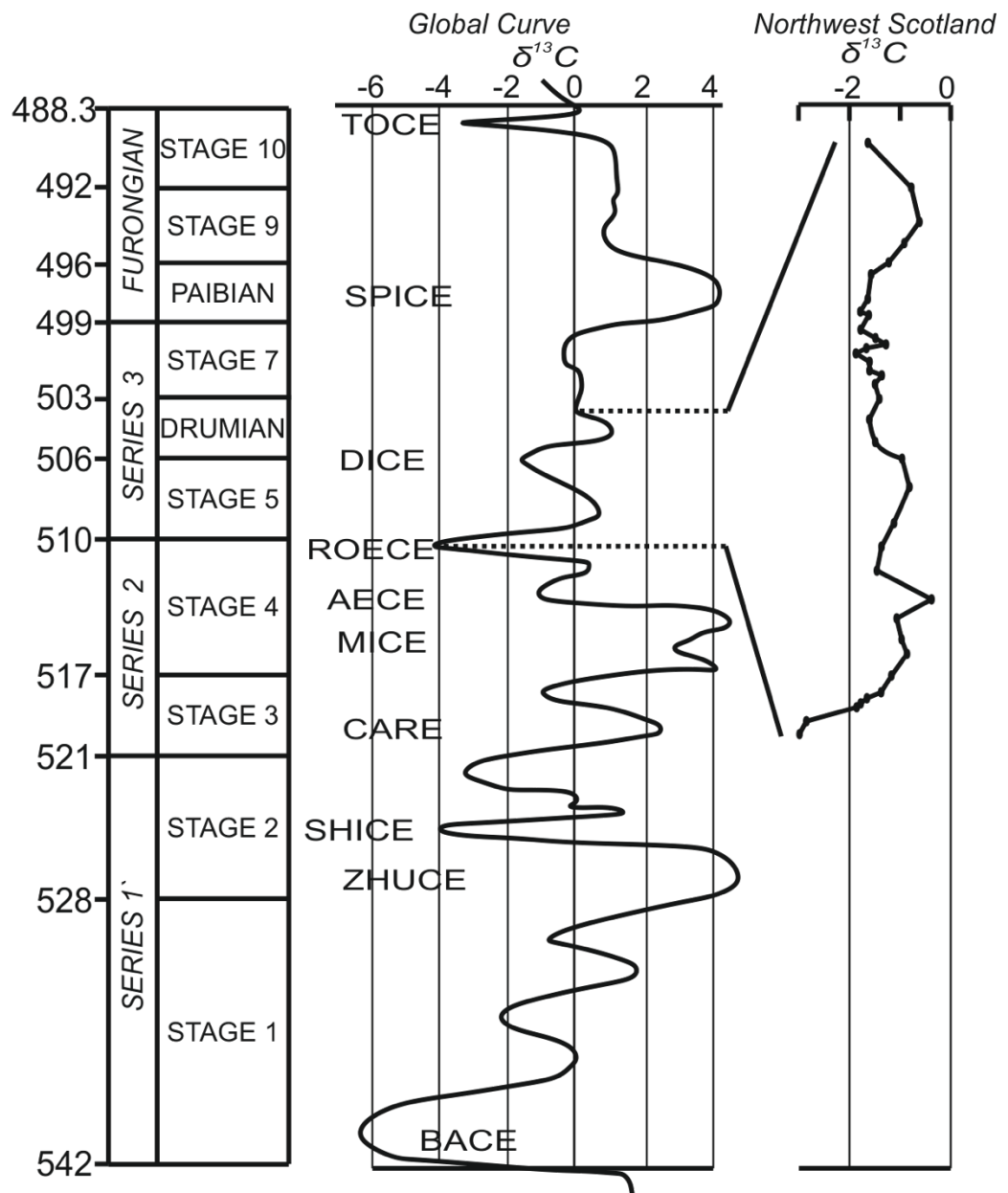

Figure 2.6: Global Cambrian carbon isotope curve (Zhu *et al*. 2006) showing the proposed correlation with the Scottish sections.

The next major facies change is centred on another thin microconglomerate (bed LE17). It is similar to the lower examples, and is also interpreted to have formed during ravinement. By comparison with the basal Ghrudaidh Formation, the finely laminated strata that underlie this bed (LE16) may be highstand lagoonal facies. Thus, this succession of Beds

(LE16 - 18), chemostratigraphically correlated with the Stage 5-Drumian boundary, probably records the regressive-transgressive couplet seen elsewhere in the world at this level (e.g. Montañez et al., 1996; Babcock et al., 2004; Alvaro et al., 2013).

2.8   Conclusions

The NW Scotland sections reveal a clear sequence of events across the Series 2 – Series 3 boundary and help evaluate some of the cause-and-effect relationships of this dynamic interval.

The later part of the ROECE is preserved in the $\delta^{13}C_{carb}$ record of the basal Ghrudaidh Formation with the lowpoint of this excursion probably occurring earlier during deposition of the Salterella Grit Member. Sequence boundary formation (perhaps the equivalent of the Hawke Bay event in North America) lead to the development of an erosive surface by ravinement processes that is mantled by a thin conglomerate near the base of the Ghrudaidh Formation. The overlying strata records transgression with an increasingly distal hinterland supply. No lowstand facies are developed because of the proximal setting on this Laurentian platform. The formational boundary, 2 m below the sequence boundary, is interpreted to be simply a facies contact that marks coastal progradation with inner shelf tidal clastic facies replaced by intertidal clastics and dolomitic lagoonal facies.

The Stage 5 – Drumian boundary, identified from carbon isotope oscillations (DICE), is found within the upper Ghrudaidh Formation and this too records an amalgamated sequence boundary/flooding surface with lagoonal facies transgressed by a conglomerate developed on a ravinement surface. The base of the Drumian in Gondwana is marked by the spread of anoxic facies by marine transgression (Alvaro et al., 2013). This level is also associated with trilobite turnover but the lack of fossils in the Scottish strata does not permit evaluation of this event. However, elsewhere in the world the earliest Drumian saw a major transgression and spread of anoxic facies, especially in Gondwanan sections (Alvaro et al., 2013). From our section at Loch Eriboll the dark grey, laminated dolomites (LE 18) could be a Laurentian development of this transgressive anoxic phase.

Olenellus occurs in the basal Ghrudaidh Formation within the highstand facies, but below the sequence boundary. Thus, the ROECE extinctions, which removed the olenellids, may have post-dated the peak negative values of ROECE. A similar post-excursion extinction of redlichiid trilobites is also seen in South China (Montañez et al., 2000; Zhu et al., 2004; Peng, Babcock and Cooper, 2012). This has a bearing on proposed extinction mechanisms. Montañez et al., (2000) argued that the incursion of deep anoxic waters (with a light carbon isotope signature derived from remineralized organic matter), into shallower waters may have triggered a biomass crash and trilobite extinction. The mistiming of the ROECE and extinctions in Scotland (and also in China e.g. Zhu et al., 2004) does not support this scenario. However, trilobites are exceptionally rare in the Ghrudaidh Formation and it is possible that the occasional *Olenellus* fossils are holdovers that post-date the main extinction. Further collecting is required in more fossiliferous sections worldwide to fully evaluate this extinction event.

2.9 References:

Ahlberg, P. E. R., Axheimer, N., Babcock, L. E., Eriksson, M. E., Schmitz, B., Terfelt, F. (2009). Cambrian high-resolution biostratigraphy and carbon isotope chemostratigraphy in Scania, Sweden: first record of the SPICE and DICE excursions in Scandinavia. *Lethaia*, *42(1)*, 2-16.

Álvaro, J. J., Bauluz, B., Subías, I., Pierre, C., Vizcaïno, D. (2008). Carbon chemostratigraphy of the Cambrian-Ordovician transition in a midlatitude mixed platform, Montagne Noire, France. *Geological Society of America Bulletin, 120(7-8)*, 962-975.

Álvaro, J. J., Debrenne, F. (2010). The Great Atlasian Reef complex: an early Cambrian subtropical fringing belt that bordered West Gondwana. *Palaeogeography, Palaeoclimatology, Palaeoecology, 294(3)*, 120-132.

Álvaro, J. J., Ahlberg, P., Babcock, L. E., Bordonaro, O. L., Choi, D. K., Cooper, R. A., Jago, J. B. (2013). Global Cambrian trilobite palaeobiogeography assessed using parsimony analysis of endemicity. *Geological Society, London, Memoirs, 38(1)*, 273-296.

Babcock, L. E., Rees, M. N., Robison, R. A., Langenburg, E. S., Peng, S. (2004). Potential Global Standard Stratotype-section and Point (GSSP) for a Cambrian stage boundary defined by the first appearance of the trilobite Ptychagnostus atavus, Drum Mountains, Utah, USA. *Geobios, 37(2),* 149-158.

Babcock, L. E., Robison, R. A., Rees, M. N., Peng, S., Saltzman, M. R. (2007). The global boundary stratotype section and point (GSSP) of the Drumian Stage (Cambrian) in the Drum Mountains, Utah, USA. *Episodes, 30(2),* 85.

Brasier, M. D., Corfield, R. M., Derry, L. A., Rozanov, A. Y., Zhuravlev, A. Y. (1994). Multiple δ^{13}C excursions spanning the Cambrian explosion to the Botomian crisis in Siberia. Geology, **22(5)**, 455-458.

Debrenne, F., Rozanov, A. Y., Webers, G. F. (1984). Upper Cambrian Archaeocyatha from Antarctica. *Geological Magazine, 121(04),* 291-299.

Fan, R., Deng, S., Zhang, X. (2011). Significant carbon isotope excursions in the Cambrian and their implications for global correlations. *Science China Earth Sciences, 54(11)*, 1686-1695.

Fritz, W. H., Yochelson, E. L. (1988). The status of Salterella as a Lower Cambrian index fossil. *Canadian Journal of Earth Sciences, 25(3)*, 403-416.

Guo, Q., Strauss, H., Liu, C., Zhao, Y., Yang, X., Peng, J., Yang, H. (2010). A negative carbon isotope excursion defines the boundary from Cambrian Series 2 to Cambrian Series 3 on the Yangtze Platform, South China. *Palaeogeography, Palaeoclimatology, Palaeoecology, 285(3)*, 143-151.

Howley, R. A., Jiang, G. (2010). The Cambrian Drumian carbon isotope excursion (DICE) in the Great Basin, western United States. *Palaeogeography, Palaeoclimatology, Palaeoecology, 296(1)*, 138-150.

Huselbee, M. Y., Thomas, A. T. (1998). Olenellus and conodonts from the Durness Group, NW Scotland, and the correlation of the Durness succession. Scottish Journal of Geology, **34(1)**, 83-88.

Ishikawa, T., Ueno, Y., Shu, D., Li, Y., Han, J., Guo, J. Komiya, T (2014). The δ 13 C excursions spanning the Cambrian explosion to the Canglangpuian mass extinction in the Three Gorges area, South China. *Gondwana Research, 25(3),* 1045-1056.

Maloof, A. C., Porter, S. M., Moore, J. L., Dudás, F. Ö., Bowring, S. A., Higgins, J. A., Eddy, M. P. (2010). The earliest Cambrian record of animals and ocean geochemical change. *Geological Society of America Bulletin, 122(11-12)*, 1731-1774.

McKie, T. (1989). Barrier island to tidal shelf transition in the early Cambrian Eriboll Sandstone. *Scottish Journal of Geology, 25(3)*, 273-293.

McKie, T. (1990). Tidal and storm influenced sedimentation from a Cambrian transgressive passive margin sequence. *Journal of the Geological Society, 147(5)*, 785-794.

McKie, T. (1993). Relative sea-level changes and the development of a Cambrian transgression. *Geological Magazine, 130(02)*, 245-256.

Montañez, I. P., Banner, J. L., Osleger, D. A., Borg, L. E., Bosserman, P. J. (1996). Integrated Sr isotope variations and sea-level history of

Middle to Upper Cambrian platform carbonates: Implications for the evolution of Cambrian seawater ^{87}Sr/^{86}Sr. *Geology, 24(10)*, 917-920.

Montañez, I. P., Osleger, D. A., Banner, J. L., Mack, L. E., Musgrove, M. (2000). Evolution of the Sr and C isotope composition of Cambrian oceans. *GSA today, 10(5)*, 1-7.

Palmer, A. R. (1998). Terminal early Cambrian extinction of the Olenellina: documentation from the Pioche Formation, Nevada. *Journal of Paleontology, 72(04)*, 650-672.

Palmer, A. R., James, N. P. (1980). The Hawke Bay event: a circum-Iapetus regression near the Lower–Middle Cambrian boundary. *The Caledonides in the USA, 2,* 15-18.

Peng, S., Babcock, L. E., Cooper, R. A. (2012). The Cambrian Period. In The Geologic Time Scale (2012) 2-Volume Set. (eds Gradstein, F.M.; Ogg, G.& Schmitz, M.), pp.437-488, *Elsevier*.

Perejón, A., Moreno-Eiris, E., Bechstädt, T., Menéndez, S., Rodríguez-Martínez, M. (2012). New Bilbilian (early Cambrian) archaeocyath-rich thrombolitic microbialite from the Láncara Formation (Cantabrian Mts., northern Spain). *Journal of Iberian Geology, 38(2)*, 313-330.

Pratt, B. R., Bordonaro, O. L. (2014). Early middle Cambrian trilobites from La Laja Formation, Cerro El Molle, Precordillera of western Argentina. *Journal of Paleontology, 88(5)*, 906-924.

Raine, Robert J., M. Paul Smith, (2012). Sequence stratigraphy of the Scottish Laurentian margin and recognition of the Sauk megasequence, in The great American carbonate bank: The geology and economic resources of the Cambrian– Ordovician Sauk megasequence of Laurentia (eds J. R. Derby, R. D. Fritz, S. A. Longacre, W. A. Morgan, and C. A. Sternbach), pp 575-598 *AAPG Memoir 98*.

Sloss, L. L. (1963). Sequences in the cratonic interior of North America. *Geological Society of America Bulletin, 74(2)*, 93-114.

Smith, E. F., Macdonald, F. A., Petach, T. A., Bold, U., Schrag, D. P. (2015). Integrated stratigraphic, geochemical, and paleontological

late Ediacaran to early Cambrian records from southwestern Mongolia. *Geological Society of America Bulletin, 128(3-4)*, 442-468.

Wang, X., Hu, W., Yao, S., Chen, Q., Xie, X. (2011). Carbon and strontium isotopes and global correlation of Cambrian Series 2-Series 3 carbonate rocks in the Keping area of the northwestern Tarim Basin, NW China. *Marine and Petroleum Geology, 28(5)*, 992-1002.

Wright, D. T., Knight, I. (1995). A revised chronostratigraphy for the lower Durness Group. *Scottish Journal of Geology, 31(1)*, 11-22.

Zhang, W., Shi, X., Jiang, G., Tang, D., Wang, X. (2013). Mass-occurrence of oncoids at the Cambrian Series 2–Series 3 transition: Implications for microbial resurgence following an Early Cambrian extinction. *Gondwana Research. 28(1)*, 432-450.

Zhu, M. Y., Zhang, J. M., Li, G. X., Yang, A. H. (2004). Evolution of C isotopes in the Cambrian of China: implications for Cambrian subdivision and trilobite mass extinctions. *Geobios, 37(2)*, 287-301.

Zhu, M. Y., Babcock, L. E., Peng, S. C. (2006). Advances in Cambrian stratigraphy and paleontology: integrating correlation techniques, paleobiology, taphonomy and paleoenvironmental reconstruction. *Palaeoworld, 15(3)*, 217-222.

Zhuravlev, A. Y., Wood, R. A. (1996). Anoxia as the cause of the mid-Early Cambrian (Botomian) extinction event. *Geology, 24(4)*, 311-314.

3. Chapter 3: Trilobite extinctions, facies changes and the ROECE carbon isotope excursion at the Cambrian Series 2 – Series 3 boundary, Great Basin, western USA.

This chapter is published as:

3.1. Abstract

The mass extinction of the olenellid trilobites occurred around the Cambrian Series 2 – Series 3 boundary. Like many other crises, it coincided with a negative carbon isotope excursion but the associated palaeoenvironmental changes remain unclear. To investigate the causal mechanism for this event, we report facies changes, pyrite framboid petrography and carbon isotope values from Cambrian Series 2 – Series 3 (traditionally Early – Middle Cambrian) boundary strata of the Carrara Formation (Death Valley region, California) and Pioche Formation (Nevada). These data reveal regionally changing water depths from high-energy, nearshore facies (oolitic grainstone) to more offshore silty marl and finer-grained carbonate mudstone. In the Carrara Formation, the series boundary occurs within a deepening succession, transitioning from high-energy, nearshore facies (oolitic grainstone and oncolitic packstone) to offshore marl, the latter of which contains pyrite framboid populations indicative of low-oxygen (dysoxic) depositional conditions. Intermittent dysoxia persisted below sub-wave base settings throughout the early and middle Cambrian, but did not intensify at the time of extinction, arguing against anoxia as a primary cause in the olenellid trilobite extinction. Within both field areas, the extinction interval coincided with a minimum in $\delta^{13}C_{carb}$ values, which we interpret as the regional manifestation of the Redlichiid-Olenellid Extinction Carbon isotope Excursion (ROECE). The Series 2 – Series 3 boundary is

reported to closely coincide with a large-amplitude sea-level fall that produced the Sauk I/II sequence boundary, but the placement of the Series 2 – Series 3 boundary within a transgressive interval of the Carrara Formation shows that this is not the case. The main sequence boundary in the succession occurs much lower in the succession (at the top of the Zabriskie Quartzite) and therefore precedes the extinction of the olenellids and ROECE.

Keywords: Olenellid extinction, Carrara Formation, Pyramid Shale Member, Pioche Formation, C-Shale Member

3.2. Introduction

The first major biotic crisis of the Phanerozoic occurred during the Cambrian Series 2, an interval that saw the collapse of archaeocyathan reefs (Newell, 1972; Boucot, 1990; Debrenne, 1991; Zhuravlev and Wood, 1996). This was followed, at the Series 2 - Series 3 boundary, by severe generic-level losses of olenellid and redlichiid trilobites (Palmer, 1998; Zhu et al., 2004; Zhu et al., 2006; Fan et al., 2011; Wang et al., 2011; Zhang et al., 2013). This trilobite extinction has been used to delineate the Series 2 - Series 3 boundary; however, the boundary remains unratified as international correlation is confounded by a lack of globally-distributed taxa at this time (Sundberg et al., 2016). The trilobite extinction coincides with a major negative $\delta^{13}C$ excursion that has been termed the Redlichiid-Olenellid Extinction Carbon Isotope Excursion or ROECE (Zhu et al. 2004, 2006).

In the western Great Basin of the United States, a Cambrian sedimentary succession developed on a rapidly subsiding passive margin (Prave, 1999; Stewart, 1972; Fedo and Cooper, 2001; Hogan et al., 2011; Keller et al., 2012; Morgan, 2012). Sections in the southern Nopah Ranges (Keller et al., 2012) expose strata from Cambrian Sauk I and Sauk II supersequences that are of importance to this study (Prave, 1991). These are widespread, large-scale Laurentian sequences that provide a regional stratigraphic framework. The transition from Sauk I to Sauk II records a major lithological change that saw the siliciclastic deposition of the Zabriskie Quartzite replaced by carbonate deposition of the Carrara Formation (Keller et al., 2012; Morgan, 2012). The contact between these two units is

considered to be the Sauk I/ Sauk II sequence boundary (Keller et al., 2012; Morgan, 2012).

Throughout the Phanerozoic the relationship between environmental perturbation and extinction is a common focus of studies, including those in the Cambrian (Hallam and Wignall, 1997; Wignall, 2015). In particular, sea-level change, marine anoxia, carbon isotope excursions and eruptions of LIPs (large igneous provinces) often coincide with mass extinctions (Zhuravlev and Wood, 1996; Wignall, 2001; Glass and Phillips, 2006; Jourdan et al., 2014). Thus, Zhuravlev and Wood (1996) noted the temporal link between widespread deposition of black shales and the disappearance of the archaeocyathans in the Cambrian of Siberia, and trilobite extinctions at "biomere" boundaries are also ascribed to dysoxia (Palmer, 1984). However, the role of anoxia in Cambrian extinctions has to be viewed in the context of persistently oxygen-restricted oceans at this time (e.g. Montañez et al., 2000; Hurtgen et al., 2009; Pruss et al., 2010; Gill et al., 2011; Saltzman et al., 2015; Tarhan et al., 2015).

Volcanism may also have played a role in ROECE (Glass and Phillips, 2006). The Kalkarindji LIP is a Cambrian flood basalt province of northern and central Australia with an estimated original surface area of ~ 2.1×10^6 km^2 (Glass and Phillips, 2006; Jourdan et al., 2014; Marshall et al., 2016). Latest dating efforts yield a zircon age of 510.7 ± 0.6 Ma, which is close to that of the Cambrian Series 2 - Series 3 boundary (Jourdan et al., 2014).

In order to improve our understanding of the events associated with ROECE, this study examines sections spanning the Cambrian Series 2 - Series 3 boundary interval in the western Great Basin. The olenellid extinction horizon has been located within the Pioche Formation in Nevada (Palmer, 1998). We have examined this level and the correlative levels in the Carrara Formation in California in order the examine changes of lithofacies, carbon isotope variability and pyrite petrography.

3.3. Geological background and biostratigraphy

Following breakup of the Rodinia supercontinent in the late Neoproterozoic, the northwestern margin of Laurentia subsided rapidly (Bond and Kominz, 1984; Levy and Christie-Blick, 1991; Prave, 1999; Howley et al., 2006). By the early Cambrian, the western Great Basin (USA) was positioned along the western margin of Laurentia where a wide, clastic-dominated shelf developed in an equatorial setting (Palmer and Halley, 1979; MacNiocaill and Smethurst, 1994; Fig. 3.1). Clastic input decreased in late Series 2 and was replaced by carbonate deposition (Erdtmann and Miller, 1981; Howley et al., 2006; Landing, 2012).

We have assessed environmental conditions across the Series 2 – Series 3 boundary from sections in the Great Basin including Emigrant Pass (Nopah Range, Death Valley, eastern California), and Oak Springs Summit (Burnt Springs Range, eastern Nevada; Fig. 3.1). The regional lithostratigraphy of the Pioche Formation (at Oak Springs Summit) was described in detail by Merriam and Palmer (1964), and the Carrara Formation (at Emigrant Pass) by Palmer and Halley (1979). In addition, we examined a section of the Pioche Formation at Ruin Wash in eastern Nevada.

3.3.1. Emigrant Pass

At Emigrant Pass the Zabriskie Quartzite and Carrara Formation are easily accessible and well exposed. The strata are seen on the north side of Old Spanish Trail Highway as a continuous section of quartz arenite and shale forming slopes and moderately steep hillsides with limestone forming prominent ledges (Figs. 3.1 and 3.2). The Zabriskie Quartzite is dominated by burrowed and hummocky cross-bedded quartz arenite beds (Prave, 1991; Keller et al., 2012). It lacks age-diagnostic fossils, but rocks immediately above and below have yielded fauna from the *Bonnia-Olenellus* trilobite zone of Series 2 (Diehl, 1974; Palmer and Halley, 1979; Prave, 1991; Peng et al., 2012).

The Carrara Formation comprises cycles of silty marl and limestone with a trilobite fauna spanning the *Bonnia-Olenellus* to the *Glossopleura* zones, and thus the Series 2 – Series 3 boundary (Adams, 1995; Palmer
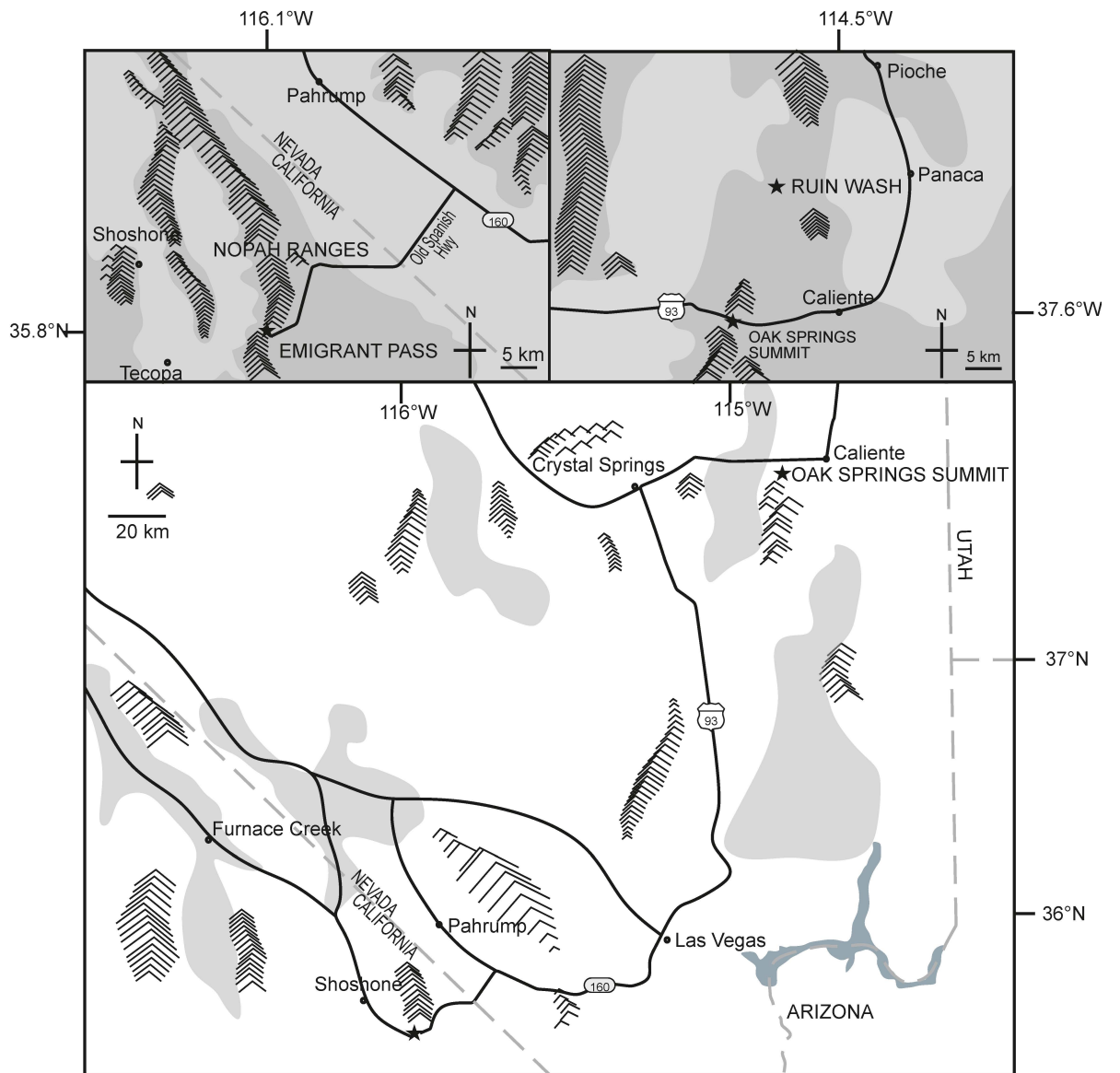
Figure 3.1: Location map showing study sections at Emigrant Pass, Death Valley region, California (35° 53' 29.24"N, 116° 04' 39.08"W) and Oak Springs Summit, Burnt Spring Range, Lincoln County, Nevada (37°37'04.32"N 114°43'17.20"W). Star indicates approximate location of field area during the Cambrian Series 2 (after McKerrow et al., 1992).

and Halley, 1979; Sundberg and McCollum, 2000; Babcock et al., 2012; Keller et al., 2012; Fig. 3.3). The unit has been divided into nine members in the western Great Basin: Eagle Mountain Shale, Thimble Limestone, Echo Shale, Gold Ace Limestone, Pyramid Shale, Red Pass Limestone, Pahrump Hills Shale, Jangle Limestone and the Desert Range Limestone (Palmer and Halley, 1979). However, there is significant lateral variation within the Carrara Formation and at Emigrant Pass, the Thimble Limestone is not present (Palmer and Halley, 1979; Adams and Grotzinger, 1996). Overall the carbonate content of the Carrara Formation decreases in more basinward settings to the west (Hogan et al., 2011; Keller et al., 2012; Foster, 2014). Within the Carrara Formation at Emigrant Pass, five members are important to this study.

The Eagle Mountain Shale Member consists of green to grey-brown silty shale with interbedded lenses and beds of bioclastic limestone developed towards the top (Palmer and Halley, 1979). This is overlain by the Echo Shale Member which consists of green, platy shale and brown-orange limestone. The Echo Shale is correlated with the basal Combined Metals Member of the Pioche Formation in eastern Nevada (Palmer and Halley, 1979). The succeeding Gold Ace Limestone is a prominent, cliff-forming limestone (Cornwall and Kleinhampl, 1961). The strata include thin to medium-bedded lime mudstone, with dolomitic beds and oncolitic limestone (Palmer and Halley, 1979). Based on shared trilobite zones, the Gold Ace Limestone correlates with the Combined Metals Member of the Pioche Formation at Oak Springs Summit (Merriam and Palmer, 1964).
The overlying Pyramid Shale Member is a green shale with interbeds of brown and maroon silty marl and lenses of oncolitic and bioclastic limestone. Trilobite biostratigraphy indicates the Pyramid Shale is equivalent to two members of the Pioche Formation in eastern Nevada: the C-Shale Member and the Susan Duster Limestone Member (Palmer and Halley, 1979; Palmer, 1998). The Red Pass Limestone Member is the youngest unit examined in Death Valley. It forms prominent cliffs of oncolitic and bioclastic limestone, laminated lime mudstone and fenestral lime mudstone (Palmer and Halley, 1979). There is no equivalent limestone unit in the Pioche Formation of Nevada (Palmer and Halley, 1979).
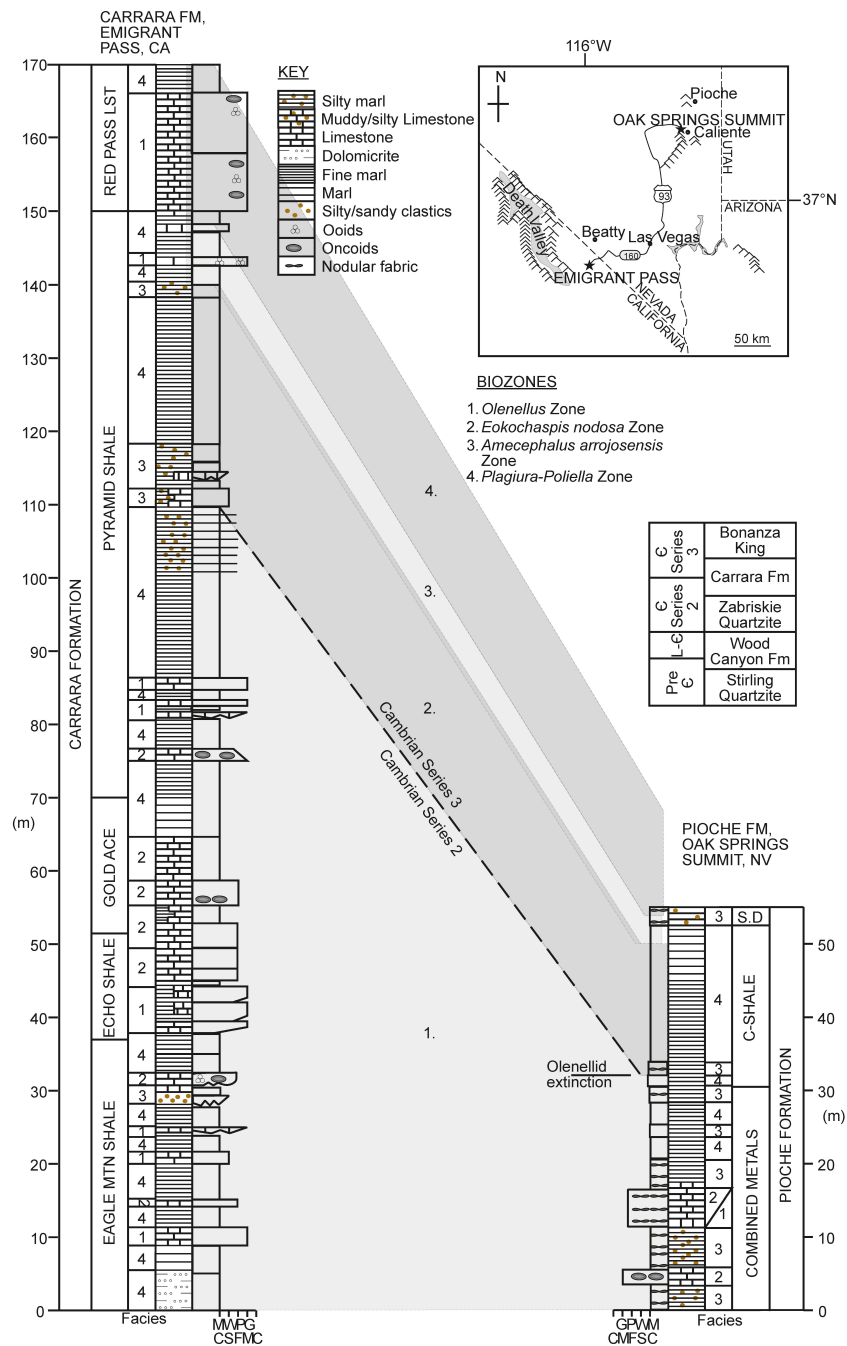
Figure 3.2: Biostratigraphic correlation of the trilobite zones of the Carrara and Pioche formations (Palmer and Halley, 1979; Sundberg and McCollum, 2000). Facies column is based on field and petrographic observations, and numbers relate to facies detailed in Table 3.1. A generalised stratigraphic column of Precambrian and Cambrian formations in Death Valley is given (from Corsetti and Hagadorn, 2000).

3.3.2. Oak Springs Summit

At Oak Springs Summit, the Pioche Formation crops out to the west of a parking area in a dry river bed. Limestone forms more prominent ledges and platforms whilst shale forms recessively weathered outcrop (Figs. 3.1 and 3.2). The Combined Metals Member is composed of silty, oncolite-bearing dark limestone with *Olenellus* (Palmer, 1998; Sundberg and McCollum, 2000; Hollingsworth et al., 2011). It is overlain by the C- Shale Member (formerly the Comet Shale), a series of shale and thin-bedded limestone beds with pinch-and-swell bed boundaries (Palmer, 1998; Sundberg and McCollum, 2000). The Series 2 – Series 3 boundary is placed at the base of the C-Shale due to the sudden disappearance of the Olenellidae, and their replacement by a fauna dominated by *Eoptychoparia piochensis* at this level (Palmer, 1998; Sundberg and McCollum, 2000). The succeeding Susan Duster Limestone Member is a well-bedded, grey marl with occasional argillaceous and bioclastic limestone beds composed of trilobite fragments (Merriam and Palmer, 1964).

3.3.3. Biostratigraphy

Trilobite assemblages from the Carrara and Pioche formations belong to the Olenellus, Eokochaspis nodosa, Amecephalus arrojosensis and the Plagiura-Poliella zones that provide a framework for regional correlation (Merriam and Palmer, 1964; Palmer and Halley, 1979; Fig. 3.3). The Olenellus Zone ranges from the Zabriskie Quartzite to the basal portion of the Pyramid Shale Member within Death Valley (Palmer and Halley, 1979; Fig. 3.2). In Nevada, this zone spans the Delamar Member to the base of the C-Shale (Merriam and Palmer, 1964; Sundberg and McCollum, 2000). All olenellid trilobites disappear over a ~ 2 cm interval at the top of the zone, forming a distinct extinction horizon (Palmer, 1998; Fig. 3.2). This is immediately followed by first appearance of the ptychopariid trilobite Eokochaspis nodosa, which defines both the base of the E. nodosa Zone, and the Series 2 – Series 3 boundary (Sundberg and McCollum, 2000; Fig. 3.2). E. nodosa Zone faunas also occur in the Pyramid Shale Member in Death Valley (Sundberg and McCollum, 2000).

The succeeding *Amocephalus arrojosensis* Zone contains *A. arrojosensis*, *Mexicella robusta* and *Kochina? walcotti*. The zone is best

defined at Hidden Valley, Nevada, where its base is 30 m above the base of the C-Shale Member (Merriam and Palmer, 1964), but it has not been recorded in the Carrara Formation due to a paucity of fossils above the *E. nodosoa* Zone in the Pyramid Shale (Palmer and Halley, 1979). However, trilobites, from the *Plagiura- Poliella* Zone, reappear in the uppermost Pyramid Shale and lower Red Pass Limestone (Palmer and Halley, 1979).

3.4. Methods

Sedimentary logging of the Carrara and Pioche formations was undertaken. At Emigrant Pass, 170 m of the Carrara Formation was logged from the base of the formation (at the contact with the Zabriskie Quartzite) up to the Red Pass Limestone Member. At Oak Springs Summit a 53 m-thick section of the Pioche Formation was logged, ranging from the basal Combined Metals Member to Susan Duster Limestone Member, an interval correlative with the Emigrant Pass section based on trilobite biostratigraphy Merriam and Palmer, 1964; Palmer and Halley, 1979; Fig. 3.2). From these logs, four facies were defined (discussed below, Table 3.1). At the two study sections, 30 samples from the Pioche Formation and 57 samples from the Carrara Formation were analysed for $\delta^{13}C_{carb}$ (Table 3.2). In Lincoln County, Nevada, we also sampled the Ruin Wash location (Palmer, 1998; Lieberman, 2003) for additional facies and framboid analysis. Ruin Wash provided a second section (after Oak Springs Summit) where the extinction horizon of the olenellids is clearly seen (see Appendix A). Facies analysis was undertaken in the field and complemented by petrographic examination of 49 thin sections.
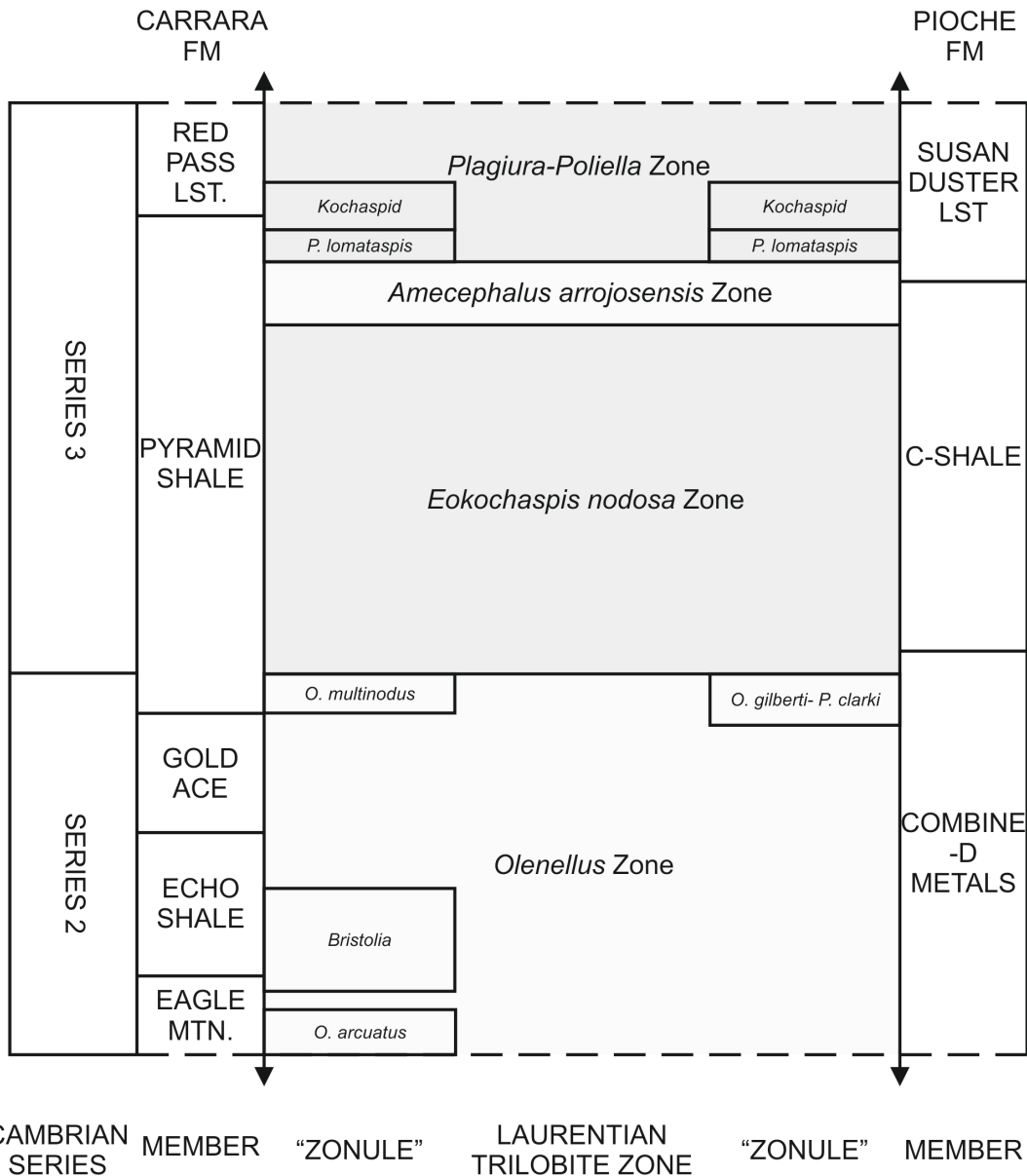
Figure 3.3: Correlation of trilobite biozones within the Carrara and Pioche formations (Merriam and Palmer, 1965; Palmer and Halley, 1979; Sundberg and McCollum, 2000). *O.* **is** *Olenellus*, *P.* **is** *Poliella*.

In order to evaluate redox conditions, pyrite framboid size distribution was also assessed on 21 samples taken at sub-metre scale intervals, 3.5 metres either side of the *Olenellus* biozone boundary at each of the three locations in order to assess any evidence for redox variation across this targeted interval. Using a scanning electron microscope (FEI Quanta 650 FEG-ESEM) in backscatter mode samples were scanned for amorphous pyrite and framboidal pyrite content. Pyrite framboids sizes were measured on-

screen using built-in measurement software, and their size distribution counted (see Bond and Wignall (2010) for procedure).

The calcite carbon (^{13}C / ^{12}C) and oxygen (^{18}O / ^{16}O) isotope values of powdered bulk sediment samples were measured on a total of 98 samples at the GeoZentrum Nordbayern, FAU Erlangen-Nurnberg, Germany (27 samples) and the School of Environmental Sciences, University of Liverpool, UK (71 samples). Carbon dioxide was prepared by reaction with phosphoric acid either at 70°C using a Gasbench II preparation system (FAU) or at 25 ^{o}C using the classical, 'sealed vessel' method (UoL). Mass ratios of the resultant purified gases were measured with a ThermoFisher Delta V plus mass spectrometer operating in continuous flow mode (FAU) or a VG SIRA 10 dual-inlet mass spectrometer (UoL). Raw gas data were corrected for ^{17}O effects and calibrated to the VPDB scale using a combination of international reference materials (δ^{13}C values are assigned as +1.95 ‰ to NBS 19 and – 46.6 ‰ to LSVEC and δ^{18}O values of –2.20 ‰ to NBS19 and –23.2 ‰ to NBS18) and laboratory quality control materials and reported as conventional delta (δ) values. Analytical precision (1 σ) is estimated to be better than 0.1 ‰ for both isotope ratios based on replicate analysis of standards. Some notable differences in oxygen isotope values were reported where specific samples were duplicated by both laboratories. The reason for these differences is uncertain. Although some discrepancies were found to be significant, they do not impact on either the palaeoenvironmental or chemostratigraphic interpretation of the carbon isotope data.

The topmost 8 samples of the Carrara Formation were analysed at the University of Massachusetts, Amherst. Powdered, homogenized samples were analysed for $\delta^{13}C_{carb}$ and $\delta^{18}O_{carb}$ values using a Finnigan Delta XL+ isotope ratio mass spectrometer with an automated carbonate prep system (Kiel III). We report results as the per mille difference between sample and the VPDB standard in delta notation where δ^{18}O or δ^{13}C = (R_{sample} / $R_{standard}$ − 1) x 1000, and R is the ratio of the minor to the major isotope. Results were calibrated using a house standard (crushed, washed and sieved marble) with VPDB values of +1.28 for δ^{13}C ‰ and –8.48 ‰ for δ^{18}O. Reproducibility of standard materials is 0.1 ‰ for δ^{18}O and 0.05 ‰ for δ^{13}C.

Total carbon (TC) and total organic carbon (TOC), following removal of calcite by acid decomposition of bulk sediment samples, was measured using a LECO SC-144DR Dual Range carbon and sulphur analyser at the University of Leeds. Total inorganic carbon (TIC) was subsequently calculated by difference (TIC = TC - TOC). An estimate of the calcite content for each sample was made by assuming that all TIC is hosted by calcite (wt % calcite = TIC x 8.333).

3.5. Results

3.5.1. Facies Analysis

Four facies and nine sub-facies were identified (Table 3.1): grainstone, packstone, silty marl and marl and they have been grouped into an onshore-offshore trend spanning shallow subtidal to outer shelf environments (Table 3.1). The shallowest strata consist of grainstone facies with common shell hash that is often abraded. Beds are typically decimetres thick and can show a hummocky top surface and sharp, erosive bases. Inclined stacks of flat-pebble intraclasts with herringbone-like cross stratification are present, suggesting storm wave processes (Fig. 3.4 D). Bioturbated packstone, with sub-facies of oncolitic, bioclastic and silty packstone varieties (Fig. 3.5 B), are interpreted to be a deeper facies based on the presence of a micritic mud matrix. Deeper water silty marl include fissile, homogenous and thoroughly bioturbated variants. Deepest-water, most offshore successions are dominated by fine grained marl, including sub-facies of laminated, pyritic dolomicrite and bioturbated marl with ichnofabric index (II) values of 2 - 3 (II2 and II3) in the scheme of Droser and Bottjer (1986).

The facies distribution reveals consistent trends in the two principal study sections. The base of the Carrara Formation, seen at Emigrant Pass, is dominated by deeper water facies (Facies 4) of the Eagle Mountain Shale. Commonly, the marl has a grey-green colour produced by the abundance of chlorite and clinochlore in the matrix (Figs. 3.4 F, 3.5 A and 3.6 E).
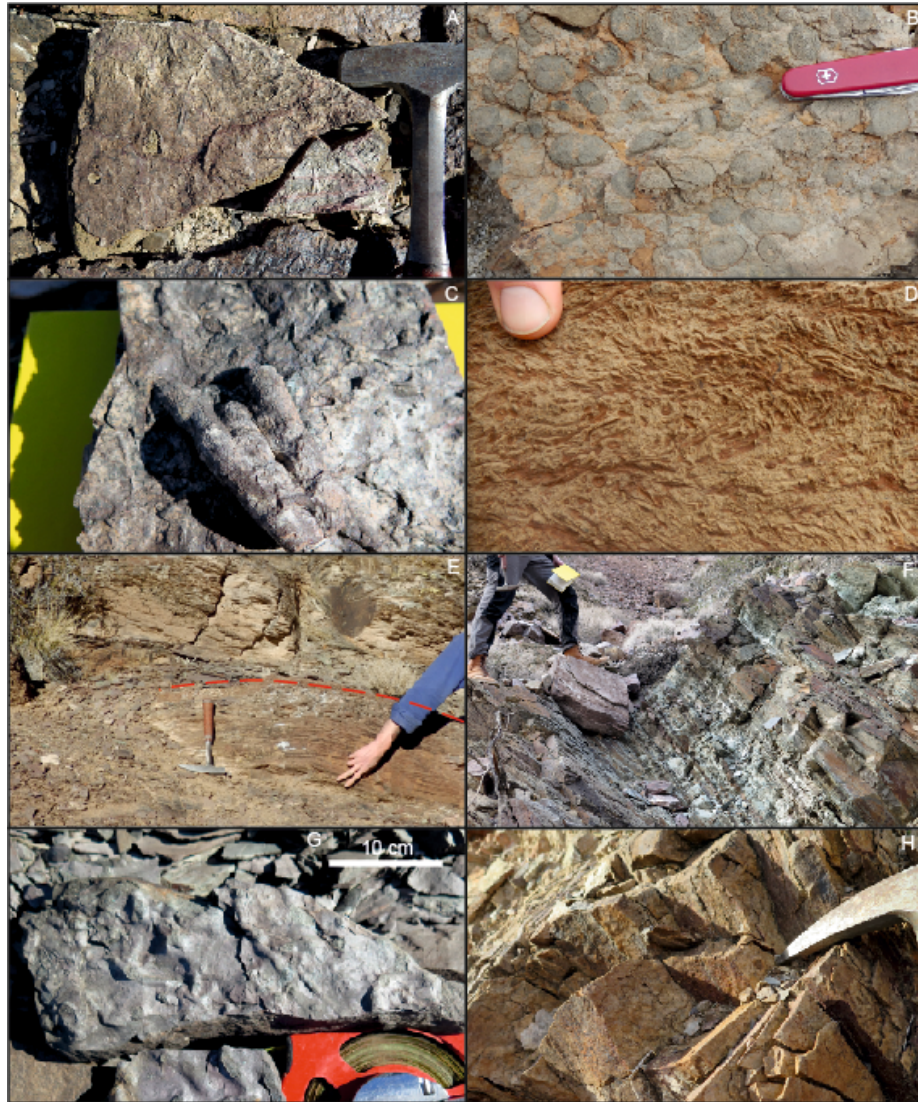
Figure 3.4: Field photographs. A. Trilobite debris (spines and carapaces and hyoliths) in a bioclastic hash on bedding planes of oolitic grainstone, Carrara Formation. **B.** Oncolitic packstone facies at Emigrant Pass. **C.** Bifurcating burrows in well bioturbated silty marl at Emigrant Pass, notebook for scale. **D.** Oolitic grainstone facies showing inclined chevron-style packing of thin intraclast and bioclasts (hyolith, ooid and other detrital fragments). **E.** Olenellid extinction level at the base of the C-Shale Member at Oak Springs Summit. Red line indicates extinction horizon from Palmer (1998). **F.** Fissile, laminated marl and silty marl in the lower Eagle Mountain Shale at Emigrant Pass. **G.** *Thalassinoides* in fine-grained, silty marl of the Carrara Formation. **H.** Vertical burrows (at the hammer tip) in silty marl beds of the Carrara Formation.
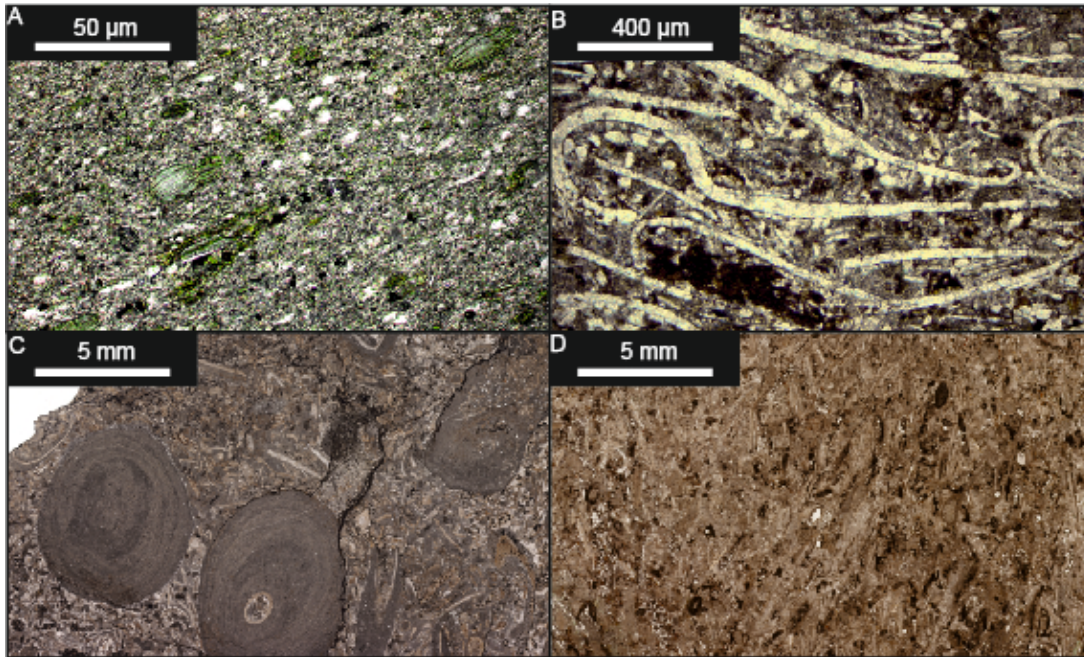
Figure 3.5:. Scans of thin sections and photomicrographs. A. Photomicrograph of a range of chlorite in the silty marl facies immediately above the extinction horizon at Oak Springs Summit. Chlorite occurs as elongate grains and also as cement. B: Photomicrograph of a silty bioclastic packstone in the upper Eagle Mountain Shale. C: Scan of slide of oncolitic packstone (Eagle Mountain Shale) showing oncoids with bioclastic nucleus of echinoderm plates amongst a matrix of shell detritus and micrite. D: Scan of slide of bioclastic grainstone. Elongate, trilobite fragments dominate this facies alongside hyolith remains and echinoderm plates. Dark brown mineral growth shows iron oxide preferentially replacing shell material.

Laminated intervals are common, although these occur interbedded with burrowed strata suggesting there were frequent fluctuations of redox conditions.

The exception to the generally quiet, low-energy deposition of the Eagle Mountain Shale is recorded by a sharp, erosive-based bed of Facies 1 developed just over 30 m above the base of the section. This shelly, oncolitic packstone contains rip-up clasts of the underlying marl and sole marks on its base (Fig. 3.7 A). Internally, thin intraclasts and shells display a chevron-stacking pattern (Fig. 3.4 D). A major storm event seems likely to have

104
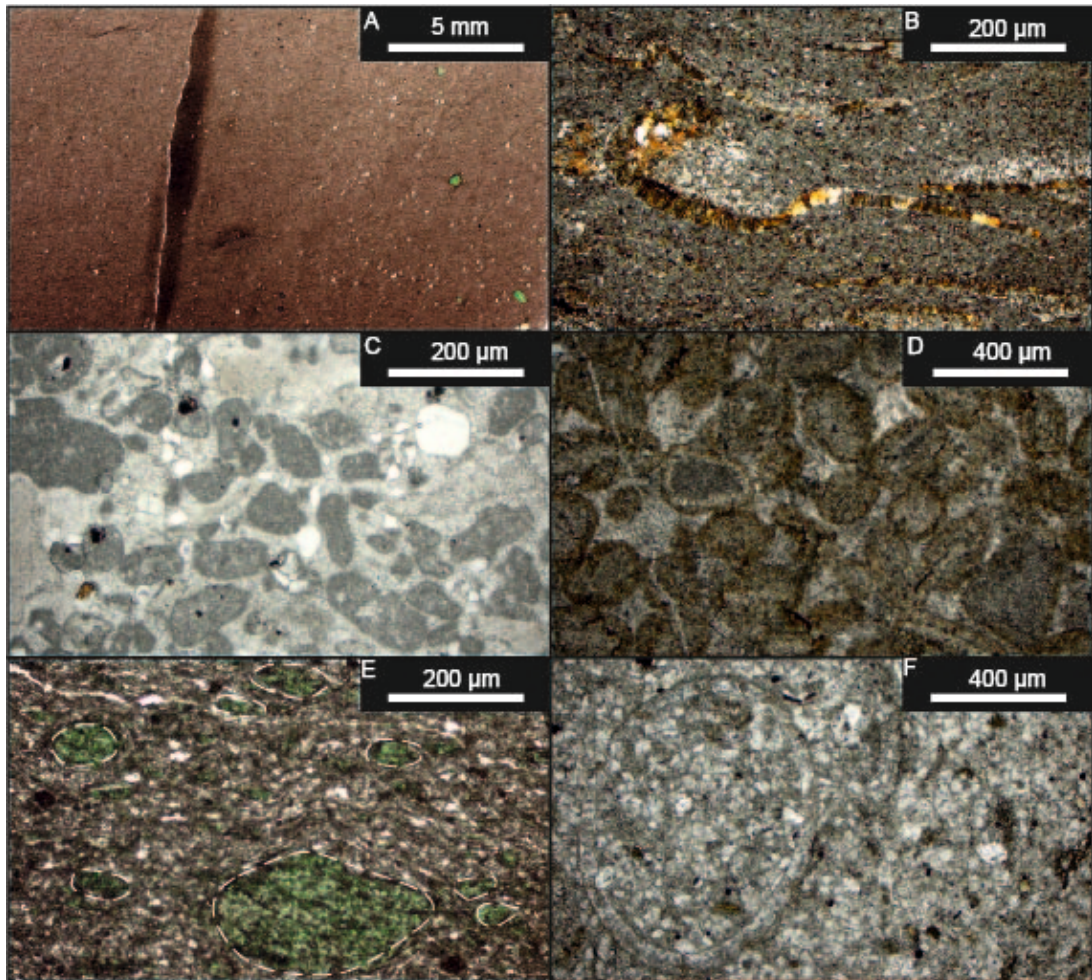
Figure 3.6: Scans of thin sections and photomicrographs. A: Scan of silty marl showing quartz grains and detrital chlorite grains (green). B: Photomicrograph of marl facies in the Combined Metals Member, Pioche Formation. Trilobite carapace exhibits brown needle like iron oxide replacement of the calcite shell. C: Photomicrograph of peloidal grainstone facies in the Combined Metals Member, Pioche Formation. Well rounded micrite pellets alongside rounded quartz grains amongst a fine micrite matrix. D: Photomicrograph of oolitic, bioclastic grainstone with iron oxides partially replacing ooids. E: Photomicrograph of silty chloritic limestone showing rounded chlorite grains (white dashed lines). F: Photomicrograph of chloritic silty marl facies showing sub-angular to angular quartz sand grains alongside hyolith and trilobite debris.

produced this horizon with the shell-stacking produced by powerful bi-directional currents. The succeeding Echo Shale and Gold Ace members record shallowing. Grainstone and packstone dominate this 20-m-thick interval which includes erosive-based oncolitic packstone beds (Fig. 3.7 B). Above this in the Pyramid Shale Member marl facies dominate, taken to be indicative of a sustained deepening. Grainstone and packstone facies developed in the lower ~ 15 m of the member are interpreted to have been transported during storm events. It is within this transgressive phase that the Series 2 – Series 3 boundary is recorded, along with the olenellid extinction (Foster, 2014). Deep-water sedimentation is abruptly terminated by the development of shallow-water grainstone at the base of the Red Pass Limestone Member (Fig. 3.7). Ooids and abraded fossil material (Table 3.1, Sub-Facies 1.1) suggest a nearshore setting.

The Pioche Formation at Oak Springs Summit records a more distal version of the succession seen within the Carrara Formation with relatively deep-water Facies 3 and 4 dominating (Fig. 3.2), though the same overall deepening-upwards trend is seen. Thus, the lower half of the Combined Metals Member consists of alternating silty marl and packstone. Above this, the remainder of the section is dominated by deeper-water facies (Fig. 3.2). The uppermost Combined Metals Member and the majority of the C-Shale Member record a similar transgressive deepening seen within the Pyramid Shale Member of the Carrara Formation. The olenellid extinction level occurs within this transgressive succession between a marl and a silty marl in the base of the C-Shale Member (Fig. 3.4 E). This minor facies shift does not represent a significantly different environment and as such extinction is not thought to be a function of facies change. Immediately above the extinction horizon, chlorite in the form of both rounded grains and cement becomes common (Fig. 3.5 A). The remainder of the C-Shale Member is a thick package of marl that transitions to silty marl at the base of the Susan Duster Limestone.

3.5.2. Pyrite Framboid Analysis

Framboid size analysis was performed on the Series 2 – Series 3 boundary strata (and thus the extinction horizon) from the Pioche Formation at Oak Springs Summit, where 11 samples were collected in a 7 m interval

spanning 3.5 m either side of the extinction horizon. All samples contained abundant scattered crystals of pyrite ranging in size from 1-10 μm, often found agglomerated in clustered patches. Five samples yielded framboids preserved as iron oxyhydroxides due to weathering, with only minor amounts of original pyrite preserved in their core. The framboids showed a size distribution spanning an anoxic-dysoxic range (Fig. 3.8). The most dysoxic sample (smallest mean framboid diameter size and size range, lowest standard deviation) occurred in a marl approximately 1 m below the extinction horizon. Dysoxic framboid populations also occurred in the 1 m of strata overlying the extinction level. However, a sample from 20 cm below the extinction level did not yield any pyrite framboids suggesting fully oxygenated conditions. This variable degree of oxygen-restriction suggested by the framboid analysis is also seen in the variability of the associated sedimentary fabrics, which varies from laminated to slightly burrowed (II2).

Seven samples were also analysed from the Pioche Formation at Ruin Wash where the olenellid extinction horizon has been located within a succession of marls (Palmer, 1998; Lieberman, 2003; Appendix A). Generally, framboidal pyrite was absent at this location with the exception of two samples from 10 and 15 cm below the extinction horizon where they had size ranges that plot in the anoxic field (Fig. 3.8). An additional four samples from around the extinction horizon at Emigrant Pass were also analysed. In this case, all samples only yielded scattered pyrite crystals but not framboids, suggesting better oxygenated conditions in this shallower-water section.

It is important to address that a drawback of the pyrite framboid proxy is the problem with distinguish between a euxinic (O_2 free, H_2S excess) or ferruginous (O_2 free, Fe^{2+} excess) water column. The factor controlling pyrite formation and size growth is its ambient buoyancy in the water column during formation, which is crossed once it reaches a diameter of ~5-6 μm (Wilkin et al., 1996) therefore euxinic size distributions could potentially accumulate under a ferruginous water column (e.g. Hammarlund et al., 2012). Despite this, there remains a strong contrast between euxinic size distributions and dysoxic populations.

3.5.3. Chemostratigraphy

In the basal 20 m of the Carrara Formation $\delta^{13}C$ values are highly variable and do not show a clear trend (Fig. 3.7), but they then begin to stabilise around –2 ‰ before a consistent positive trend develops. In the Pyramid Shale Member the base of the negative excursion begins with at –0.1 ‰, above this $\delta^{13}C_{carb}$ values begin a decline to a lowpoint at 105 m of –3.5 ‰ (a negative shift of 3.4 ‰). In the overlying 25 m, no data was obtained because carbonate values were too low for analysis. Above this gap, $\delta^{13}C_{carb}$ values show a positive trend, returning to values around –0.1 ‰, similar to those from the base of the section.

Barring one outlier at the base of the section, $\delta^{13}C_{carb}$ values from the first 13 m of the Pioche Formation remain around –2.5 ‰ before there is a sharp, positive shift to –1.0 ‰ over the next 15 m (Fig. 3.7). From this value of –1.0 ‰ a negative shift occurs, resulting in peak negative values of –4.8 ‰. The nadir at the base of the C-Shale Member marks an overall shift of –3.8 ‰, a similar size to that found at Emigrant Pass. At the top of the section values return to around 0 ‰.

3.6. Discussion

3.6.1. Carbon isotopes and diagenesis

In order to evaluate the reliability of our isotope data we assess the preservation of a primary carbon isotope signal in our samples. In both the Carrara and Pioche formations the isotope analyses are derived from samples with a wide range of carbonate values (Table 3.2). The high TIC samples are likely to record primary carbon isotope signatures since they are buffered from external change by a large carbonate-carbon reservoir (Saltzman and Thomas, 2012). Lower TIC samples are more susceptible to post depositional isotopic alteration or addition of carbonate with a non-primary carbon isotope composition (Brand and Veizer, 1981; Banner and Hanson, 1990; Marshall, 1992). In both sections, the excursion to the lowest δ13Ccarb values occurs at the level of the trilobite extinction (mid-Pyramid Shale, Carrara Formation and basal C-Shale, Pioche Formation) where TIC is < 2 wt. %. Here we assess the preservation of a primary carbon isotope composition, particularly in samples with low TIC.

Two diagenetic processes can alter the primary isotopic composition: recrystallization of carbonate or precipitation of additional authigenic carbonate with a distinct isotope composition (Marshall, 1992). Both marine pore fluids and meteoric waters can have dissolved inorganic carbon (DIC) enriched in ^{12}C from the oxidation of organic matter and these mechanisms have differing predictions of the $\delta^{13}C_{carb}$ and $\delta^{18}O_{carb}$ values preserved (Marshall, 1992). Both the Carrara and Pioche formations display commonalities in their relationships between their $\delta^{13}C_{carb}$ and $\delta^{18}O_{carb}$ ratios and their TIC and TOC concentrations. Firstly (point 1), neither formation shows a clear relationship between $\delta^{13}C_{carb}$ and $\delta^{18}O_{carb}$ (Appendix B 2 and 3). Secondly (point 2), samples with the most negative $\delta^{13}C_{carb}$ and the most positive $\delta^{18}O_{carb}$ are mostly characterised by low TIC (defined as < 2 wt. %). Both the Carrara and Pioche formations exhibit generally low TOC (point 3). In the Carrara Formation TOC concentrations range from 5.17 to 0.0 wt. % TOC with a mean concentration of 0.14 wt. % TOC. In the Pioche Formation concentrations range from 2.69 to 0.0 wt. % TOC, with a mean of 0.12 wt. % TOC. Finally (point 4), high TOC samples are characterised by more positive $\delta^{13}C_{carb}$. The major difference between the sections for these parameters is a much clearer positive relationship between TIC and $\delta^{13}C_{carb}$ within the Pioche Formation.
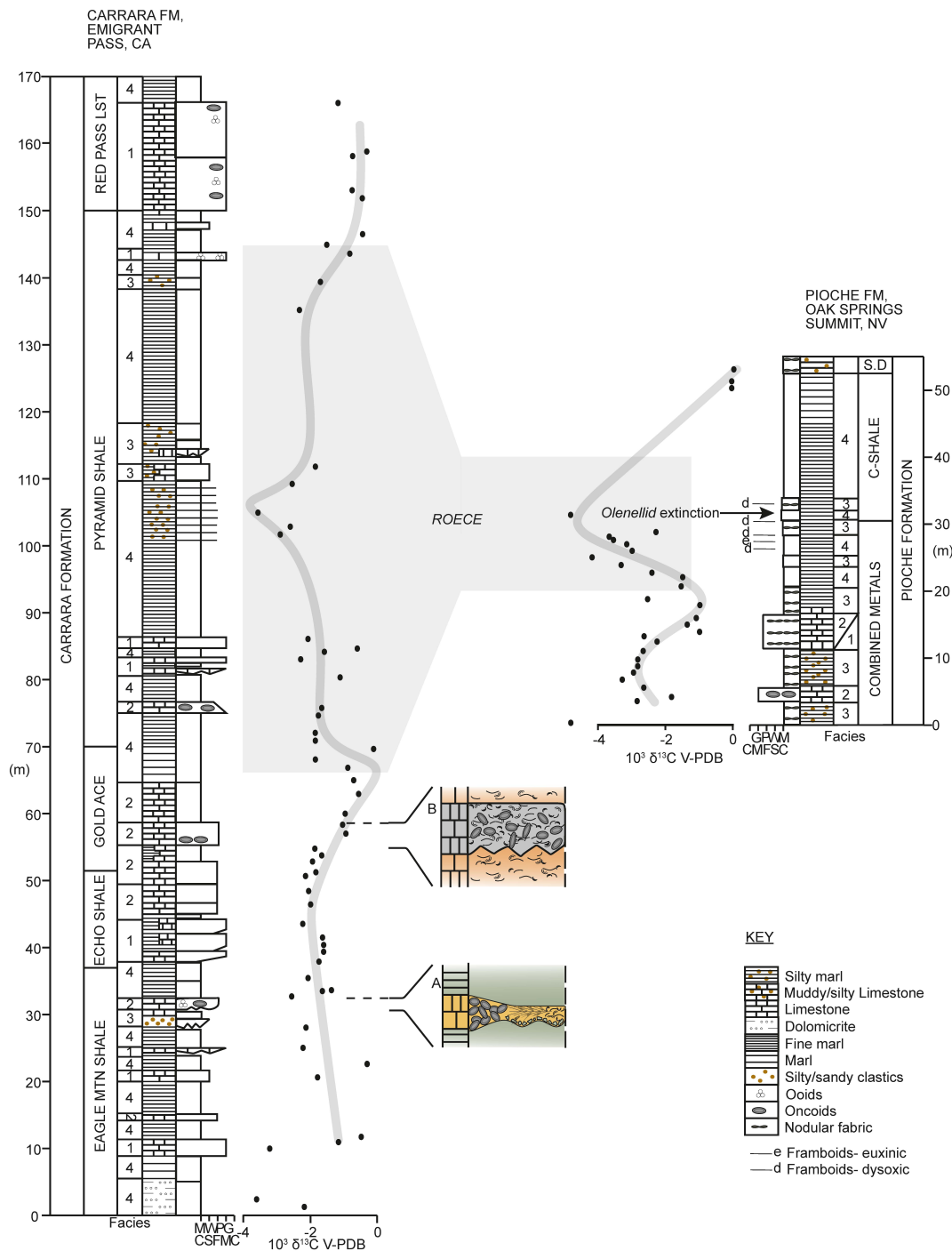
Figure 3.7: Carbon isotope chemostratigraphy of the Carrara Formation at Emigrant Pass and Pioche Formation at Oak Springs Summit. A. Inset log shows contact between silty micrite and an erosive-based oncolitic packstone with rip up clasts of the underlying silty micrite. This horizon grades laterally into an oolitic grainstone. B. Inset log of contact between silty bioclastic packstone and an erosive-based oncolitic packstone. Both erosional surfaces mark the transport of shallow water bioclastic material during storm events.

These observations rule out wholesale recrystallization in a meteoric fluid since neither section displays a positive correlation between $\delta^{18}O_{carb}$ and $\delta^{13}C_{carb}$ (point 1, Appendix B 2 and 3). The generally low TOC concentrations and the relationship between TOC and $\delta^{13}C_{carb}$ (point 3 and 4) also makes localised precipitation of organic-carbon derived DIC doubtful. From the relationships between $\delta^{18}O_{carb}$ and TIC (point 2) it is likely that a proportion of the low TIC samples (< 2 wt. %) have undergone variable resetting of their $\delta^{18}O_{carb}$ towards more positive values. This observation is not consistent with precipitation of additional carbonate from unmodified meteoric or marine early diagenetic pore fluids, where the expectation would be a change towards more negative $\delta^{18}O_{carb}$ values (Marshall, 1992; Knauth and Kennedy, 2009; Cochran et al., 2010; Saltzman and Thomas, 2012). The remaining possibility to explain the oxygen isotope relationships is variable exchange with, or precipitation of carbonate from, a hypothetical high $\delta^{18}O$ fluid (Glumac and Walker, 1998). Since the climate at both sites is currently arid, one possibility is that the fluid in question is derived from evaporated modern meteoric water, but other possibilities exist (Saltzman and Thomas, 2012).

The relationships between δ13Ccarb and TIC differ somewhat from those between δ18Ocarb and TIC: from the Carrara Formation, the range of δ13Ccarb in the < 2 wt. % TIC samples overlaps strongly with the range found in near pure limestone samples suggesting that the influence of diagenetic process on δ13Ccarb at this site is likely to be minimal (Appendix B 4). In contrast, samples from the Pioche Formation display a much clearer division between these two groups (TIC groups annotated in Appendix B 5). This suggests that the influence of post-depositional process on δ13Ccarb may have been more pronounced at this site. However, the δ18Ocarb ranges of both high and low TIC samples of the Pioche Formation overlap (Appendix B 6), indicating that at least some of the carbon isotope values have undergone minimal resetting.
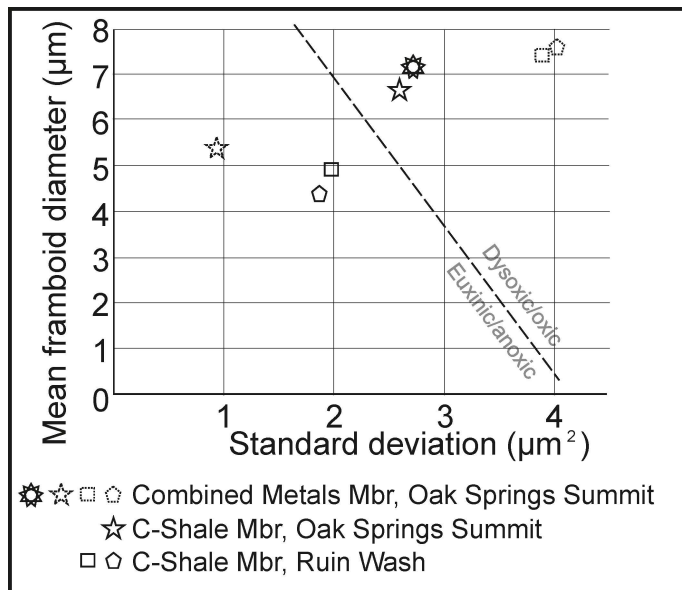
Figure 3.8: Size versus standard deviation for framboids from Series 2 - Series 3 boundary strata of California and Nevada showing the presence of oxygen-restricted facies. The threshold separating euxinic/anoxic and dysoxic/oxic size ranges in modern environments is from Wilkin et al. (1996).

In summary, there is clear evidence for a variable degree of oxygen isotope resetting towards more positive values, which is particularly pronounced in samples with low TIC (< 2 wt. %). There is also some evidence of concurrent variable resetting of carbon isotopes to more negative values in low TIC samples, with this being somewhat more pronounced in the Pioche Formation. Nonetheless, the presence of the negative $\delta^{13}C_{carb}$ values and the consistency of the magnitude of the excursion at level of the Series 2 – Series 3 boundary (e.g., Zhu et al., 2006; Faggetter et al., 2016), correlated independently by biostratigraphy between the two sections suggest that these samples record a predominantly primary signal. As such, we conclude that the negative $\delta^{13}C_{carb}$ excursion within the Carrara and Pioche formations preserves a primary record, given its co-occurrence with the olenellid extinction horizon, we interpret it to be ROECE.

3.6.2. Extinction and palaeoenvironmental change

Identification of the ROECE in the Pioche and Carrara formations (Fig. 3.7) confirms the close temporal relationship between trilobite extinctions and carbon isotope excursions (Zhu et al., 2006; Faggetter et al.,

2016). It also allows examination of the associated facies and relative sea-level changes at this time. Initially the Sauk I/ Sauk II supersequence boundary was placed around the Series 2 – Series 3 boundary (Sloss, 1963). However, more recently this has been placed lower in the succession at the top of the Zabriskie Quartzite, underlying the Carrara Formation (Prave, 1991). Thus, the Carrara Formation falls entirely within Sauk II (Keller et al., 2003, 2012; Morgan, 2012). Nonetheless, there are alternative regression surfaces in the Carrara Formation. A candidate for a sequence boundary occurs at the base of the Red Pass Limestone where there is a sharp transition from deep-water to shallow-water. This level lies around 45 m above ROECE in the Carrara Formation.

Rather than regression, the olenellid extinction occurs within a deepening succession. Transgression and shelf anoxia often go hand-in-hand, and oxygen stress has been implicated in ROECE extinction (Montañez et al., 2000). However, at Oak Springs Summit, pyrite framboid analysis suggests dysoxic but not euxinic conditions in the extinction interval, and the shallower study locations show no evidence for oxygen restriction. The evidence for intensified oxygen-restricted deposition at the trilobite extinction level is therefore weak. It also noteworthy that low-oxygen conditions were common in Cambrian oceans (Hurtgen et al., 2009; Pruss et al., 2010; Gill et al., 2011), and there is no suggestion that anoxia was intensified at the level of ROECE.

The Series 2 – Series 3 boundary interval saw the eruption of the Kalkarindji flood basalt province (Glass and Phillips, 2006; Jourdan et al., 2014; Marshall et al., 2016). In younger intervals of the Phanerozoic, the formation of large igneous provinces frequently coincides with mass extinctions (Wignall, 2015; Bond and Grasby, 2016) and the eruption of large volumes of volcanic volatiles provides a causal mechanism for driving biologic crises. The contemporaneous negative $\delta^{13}C$ signal of ROECE is often seen at times of LIP eruptions and may record the influx of isotopically-light volcanic CO_2 (e.g., Payne et al. 2004). Thus, in many regards the ROECE has the hallmarks of later Phanerozoic LIP-related mass extinctions although evidence for the commonly associated environmental changes

such as the spread of anoxia (Wignall, 2015), is not clearly established for this Cambrian example.

3.7. Conclusions

In the western Great Basin, USA, the extinction of the dominant olenellid trilobites occurs within a deepening-upward shelf succession. A major –3.5‰ negative carbon isotope excursion (ROECE) occurs at the same level. This extinction/isotope event occurs around the Cambrian Series 2 – Series 3 boundary interval. Pyrite framboid size distribution data and laminated facies suggest periodic dysoxia occurred in the facies immediately surrounding the extinction horizon. However, these conditions were neither widespread (shallower-water boundary sections in Death Valley do not record oxygen starvation) nor especially unusual (laminated strata are sporadically developed throughout the offshore units of the Carrara Formation) suggesting dysoxia did not play a major role in the extinction. The environmental effects of the contemporaneous Kalkarindji flood basalt province of Australia provide a better potential causal for the extinction at the Series 2 – Series 3 boundary, although detailed correlation with the sections in North America is required.

3.8. References

Adams, R. D. (1995). Sequence-stratigraphy of Early-Middle Cambrian grand cycles in the Carrara Formation, southwest Basin and Range, California and Nevada. In *Sequence Stratigraphy and Depositional Response to Eustatic, Tectonic and Climatic Forcing* (pp. 277-328). Springer Netherlands.

Adams, R.D., Grotzinger, J. P. (1996). Lateral continuity of facies and parasequences in Middle Cambrian platform carbonates, Carrara Formation, southeastern California, USA. *Journal of Sedimentary Resesearch*, *66*(6), 1079-1090.

Banner, J.L., Hanson, G. N. (1990). Calculation of simultaneous isotopic and trace element variations during water-rock interaction with applications to carbonate diagenesis. *Geochim. Cosmo. Acta 54*(11), 3123-3137.

Bond, D.P.G., Grasby, S.E. (2016). On the causes of mass extinctions. *Palaeogeography, Palaeoclimatology, Palaeoecology. (In this issue).*

Bond, D.P.G, Wignall, P.B. (2010). Pyrite framboid study of marine Permian-Triassic boundary sections: a complex anoxic event and its relationship to contemporaneous mass extinction. *Geological Society of America Bulletin*, *122*(7-8), 1265-1279.

Bond, G. C., and Kominz, M. A. (1984). Construction of tectonic subsidence curves for the early Paleozoic miogeocline, southern Canadian Rocky Mountains: Implications for subsidence mechanisms, age of breakup, and crustal thinning. *Geological Society of America Bulletin*, *95*(2), 155-173.

Boucot, A. J. (1990). Phanerozoic extinctions: How similar are they to each other? In *Extinction Events in Earth History* (pp. 5-30). Springer Berlin Heidelberg.

Brand, U., Veizer, J. (1981). Chemical diagenesis of a multicomponent carbonate system-2: stable isotopes. *Journal of Sedimentary Petrology*, *51*(3), 987-997.

Cochran, J. K., Kallenberg, K., Landman, N. H., Harries, P. J., Weinreb, D., Turekian, K. K., Cobban, W. A. (2010). Effect of diagenesis on the Sr, O, and C isotope composition of late Cretaceous mollusks from the Western Interior Seaway of North America. *American Journal of Science*, *310*(2), 69-88.

Cornwall, H. R., Kleinhampl, F. J. (1961). Geology of the Bare Mountain Quadrangle, Nevada. USGS Report No. 157.

Corsetti, F. A., and Hagadorn, J. W. (2000). Precambrian-Cambrian transition: Death Valley, United States. Geology, 28(4), 299-302.

Debrenne, F. (1991). Extinction of the Archaeocyatha. *Historical Biology*, 5 (2-4), 95-106.

Diehl, P. E. (1974). Stratigraphy and sedimentology of the Wood Canyon Formation, Death Valley area, California. *Death Valley Region, California and Nevada, Geol Soc Am, Cordilleran Section Annual Meeting, 70th, Las Vegas, Nevada, 1974, Guidebook, p.* 37-48.

Droser, M.L., Bottjer, D.J. (1986). A semiquantitative field classification of ichnofabric: research method paper. *Journal of Sedimentary Research*, *56*(4), 558-559.

Erdtmann, B.D., Miller, J.F. (1981). Eustatic control of lithofacies and biofacies changes near the base of the Tremadocian. In *Short Papers for the Second International Symposium on the Cambrian System. USGS Open-File Report,* 81-743, 78-81.

Faggetter, L.E., Wignall, P.B., Pruss, S.B., Sun, Y., Raine, R.J., Newton, R.J., Widdowson, M., Joachimski, M.M., Smith, P.M. (2016). Sequence stratigraphy, chemostratigraphy and facies analysis of Cambrian Series 2 - Series 3 boundary strata in northwest Scotland. *Geological Magazine*, pp. 1-13

Fan, R., Deng, S., Zhang, X. (2011). Significant carbon isotope excursions in the Cambrian and their

implications for global correlations. *Science China Earth Sciences*, 54(11), 1686-1695.

Fedo, C.M., Cooper, J.D. (2001). Sedimentology and sequence stratigraphy of Neoproterozoic and Cambrian units across a craton-margin hinge zone, southeastern California, and implications for the early evolution of the Cordilleran margin. *Sedimentary Geology*, *141*, 501-522.

Foster, J. (2014). *Cambrian ocean world: ancient sea life of North America*. Indiana University Press, 432 pp.

Gill, B.C., Lyons, T.W., Young, S.A., Kump, L.R., Knoll, A.H., Saltzman, M.R. (2011). Geochemical evidence for widespread euxinia in the Later Cambrian ocean. *Nature*, *469*(7328), 80-83.

Glass, L.M., Phillips, D. (2006). The Kalkarindji continental flood basalt province: a new Cambrian large igneous province in Australia with possible links to faunal extinctions. *Geology*, *34*(6), 461-464.

Glumac, B., Walker, K.R. (1998). A Late Cambrian positive carbon-isotope excursion in the southern Appalachians: Relation to biostratigraphy, sequence stratigraphy, environments of deposition, and diagenesis. *Journal of Sedimentary Research*, *68*(6), 1212-1222

Hallam, A., Wignall, P.B. (1997). *Mass extinctions and their aftermath*. Oxford University Press, Oxford, 320pp.

Hammarlund, E. U., Dahl, T. W., Harper, D. A., Bond, D. P., Nielsen, A. T., Bjerrum, C. J., Canfield, D. E. (2012). A sulfidic driver for the end-Ordovician mass extinction. *Earth and Planetary Science Letters*, *331*, 128-139.

Hollingsworth, J.S., Sundberg, F.A., Foster, J.R. (2011). Cambrian stratigraphy and paleontology of Northern Arizona and Southern Nevada. *Museum of Northern Arizona Bulletin*, *67*, 321.

Hogan, E.G., Fedo, C.M., Cooper, J.D. (2011). Reassessment of the basal Sauk Supersequence boundary across the Laurentian craton-margin hinge zone, southeastern California. *The Journal of Geology*, *119*(6), 661-685.

Howley, R.A., Rees, M. N., Jiang, G. (2006). Significance of Middle Cambrian mixed carbonate-siliciclastic units for global correlation: southern Nevada, USA. *Palaeoworld*, *15*(3), 360-366.

Hurtgen, M.T., Pruss, S. B., Knoll, A. H. (2009). Evaluating the relationship between the carbon and sulfur cycles in the later Cambrian ocean: an example from the Port au Port Group, western Newfoundland, Canada. *Earth and Planetary Science Letters*, *281*(3), 288-297.

Jourdan, F., Hodges, K., Sell, B., Schaltegger, U., Wingate, M.T. D., Evins, L.Z., Blenkinsop, T. (2014). High-precision dating of the Kalkarindji large igneous province, Australia, and synchrony with the Early-Middle Cambrian (Stage 4-5) extinction. *Geology*, *42*(6), 543-546.

Keller, M., Cooper, J., Lehnert, O. (2003). Sauk sequence sequences (southern Great Basin) [abstract]. In: Geological Society of American *Abstracts with Programs,* Vol. 35, No.6, September 2003, p.543

Keller, M., Cooper, J.D., Lehnert, O. (2012). Sauk megasequence supersequences, southern Great Basin: Second-order accommodation events on the southwestern Cordilleran margin platform, in J.R. Derby, R.D. Fritz, S.A. Longacre, W.A. Morgan, and C.A. Sternbach, eds., *The great American carbonate bank: The geology and economic resources of the Cambrian- Ordovician Sauk megasequence of Laurentia*: AAPG Memoir 98, p. 873- 896

Knauth, L.P., Kennedy, M.J. (2009). The late Precambrian greening of the Earth. *Nature*, *460*(7256), 728-732.

Landing, Ed, (2012). The great American carbonate bank in eastern Laurentia: Its births, deaths, and linkage to paleooceanic oxygenation (Early Cambrian - Late Ordovician), in J. R. Derby, R. D. Fritz, S. A. Longacre, W. A. Morgan, and C. A. Sternbach, eds., *The great American carbonate bank: The geology and economic resources of the Cambrian - Ordovician Sauk megasequence of Laurentia*: AAPG Memoir 98, p. 451 - 492.

Levy, M., Christie-Blick, N. (1991). Tectonic subsidence of the early
    Paleozoic passive continental margin in eastern California and southern
    Nevada. *Geological Society of America Bulletin*, *103*(12), 1590-1606.

Lieberman, B.S. (2003). A new soft-bodied fauna: the Pioche Formation of
    Nevada. *Journal of Paleontology*, *77*(04), 674-690.

MacNiocaill, C., Smethurst, M.A. (1994). Palaeozoic palaeogeography of
    Laurentia and its margins: a reassessment of palaeomagnetic
    data.*Geophysical Journal International*, *116*(3), 715-725.

Marshall, J.D. (1992). Climatic and oceanographic isotopic signals from the
    carbonate rock record and their preservation. *Geological
    magazine*, *129*(02), 143-160.

Marshall, P.E., Widdowson, M., Murphy, D. T. (2016). The giant lavas of
    Kalkarindji: rubbly pāhoehoe lava in an ancient continental flood basalt
    province. *Palaeogeography, Palaeoclimatology, Palaeoecology*, *441*,
    22-37.

McKerrow, W.S., Scotese, C.R., Brasier, M.D. (1992). Early Cambrian
    continental reconstructions. *Journal of the Geological Society, 149(4),*
    599-606.

Merriam, C.W., Palmer, A.R. (1964*).* Cambrian rocks of the Pioche mining
    district, Nevada, with a section on Pioche shale faunules (No. 469).
    USGS Professional Paper, 264-D, 53-86

Montañez, I.P., Osleger, D. A., Banner, J.L., Mack, L. E., Musgrove, M.
    (2000). Evolution of the Sr and C isotope composition of Cambrian
    oceans. *GSA today*, *10*(5), 1-7.

Morgan, W.A. (2012). Sequence stratigraphy of the great American
    carbonate bank, *in,* Derby, J.R., Fritz, R.D., Longacre, S.A., Morgan,
    W.A., and Sternbach, C.A., eds., The Great American Carbonate Bank:
    The Geology and Economic Resources of the Cambrian-Ordovician
    Sauk Megasequences of Laurentia: Association of American Petroleum
    Geologists Memoir 98, p.37-79.

Newell, N.D. (1972). The evolution of reefs. *Scientific American*, 226, 54-65.

Palmer, A.R., Halley, R.B. (1979). Physical stratigraphy and trilobite biostratigraphy of the Carrara Formation (Lower and Middle Cambrian) in the southern Great Basin. *USGS Professional Paper,* No.1047*.*

Palmer, A. R. (1984). The biomere problem: evolution of an idea. *Journal of Paleontology*, 599-611.

Palmer, A.R. (1998). Terminal early Cambrian extinction of the Olenellina: documentation from the Pioche Formation, Nevada. *Journal of Paleontology*, 72 (04), 650-672.

Payne, J.L., Lehrmann, D.J., Wei, J., Orchard, M. J., Schrag, D. P., Knoll, A.H. (2004). Large perturbations of the carbon cycle during recovery from the end-Permian extinction. *Science*, *305*(5683), 506-509.

Peng, S., Babcock, L.E., Cooper, R.A. (2012). The Cambrian Period. . In: Gradstein, F., Ogg, J., Schmitz, M., Ogg, G. (Eds). *The Geologic Time Scale* 2012, Elsevier, Boston, 2, 437-488.

Prave, A.R. (1991). Depositional and sequence stratigraphic framework of the Lower Cambrian Zabriskie Quartzite: implications for regional correlations and the Early Cambrian paleogeography of the Death Valley region of California and Nevada. *Geological Society of America Bulletin*, 104(5), 505-515.

Prave, A. R. (1999). Two diamictites, two cap carbonates, two δ13C excursions, two rifts: the Neoproterozoic Kingston Peak Formation, Death Valley, California. *Geology*, 27(4), 339-342.

Pruss, S.B., Finnegan, S., Fischer, W.W., Knoll, A.H. (2010). Carbonates in skeleton-poor seas: new insights from Cambrian and Ordovician strata of Laurentia. *Palaios*, *25*(2), 73-84.

Saltzman, M.R., Thomas, E. (2012). Chapter 11- Carbon isotope stratigraphy. In: Gradstein, F., Ogg, J., Schmitz, M., Ogg, G. (Eds). *The Geologic Time Scale* 2012, Elsevier, Boston, *1*, 207-232.

Saltzman, M.R., Edwards, C.T., Adrain, J.M., Westrop, S.R. (2015). Persistent oceanic anoxia and elevated extinction rates separate the Cambrian and Ordovician radiations. *Geology*, *43*(9), 807-810.

Sloss, L.L. (1963). Sequences in the cratonic interior of North America. Geological Society of America Bulletin, 74(2), 93-114.

Stewart, J. H. (1972). Initial deposits in the Cordilleran geosyncline: Evidence of a late Precambrian (< 850 my) continental separation. *Geological Society of America Bulletin*, *83*(5), 1345-1360.

Sundberg, F.A., McCollum, L.B. (2000). Ptychopariid trilobites of the lower-middle Cambrian boundary interval, Pioche Shale, southeastern Nevada*. Journal of Paleontology*, 74(4), 604-630.

Sundberg, F. A., Geyer, G., Kruse, P. D., McCollum, L. B., Pegel, T. V., Zylinska, A., Zhuravlev, A. Y. (2016). International correlation of the Cambrian Series 2 - 3, stages 4 - 5 boundary interval. *Australasian Palaeontological Memoirs*, 49, 83-124

Tarhan, L. G., Droser, M.L., Planavsky, N. J., Johnston, D.T. (2015). Protracted development of bioturbation through the early Palaeozoic Era. *Nature Geoscience*, 8, 865-869.

Wang, X., Hu, W., Yao, S., Chen, Q., Xie, X. (2011). Carbon and strontium isotopes and global correlation of Cambrian Series 2 - Series 3 carbonate rocks in the Keping area of the northwestern Tarim Basin, NW China. *Marine and Petroleum Geology*, 28(5), 992-1002.

Wignall, P.B. (2001). Large igneous provinces and mass extinctions. *Earth-Science Reviews*, 53(1), 1-33.

Wignall, P.B. (2015). *The Worst of Times: How Life on Earth Survived Eighty Million Years of Extinctions*. Princeton University Press.

Wilkin, R. T., Barnes, H. L., Brantley, S.L. (1996). The size distribution of framboidal pyrite in modern sediments: an indicator of redox conditions. *Geochimica et Cosmochimica Acta*, *60*(20), 3897-3912.

Zhang, W., Shi, X., Jiang, G., Tang, D., Wang, X. (2013). Mass-occurrence of oncoids at the Cambrian Series 2 - Series 3 transition: Implications for microbial resurgence following an Early Cambrian extinction*. Gondwana Research*, 28(1), 432-450.

Zhu, M. Y., Zhang, J. M., Li, G. X., Yang, A. H. (2004). Evolution of C isotopes in the Cambrian of China: implications for Cambrian subdivision and trilobite mass extinctions. *Geobios*, 37(2), 287-301.

Zhu, M.Y., Babcock, L.E., Peng, S.C. (2006). Advances in Cambrian stratigraphy and paleontology: integrating correlation techniques, paleobiology, taphonomy and paleoenvironmental reconstruction. *Palaeoworld*, 15(3), 217-222.

Zhuravlev, A.Y., Wood, R. A. (1996). Anoxia as the cause of the mid-Early Cambrian (Botomian) extinction event. *Geology*, 24(4), 311-314.

4. Chapter 4: The search for mercury anomalies at the Cambrian Series 2 – Series 3 boundary: evidence for increased volcanic activity coincident with extinction?

Faggetter, L.E., Wignall, P.B., Pruss, S.B., Jones, D.S., Grasby, S., Widdowson, M. Newton, R.J. The search for mercury anomalies at the Cambrian Series 2 – Series 3 boundary: evidence for increased volcanic activity coincident with extinction?
This chapter is formatted for submission to *Chemical Geology.*

4.1. Abstract

The mass extinction of trilobites at the Cambrian Series 2 – Series 3 boundary provides one of the first potential links between volcanism and biotic crises in the geological record. However, the precise timing of flood basalt volcanism (Kalkarindji Province, Australia) and the trilobite extinctions, best recorded from North America, is not known. Mercury (Hg) enrichment in the sedimentary record provides a potential proxy for volcanism which may facilitate improved chronologies of eruption and extinction. Here we report Hg records for three sections from mid-shelf strata of the Great Basin (south-western USA) that straddle the Series 2 – Series 3 boundary. One section (Oak Springs Summit, NV) contains Hg enrichment at the start of the extinction interval, but mercury anomalies are also present at lower levels. These older anomalies may record either earlier phases of large-scale Kalkarindji volcanism, eruptions in other locations, or may be the products of early diagenetic remobilization of Hg. In the Carrara Formation at Emigrant Pass, CA, the precise extinction horizon is not well defined, but a carbon isotope anomaly (the ROECE, redlichiid-olenellid extinction and carbon isotope event) provides a stratigraphic tie point to the Oak Springs Summit section. At Emigrant Pass, Hg enrichments precede the ROECE interval and are absent in the inferred extinction zone. The Pioche Formation at Ruin Wash, NV, lacks Hg enrichment at the extinction horizon but contains older enrichments. The inconsistent Hg records between the three sections suggest that factors controlling Hg accumulation and preservation in marine sedimentary environments are not fully understood.

4.2. Introduction

The connection between large igneous province (LIP) eruptions and Phanerozoic mass extinctions is well established (e.g. Wignall, 2001; Kravchinsky, 2012; Bergquist, 2017; Ernst and Youbi, 2017), though any such link in the Cambrian is poorly understood (Wignall, 2015). The best candidate LIP is the Kalkarindji Province (including the Antrim lavas) of northern and western Australia; this has been most accurately dated by a single zircon (Milliwindi dyke) U-Pb age of 510.7 ± 0.6 Ma (Jourdan et al., 2014), and supports the previously reported ^{40}Ar/^{39}Ar date of 507.5 ± 1.6 Ma determined for its extrusive portion (i.e., Antrim Lavas; Glass and Phillips, 2006). This LIP currently has a surface exposure of c. 425 000 km^2 in northern and central Australia (Veevers, 2001), but was likely erupted over a vast area; its scattered remnant indicating a possible original extent of >2 million km^2 (Glass and Phillips, 2006, Jourdan et al., 2014). Further, the province may even be comparable with the larger Phanerozoic LIPs since it may correlate with volcanics of comparable age and/or composition preserved in the Tarim Block in NW China and the North China Block (Li et al., 1996, 2008), and the Sibumasu terrane preserved in current day Thailand through to Myanmar (Zhu et al., 2012; Cocks and Torsvik, 2013).

The age of the Kalkarindji places the province's eruption close to the Cambrian Series 2 – Series 3 boundary (traditionally Lower – Middle) and thus potentially contemporaneous with the extinction of the redlichiid and olenellid trilobites (Palmer, 1998; Jourdan et al., 2014; Zhang et al., 2015; Faggetter et al., 2017). The extinction of the latter group has been well studied in the western USA but locating the level that coincides with the Kalkarindji eruptions has hitherto been difficult to locate due to a lack of an eruption proxy. Currently the U-Pb zircon date of 510.7 ± 0.6Ma (Jourdan et al., 2014) underpins this close comparable age (within 1myr) to the provisional age of the Series 2 – Series 3 boundary and association with trilobite extinction (Glass and Phillips, 2006; Hough et al., 2006; Jourdan et al., 2014).

Testing a causal link between the Kalkarindji and the Series 2 – Series 3 extinctions requires improved correlations between the volcanic event(s) and the trilobite extinctions. Recently, Hg concentrations in the

sedimentary record have provided a proxy for both regional and global volcanic activity (e.g. Schuster et al., 2002) and thus offers the potential to correlate the interval of extinction with evidence for volcanism in the same stratigraphic sections (Percival et al., 2015; Font et al., 2016; Grasby et al., 2016; Thibodeau et al., 2016; Jones et al., 2017; Gong et al., 2017). The value of this technique has been demonstrated at several key mass extinction and oceanic anoxic events events including those at the Ordovician–Silurian; latest Permian; Permian-Triassic; end-Triassic; early Jurassic and end-Cretaceous events (Sanei et al., 2012; Percival et al., 2015; Thibodeau et al., 2016; Font et al., 2016; Grasby et al., 2016; Gong et al., 2017). Here we present sedimentary Hg records for strata in which the trilobite extinction horizons have been constrained, and evaluate the potential of this LIP to produce this sedimentary geochemical record.

Volcanism represents a primary source of gaseous Hg^0 to Earth's surface; unlike other volcanic trace metals, its long atmospheric residence time (0.5-2 years) permits hemispheric circulation and establishes its potential as a tracer for volcanism (Pyle and Mather, 2003; Percival et al., 2015, 2017). Atmospheric oxidation of Hg^0 by halogens, ozone and radicals forms reactive Hg^{2+}, a soluble ion which is deposited during precipitation. Horowitz et al. (2017) found that, during its residence in the troposphere, Hg is most effectively oxidised by bromine (Br), forming atmospheric HgBr complexes. As the largest source of atmospheric Br is organobromines - which are produced as a by-product of phytoplankton photosynthesis - the most effective oxidation and deposition of Hg^{2+} occurs above and, subsequently to, the marine realm (Horowitz et al., 2017). In modern oceans ~49% of marine Hg deposition occurs in tropical oceans due to the greater availability of productivity-driven organobromines and other oxidising radicals at these latitudes (Horowitz et al., 2017). Once in the marine realm Hg^{2+} forms complexes with clay minerals (Kongchum et al., 2011), organic matter (Benoit et al., 2001), and, in anoxic/euxinic conditions, it can be scavenged from seawater as sulphide complexes (Benoit et al., 1999). The effective oxidation of Hg^0 by marine organobromines and the complexing of Hg by organics and sulphides in the marine realm establishes marine sediments as an efficient sink of atmospheric Hg (Benoit et al., 1999; Emili et

al., 2011; Horowitz et al., 2017). Therefore, marine siliciclastic and carbonate rocks can act as an important repository of Hg during times of heightened environmental loading (Percival et al., 2015; Grasby et al., 2016).

The Cambrian Period is marked by large oscillations of the marine dissolved inorganic carbon isotope record which, at times, coincided with intensified extinction rates (Brasier et al., 1994; Montañez et al., 2000; Zhu et al., 2006). At the Cambrian Series 2 – Series 3 boundary, a negative $\delta^{13}C$ excursion referred to as the Redlichiid – Olenellid Extinction Carbon isotope Excursion (ROECE) has been documented from Laurentia (Montańez, 2000; Faggetter et al., 2017), Gondwana (Schmid, 2017) and China (e.g. Fan et al., 2011; Wang et al., 2011; Chang et al., 2017; Ren et al., 2017). This saw major trilobite losses in both Gondwana and Laurentia (Montañez et al., 2000; Zhu et al., 2004, 2006; Faggetter et al., 2017; Ren et al., 2017). The Series 2 – Series 3 boundary age (~509 Ma, Ogg et al., 2016) approximately coincides with the 510.7 ± 0.6 Ma age of the Kalkarindji Province (Jourdan et al. 2014) but detailed correlation is lacking. We attempt to resolve this issue by examining sedimentary Hg concentrations in Series 2 – Series 3 Cambrian sections of the western USA. We have analysed Hg concentrations and Hg/ total organic concentration (TOC) from two formations and three sections in the western Great Basin: the Carrara Formation, Emigrant Pass (Death Valley, CA) and the Pioche Formation at Oak Springs Summit and Ruin Wash (Lincoln County, NV). These sections have an established biostratigraphic framework (Palmer, 1998; Webster et al., 2008; Faggetter et al., 2017) and also a record of trilobite extinction at Oak Springs Summit and Ruin Wash.

4.3. Study Area

Cambrian successions of the western Great Basin (USA) constitute the primary field locations of this study. Following the breakup of the supercontinent Rodinia in the late Neoproterozoic, a broad, equatorial clastic shelf developed on the rapidly subsiding Laurentian margin (Prave, 1991; Howley et al., 2006). During Cambrian Series 2, deposition in the Great

Figure 4.1: Cambrian global palaeogeography at 510 million years ago showing approximate palaeoposition of study sections, adapted from Scotese (2016). Location of Kalkarindji LIP and extent of modern outcrop taken from Marshall (2016).

510 Ma

(a) Laurentia
(b) Siberia
(c) Baltica
(d) Gondwana

Kalkarindji LIP

Approximate location of
western Great Basin study sections
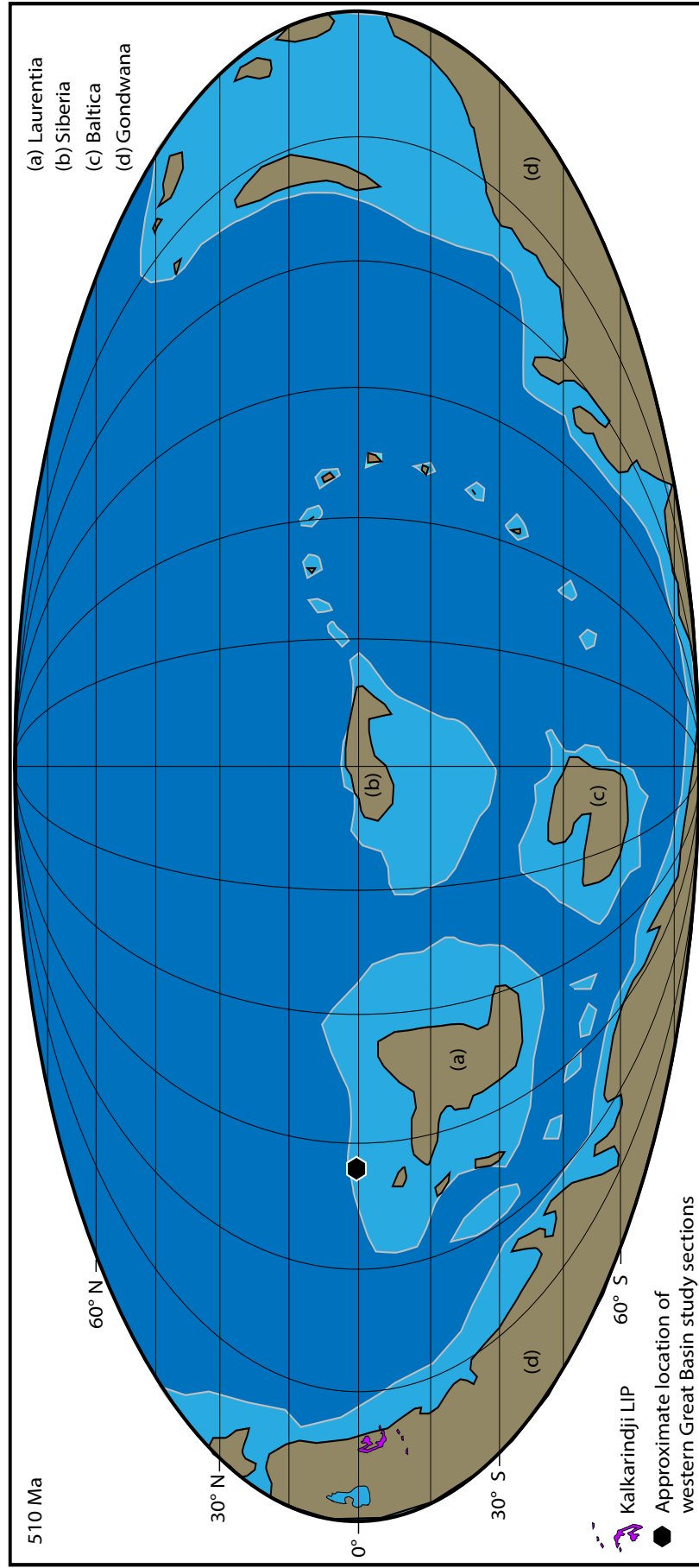
Basin was on a broad shelf located on the north-western margin of Laurentia (Fig. 4.1). Clastic deposition was waning and, by Series 3, it had been replaced by carbonate production, resulting in the formation of an extensive carbonate shelf (Fig. 4.1; Howley et al., 2006; Landing, 2012). We present data from two formations spanning the Cambrian Series 2 – Series 3 boundary in the western Great Basin: the Carrara Formation of Death Valley exposed at Emigrant Pass, California, and the Pioche Formation of eastern Nevada exposed at Oak Springs Summit and Ruin Wash. Both formations comprise alternating siliciclastic- and limestone-dominated units (Merriam and Palmer, 1964; Palmer and Halley, 1979; Faggetter et al., 2017). At Oak Springs Summit and Ruin Wash, the Pioche Formation records the abrupt extinction of the olenellid trilobites, making these two sections candidates for paired Hg-biostratigraphic studies. At Emigrant Pass there is a paucity of trilobite fossils, but $\delta^{13}C$ correlation, based on the presence of the ROECE, allows an extinction interval to be inferred at the boundary between the *Olenellus* and *Eokochaspis nodosa* biozones in the mid Pyramid Shale (Fig, 2; Zhu et al., 2004, Faggetter et al., 2017). As a further stratigraphic tie point between the two formations, the extinction horizon within the Pioche Formation represents the top of the *Olenellus* biozone (Palmer, 1998; Sundberg and McCollum, 2000).

4.4. Methods

We analysed total Hg content in whole-rock powders from 93 samples taken from the three Series 2 – Series 3 boundary sections in the western US (Figs. 4.2, 4.3, 4.4). The samples from Emigrant Pass and Oak Springs Summit were run at the Geological Survey of Canada with a LECO® AMA254 mercury analyser (10% precision, 5% relative standard deviation (RSD), Hall and Pelchat, 1997). Whole rock powders from Ruin Wash, as well as a duplicate sample set from Oak Springs Summit, were analysed at Amherst College (Massachusetts, USA) using a Teledyne Leeman Labs Hydra II$_C$ mercury analyser (RSD <10%). Duplicate samples returned a correlation coefficient of 0.99, indicating a robust positive correlation between the results from the two laboratories.
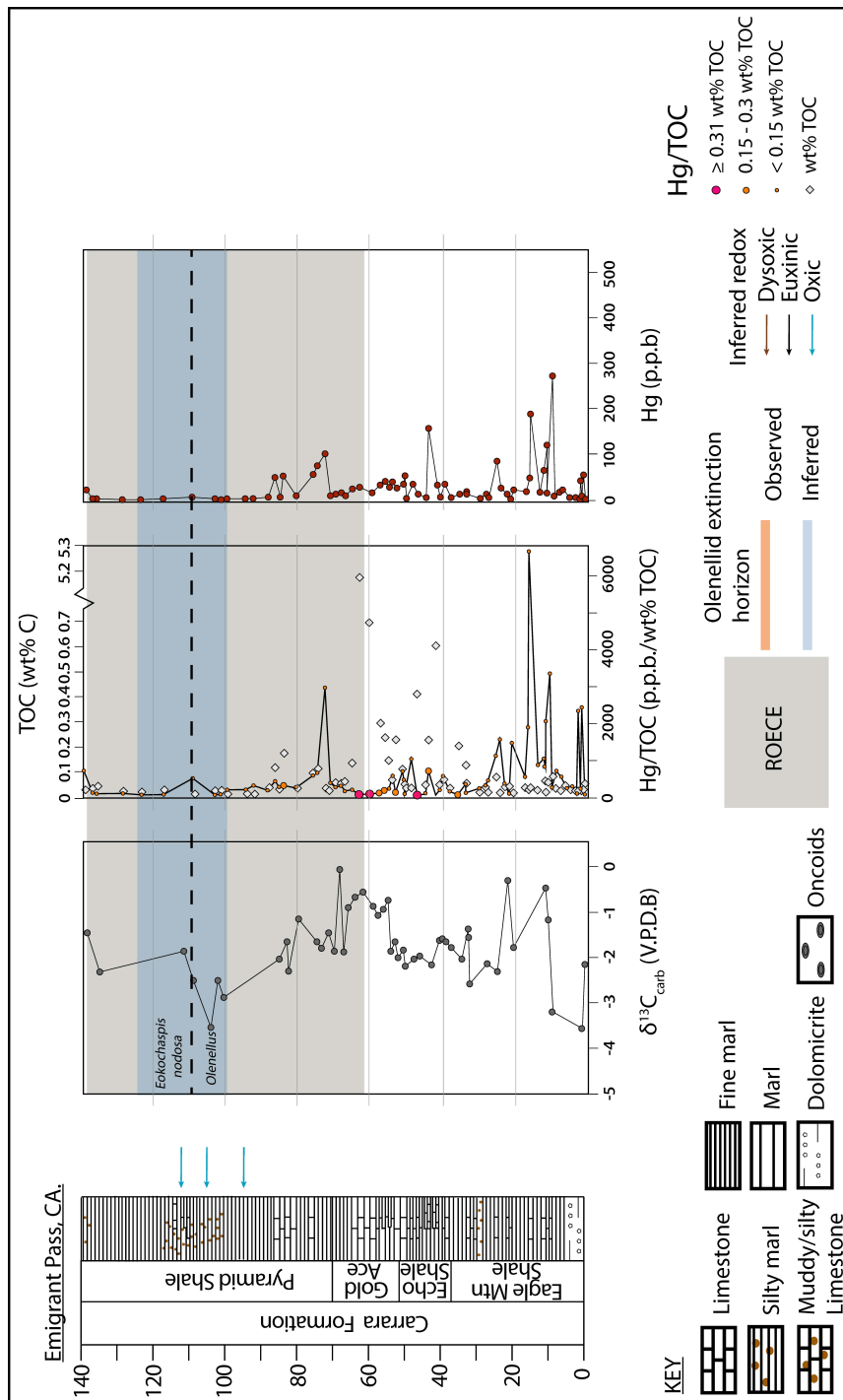
Figure 4.2: Geochemical data from Emigrant Pass, Carrara Formation: TOC wt % C, δ¹³C_carb (permil), Hg (ppb) and Hg/TOC (ppb/ wt % C). The position of the *Olenellus - Eokochaspsis nodosa* biozone boundary is from Palmer and Halley (1979) inferred redox conditions are based on framboid size distribution data from Faggetter et al. (2017).

Whole-rock powders were decarbonated using hydrochloric acid and their carbonate content was calculated by mass loss following acid digestion. With the exception of Ruin Wash samples, TOC was measured from insoluble residues at the University of Leeds using a LECO® SC-144DR Dual Range carbon and sulphur analyser. The carbon content of insoluble residues from Ruin Wash was measured with a Costech ECS 4010 elemental analyser at Amherst College in order to generate TOC measurements, with RSD <5%.

Inorganic carbon isotope values from Emigrant Pass and Oak Springs Summit are given in Faggetter et al. (2017), and new inorganic carbon isotope values from Ruin Wash are presented here. Whole-rock powders were analysed at the GeoZentrum Nordbayern, FAU Erlangen-Nuremberg, Germany, where carbon dioxide was prepared via reaction with phosphoric acid at 70°C using a Gasbench II preparation system and calcite carbon isotope values measured by a ThermoFisher Delta V plus mass spectrometer in continuous flow mode. Isotope ratios are reported relative to the V-PDB standard, with a reproducibility of ±0.06‰ for $\delta^{13}C$ and 0.05‰ for $\delta^{18}O$.

Inferred redox conditions (Figs. 4.2, 4.3, 4.4) are based upon pyrite framboid size distribution from 19 samples from Faggetter et al. (2017), assessed using a scanning electron microscope (FEI Quanta 650 FEG-ESEM) in backscatter mode following Bond and Wignall (2010) for procedure.

4.5. Results

4.5.1. TOC concentrations

Throughout all three sections TOC content is generally very low and exhibits a strong correlation with facies (Fig. 4.5). The lowest TOC values (<0.15 wt% TOC) of both the Carrara and Pioche formations are found in the marl facies coinciding with extremely low/carbonate free intervals such as the C-Shale Member of the Pioche Formation (Fig. 4.5). In the Pioche Formation, higher TOC values are preserved in limestone of the Combined Metals Member, at Oak Springs Summit the most TOC rich interval (0.48 –
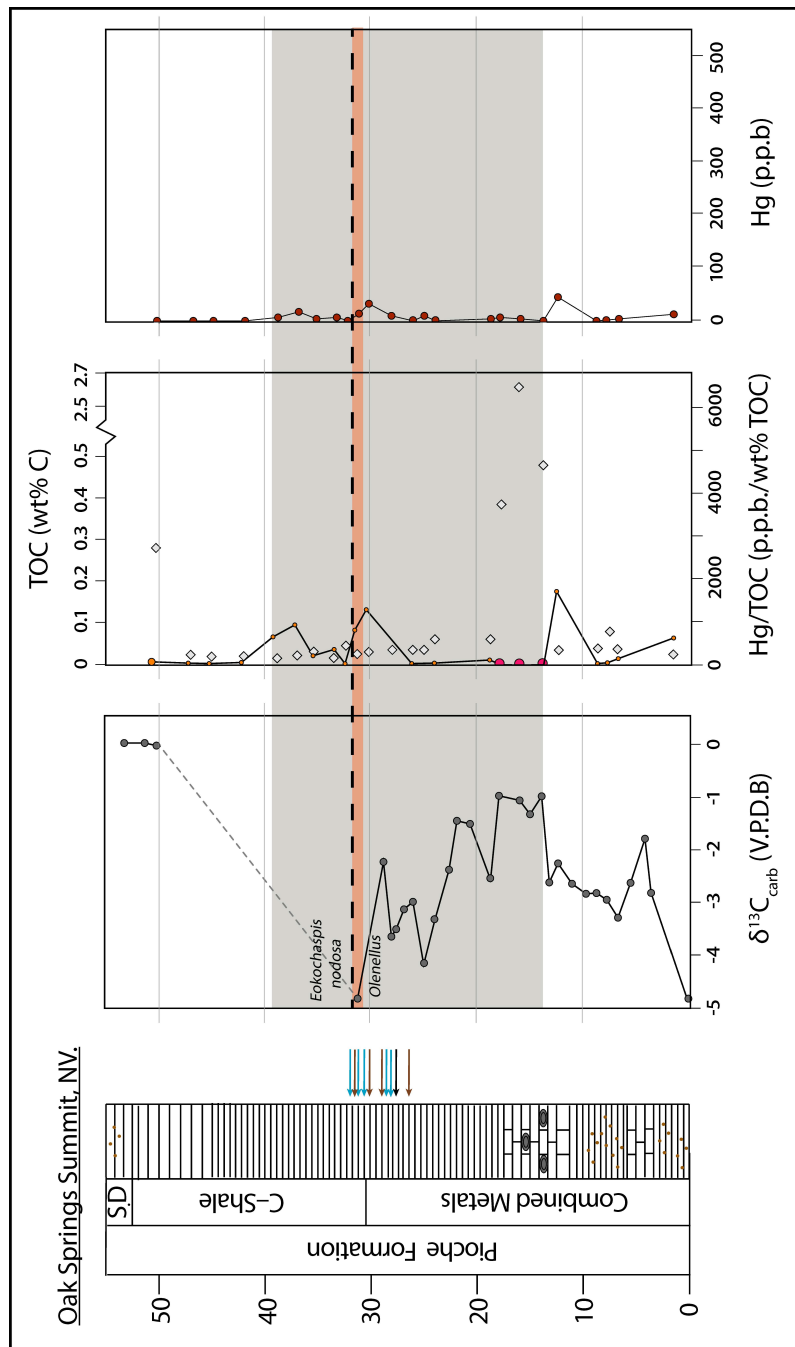
Figure 4.3: Geochemical data from Oak Springs Summit, Pioche Formation: TOC wt % C, δ¹³C_carb (permil), Hg (ppb) and Hg/TOC (ppb/ wt % C). The position of the *Olenellus - Eokochaspsis nodosa* biozone boundary is from Palmer (1998), inferred redox conditions are based on framboid size distribution data from Faggetter et al. (2017). See Fig. 4.2 for key.

2.69 wt% TOC) occurs within an oncoidal limestone of the Combined Metals Member (Fig. 4.5). The majority of the Carrara Formation is composed of marl with very low (<0.15 wt%) TOC content, the exception being TOC richer intervals within the Echo Shale and Gold Ace members where TOC spans the greatest range of all three sections (<0.15 – 5.17 wt% TOC) (Fig. 4.5). TOC content in the Carrara and Pioche formations is generally very low (<0.5 wt%) however, from all sections, Hg enrichments and Hg/TOC excursions are returned from samples with high and low TOC wt% values (Fig. 4.6).

4.5.2. Inorganic carbon isotope record and extinction

The inorganic carbon isotope record from the Carrara Formation at Emigrant Pass and the Pioche Formation at Oak Springs Summit are discussed in Faggetter et al. (2017) who report a C isotope excursion of ~-3.8 ‰ interpreted to be the ROECE excursion. Within the Pioche Formation at Oak Springs Summit, peak negative inorganic carbon isotope values coincide with the extinction horizon of the olenellid trilobites; as such it is expected that ROECE would be present across the extinction horizon at Ruin Wash (Palmer 1998; Faggetter et al., 2017). However, this is difficult to establish at Ruin Wash because extremely low carbonate content (below detection limits) in the marl of the C-Shale Member does not allow measurement of a continuous inorganic carbon isotope curve through the Pioche Formation. The ROECE is also observed within the Pyramid Shale Member of the Carrara Formation, but unlike the Pioche Formation, there is no trilobite fauna to delineate a clear extinction horizon at Emigrant Pass (Fig. 4.2). An inferred extinction interval is therefore proposed at Emigrant Pass within the Pyramid Shale Member (Fig. 4.2), based on the biostratigraphic boundary between the *Olenellus* Zone and the *Eokochaspis nodosa* Zone (Fig. 4.2; see Palmer and Halley, 1979; Faggetter et al, 2017).

4.5.3. Hg concentrations, Hg/TOC ratios and extinction

The Carrara and Pioche formations in our study locations all show local enrichments in Hg concentrations (ppb) and excursions in Hg/TOC (ppb/wt% TOC) ratios (Figs. 4.2, 4.3, 4.4). Where samples have returned
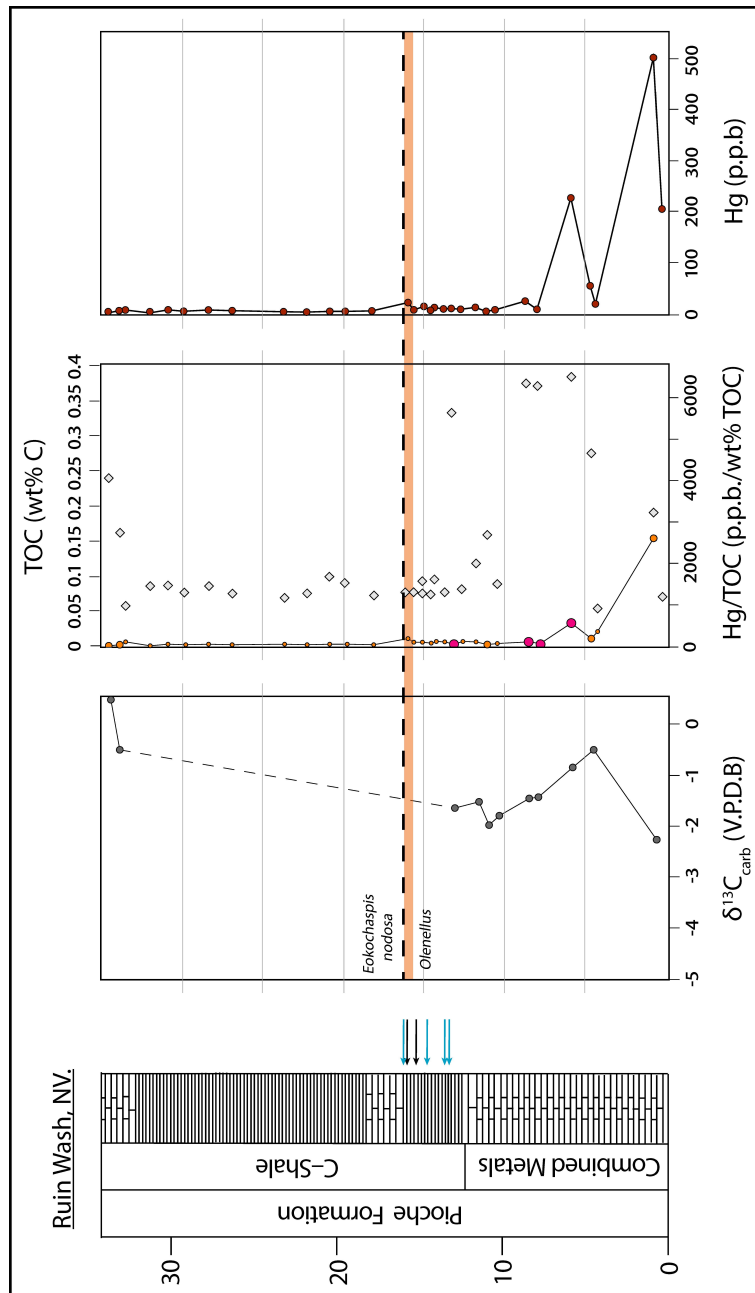
Figure 4.4: Geochemical data from Ruin Wash, Pioche Formation: TOC wt % C, δ¹³C_carb (permil), Hg (ppb) and Hg/TOC (ppb/ wt % C). The position of the *Olenellus* - *Eokochaspsis nodosa* biozone boundary is from Palmer (1998), inferred redox conditions are based on framboid size distribution data from Faggetter et al. (2017). See Fig. 4.2 for key

extremely low TOC of <0.01 wt% C, Hg/TOC results are discounted and not plotted in figures but are included in Table 4.1.

Carrara Formation, Emigrant Pass

The Carrara Formation at Emigrant Pass exhibits background Hg concentrations of <50 ppb throughout the section (Fig. 4.2). A number of prominent enrichments occur in the first 90 m, with the most enriched

sample containing 270 ppb Hg in the basal Eagle Mountain Shale member. Smaller enrichments recorded by one or two data points each occur in the Echo Shale, Gold Ace and Pyramid Shale members. Within the ROECE interval Hg values are elevated at the beginning of the δ^{13}C excursion before concentrations return to low levels for the remainder of the section.

As Hg in marine sediments is commonly bound to organic matter we also present Hg/TOC ratios (Fig. 4.2; Sanei et al, 2012). These show that Hg/TOC enrichments in the Carrara Formation occur in two distinct pulses: an initial, multi-peak enrichment in the basal 30m of the Eagle Mountain Shale Member, and another during early ROECE at the base of the Pyramid Shale Member.

Pioche Formation, Oak Springs Summit

Background Hg concentrations in the Pioche Formation at Oak Springs Summit are <10 ppb (Fig. 4.3). A single elevated value (46 ppb Hg) occurs in the Combined Metals Member, just below the base of the ROECE, and a smaller enrichment (32 ppb Hg) coincides with our peak negative ROECE value and the olenellid extinction horizon at the base of the C-Shale Member. Finally, there is a small increase in Hg concentration (17 ppb) at ~35m in the section. There are three prominent Hg/TOC spikes at Oak Springs Summit (Fig. 4.3), which all correspond with the levels of Hg enrichments (Fig. 4.3).

Pioche Formation, Ruin Wash

Hg values at Ruin Wash are highest (up to 500 ppb) at the base of the measured section in the basal ~5m of the Combined Metals Member (Fig. 4.4). Peaks are around an order of magnitude higher than the maximum values seen at Oak Springs Summit. Above the level of elevated
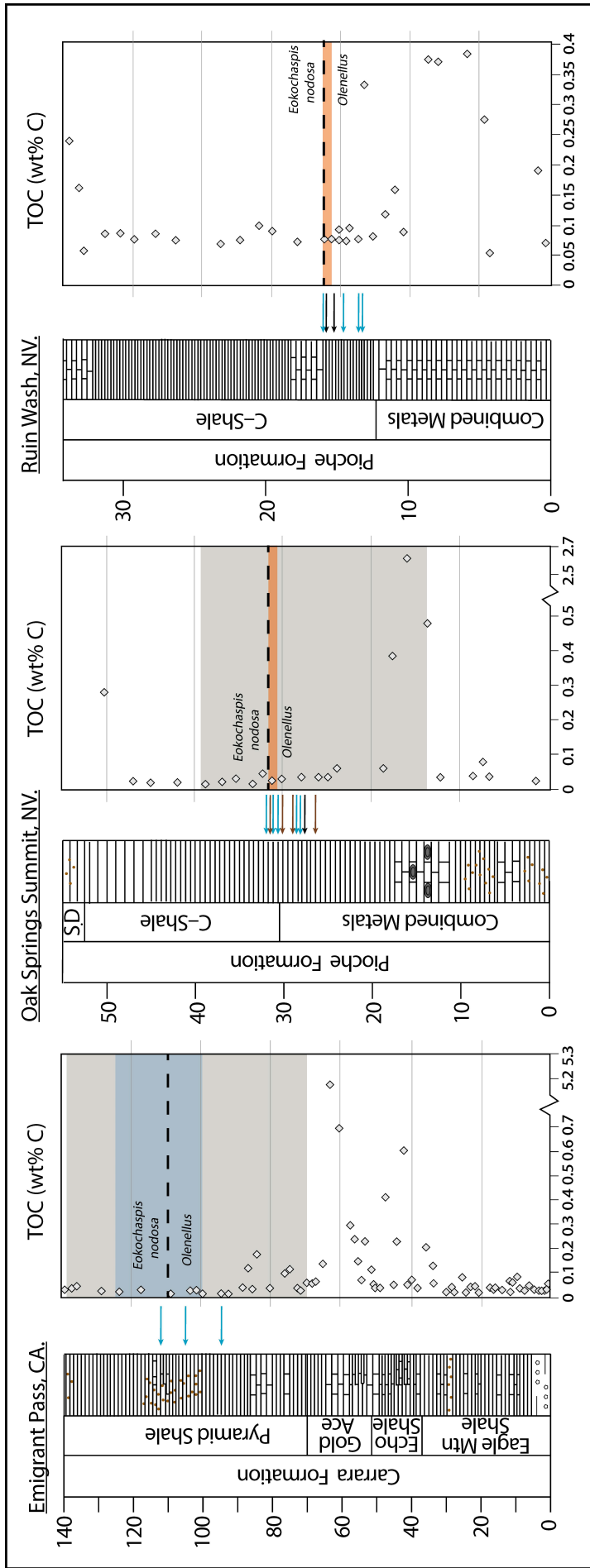
Figure 4.5: Stratigraphic columns showing TOC wt % C through the Carrara and Pioche formations. See Fig. 4.2 for key.

135

values at Ruin Wash, Hg concentrations are consistently <5 ppb, and there is no increase at the olenellid extinction horizon.

The highest Hg/TOC ratios at Ruin Wash coincide with the increased Hg concentrations and shows the same overall trends seen in the elemental concentrations (Fig. 4.4).
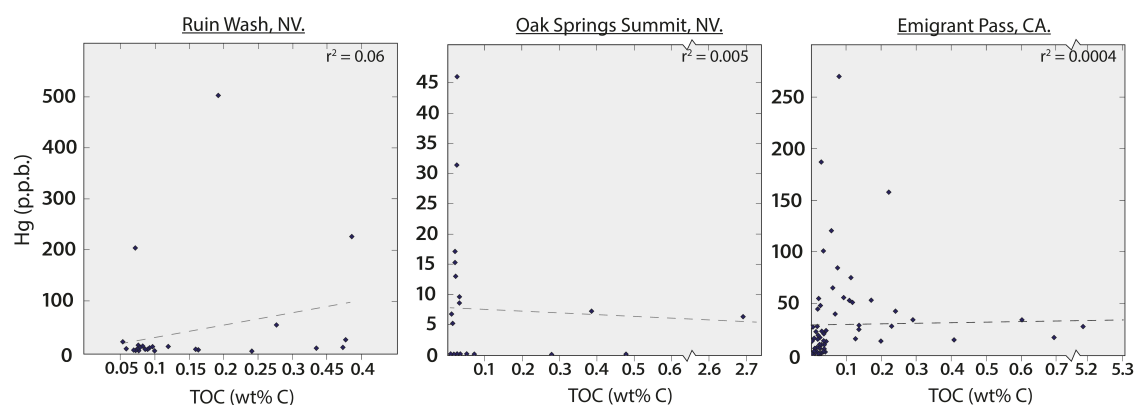
Figure 4.6: Cross plots of TOC wt % C vs. Hg (ppb) for the Carrara and Pioche formations.

4.6. Discussion

Between the Pioche and Carrara formations we observe an inconsistent correspondence between the olenellid trilobite extinction, ROECE and sedimentary Hg enrichments (Fig. 4.7). We review possible points for correlation between sections (e.g. ROECE interval and the trilobite extinction) and discuss processes which may account for our varied Hg record.

4.6.1. ROECE, Hg and Hg/TOC correlation

To assess any correlation between the timing of Hg enrichment and ROECE, we delineate the base of the excursion based on the following two criteria. Firstly, the onset of ROECE should be present within the Pyramid Shale Member of the Carrara Formation and the upper Combined Metals Member of the Pioche Formation, this is based on the initial discovery by Montañez et al. (2000) of an abrupt negative carbon isotope excursion within the *Olenellus* trilobite biozone, but immediately preceding the olenellid extinction. Secondly, given this stratigraphic constraint, we mark the onset of the excursion as the base of the negative inflexion interpreted within these

136
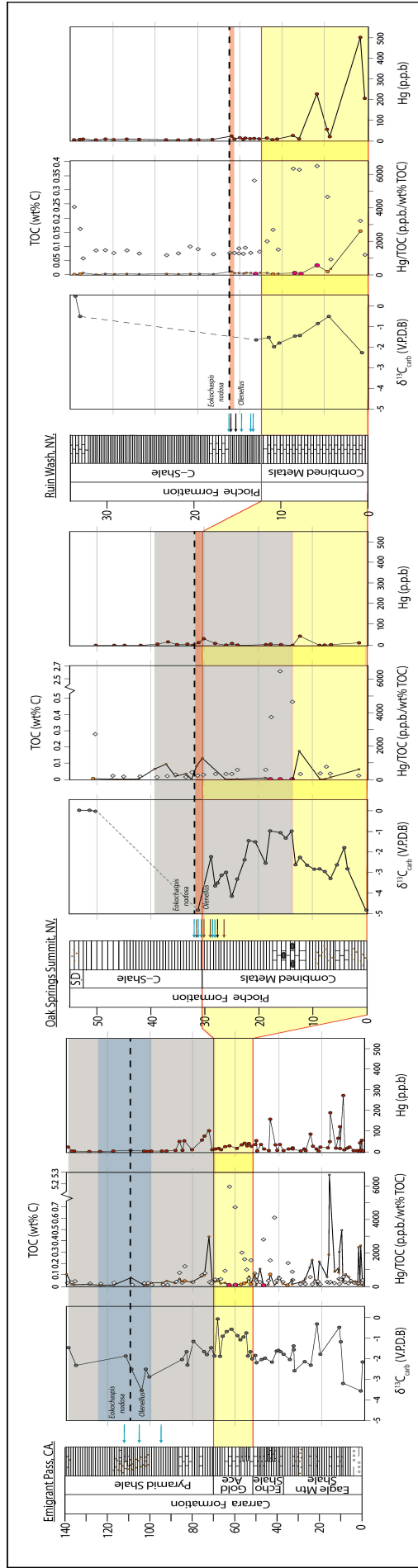
Figure 4.7: Summary of Hg (ppb) and Hg/TOC (ppb/ wt % C) from the Carrara and Pioche formations. The position of the *Olenellus - Eokochaspsis nodosa* biozone boundary is from Palmer (1998), inferred redox conditions are based on framboid size distribution data from Faggetter et al. (2017). The yellow highlight correlates the Gold Ace Member of the Carrara Formation with the Combined Metals Member of the Pioche, after Palmer (1998). See Fig. 4.2 for key.

members, i.e. ~60m at Emigrant Pass and ~13m at Oak Springs Summit (Fig. 4.7). Between the Carrara and Pioche formations, our data show no clear relationship between the onset of ROECE and Hg or Hg/TOC enrichments; at Emigrant Pass an enrichment occurs around 10m above the base of ROECE and at Oak Springs Summit an enrichment occurs ~1m below the base of the excursion. It is clear from enrichments in the Eagle Mountain Shale Member of the Carrara Formation and in the Combined Metals Member of the Pioche Formation, that the majority of Hg and Hg/TOC excursions occur before the ROECE interval.

4.6.2. Extinction, Hg and Hg/TOC

In the Pioche Formation at Oak Springs Summit, a small Hg (32 ppb, above background for this section) and Hg/TOC excursion corresponds closely with the extinction horizon and the top of the *Olenellus* biozone (Figs. 4.3, 4.7). However, between our sections the relationship between olenellid extinction and Hg or Hg/TOC enrichment is also inconsistent (Fig. 4.7). There is no enrichment coincident with the top of the *Olenellus* biozone at Emigrant Pass, nor at the extinction horizon at Ruin Wash (Figs. 4.4, 4.7).

The issue of correlating Hg between the Carrara and Pioche formations is further complicated by high levels of Hg enrichment lower in the sections. This is seen in the Combined Metals Member a considerable distance below the olenellid extinction level at Ruin Wash, and in the Eagle Shale Member at Emigrant Pass. Palmer (1998) correlates the Combined Metals Member of the Pioche Formation to the Gold Ace Member of the Carrara Formation (Fig. 4.7 highlighted in yellow); thus, we cannot compare the enrichments in the Eagle Shale Member to the Pioche Formation because they are older than the base of our Pioche Formation sections.

The inconsistency of the relationship between Hg, ROECE and extinction across all three sections challenges the conventional use of Hg as a tracer for global environmental Hg loading. Previous Hg chemostratigraphies invoked to trace global LIP eruptions predict, and exhibit, synchronous Hg signals across regional and global sites (e.g. Percival et al., 2015, 2017). The lack of an unambiguous Hg signal across our sections questions the rationale of our Hg chemostratigraphy as

recording a single global event resulting in increased environmental Hg loading causing sedimentary Hg enrichments.

The observed heterogeneity of enrichments in Hg and Hg/TOC values could be caused by several factors related to sampling, environmental and diagenetic factors. The elevated values in the Eagle Shale Member at Emigrant Pass come from a level below the sampled horizon at other sections and thus its geographic extent is untested. However, the missing peak of Hg and Hg/TOC values during the olenellid extinction at Ruin Wash seems unlikely to be due to a lack of sampling because this interval is amongst the most densely sampled of our study.

The inconsistent Hg data from our three sections demonstrate that volcanic loading and binding to organic matter cannot be the sole drivers of the Hg record in these strata. We therefore consider the possible roles that redox variations and binding to clays (and possibly sulphides e.g. Benoit et al., 1999) may have played in controlling Hg chemostratigraphy. We present a discussion on processes other than volcanic Hg bound to organic matter which may affect the Hg record in ancient rocks.

4.6.3. Hg enrichments, redox variation and TOC

The redox state of the sediment and water column can play an important role in mobilising or re-mobilising Hg species and enhancing or sequestering Hg release between the sediment and water column (Emili et al., 2011). In the modern ocean, persistent anoxic conditions in the water column optimises bacterial Hg methylation, resulting in increased Hg drawdown to sediments and enhancement of methylmercury (MeHg) burial (Mason et al., 1993; Monperrus et al., 2007; Emili et al., 2011; Yin et al., 2017). This means that after continued anoxic conditions, sediments act as a Hg sink (Emili et al., 2011). This mobilisation of Hg between the water column and sediment can be reversed in transition from oxic to anoxic conditions. Hg and MeHg previously scavenged under oxic conditions and sequestered in sediments, are then re-mobilised during an upward shift of the anoxic zone to the sediment – water interface, enhancing the release of Hg and MeHg back into the water column (Emili et al., 2011). Emili et al. (2011) modelled Hg cycling between the sediment and water column under anoxic conditions and found a strong redox control on the mobility of Hg.

They found that benthic Hg flux from the sediment to water column is highest during anoxic conditions and is also accentuated during SO_4 reduction in euxinic conditions. Previous assessment of redox states within the Carrara and Pioche formations found intermittent periods of dysoxia during the olenellid extinction interval (Webster et al., 2008; Faggetter et al., 2017). Oxygen limitation was not considered severe enough to drive extinction (Faggetter et al. 2017), but it is plausible that fluctuating redox conditions could have altered drawdown of Hg from the water column to the sediments (Horowitz et al., 2017) during times of heightened Hg loading. Euxinic strata are developed during the trilobite extinction level at Ruin Wash but there is no corresponding Hg anomaly. Given evidence for euxinic conditions at Ruin Wash, but not Oak Springs Summit, we suggest that varying behaviour of Hg under different redox conditions could underlie the differing relationship between Hg and extinction in the Pioche Formation.

It is important to note that previously published studies reporting Hg sedimentary trends across multiple sections similarly reveal variable Hg and Hg/TOC ranges between localities (e.g. Grasby et al., 2016; Jones et al., 2017). Accordingly, such discrepancies may be an inherent component of volcanically-derived deposition and fixation in marine sediments. For instance, a variable record of Hg enrichment during anoxia-related extinction is reported during the Toarcian (Early Jurassic) extinction (Percival et al., 2015). This event coincides with the organic-rich shales of the Jet Rock in northern England, but these sediments lack the Hg enrichment that otherwise might be expected given contemporaneous eruption of the Karoo-Ferrar flood basalt province. In explanation, Percival et al. (2015) argue that efficient organo-Hg scavenging in organic-rich euxinic settings may have caused over-printing of the Hg/TOC anomaly by excess organic matter deposition. However, such a mechanism is unlikely in our reported Cambrian examples because TOC values in the C-Shale at Ruin Wash are low (<1 wt %). The Carrara and Pioche formations are similarly characterised by low TOC and a range of Hg concentrations and Hg/TOC values; we interpret this signature as showing that even in organic-poor rocks it is possible to record elevated Hg concentrations during times of heightened environmental loading (Figs. 4.5, 4.6). At Oak Springs Summit Hg and Hg/TOC excursions

occur in samples containing low TOC (<0.15 wt% C), whilst at Emigrant
Pass and Ruin Wash enrichments occur across a range of wt% TOC values
(Fig. 4.6). The clear absence of a strong correlation between Hg and TOC
(Fig. 4.5) at Emigrant Pass and Ruin Wash sections therefore indicates that
Hg enrichment is not a sole function of variable TOC. At Oak Springs
Summit low TOC values record a range of Hg concentrations, which, when
normalised to TOC, remain as Hg/TOC excursions. To summarise, we posit
that at Oak Springs Summit these anomalies are not exclusively a function
of low TOC.

4.6.4. Hg as an indicator of volcanism

Whilst clarifying the association between extinction, volcanism, Hg
enrichment and large negative carbon isotopic excursions is extremely
complex, massive volcanism has been implicated as a mechanism behind
excursions associated with extinction events (Payne et al., 2004; Blackburn
et al., 2013; Dal Corso et al., 2014; Percival et al., 2017). Our data shows
that at Emigrant Pass the base of ROECE interval is marked by a Hg
enrichment, but there is no strong evidence that the entire ROECE coincides
with prolonged Hg enrichments.

The pre-ROECE levels of Hg enrichment observed at Emigrant Pass
and Ruin Wash are enigmatic, and it is currently unclear if they record a
local volcanic source, an early eruptive pulse of the Kalkarindji LIP, or are
unrecognized diagenetic artefacts. Further work is required to determine
how widespread these perturbations are, both within Laurentia and globally.
Further dating efforts within the Kalkarindji may also help clarify its
emplacement history and whether initial pulses were considerably earlier
than current geochronological constraints. Current age dating of the
Kalkarindji Province suggest the eruption onset could plausibly predate the
Series 2 – Series 3 boundary raising the possibility that the Hg record from
the Great Basin records other volcanic eruptions. If this proves to be the
case, then the search for Hg anomalies may not be a useful marker for
independently implicating specific volcanic sources.

While the lack of a consistent Hg record between sections prevents
us from arguing strongly for a volcanogenic source of Hg, it is not
implausible that Hg from the Kalkarindji LIP could have been deposited in

western Laurentia. While our data do not establish an unequivocal link to the Kalkarindji LIP, sedimentary Hg anomalies in both the modern and in geological history have been linked to LIPs and active volcanism (e.g. Schuster et al., 2002; Sanei et al., 2012; Grasby et al., 2013; Sial et al., 2013, 2014; Percival et al., 2015; Grasby et al., 2016; Thibodeau et al., 2016; Percival et al., 2017; Gong et al., 2017). Field observations of the Kalkarindji Blackfella Rockhole Member (BRM) by Marshall et al. (2016) detail an eruption style (for the BRM) analogous to fissure eruptions observed from Laki eruptions and similarly analogous to those described by Glaze et al. (2017). Glaze et al. (2017) argue that this type of eruption style can transport volcanogenic volatiles into the stratosphere from fire fountain eruptions driving thermal uplift above buoyant ash and gas plumes. We suggest that the eruptive style associated with the BRM could have produced buoyant ash and gas plumes capable of delivering volcanogenic volatiles, including Hg, into the stratosphere (Glaze et al., 2017). Coupled with this, the palaeoposition of Kalkarindji at low latitudes (Fig. 4.1) would have been favourable for the hemispheric (and possibly global) circulation of volcanogenic volatiles transported to the stratosphere via a buoyant plume (Marshall et al., 2016; Glaze et al., 2017). When assessing the temporal coincidence between the Kalkarindji and the Series 2 – Series 3 boundary age of our sections, the proximity to our study locations (Fig. 4.1) and the evidence for sedimentary Hg in our sections (Fig. 4.2), we suggest that some of the Hg enrichments within the Carrara and Pioche formations may be related to increased volcanic activity at the time.

4.7. Conclusion

Here were report sedimentary Hg and Hg/TOC enrichments from both the Carrara and Pioche formations of the western Great Basin, USA. These successions are constrained within a biostratigraphic and chemostratigraphic framework to record the Cambrian Series 2 – Series 3 boundary. At this time, within the Pioche Formation, the extinction of the Laurentian olenellid trilobite is clearly observable. The ROECE negative inorganic carbon isotope excursion is present at two of our three sections (Emigrant Pass, Carrara Formation and Oak Springs Summit, Pioche

Formation). In the Carrara Formation, the majority of Hg enrichments predate ROECE, with a single enrichment occurring just above the base of the excursion. At Oak Springs Summit ROECE is preceded by Hg enrichment.

Within the Pioche Formation at Oak Springs Summit the extinction horizon of the olenellid trilobites is marked by positive Hg and Hg/TOC excursions, however, a similar excursion is not apparent at the equivalent horizon from Ruin Wash. The failure to locate enrichment in the euxinic Ruin Wash section suggest that other factors, as yet unclear in our sections, also play a role. Our data supports the theory that Hg and Hg/TOC enrichments within the Carrara and Pioche formations are not solely derived from enhanced TOC preservation, but that inconsistent Hg trends may have resulted from little understood diagenetic processes. We also conclude that given the strong control exhibited on Hg flux, speciation and accumulation by anoxia in the modern, the role of redox states in deep time is important when assessing the record of Hg in rocks.

The timing, volume and palaeo-position of this province makes it a probable candidate as the source of environmental loading and subsequent Hg enrichments in the Carrara and Pioche formations. Thus, the Kalkarindji LIP potentially contributed to the Hg concentrations at the Cambrian Series 2 – Series 3 boundary, but the occurrence of precursor levels of Hg enrichment either point to hitherto unrecognised phases of volcanism within the Province or the possibility of other unknown volcanic episodes.

Acknowledgments

4.8. References

Benoit, J.M., Gilmour, C.C., Mason, R.P., Heyes, R., (1999). Sulfide controls on mercury speciation and bioavailability to methylating bacteria in sediment pore waters. Environ. Sci. Technol. 33, 951–957.

Benoit, J.M., Mason, R.P., Gilmour, C.C., Aiken, G.R., (2001). Constants for mercury binding by dissolved organic matter isolates from the Florida Everglades. Geochim. Cosmochim. Acta 65, 4445–4451.

Bergquist, B. A. (2017). Mercury, volcanism, and mass extinctions. *Proceedings of the National Academy of Sciences*, 201709070.

Blackburn, T. J., Olsen, P. E., Bowring, S. A., McLean, N. M., Kent, D. V., Puffer, J., Et-Touhami, M. (2013). Zircon U-Pb geochronology links the end-Triassic extinction with the Central Atlantic Magmatic Province. *Science*, *340*(6135), 941-945.

Bond, D. P., Wignall, P. B. (2010). Pyrite framboid study of marine Permian–Triassic boundary sections: a complex anoxic event and its relationship to contemporaneous mass extinction. *Geological Society of America Bulletin*, *122*(7-8), 1265-1279.

Brasier, M. D., Corfield, R. M., Derry, L. A., Rozanov, A. Y., Zhuravlev, A. Y. (1994). Multiple δ13C excursions spanning the Cambrian explosion to the Botomian crisis in Siberia. *Geology*, *22*(5), 455-458.

Chang, C., Hu, W., Wang, X., Yu, H., Yang, A., Cao, J., Yao, S. (2017). Carbon isotope stratigraphy of the lower to middle Cambrian on the eastern Yangtze Platform, South China. *Palaeogeography, Palaeoclimatology, Palaeoecology*, *479*, 90-101.

Cocks, L. R. M. and Torsvik, T.M. (2013). The dynamic evolution of the Palaeozoic geography of eastern Asia. *Earth-Science Reviews* 117: 40-79.

Dal Corso, J., Marzoli, A., Tateo, F., Jenkyns, H. C., Bertrand, H., Youbi, N., Cirilli, S. (2014). The dawn of CAMP volcanism and its bearing on the end-Triassic carbon cycle disruption. *Journal of the Geological Society*, *171*(2), 153-164.

Emili, A., Koron, N., Covelli, S., Faganeli, J., Acquavita, A., Predonzani, S., De Vittor, C. (2011). Does anoxia affect mercury cycling at the sediment–water interface in the Gulf of Trieste (northern Adriatic Sea)? Incubation experiments using benthic flux chambers. *Applied geochemistry*, *26*(2), 194-204.

Ernst, R.E. and Youbi, N. (2017). How large igneous provinces affect global climate, sometimes cause mass extinction, and represent natural markers in the geological record. Palaeogeography, Palaeoclimatology, Palaeoecology

Faggetter, L.E., Wignall, P.B., Pruss, S.B., Newton, R.J., Sun, Y.D. and Crowley, S. (2017). Trilobite extinctions, facies changes and the ROECE carbon isotope excursion at the Cambrian Series 2-3 boundary, Great Basin, western USA. Palaeogeography, Palaeoclimatology, Palaeoecology

Fan, R., Deng, S., Zhang, X. (2011). Significant carbon isotope excursions in the Cambrian and their implications for global correlations. *Science China Earth Sciences*, *54*(11), 1686-1695.

Font, E., Adatte, T., Sial, A. N., de Lacerda, L. D., Keller, G., Punekar, J. (2016). Mercury anomaly, Deccan volcanism, and the end-Cretaceous mass extinction. *Geology*, *44*(2), 171-174.

Glass, L. M., and Phillips, D. (2006). The Kalkarindji continental flood basalt province: A new Cambrian large igneous province in Australia with possible links to faunal extinctions. *Geology*, *34*(6), 461-464.

Glaze, L. S., Self, S., Schmidt, A., Hunter, S. J. (2017). Assessing eruption column height in ancient flood basalt eruptions. *Earth and Planetary Science Letters*, *457*, 263-270.

Gong, Q., Wang, X., Zhao, L., Grasby, S. E., Chen, Z. Q., Zhang, L., Li, Z. (2017). Mercury spikes suggest volcanic driver of the Ordovician-Silurian mass extinction. *Scientific Reports*, *7*.

Grasby, S. E., Sanei, H., Beauchamp, B., Chen, Z. (2013). Mercury deposition through the Permo–Triassic biotic crisis. *Chemical Geology*, *351*, 209-216.

Grasby, S.E., Beauchamp, B., Bond, D.P.G., Wignall, P.B., Sanei, H. (2016). Mercury anomalies associated with three extinction events (Capitanian crisis, latest Permian extinction and the Smithian/Spathian extinction) in NW Pangea. Geological Magazine 153, 285-297. doi:10.1017/S0016756815000436

Hall, G. E., and Pelchat, P. (1997). Evaluation of a direct solid sampling atomic absorption spectrometer for the trace determination of mercury in geological samples. *Analyst*, *122*(9), 921-924.

Horowitz, H. M., Jacob, D. J., Zhang, Y., Dibble, T. S., Slemr, F., Amos, H. M., Sunderland, E. M. (2017). A new mechanism for atmospheric mercury redox chemistry: Implications for the global mercury budget. *Atmospheric Chemistry and Physics*, *17*(10), 6353-6371.

Hough, M.L., Shields, G.A., Evins, L.Z., Strauss, H., Henderson, R.A., Mackenzie, S. (2006). A major Sulphur isotope evnt at *c.* 510 Ma: a possible anoxia-extinction-volcanism connection during the Early-Middle Cambrian transition? Terra Nova 18, 257-263. doi: 10.1111/j.1365-3121.2006.00687.x

Howley, R.A., Rees, M. N., Jiang, G. (2006). Significance of Middle Cambrian mixed carbonate-siliciclastic units for global correlation: southern Nevada, USA. *Palaeoworld*, *15*(3), 360-366.

Jones, D. S., Martini, A. M., Fike, D. A. Kaiho, K. (2017). A volcanic trigger for the Late Ordovician mass extinction? Mercury data from south China and Laurentia. *Geology*, *45*(7), 631-634.

Jourdan, F., Hodges, K., Sell, B., Schaltegger, U., Wingate, M.T. D., Evins, L.Z., Blenkinsop, T. (2014). High-precision dating of the Kalkarindji large igneous province, Australia, and synchrony with the Early–Middle Cambrian (Stage 4–5) extinction. *Geology*, *42*(6), 543-546.

Kongchum, M., Hudnall, W. H., Delaune, R. D. (2011). Relationship between sediment clay minerals and total mercury. *Journal of Environmental Science and Health, Part A*, *46*(5), 534-539.

Kravchinsky, V.A., (2012). Paleozoic large igneous provinces of Northern Eurasia: Correlation with mass extinction events. *Glob. Planet. Change* 86–87, 31–36. doi:10.1016/j.gloplacha.2012.01.007

Landing, E. (2012). The great American carbonate bank in eastern Laurentia: Its births, deaths, and linkage to paleooceanic oxygenation (Early Cambrian – Late Ordovician), in J. R. Derby, R. D. Fritz, S. A. Longacre, W. A. Morgan, and C. A. Sternbach, eds., *The great American carbonate bank: The geology and economic resources of the*

Cambrian – Ordovician Sauk megasequence of Laurentia: AAPG Memoir 98, p. 451 – 492.

Li, Z. X., Zhang, L., Powell, C. M. (1996). Positions of the East Asian cratons in the Neoproterozoic supercontinent Rodinia. *Australian Journal of Earth Sciences*, *43*(6), 593-604.

Li, Z. X., Bogdanova, S. V., Collins, A. S., Davidson, A., De Waele, B., Ernst, R. E., Karlstrom, K. E. (2008). Assembly, configuration, and break-up history of Rodinia: a synthesis. *Precambrian research*, *160*(1), 179-210.

Marshall, P. E., Widdowson, M., Murphy, D. T. (2016). The Giant Lavas of Kalkarindji: rubbly pāhoehoe lava in an ancient continental flood basalt province. *Palaeogeography, Palaeoclimatology, Palaeoecology*, *441*, 22-37.

Mason, R. P., Fitzgerald, W. F., Hurley, J., Hanson, A. K., Donaghay, P. L., Sieburth, J. M. (1993). Mercury biogeochemical cycling in a stratified estuary. *Limnology and Oceanography*, *38*(6), 1227-1241.

Merriam, C. W., Palmer, A. R. (1964). *Cambrian rocks of the Pioche mining district, Nevada, with a section on Pioche shale faunules* (No. 469). United States Government Printing Office.

Monperrus, M., Tessier, E., Amouroux, D., Leynaert, A., Huonnic, P., Donard, O. F. X. (2007). Mercury methylation, demethylation and reduction rates in coastal and marine surface waters of the Mediterranean Sea. *Marine Chemistry*, *107*(1), 49-63.

Montañez, I. P., Osleger, D. A., Banner, J. L., Mack, L. E., Musgrove, M. (2000). Evolution of the Sr and C isotope composition of Cambrian oceans. *GSA today*, *10*(5), 1-7.

Ogg, J. G., Ogg, G., Gradstein, F. M. (2016). *A Concise Geologic Time Scale: 2016*. Elsevier.

Palmer, A.R. (1998). Terminal early Cambrian extinction of the Olenellina: documentation from the Pioche Formation, Nevada. *Journal of Paleontology*, 72 (04), 650-672.

Palmer, A. R., Halley, R. B. (1979). Physical stratigraphy and trilobite biostratigraphy of the Carrara Formation (Lower and Middle Cambrian) in the southern Great Basin (No. 1047). *US Govt. Print. Off.*

Payne, J.L., Lehrmann, D.J., Wei, J., Orchard, M.J., Schrag, D.P., Knoll, A.H. (2004). Large perturbations of the carbon cycle during recovery from the end-Permian extinction. Sci- ence 305 (5683), 506–509.

Percival, L.M.E., Witt, M.L.I., Mather, T.A., Hermoso, M., Jenkyns, H.C., Hesselbo, S.P., Al-Suwaidi, A.H., Storm, M.S., Xu, W., Ruhl, M. (2015). Globally enhanced mercury deposition during the end-Pliensbachian extinction and Toarcian OAE: A link to the Karoo-Ferrar Large Igneous Province. Earth ad Planetary Science Letters 428, 267-280. http://dx.doi.org/10.1016/j.epsl.2015.06.064

Percival, L. M., Ruhl, M., Hesselbo, S. P., Jenkyns, H. C., Mather, T. A., Whiteside, J. H. (2017). Mercury evidence for pulsed volcanism during the end-Triassic mass extinction. *Proceedings of the National Academy of Sciences*, 201705378.

Prave, A.R. (1991). Depositional and sequence stratigraphic framework of the Lower Cambrian Zabriskie Quartzite: implications for regional correlations and the Early Cambrian paleogeography of the Death Valley region of California and Nevada. *Geological Society of America Bulletin*, 104(5), 505-515.

Pyle, D.M., Mather, T.A. (2003). The importance of volcanic emissions for the global atmo spheric mercury cycle: Atmospheric Environment, v. 37, p. 5115–5124, doi:10.1016/j.at- mosenv.2003.07.011.

Ren, Y., Zhong, D., Gao, C., Liang, T., Sun, H., Wu, D., Zheng, X. (2017). High-resolution carbon isotope records and correlations of the lower Cambrian Longwangmiao formation (stage 4, Toyonian) in Chongqing, South China. *Palaeogeography, Palaeoclimatology, Palaeoecology*.

Sanei, H., Grasby, S., Beauchamp, B. (2012). Latest Permian mercury anomalies. *Geology 40*, 63–66.

Schuster, P. F., Krabbenhoft, D. P., Naftz, D. L., Cecil, L. D., Olson, M. L., Dewild, J. F., Abbott, M. L. (2002). Atmospheric mercury deposition

during the last 270 years: a glacial ice core record of natural and anthropogenic sources. *Environmental science & technology, 36*(11), 2303-2310.

Scotese, C.R. (2016). PALEOMAP PaleoAtlas for GPlates and the PaleoData Plotter Program, PALEOMAP Project, http://www.earthbyte.org/paleomappaleoatlas-for-gplates/

Sial, A. N., Lacerda, L. D., Ferreira, V. P., Frei, R., Marquillas, R. A., Barbosa, J. A., Pereira, N. S. (2013). Mercury as a proxy for volcanic activity during extreme environmental turnover: The Cretaceous–Paleogene transition. *Palaeogeography, Palaeoclimatology, Palaeoecology, 387*, 153-164.

Sial, A. N., Chen, J., Lacerda, L. D., Peralta, S., Gaucher, C., Frei, R., Pereira, N. S. (2014). High-resolution Hg chemostratigraphy: A contribution to the distinction of chemical fingerprints of the Deccan volcanism and Cretaceous–Paleogene Boundary impact event. *Palaeogeography, Palaeoclimatology, Palaeoecology, 414*, 98-115.

Schmid, S. (2017). Chemostratigraphy and palaeo-environmental characterisation of the Cambrian stratigraphy in the Amadeus Basin, Australia. *Chemical Geology, 451*, 169-182.

Sundberg, F. A., McCollum, L. B. (2000). Ptychopariid trilobites of the lower-middle Cambrian boundary interval, Pioche Shale, southeastern Nevada. *Journal of Paleontology, 74*(4), 604-630.

Thibodeau, A.M., Ritterbush, K., Yager, J.A., West, A.J., Ibarra, Y., Bottjer, D.J., Berelson, W.M., Bergquist, B.A., Corsetti, F.A. (2016). Mercury anomalies and the timing of biotic recovery following the end-Triassic mass extinction. Nature Communications 7:11147, doi: 19.1038/ncomms11147

Veevers, J.J. (2001). Atlas of billion-year old earth history of Australia and neighbours in Gondwanaland. *GEMOC Press*, Sydney, Australia.

Wang, X., Hu, W., Yao, S., Chen, Q., Xie, X. (2011). Carbon and strontium isotopes and global correlation of Cambrian Series 2-Series 3 carbonate rocks in the Keping area of the northwestern Tarim Basin, NW China. *Marine and Petroleum Geology, 28*(5), 992-1002.

Webster, M., Gaines, R. R., Hughes, N. C. (2008). Microstratigraphy, trilobite biostratinomy, and depositional environment of the "Lower Cambrian" Ruin Wash Lagerstätte, Pioche Formation, Nevada. *Palaeogeography, Palaeoclimatology, Palaeoecology*, *264*(1), 100-122.

Wignall, P. B. (2001). Large igneous provinces and mass extinctions. *Earth-science reviews*, *53*(1), 1-33.

Wignall, P.B., (2015). *The worst of times: how life on Earth survived 80 million years of extinction*. Princeton University Press, 199 pp.

Yin, R., Xu, L., Lehmann, B., Lepak, R. F., Hurley, J. P., Mao, J., Hu, R. (2017). Anomalous mercury enrichment in Early Cambrian black shales of South China: Mercury isotopes indicate a seawater source. *Chemical Geology*.

Zhang, W.H., Shi, X.Y., Jiang, G.Q., Tang, D.J., Wang, X.Q. (2015). Mass-occurrence of oncoids at the Cambrian Series2-Series 3 transition: Implications for microbial resurgence following an Early Cambrian extinction. Gondwana Research 28, 432-450. http://dx.doi.org/10.1016/j.gr.2014.03.015

Zhu, M. Y., Zhang, J. M., Li, G. X., Yang, A. H. (2004). Evolution of C isotopes in the Cambrian of China: implications for Cambrian subdivision and trilobite mass extinctions. *Geobios*, 37(2), 287-301.

Zhu, M. Y., Babcock, L. E., Peng, S. C. (2006). Advances in Cambrian stratigraphy and paleontology: integrating correlation techniques, paleobiology, taphonomy and paleoenvironmental reconstruction. *Palaeoworld*, *15*(3), 217-222.

Zhu, D. C., Zhao, Z. D., Niu, Y., Dilek, Y., Wang, Q., Ji, W. H., Mo, X. X. (2012). Cambrian bimodal volcanism in the Lhasa Terrane, southern Tibet: record of an early Paleozoic Andean-type magmatic arc in the Australian proto-Tethyan margin. *Chemical Geology*, *328*, 290-308.

5. Chapter 5: Carbon isotope chemostratigraphy and Hg concentrations across the Cambrian Series 2 – 3 boundary, south Georgina Basin, Australia.

Faggetter, L.E., Wignall, P.B., Poulton, S.W., Jones, D. S., Sun, Y., Newton, R.J.

5.1 Foreword

This chapter examines the nature of environmental change, carbon cycling and extinction at the Cambrian Series 2 – Series 3 boundary from three locations in Australia's Georgina Basin. Due to the proximity of the Georgina Basin to the basalts of the Kalkarindji large igneous province (LIP), and the overlap in time between deposition of Cambro-Ordovician successions and the age of the Kalkarindji basalts; these locations were chosen for their potential to record a local and regional sedimentary signal of the LIP, the preliminary findings are presented here.

5.2 Introduction

The oldest known Phanerozoic large igneous province (LIP) is Australia's Kalkarindji LIP. It now crops out as scattered basaltic suites (Fig. 5.1) with an estimated original areal extent of ~ 55,000km^2 (Bultitude, 1972; Cutovinos et al., 2002; Marshall et al., 2016). If the eroded remnant of the Kalkarindji were originally connected as a continuous terrane of lava fields, then it may have covered a more substantial area; closer to ~400,000km^2, with an original volume of ~1.5 x 10^{5}km^3 (Veevers, 2001). If accurate, these estimates suggest a size similar to the Columbia River Basalt Province, one of the smallest LIPs (Glass and Phillips, 2006; Bryan et al., 2010). Radiometric dating is essential in constraining the emplacement age of Kalkarindji and most ages for the Province consist of ^{40}Ar/^{39}Ar dates with large errors (508-505 ± 2 Ma; Glass and Phillips 2006). A single, more

robust, U-Pb zircon age of 510.7 ± 0.6Ma (Jourdan et al., 2014) invites a close comparison to the (unratified) age of the Cambrian Series 2 – Series 3 boundary of 509 Ma (Ogg et al., 2016).
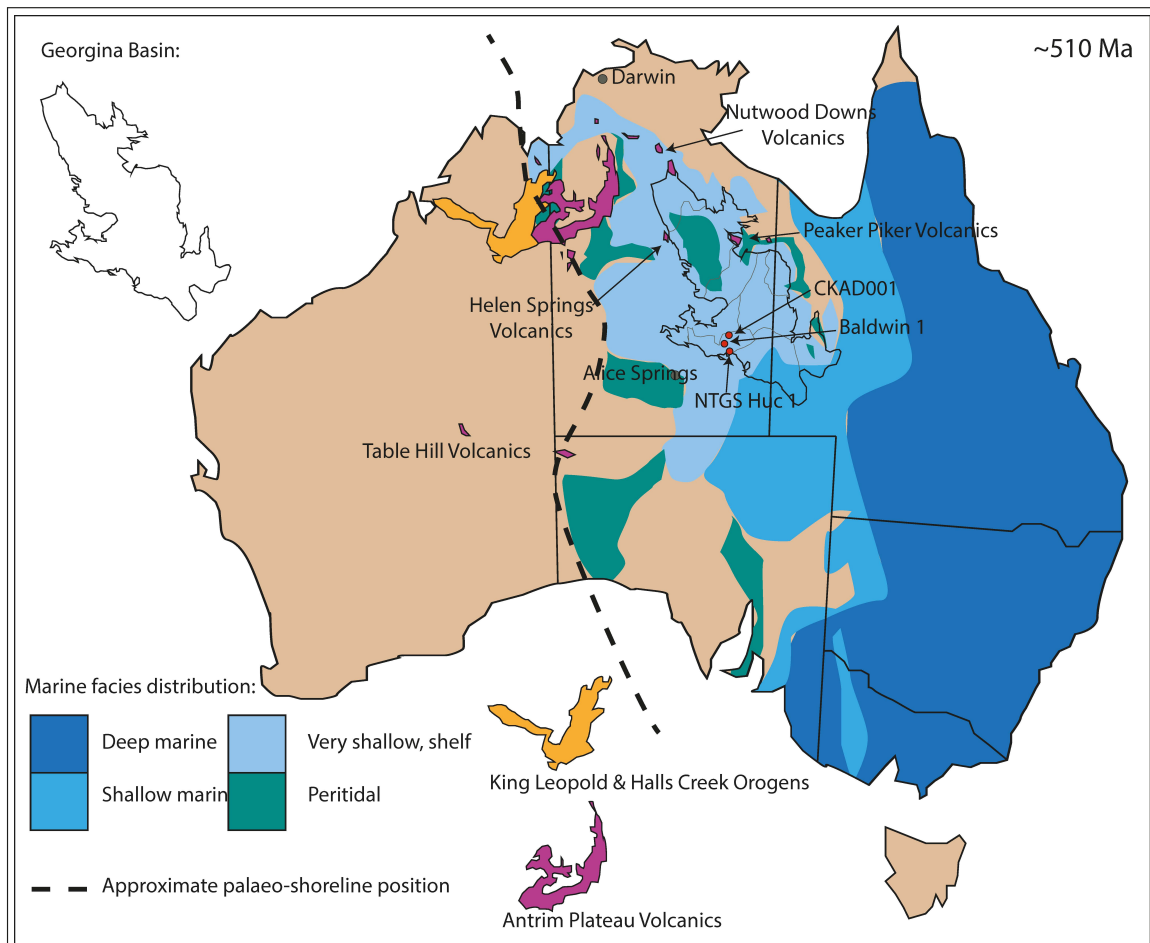
Figure 5.1: Map of Australia showing the Georgina Basin and the locations of cores CKAD001, NTGS Huc 1 and Baldwin 1. The location and outline of Kalkarindji LIP outcrops are taken from Marshall et al. (2016) Distribution of marine facies modified from Munson et al. (2013) and approximate position of palaeo-shoreline from Torsvick and Cocks (2013).

The Cambrian system exhibits highly variable biogeochemical cycles; the carbon cycle underwent large δ^{13}C oscillations (Brasier, 1994; Zhu et al., 2006); marine environments were at least periodically anoxic (e.g. Zhuravlev and Wood, 1996; Hough et al., 2006; Hurtgen et al., 2009; Jiang et al., 2009; Gill et al., 2011) and diversification following the Cambrian Explosion experienced several setbacks by way of extinction events (e.g. Zhuravlev and Wood, 1996; Palmer, 1998; Saltzman et al., 2000; Zhu et al, 2006; Faggetter et al., 2017). The Cambrian Series 2 – Series 3 boundary embodies all of these phenomena: on the Laurentian continent. The boundary is marked by the extinction of the olenellid trilobites and the associated negative inorganic carbon isotope excursion, the Redlichiid Olenellid Extinction Carbon Isotope Excursion (ROECE; Faggetter et al., 2017, whilst on Gondwana, the redlichiid trilobites did not survive after the

152

base of Series 3 (Zhu et al., 2004; 2006). This interval coincided with a major transgression on the Gondwanan continent (Southgate and Shergold, 1991) and the eruption of the Kalkarindji LIP (Jourdan et al., 2014). Since the connection between LIPs and mass extinction events is well developed throughout the Phanerozoic (e.g. Sanei et al., 2012; Percival et al., 2015; Thibodeau et al., 2016; Font et al., 2016; Grasby et al., 2016; Gong et al., 2017), the apparent temporal correspondence between the Kalkarindji LIP and extinction at the Series 2 – Series 3 boundary has led to the suggestion that this represents an early Palaeozoic LIP-extinction connection (Jordan et al., 2014). For other Phanerozoic LIP-extinction events, recent studies have used of mercury (Hg) as a tracer for amplified environmental loading derived from increased volcanic activity (e.g. Percival et al., 2015; 2017; Thibodeau et al., 2016; Jones et al. 2017). As such, three drill cores from the Dulcie Syncline in the southern Georgina Basin in Australia's Northern Territory (Fig. 5.1), spanning the Cambrian Series 2 – Series 3 boundary (Fig. 5.2), have been investigated for evidence of volcanism at this time, including possible Hg enrichments. Carbonate successions of this region were intersected by drill cores CKAD001, NTGS Huc 1 and Baldwin 1; the proximity of the Georgina Basin to the Kalkarindji basalts therefore represents a potential "ground zero" sedimentary archive of volcanism at this time.
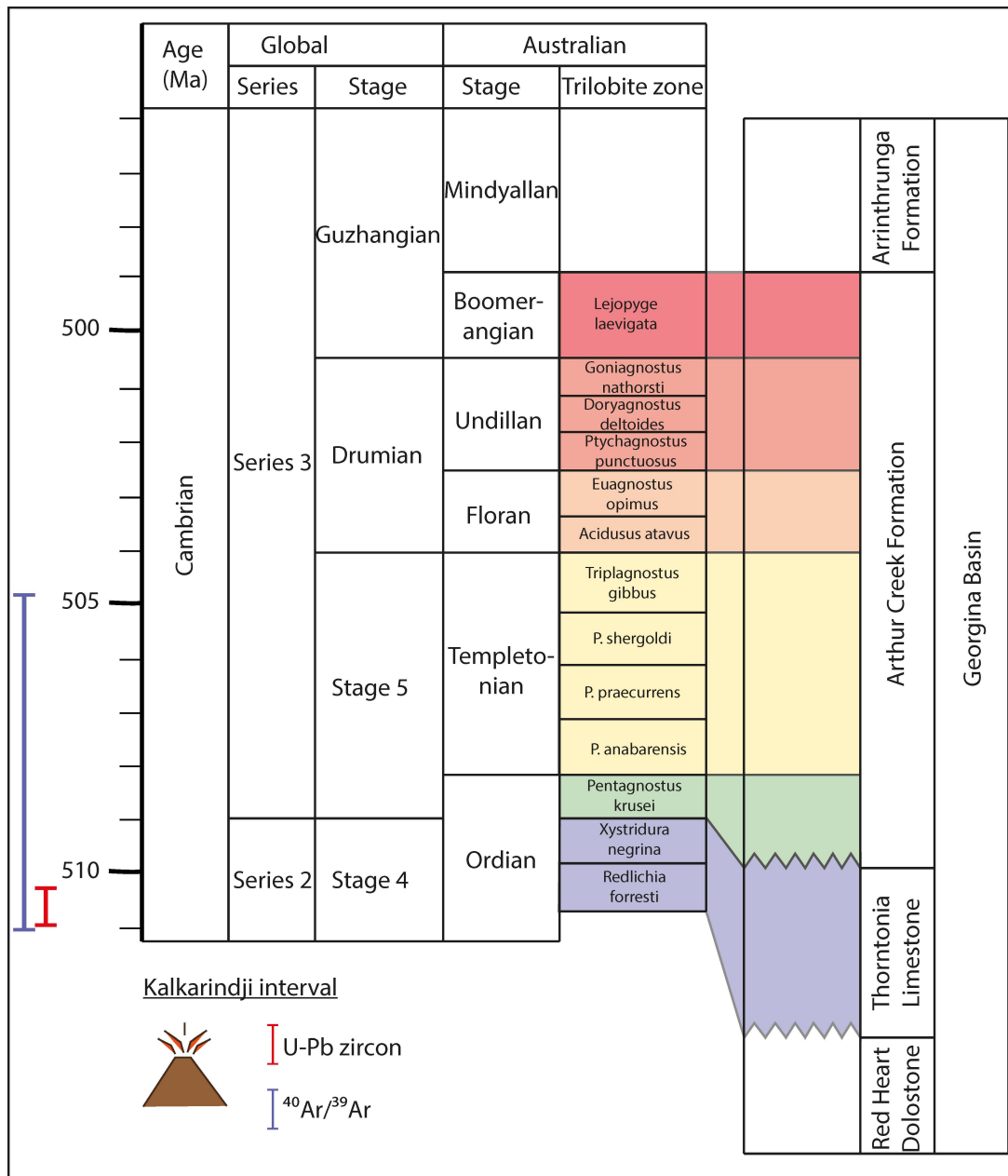
Figure 5.2: Global correlation of Cambrian Stages with trilobite biostratigraphy of Smith et al. (2013) alongside a schematic log of studied formations. U-Pb zircon date from Jourdan et al. (2014), ^{40}Ar/^{39}Ar date from Glass and Phillips (2006).

5.3 Geological Setting

The "Centralian Superbasin" (CS) makes up a series of originally interconnected intracratonic basins (Officer- Amadeus-Ngalia-Georgina) that overlay a thick crust of Archean to Mesoproterozoic terranes across Australia's Northern Territory, Queensland, South Australia and Western Australia (Walter et al., 1995; Walter and Veveers,1997). The formation of the CS, ca. 800 Ma, has been linked to crustal sag in response to mantle activity initiated by a thermal blanketing effect on the Rodinian supercontinent (Lindsay, 2002). Following sagging, compressional dynamics prevailed in the Neoproterozoic and the CS was restructured into a series of largely independent foreland basins separated by uplifted basement blocks (Lindsay, 2005; Schmid, 2017). In the north of the CS, the outpouring of tholeiitic basalt from the Antrim Plateau Volcanics (a sub-province of the Kalkarindji LIP; Marshall et al., 2016) resulted in the subsidence of smaller intracratonic basins (Warburton, Ord, Daly and Wiso basins) and the initiation of early Palaeozoic depocentres across what is now Australia's Northern Territory (Lindsay, 2005). The CS is infilled with a succession of Neoproterozoic-Palaeozoic sediments, mostly equatorial carbonates, that provide an excellent record of the metazoan radiation in the early Cambrian (Brasier et al., 1995; Lindsay, 2005; Creveling et al., 2014). Of interest to this study are the Thorntonia Limestone and Arthur Creek formations.

The Georgina Basin is an extensive (325,000km^2) Neoproterozoic to early Palaeozoic intracratonic sedimentary basin in the Australian Northern Territory and Queensland that can be divided into a number of sub-basins (Fig. 5.1; Lindsay, 2002, 2005; Smith et al., 2015). In the early Cambrian Series 2 (~518 – 511Ma) the southern part of the Basin was characterised by depositional hiatus and erosion (Pagès and Schmid, 2016), followed by transgression and the establishment of carbonate deposition. Pagès and Schmid (2016) linked the subsidence of the Mount Isa Block (on the eastern margin of the Georgina Basin) to the opening of an epeiric seaway. To the west of the Georgina Basin the Kalkarindji LIP exists as scattered outcrops of tholeiitic basalt, thickest along the Negri fault line (Glass, 2002; Marshall et al., 2016). The tectonic history of the Georgina Basin is complex, however, Buick et al. (2005) proposed a link between synchronous rifting

located between the Georgina Basin and Amadeus to the south-west, and the emplacement of the Kalkarindji LIP.

Four major Cambrian carbonate formations are developed in the southern Georgina Basin: the Red Heart Dolostone, Thorntonia Limestone, Arthur Creek and Arrinthrunga formations (Fig. 5.2). Core material presented in this study is from three drill holes: CKAD001, NTGS Huc1 and Baldwin 1; all of which were drilled through the Palaeoproterozoic- Palaeozoic succession of the Dulcie Syncline of the south Georgina Basin. Starting with the oldest, the Red Heart Dolostone is the first Palaeozoic carbonate succession in the Georgina Basin and it shows substantial thickness changes across the region (Kruse et al., 2013). It is an archaeocyath-bearing dolostone with variable clastic input. The precise age of archaeocyathan assemblages is problematic, but they likely belong to Cambrian Series 2 (Nicolaides, 1995; Lindsay, 2005). The overlying Thorntonia Limestone is a platform carbonate which is widespread across the Georgina Basin and lies discomformably upon the Red Heart Dolostone (Lindsay, 2005). It is predominantly a dark grey carbonate mudstone with occasional fossil hash beds (hyoliths, agnostid trilobites, rare brachiopods; Laurie 2005). Chert nodules and other textural features suggest evaporitic conditions at times (Lindsay, 2005) and Ambrose et al. (2001) describe it as a shallow, peritidal to subtidal transgressive unit spanning the Ordian and early Templetonian (Fig. 5 2; ~509 – 506Ma). The succeeding Arthur Creek Formation rests on a phosphatic hardground/karstic surface on top of the Thorntonia Limestone and marks the onset of anoxic conditions in the basin. The base of the formation is a dark grey to black, laminated pyritic shale with a very high organic content (Lindsay, 2005). The basal Arthur Creek "Hot Shale" is considered a world-class petroleum source rock and grades upward into a dark grey, laminated carbonate (Nicolaides, 1995). Finally, the Arrinthrunga Formation is the youngest formation penetrated by any of the cores in this study; it is a mixed carbonate and siliciclastic unit which sits conformably on top the Arthur Creek Formation (Kruse, 2013).

5.4 Methods

All analysis was completed on rock chips from core material collected at the Northern Territory Geological Survey (NTGS) Core Repository in Alice Springs, NT. Carbon and sulphur content was analysed from bulk rock powders at the University of Leeds on a LECO® SC-144DR Dual Range carbon and sulphur analyser. Total organic carbon was calculated through mass lost following digestion using 10% hydrochloric acid and measured on the LECO® SC-144DR at the University of Leeds. Inorganic carbon isotope values were measured from whole-rock powders at the GeoZentrum Nordbayern, FAU Erlangen-Nuremberg, Germany, where carbon dioxide was prepared via reaction with phosphoric acid at 70°C using a Gasbench II preparation system and calcite carbon ($^{13}C/^{12}C$) isotope values measured by a ThermoFisher Delta V plus mass spectrometer in continuous flow mode.

Total Hg content was measured from whole-rock powders at Amherst College (Massachusetts, USA) by D. Jones using a Teledyne Leeman Labs Hydra II$_C$ mercury analyser.

5.5 Results

5.5.1 CKAD001:

Drill hole CKAD001 intersects (in stratigraphic order descending down-hole) the Arthur Creek Formation, Thorntonia Limestone and the Red Heart Dolostone. For the purpose of this study, 104.98 m (between depths 498.02-603.00m) was sampled at a sub-metre resolution (Table 5.1, Fig. 5.3).

The base of the Thorntonia Limestone is placed at this gradational transition from carbonate to brown carbonate sandstone and breccia at 590m. Underlying this, the Red Heart Dolostone is a cream/brown carbonate sandstone. The top of the Thorntonia Limestone is marked by vuggy carbonates suggesting karstification/ evaporitic conditions. The Thorntonia exhibits common convoluted laminae, stylolite dissolution horizons and ball and pillow compaction structures are noted, as well as microbial laminations, breccia, pebble conglomerates and pyritic intervals. Extremely high (up to 35 wt%) TOC values in the Thorntonia Limestone depict oil shows throughout this core, exemplified by TOC peaks between ~550-575 m. A ~23.5m thick
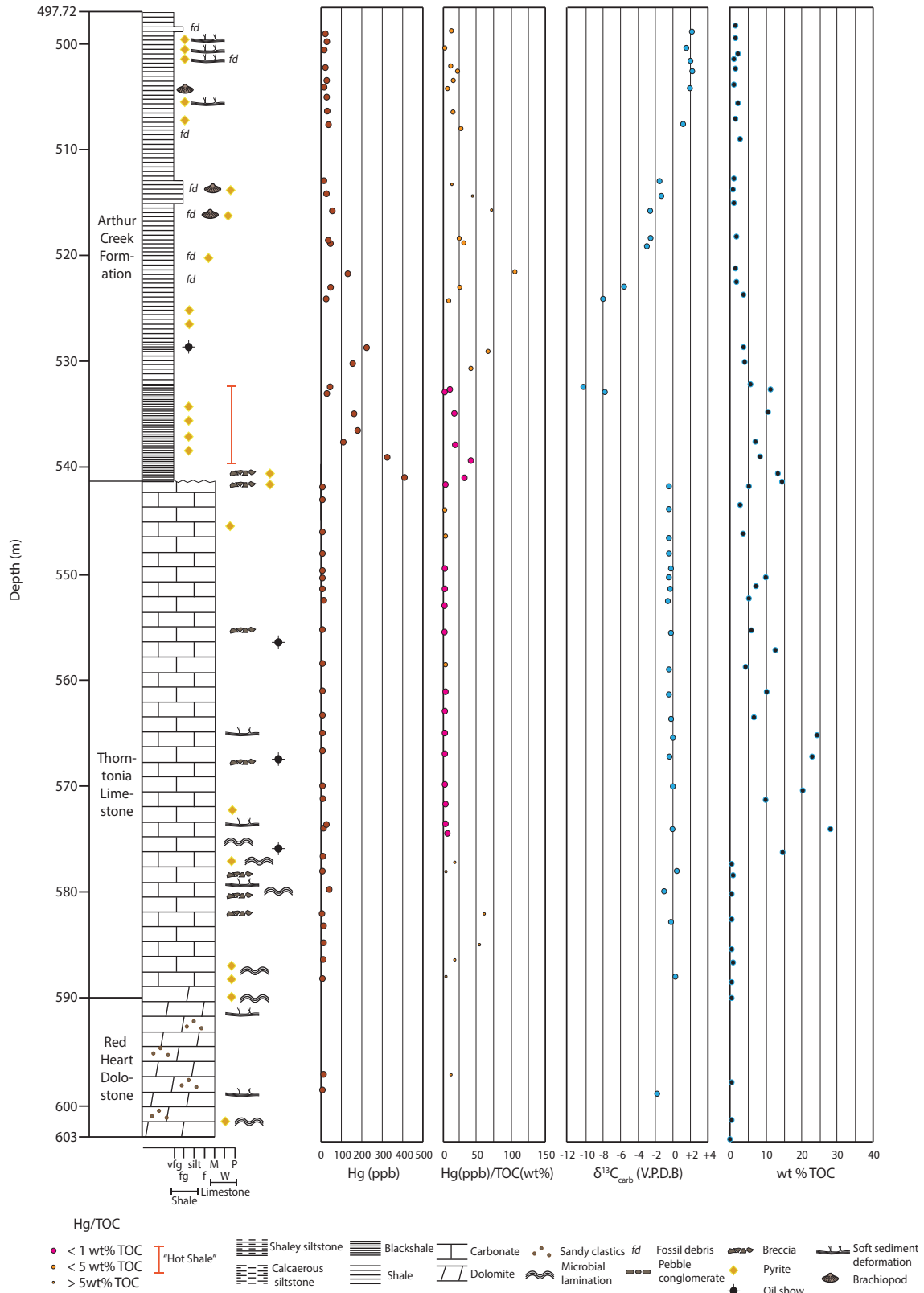
Figure 5.3: Stratigraphic log, δ¹³C, Hg, Hg(ppb)/TOC(wt%) and TOC (wt%). data for drill core CKAD001

pyritic black shale with high TOC wt % (up to ~15 wt %) and hydrocarbon shows marks the base of the Arthur Creek Formation and is interpreted as the Arthur Creek "Hot Shale" (Fig 5.3; Lindsay et al., 2005). The age of the Arthur Creek Formation is given by trilobite occurrences (Laurie, 2014). The presence of the agnostid trilobite *Xystridura*? *templetonensis* (516.16m-516.55m and 518.0m-518.3m) indicates the early to middle Templetonian, and the presence of agnostid trilobite *Pentagnostus shergoldi* (517.75m and 521.46.m- 521.6 m) indicates a middle Templetonian age (Fig. 5.2; Laurie, 2014).

Inorganic carbon isotope record

The $\delta^{13}C_{carb}$ record from CKAD001 (Fig. 5.3) shows two broad characteristics; stable values around 0‰ for much of the Thorntonia Limestone followed by a negative excursion in the base of the Arthur Creek Formation where values drop abruptly from to ~-10‰ before showing a steady positive shift back to values of ~2‰ (Fig. 5.3). Cross plotting of $\delta^{13}C_{carb}$ and $\delta^{18}O_{carb}$ (Fig. 5.5), used to assess for any diagenetic alteration, shows clustering of most samples with the most negative $\delta^{13}C$ samples sitting as outliers (as circled in yellow).

Hg concentrations and Hg/TOC ratios

Hg concentrations from CKAD001 (Fig. 5.3) also show two main trends. Background concentrations of <10 ppb prevail throughout most of the Thorntonia Limestone. Above this, Hg concentrations are very low (<10ppb) in the basal sample from the Arthur Creek Formation, but then rise abruptly to the highest recorded value (410 ppb Hg at 540 m). Hg concentrations remain high for around ~20m (spanning core depth ~540m – 520m) in the black shales and then return to low background levels.

When normalised to TOC, two enrichment intervals can be seen, one in the basal Thorntonia Limestone (~580 – 590 m) and another in the Arthur Creek Formation (530m – 510m) (Fig. 5.3) with low, stable values at other levels. The peak Hg values in the basal black shales of the Arthur Creek Formation become less distinct when normalised to TOC, with the peak

Hg/TOC values occurring a considerable distance above the base of the Formation at ~520 m (Fig. 5.3) before ratios return to background levels.

5.5.2 NTGS Huc 1

NTGS Huc 1 penetrated the Arthur Creek and the underlying Errarra formations. The latter formation is an archaeocyath-bearing dolomite equivalent to the Red Heart Dolostone which is conformably overlain by the Arthur Creek Formation (Laurie and Shergold, 1985), which is predominantly a calcareous siltstone (with abundant pyrite and rare brachiopods at ~220 m), with intermittent thin limestone and dolomite horizons.

Inorganic carbon isotope record

The $\delta^{13}C_{carb}$ values from NTGS Huc 1 exhibit two clear trends (Fig. 5.4). At the base of the section, in the upper Errarra Formation, $\delta^{13}C_{carb}$ values are initially ~-1‰ before base of the Arthur Creek Formation is marked by an abrupt negative shift from ~-1‰ to ~-9‰ (8‰ negative shift) at the base of the Arthur Creek Formation. This short, sharp, negative excursion occurs in dark, pyritic, microbial-laminated calcareous shale (Fig. 5.4). Above this negative excursion, $\delta^{13}C$ values return to +2‰ before beginning a gradual decline to ~-3‰ at the top of the core. Cross plots of $\delta^{13}C_{carb}$ and $\delta^{18}O_{carb}$ show little evidence for a strong correlation between the two datasets (Fig. 5.5), except for the lowest two $\delta^{13}C$ values (circled in yellow).

5.5.3 Baldwin 1

Baldwin 1 intersected the Arrinthrunga, Arthur Creek, Thorntonia Limestone and the Red Heart Dolostone formations (Fig. 5.6). The Red Heart Dolostone is primarily a stylolitic, mottled, brecciated vuggy dolostone with thin mudstone interbeds. Although precise age correlation to other sections worldwide is difficult, the presence of small shelly fossils and archaeocyath assemblages suggests correlation with the Siberian Atdabanian, global Stage 3 (Fig. 5.6; Laurie and Shergold, 1985; Kruse et al., 2013). The fossil assemblage exhibits strong faunal association with other basins of the CS and Kruse et al. (2013) posited that, during the Cambrian Stage 3, this fauna lived in an intracontinental basin in marginal
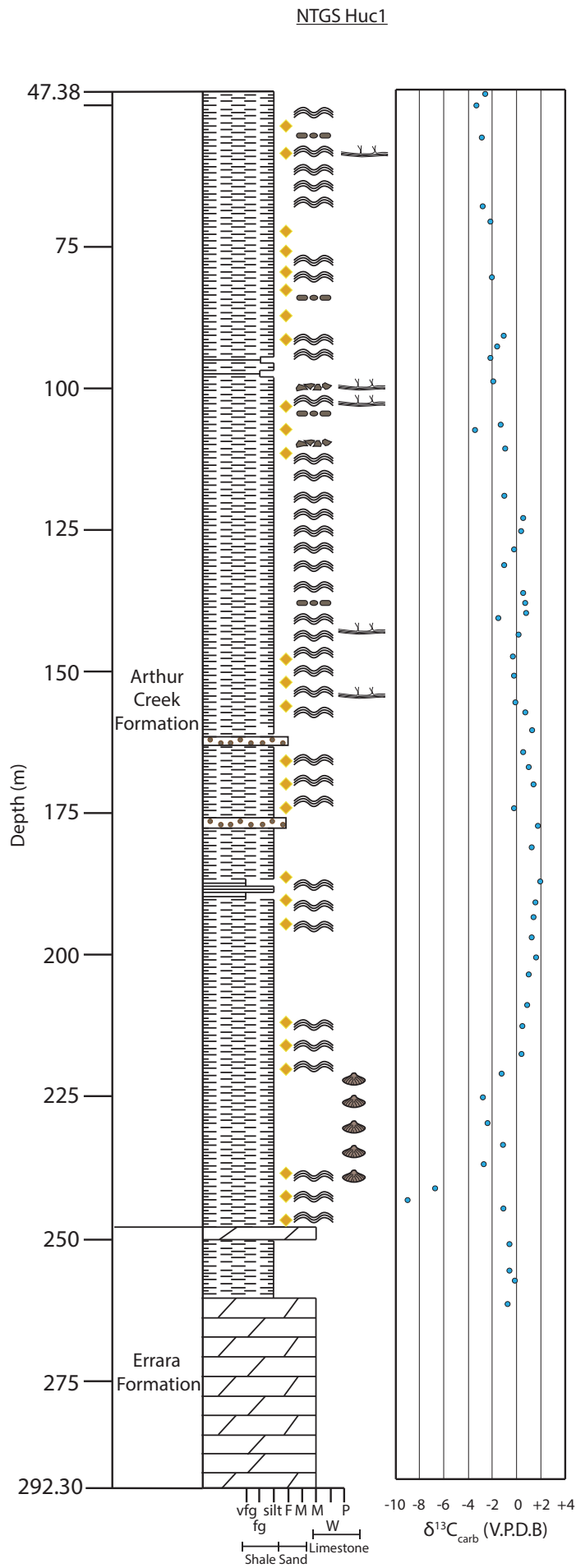
Figure 5.4: Stratigraphic log and δ¹³C data for the NTGS Huc 1 core.

See Fig. 5.3 for key.

marine environments as evidenced by calci-microbial archaeocyathan reefs. The occurrence of *Pentagnostus shergoldi* in the basal Arthur Creek Formation indicates a mid- late Templetonian age at this level in the core (Fig. 5.2).

Inorganic carbon isotope record

The Baldwin 1 $\delta^{13}C_{carb}$ curve form the upper Red Heart Dolostone through to the Arthur Creek Formation (Fig. 5.6) exhibits a very similar trend to CKAD001 and NTGS Huc 1. The upper Red Heart Dolostone has $\delta^{13}C$ values of around -1 to +1‰, and values increase slightly in the Thorntonia Limestone to 0 – +2‰. Again, at the base of the Arthur Creek Formation, in a pyritic black shale, an abrupt and short lived negative excursion sees
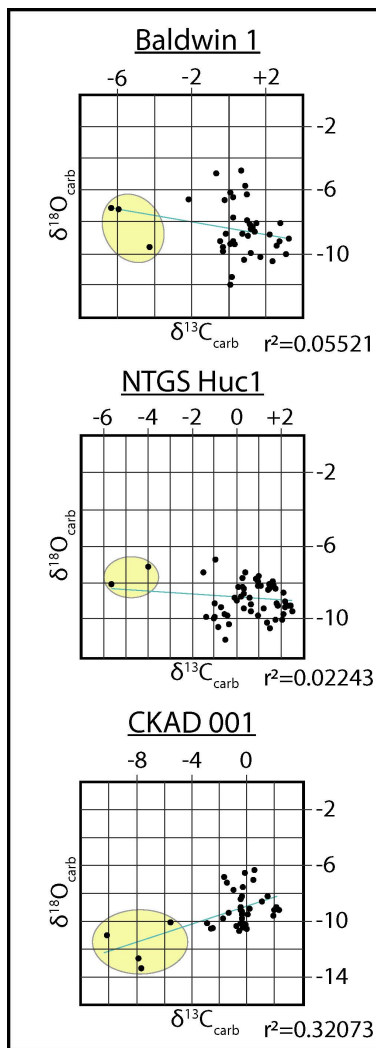
Figure 5.5: $\delta^{13}C$ and $\delta^{18}O$ cross-plots with linear trend-line and r^2 values for individual drill cores.
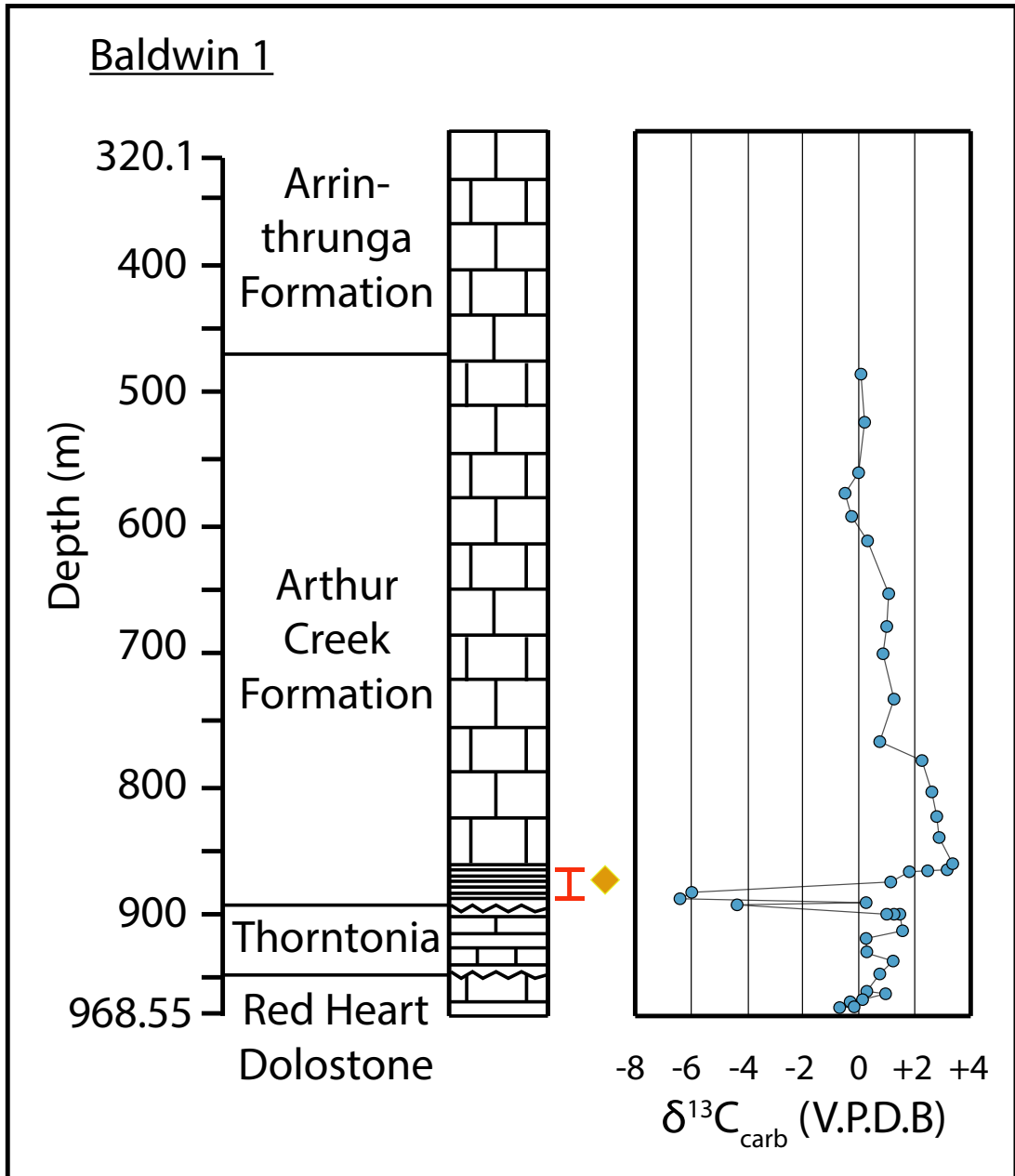
Figure 5.6: Stratigraphic log and δ^{13}C data for the Baldwin 1 core. See Fig. 5.3 for key.

values drop from ~+1‰ to -6‰. Above this δ^{13}C values recover to ~+3‰ and then exhibit a broad negative downturn to 0‰ at the top of the Arthur Creek Formation. Cross-plots of $\delta^{13}C_{carb}$ and $\delta^{18}O_{carb}$ show little evidence of covariation in the majority of samples, though the lowest δ^{13}C vales sit outside the main cluster of data points (Fig. 5.5).

5.6 Discussion

5.6.1 ROECE In Australia

The ROECE excursion is known from the Series 2 – Series 3 boundary in NW Scotland, China, the western USA (Montañez et al., 2000; Zhang et al., 2015; Fan et al., 2011; Faggetter et al., 2016; 2017; Chang et al., 2017; Ren et al., 2017; Schmid, 2017). It has also been reported from the Amadeus Basin of Australia (located to the southwest of the Georgina Basin), where there is an abrupt ~-2.5‰ $\delta^{13}C_{carb}$ shift within the upper part of the Chandler Formation. This evaporitic shallow-marine carbonate is reported to be of upper Ordian age and thus straddles the Series 2 – Series 3 boundary (Schmid, 2017). Our results from the Georgina Basin cores show stable $\delta^{13}C$ values (~0‰) throughout the Thorntonia Limestone (Figs. 5.3, 5.4, 5.6) and a major negative $\delta^{13}C$ shift in the Arthur Creek Formation (between -7‰ and -10‰) of around double the magnitude usually reported for the ROECE.

Two possibilities can be drawn from these new data. Firstly, that ROECE is absent in the Georgina Basin (potentially at the level of the hiatus represented by the karst surface at the top of the Thorntonia Limestone) and the carbon isotope excursion is entirely the product of anoxic diagenesis in the black shales of the Arthur Creek Formation. Secondly, the Ordian-Templetonian strata of the lower Arthur Creek Formation (Fig. 5.2) correlates with the upper Chandler Formation of the Amadeus Basin (Schmid, 2017) and the record of ROECE has been exaggerated by addition of isotopically light carbon produced during sulphate-reduction zone diagenesis. Diagenetic alteration of a pre-existing isotopically light organic carbon reservoir (basal "Hot Shale") is supported by the observation that, in Baldwin 1 and CKAD001, this abrupt excursion occurs within the TOC rich (<15 wt %) intensely pyritic, anoxic, black shale of the lower Arthur Creek Formation (Lindsay et al., 2005). In NTGS Huc 1, the excursion occurs in a dark, pyritic, microbially-laminated calcareous shale and/or black shales in all cores. The correspondence between light $\delta^{13}C$ values and anoxic facies is not clear cut because the latter cover a greater span in the cores than the isotope excursion. Thus, in Baldwin 1, the return to positive $\delta^{13}C$ values occurs in the upper part of the black shale in the base of the Arthur Creek Formation,

indicating that facies variations alone are not responsible for the isotopic excursion. Thus, we consider ROECE to be recorded within a transgressive episode within the Georgina Basin that saw the wide spread of anoxic facies. The development of microbially-laminated anoxic facies suggests anoxia developed in shallow waters as well as the deeper water conditions recorded by black shales.

Above the base of the Arthur Creek Formation $\delta^{13}C$ values exhibit a comparable trend across our cores. $\delta^{13}C$ values return to ~+2, creating a peak interpreted as an Ordian – early Templetonian event. This positive excursion correlates well across much of the Centralian Superbasin (Lindsay et al., 2005). Throughout the rest of NTGS Huc 1 and Baldwin 1, where a significant portion of the Arthur Creek Formation is recorded, values show a steady shift towards lighter values. NTGS Huc 1 displays two horizons with small, sharp negative excursions in line with microbially laminated strata, suggesting that diagenetic alteration to light $\delta^{13}C$ values may have occurred periodically throughout the Arthur Creek Formation.

5.6.2 Mercury anomalies and volcanism

Lithological variations can also control Hg enrichment, especially due to its affiliation with organic matter and sulphides. Mercury enrichment in CKAD001 occurs in the basal "Hot Shale" in the lower 10m of the Arthur Creek Formation raising the possibility that this signal is purely controlled by local lithology. In anoxic/ sulphidic pore water or sediment, dissolved inorganic Hg has a strong affinity with sulphide; sulphate reducing bacteria and methanogens, which complex inorganic Hg as HgS, produce bioavailable methylmercury (MeHg; Benoit et al., 1999; Ranchou-Peyrouse, et al., 2009). Compounding this, Hg adsorbs to, and is immobilised by iron sulphides (Bowyer et al., 2008). In addition, HgS is a relatively insoluble and immobile form of Hg and is therefore considered a major sink of Hg in modern sediments (Barnett and Turner, 2001; Bowyer et al., 2008). While this interaction with sulphidic pore-water and pyrite may account for the accumulation and obvious Hg enrichment in the lower Arthur Creek Formation, it does not explain the source.

When normalised to TOC (Fig. 5.3), the shape of the excursion changes and shows peak values straddling the transition from lowermost

black shales to the grey shales of the upper part of the Arthur Creek Formation. Furthermore, an additional Hg/TOC peak is seen lower in the core, in the organic-poor limestones from the lower part of the Thorntonia Limestones (Fig. 5 3). Thus, we consider that these peaks record a primary signal of intense environmental Hg loading, possibly related to volcanic activity and may therefore indicate two eruptive phases of the Kalkarindji Province. If the carbon isotope excursion at the base of the Arthur Creek Formation is the ROECE, then it indicates that these volcanic episodes straddle the Series 2 – Series 3 boundary. The current state of data makes it difficult to directly implicate volcanism in the trilobite extinctions because the precise level of the losses in Australia has yet to be determined. The crisis is better known from the Great Basin, USA, where it coincides with the ROECE (Chapter 4; Faggetter et al. 2017). This suggests that the mass extinction occurred during the Kalkarindji eruptions, albeit during an interlude in the eruptive history indicated by the Australian Hg record.

5.7   Conclusion

Carbon isotope values from three drill cores (CKAD001, Huc 1and Baldwin 1) in the Georgina Basin in central Australia, exhibit a major, negative carbon isotope excursion (between -7 and -10 ‰) in the basal part of the Arthur Creek Formation that is interpreted to be ROECE. The excursion occurs in a range of anoxic facies encountered in the basal part of the formation and light carbon, derived during anoxic diagenesis, may have helped exacerbate the magnitude of ROECE in these cores.

Evidence for the eruption interval of the Kalkarindji flood basalts in northern Australia has been sought from the cores using Hg and Hg/TOC records from the CKAD001 core. These reveal an enrichment of Hg in limestones of the basal Thorntonia Limestones and in organic-rich levels at the base of the Arthur Creek Formation. Normalising for TOC, shows there are two distinct peaks of Hg/TOC either side of the ROECE suggesting two possible phases of Kalkarindji eruptions before and after the Series 2 – Series 3 boundary. More information is needed on trilobite extinction levels in the Australian record to better evaluate the link between the phenomena

of eruptions, transgression-with-anoxia and mass extinction, although all phenomena show a reasonably close coincidence.

5.8   References

Ambrose, G. J., Kruse, P. D., Putnam, P. E. (2001). Geology and hydrocarbon potential of the southern Georgina Basin, Australia. *The APPEA Journal*, *41*(1), 139-163.

Barnett, M. O., Turner, R. R. (2001). Bioaccessibility of mercury in soils. *Soil and Sediment Contamination*, *10*(3), 301-316.

Benoit, J. M., Gilmour, C. C., Mason, R. P., Heyes, A. (1999). Sulfide controls on mercury speciation and bioavailability to methylating bacteria in sediment pore waters. *Environmental Science & Technology*, *33*(6), 951-957.

Bower, J., Savage, K. S., Weinman, B., Barnett, M. O., Hamilton, W. P., Harper, W. F. (2008). Immobilization of mercury by pyrite (FeS 2). *Environmental Pollution*, *156*(2), 504-514.

Brasier, M. D., Corfield, R. M., Derry, L. A., Rozanov, A. Y., Zhuravlev, A. Y. (1994). Multiple δ13C excursions spanning the Cambrian explosion to the Botomian crisis in Siberia. *Geology*, *22*(5), 455-458.

Bryan, S. E., Peate, I. U., Peate, D. W., Self, S., Jerram, D. A., Mawby, M. R., Miller, J. A. (2010). The largest volcanic eruptions on Earth. *Earth-Science Reviews*, *102*(3), 207-229.

Buick, I. S., Hand, M., Williams, I. S., Mawby, J., Miller, J. A., Nicoll, R. S. (2005). Detrital zircon provenance constraints on the evolution of the Harts Range Metamorphic Complex (central Australia): links to the Centralian Superbasin. *Journal of the Geological Society*, *162*(5), 777-787.

Bultitude, R.J., (1972). The Geology and Petrology of the Helen Springs, Nutwood Downs, and Peaker Piker Volcanics. *Bur. Miner. Resour. Geol. Geophys.* 1972/74.

Chang, C., Hu, W., Wang, X., Yu, H., Yang, A., Cao, J., Yao, S. (2017). Carbon isotope stratigraphy of the lower to middle Cambrian on the

eastern Yangtze Platform, South China. *Palaeogeography, Palaeoclimatology, Palaeoecology*, *479*, 90-101.

Creveling, J. R., Johnston, D. T., Poulton, S. W., Kotrc, B., März, C., Schrag, D. P., Knoll, A. H. (2014). Phosphorus sources for phosphatic Cambrian carbonates. *Geological Society of America Bulletin*, *126*(1-2), 145-163.

Cutovinos, A., Beier, P.R., Kruse, P.D., Abbot, S.T., Dunster, J.N., Brescianini, R.F. (2002). Limbunya, Northern Territory (Second Edition), 1:250 000 geological map series and explanatory notes, SE 52-07. Northern Territory Geological Survey, Darwin and Alice Springs.

Fan, R., Deng, S., Zhang, X. (2011). Significant carbon isotope excursions in the Cambrian and their implications for global correlations. *Science China Earth Sciences*, *54*(11), 1686-1695.

Font, E., Adatte, T., Sial, A. N., de Lacerda, L. D., Keller, G., Punekar, J. (2016). Mercury anomaly, Deccan volcanism, and the end-Cretaceous mass extinction. *Geology*, *44*(2), 171-174.

Gill, B. C., Lyons, T. W., Young, S. A., Kump, L. R., Knoll, A. H., Saltzman, M. R. (2011). Geochemical evidence for widespread euxinia in the Later Cambrian ocean. *Nature*, *469*(7328), 80-83.

Glass, L. M. (2002). Petrogenesis and geochronology of the north Australian Kalkarinji low-Ti continental flood basalt province. Doctoral Thesis, The Australian National University, December 2002.

Glass, L. M., Phillips, D. (2006). The Kalkarindji continental flood basalt province: A new Cambrian large igneous province in Australia with possible links to faunal extinctions. *Geology*, *34*(6), 461-464.

Gong, Q., Wang, X., Zhao, L., Grasby, S. E., Chen, Z. Q., Zhang, L., Li, Z. (2017). Mercury spikes suggest volcanic driver of the Ordovician-Silurian mass extinction. *Scientific Reports*, *7*.

Grasby, S.E., Beauchamp, B., Bond, D.P.G., Wignall, P.B., Sanei, H. (2016). Mercury anomalies associated with three extinction events (Capitanian crisis, latest Permian extinction and the Smithian/Spathian extinction) in NW Pangea. *Geological Magazine,* 153, 285-297.

Hough, M.L., Shields, G.A., Evins, L.Z., Strauss, H., Henderson, R.A., Mackenzie, S. (2006). A major Sulphur isotope evnt at *c.* 510 Ma: a possible anoxia-extinction-volcanism connection during the Early-Middle Cambrian transition? *Terra Nova,* 18, 257-263.

Hurtgen, M. T., Pruss, S. B., Knoll, A. H. (2009). Evaluating the relationship between the carbon and sulfur cycles in the later Cambrian ocean: an example from the Port au Port Group, western Newfoundland, Canada. *Earth and Planetary Science Letters*, *281*(3), 288-297.

Jiang, S. Y., Pi, D. H., Heubeck, C., Frimmel, H., Liu, Y. P., Deng, H. L., Yang, J. H. (2009). Early Cambrian ocean anoxia in south China. *Nature*, *459* (7248), E5-E6.

Kruse, P. D., Dunster, J. N., Munson, T. J., Ahmad, M., Munson, T. J. (2013). Chapter 28: Georgina Basin. *Ahmad, M. and Munson, TJ (compilers) Geology and Mineral Resources of the Northern Territory. Northern Territory Geological Survey, Special Publication*, *5*. Retrieved from:
http://www.geoscience.nt.gov.au/gemis/ntgsjspui/handle/1/81446

Laurie, J. R., Shergold, J. H. (1985). Phosphatic organisms and the correlation of Early Cambrian carbonate formations in central Australia. *BMR Journal of Australian Geology & Geophysics*, *9*, 83-89.

Laurie, J. R. (2014). Macrofossils from CKAD001, southern Georgina Basin, Northern Territory. *Northern Territory Geological Survey Reports.*

Lindsay, J. F., Kruse, P. D., Green, O. R., Hawkins, E., Brasier, M. D., Cartlidge, J., Corfield, R. M. (2005). The Neoproterozoic–Cambrian record in Australia: a stable isotope study. *Precambrian Research*, *143*(1), 113-133.

Lindsay, J. F. (2002). Supersequences, superbasins, supercontinents– evidence from the Neoproterozoic–Early Palaeozoic basins of central Australia. *Basin Research*, *14*(2), 207-223.

Marshall, P. E., Widdowson, M., Murphy, D. T. (2016). The Giant Lavas of Kalkarindji: rubbly pāhoehoe lava in an ancient continental flood basalt province. *Palaeogeography, Palaeoclimatology, Palaeoecology*, *441*, 22-37.

Montañez, I. P., Osleger, D. A., Banner, J. L., Mack, L. E., Musgrove, M. (2000). Evolution of the Sr and C isotope composition of Cambrian oceans. *GSA today*, *10*(5), 1-7.

Munson, T., Kruse, P., Ahmad, M. (2013). Chapter 22: Centralian Superbasin. *Geology and mineral resources of the Northern Territory compiled by M Ahmad and TJ Munson: Northern Territory Geological Survey, Darwin, Northern Territory, Special Publication*, *5*, 22-1.

Nicolaides, S. (1995). Origin and modification of Cambrian dolomites (Red Heart Dolomite and Arthur Creek Formation), Georgina Basin, central Australia. *Sedimentology*, *42*(2), 249-266.

Ogg, J. G., Ogg, G., Gradstein, F. M. (2016). A Concise Geologic Time Scale: 2016. *Elsevier*.

Pagès, A., Schmid, S. (2016). Euxinia linked to the Cambrian Drumian carbon isotope excursion (DICE) in Australia: Geochemical and chemostratigraphic evidence. *Palaeogeography, Palaeoclimatology, Palaeoecology*, *461*, 65-76.

Palmer, A. R. (1998). Terminal early Cambrian extinction of the Olenellina: documentation from the Pioche Formation, Nevada. *Journal of Paleontology*, *72*(4), 650-672.

Payne, J. L., Lehrmann, D. J., Wei, J., Orchard, M. J., Schrag, D. P., Knoll, A. H. (2004). Large perturbations of the carbon cycle during recovery from the end-Permian extinction. *Science*, *305*(5683), 506-509.

Percival, L.M.E., Witt, M.L.I., Mather, T.A., Hermoso, M., Jenkyns, H.C., Hesselbo, S.P., Al-Suwaidi, A.H., Storm, M.S., Xu, W., Ruhl, M. (2015). Globally enhanced mercury deposition during the end-Pliensbachian extinction and Toarcian OAE: A link to the Karoo-Ferrar Large Igneous Province. Earth ad Planetary Science Letters 428, 267-280.

Percival, L. M., Ruhl, M., Hesselbo, S. P., Jenkyns, H. C., Mather, T. A., Whiteside, J. H. (2017). Mercury evidence for pulsed volcanism during the end-Triassic mass extinction. *Proceedings of the National Academy of Sciences*, *114*(30), 7929-7934.

Poulton, S. W., Canfield, D. E. (2005). Development of a sequential extraction procedure for iron: implications for iron partitioning in continentally derived particulates. *Chemical Geology*, *214*(3), 209-221.

Ranchou-Peyruse, M., Monperrus, M., Bridou, R., Duran, R., Amouroux, D., Salvado, J. C., Guyoneaud, R. (2009). Overview of mercury methylation capacities among anaerobic bacteria including representatives of the sulphate-reducers: implications for environmental studies. *Geomicrobiology Journal*, *26*(1), 1-8.

Ren, Y., Zhong, D., Gao, C., Liang, T., Sun, H., Wu, D., Zheng, X. (2017). High-resolution carbon isotope records and correlations of the lower Cambrian Longwangmiao formation (stage 4, Toyonian) in Chongqing, South China. *Palaeogeography, Palaeoclimatology, Palaeoecology*.

Saltzman, M. R., Ripperdan, R. L., Brasier, M. D., Lohmann, K. C., Robison, R. A., Chang, W. T., Runnegar, B. (2000). A global carbon isotope excursion (SPICE) during the Late Cambrian: relation to trilobite extinctions, organic-matter burial and sea level. *Palaeogeography, Palaeoclimatology, Palaeoecology*, *162*(3), 211-223.

Sanei, H., Grasby, S., Beauchamp, B. (2012). Latest Permian mercury anomalies. Geology 40, 63–66. http://dx.doi.org/10.1130/G32596.1.

Scotese, C.R. (2016). PALEOMAP PaleoAtlas for GPlates and the PaleoData Plotter Program,PALEOMAP Project, http://www.earthbyte.org/paleomappaleoatlas-for-gplates/

Schmid, S. (2017). Chemostratigraphy and palaeo-environmental characterisation of the Cambrian stratigraphy in the Amadeus Basin, Australia. *Chemical Geology*, *451*, 169-182.

Smith, T., Kelman, A. P., Nicoll, R., Edwards, D., Hall, L., Laurie, J., Carr, L. (2013). An updated stratigraphic framework for the Georgina Basin, NT and Queensland. *The APPEA Journal*, *53*(2), 487-487.

Southgate, P. N., Shergold, J. H. (1991). Application of sequence stratigraphic concepts to Middle Cambrian phosphogenesis, Georgina Basin, Australia. *Journal of Australian Geology and Geophysics*, *12*, 119-144.

Thibodeau, A.M., Ritterbush, K., Yager, J.A., West, A.J., Ibarra, Y., Bottjer, D.J., Berelson, W.M., Bergquist, B.A., Corsetti, F.A. (2016). Mercury anomalies and the timing of biotic recovery following the end-Triassic mass extinction. Nature Communications 7:11147.

Veevers, J.J. (2001). Atlas of billion-year old earth history of Australia and neighbours in Gondwanaland. *GEMOC Press*, Sydney, Australia.

Walter, M. R., Veevers, J. J., Calver, C. R., Grey, K. (1995). Neoproterozoic stratigraphy of the centralian superbasin, Australia. *Precambrian Research*, *73*(1-4), 173-195.

Walter, M. R., Veevers, J. J. (1997). Australian Neoproterozoic palaeogeography, tectonics, and supercontinental connections. *AGSO Journal of Australian Geology and Geophysics*, *17*, 73-92.

Zhang, W., Shi, X., Jiang, G., Tang, D., Wang, X. (2015). Mass-occurrence of oncoids at the Cambrian Series 2–Series 3 transition: Implications for microbial resurgence following an Early Cambrian extinction. *Gondwana Research*, *28*(1), 432-450.

Zhu, M. Y., Zhang, J. M., Li, G. X., Yang, A. H. (2004). Evolution of C isotopes in the Cambrian of China: implications for Cambrian subdivision and trilobite mass extinctions. *Geobios*, *37*(2), 287-301.

Zhu, M. Y., Babcock, L. E., Peng, S. C. (2006). Advances in Cambrian stratigraphy and paleontology: integrating correlation techniques, paleobiology, taphonomy and paleoenvironmental reconstruction. *Palaeoworld*, *15*(3), 217-222.

Zhuravlev, A. Y., Wood, R. A. (1996). Anoxia as the cause of the mid-Early Cambrian (Botomian) extinction event. *Geology*, *24*(4), 311-314.

6. Chapter 6- Discussion, conclusions and further work

This thesis concludes with a discussion of the main findings of the chapters, addresses the questions posed in Chapter 1 and ultimately poses further research questions stemming from the trajectory of these conclusions.

The overall aim of this thesis was an attempt at answering the following research questions, and reconciling data stemming from these hypotheses;

1. What environmental change is seen in marine strata recording the Series 2 – Series 3 boundary? What was the severity and does it coincide with trilobite extinction?
2. What role did the eruption of the Kalkarindji large igneous province play in trilobite extinctions and can evidence for these eruptions be detected using mercury concentrations in far-field sedimentary successions?
3. What is the temporal relationship between carbon cycle perturbations and trilobite extinction?
4. Does sea level fall coincide with the ROECE and/or extinction?

6.1. Research question 1: What environmental change is seen in marine strata recording the Series 2 – Series 3 boundary? What was the severity and does it coincide with trilobite extinction?

Cambrian Series 2 – Series 3 boundary strata are known from all Cambrian continents, including: Laurentia (e.g. Palmer, 1998; Montañez, 2000; Webster et al., 2008; Faggetter et al., 2016, 2017), Gondwana (e.g. Álvaro et al., 2000; Hough et al., 2006; Geyer et al., 2015; Schmid, 2017) China (e.g. Quo et al., 2014; Wang et al., 2015; Chang et al., 2017; Ren et al., 2017) and Baltica (e.g. Geyer et al., 2011, 2017). This study presents geological field data from Laurentian field sites (NW Scotland and SW USA; Chapters 2 and 3, Faggetter, 2016; 2017) and the relatively poorly known eastern margin of Gondwana (Chapters 4 and 5). Despite the geographically

distant locations, all sections are predominately shallow marine carbonate or mixed siliciclastic-carbonate facies (Fig. 6.1).

6.1.1. The Laurentian record

The two main Laurentian study areas (NW Scotland and SW USA) were positioned on a broad, shallow marine carbonate platform developed on the periphery of the continent (Fig. 6.1). The strata belong to the Sauk Supersequences which record deposition during the late Neoproterozoic-early Palaeozoic (Sloss, 1963). In both locations close to the Series 2 – Series 3 boundary there is a transition from dominantly siliciclastic deposition (Ardvreck Group, Scotland; Zabriskie Quartzite, USA) to a prolonged period of carbonate production (Durness Group, Scotland; Carrara and Bonanza King formations, USA). This major lithological change occurs at the boundary between the Sauk I and Sauk II supersequences (to be discussed further in 6.4; Sloss, 1963; Prave, 1992; Keller et al., 2012; Morgan et al., 2012; Raine and Smith, 2012; Faggetter et al., 2016, 2017), pre-dating the Series 2 – Series 3 boundary in the SE USA, and post-dating it in NW Scotland (Fig. 6.1).

In Scotland, the Series 2 – Series 3 boundary is placed at the contact between the Ardvreck and Durness groups (Fig. 2.1); the Salterella Grit Member of the An t-Sròn Formation marks the upper most Ardvreck Group and the Ghrudaidh Formation the basal Durness Group (Fig. 6.1). Chapter 2 reports new observations that conditions immediately after the Series 2 – Series 3 boundary reflect a shift from tidal sandbank facies (*Skolithos* cross bedded quartz arenite of An t-Sròn Formation) to a lagoonal environment with an abundance of halite and small pyrite framboids in a dark dolomicrite (basal Ghrudaidh Formation; Fig. 2.2). The pyrite framboid size distribution analysis shows a dysoxic distribution- suggesting a restricted, evaporitic lagoonal setting with low-oxygen conditions in the base of the Ghrudaidh Formation. This marks a prominent shift away from the oxygenated, well bioturbated facies of the preceding An t-Sròn Formation, and a transition to dysoxic lagoonal facies in the basal Cambrian Series 3. Dysoxia appears to be a regional manifestation of shelf heterogeneity as
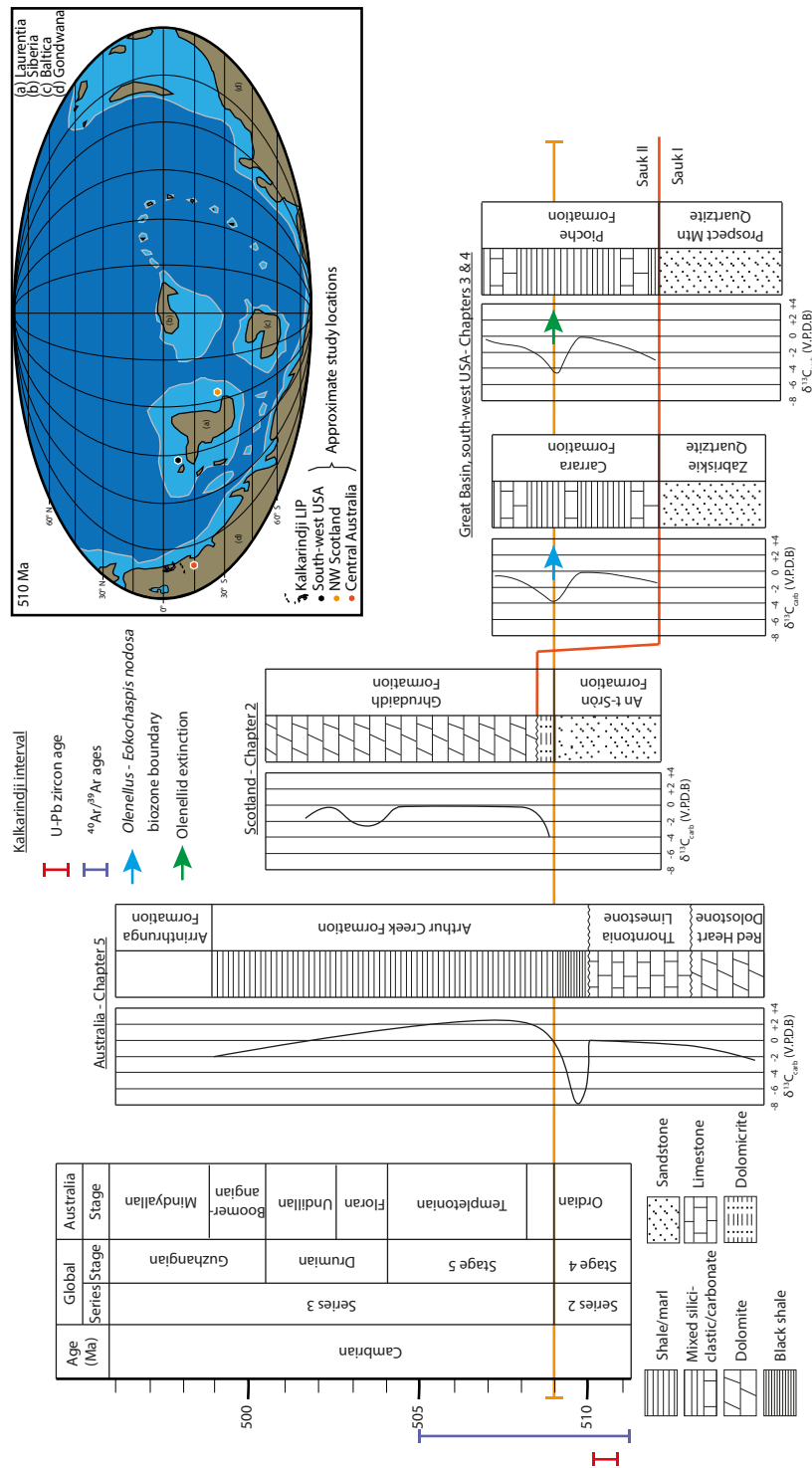
Figure 6.1: Schematic correlation of thesis regions against global Cambrian chronological timescale (Ogg et al., 2016); including individual δ13C data from each chapter, correlation of Sauk I/ Sauk II boundary, Series 2 – Series 3 boundary and extinction horizon, Kalkarindji ages (U-Pb from Jourdan et al., 2014 and 40Ar/39Ar date from Glass and Phillips, 2006) and global Cambrian palaeogeography (Scotese, 2016).

restricted facies are not well developed in other sections in NW Scotland (i.e. at Ardvreck Castle location, Fig. 2.2). Above the Series 2 – Series 3 boundary clastic input diminishes (showing only occasional aoelian quartz grain horizons) and vuggy, burrow mottled carbonate and dolomite dominate the Durness Group. This is interpreted to indicate an increasingly distal aoelian hinterland developed adjacent to marine environments in the Durness Group, a modern analogy could be drawn between this succession and the Namib Desert developed adjacent to the Atlantic coast, Namibia.

Scottish successions contain well preserved strata recording the Cambrian Series 2 – Series 3 boundary exhibiting the shift from well oxygenation open marine sandstones to low oxygen, restricted lagoonal facies and continued carbonate deposition. However, the effect of this environmental shift upon Cambrian fauna, especially trilobites, is unclear because of the paucity of trilobites, and fossils in general, in the succession. Rare *Olenellus* are found in the lower Ghrudaidh Formation may be holdovers, post-dating the olenellid extinction reported at the Series 2 – Series 3 boundary from elsewhere on Laurentia (e.g. Palmer, 1998; Lieberman, 2003; Webster et al., 2008). Regional evidence for restricted, dysoxic facies in Scotland (e.g. Loch Eriboll, Fig. 2. 2) does not invoke a compelling argument for widespread, severe environmental change recorded at the Scottish Series 2 – Series 3 boundary.

In the western Great Basin, USA, the Series 2 – Series 3 boundary is defined by the biostratigraphic transition between the *Olenellus* and *Eokochaspis-nodosa* biozones (Palmer and Halley, 1979; Sundberg and McCollum, 2000). This level is found in the Pyramid Shale Member of the Carrara Formation and at the base of the C-Shale Member, Pioche Formation (Fig. 3.2). Both the Carrara and Pioche formations are mid-shelf, mixed siliciclastic-carbonate successions recording varying higher energy grainstone and packstone conditions to quieter marl facies (Table 3.1). The olenellid extinction is clearly observed within the Pioche Formation at Oak Springs Summit and Ruin Wash, Lincoln County, Nevada, and is inferred from the *Olenellus-Eokochaspis nodosa* biozone boundary at Emigrant Pass, Death Valley, California (Figs. 3.2; 4.4). In both sections the extinction is recorded in the deepest facies, low energy, marl and silty marl, with

dysoxic and euxinic pyrite framboid analysis providing complementary evidence that the olenellid extinction co-occurred with deeper water anoxic settings, linked to transgression onto the shelf (e.g Montañez et al., 2000; Zu et al., 2006). However, similar oxygen-restricted conditions were also encountered prior to the extinction level.

6.1.2. The Gondwanan record

On Gondwana, the redlichiid trilobites are not observed to survive beyond the Series 2 – Series 3 boundary, their disappearance is thought to coincide with the olenellid extinctions on Laurentia (Zhu et al., 2006), although the exact synchronicity has not been shown. In the Georgina Basin, Australia, the Thorntonia Limestone and lower Arthur Creek Formation are of upper Ordian age, closely correlating to the age of the Series 2 – Series 3 boundary (Fig. 5.2; Smith et al., 2015). A detailed biostratigraphic framework is currently not available for the formations studied in the Georgina Basin (see Chapter 5), and as a result, a clear picture of the timing of extinction is elusive. However, the correlation of the *Redlichia forresti* trilobite biozone to the Thorntonia Limestone indicates that the last appearance of the redlichiids may have occurred in this formation. A depositional hiatus at the top of the Thorntonia Limestone is overlain by pyritic, anoxic-ferruginous conditions within the basal "Hot Shale" of the Arthur Creek Formation, marking persistent anoxic conditions in a shallow continental seaway transgressing onto the Gondwanan continent (Fig. 6.3, 6.5, 6.6; Creveling et al., 2014; Pagès and Schmid, 2016). The position of the *R. forresti* biozones in the Thorntonia Limestone (Fig. 5.2) and the overlying succession of black shales suggests that redlichiid trilobite extinction may either predate this severe anoxic event or coincide with the top of the Thorntonia Limestone and the onset of black shales.

6.2. Research question 2: What role did the eruption of the Kalkarindji large igneous province play in trilobite extinctions and can evidence for these eruptions be detected using mercury concentrations in far-field sedimentary successions?

The Kalkarindji LIP has long been implicated as a contributing factor toward extinction at the Cambrian Series 2 – Series 3 boundary (e.g. Glass

and Phillips, 2006; Hough et al., 2006; Jourdan et al., 2014). Absolute dating provides support for the approximate correspondence between eruptions and extinctions but more precise evidence can be gained using the proxy of mercury enrichment in sedimentary successions. Previous studies have demonstrated that LIP eruptions produce correlatable Hg concentration enrichments synchronous with extinction events across geographically distal regions (e.g. Percival et al., 2015; Font et al., 2016; Grasby et al., 2016; Thibodeau et al., 2016; Jones et al., 2017; Gong et al., 2017). Here, mercury (Hg) chemostratigraphy from the Great Basin, USA and the Georgina Basin, Australia is presented.

In the SW USA the olenellid extinction horizon occurs in the Pioche Formation, but the Hg records only provide inconclusive evidence for contemporaneous volcanism. Hg enrichment is seen at the extinction horizon at Oak Springs Summit, but not at Ruin Wash. At the correlative *Olenellus – Eokochaspis-nodosa* biozone boundary in the Carrara Formation, there is little evidence for elevated Hg concentrations (Fig. 4.7). The disparity in Hg signals between these locations weakens the interpretation that Hg reliably monitors flood basalt volcanism. The Kalkarindji volcanism may have caused sedimentary Hg enrichment, but the data do not unambiguously identify a volcanic signal in all sections. Chapter 4 offers a discussion of non-volcanic mechanisms for Hg variations in the rock record and caution the need for further study of Hg in deep time.

The record of sedimentary Hg from the Georgina Basin, Australia, offers more promising insights and a clearer Hg signal (see Chapter 5.5). Two distinct pulses of Hg enrichment are described, one in the lower Thorntonia Limestone, and one in the base of the Arthur Creek Formation (Fig. 5.3). These enrichment peaks display a strong similarity to previous studies using Hg as a volcanic tracer (e.g Percival et al., 2015, 2017; Grasby et al., 2016), recording definitive excursions above background levels across varying lithology; suggesting an exogenous environmental loading of Hg and subsequent enrichment in sediments.

Because the extinction level has not yet been precisely constrained, the relationship between Hg enrichments and trilobite extinction from Gondwana is therefore elusive. Given the position of the *R. forresti* trilobite

178

biozone in the Thorntonia Limestone, it is observed that Hg enrichments occur before and after the last occurrence of redlichiid trilobites on Gondwana. This suggests that if Hg is recorded volcanic activity, these episodes may have been ongoing through the Series 2 – Series 3 boundary and during the redlichiid extinction.

6.3. Research question 3: What is the temporal relationship between carbon cycle perturbations and trilobite extinction?

Montañez et al., (2000) were the first to report an abrupt negative shift in the inorganic carbon isotope record closely corresponding with trilobite extinction in marine rocks of Cambrian Series 2 – Series 3 age. Zhu et al. (2006) noted this temporal coincidence and termed the negative excursion the Redlichiid-Olenellid Extinction Carbon isotope Excursion (ROECE), which has been used to delineate the Cambrian Series 2 – Series 3 boundary and mark the extinction interval. However, previous correlation between the ROECE and trilobite extinction from North China revealed the excursion predates trilobite extinction (Zhu et al., 2004). Chapters 2 and 3 represent efforts to further constrain the temporal relationship between the two.

In NW Scotland, Chapter 2 reports the presence of the recovery from negative $\delta^{13}C_{carb}$ values (interpreted as ROECE) in the basal strata of the Ghrudaidh Formation, Durness Group (Chapter 2; Faggetter et al., 2016). However, the lack of trilobites makes comparison of extinctions and isotopic changes difficult to establish. Nonetheless, the discovering of ROECE helps clarify the age of the basal Durness Group and the identification of a higher $\delta^{13}C_{carb}$ excursion, interpreted to be the Drumian Isotope Excursion (DICE), further improves the dating of this poorly-constrained unit (Faggetter et al., 2016).

The trilobite extinction record is better known from the Great Basin, USA and a new $\delta^{13}C_{carb}$ record is presented from the Carrara and Pioche formations that identifies the presence of ROECE. From the Pioche Formation at Oak Springs Summit a large negative $\delta^{13}C_{carb}$ shift of ~-3.5‰ in the upper Combined Metals Member is interpreted to be the falling limb of ROECE (Fig. 3.7); above this construction of a $\delta^{13}C$ record is hindered by

extremely low carbonate values. Peak negative values returned from Oak Springs Summit closely correspond with the olenellid extinction horizon in the basal C-Shale Member, indicating there is a coupled extinction-excursion event within the Pioche Formation. In the Carrara Formation at Emigrant Pass, the extinction horizon is inferred to be at the *Olenellus – Eokochaspis-nodosa* biozone boundary in the middle Pyramid Shale Member (Fig. 3.7). This level coincides with a negative $\delta^{13}C_{carb}$ shift of nearly -4‰ which is inferred to be ROECE.

6.4. Research question 4: Does sea level fall coincide with the ROECE and/or extinction?

A well-studied sequence stratigraphic framework is established for the Laurentian continent, describing Neoproterozoic- early Palaeozoic continent wide sequences of sea level change, named Sauk Supersequences (Sloss, 1963). These supersequences are observable across broad swathes of Laurentian deposits, in North America and Scotland the Sauk I/ Sauk II supersequence boundary is developed close to the Series 2 – Series 3 boundary (Prave, 1992; Keller et al. 2012; Morgan et al., 2012; Raine and Smith, 2012; Faggetter et al., 2016, 2017).

In NW Scotland, Raine and Smith (2012) placed the Sauk I/ Sauk II supersequence boundary at the contact between the An t-Sròn and Ghrudaidh Formations. Chapter 2 re-appraises this sequence stratigraphic assessment and moves the boundary into the basal Ghrudaidh Formation, placing it at a ravinement surface ~2m above the formational boundary (Fig. 2.2). The previous allocation at the formational boundary only marks the facies shift from inner shelf to lagoon, whilst reassessment here considers the sequence boundary to have been amalgamated with a ravinement surface in this inner shelf location. The base-level shift is considered to be only a modest ~10m. The position of the Sauk I/ Sauk II boundary coincides with negative (-3.0‰) $\delta^{13}C$ values interpreted as ROECE, though whether it coincides with the precise nadir of the excursion is unclear.

In the Great Basin, USA a robust sequence stratigraphic framework for Sauk Supersequences has been established previously. In eastern California the Sauk I/ Sauk II supersequence boundary is placed at the

contact between the Zabriskie Quartzite and the overlying Carrara Formation (Fig. 3.2; Prave, 1992; Adams, 1995; Fedo and Cooper, 2001; Keller et al. 2012; Morgan et al., 2012). The position of the trilobite extinction delineated by the *Olenellus-Eokochaspis nodosa* biozone boundary (Fig. 3.2) and the close correspondence of ROECE to this horizon, indicates that the negative excursion and trilobite extinction co-occur within a transgressive phase of the Sauk II supersequence and not at the level of the supersequence boundary.

6.5. Context within the broader Cambrian system
Extinction at the Series 2 – Series 3 boundary is a severe punctuation of the dramatic biologic proliferation of the Cambrian Explosion.

The Cambrian is most famous for the dramatic proliferation of mineralising animals, the appearance of many of the stem groups of modern phyla and divergence amongst morphologically distinct bilaterians. The Cambrian Series 2 is in part dominated by the dramatic radiation of ecological generalists amongst arthropods, perhaps most notoriously characterised by trilobite evolution (Briggs, 2015). During the second phase of bilaterian radiation, relatively soon after the initiation of the Cambrian Explosion, the major body plans of arthropods were well established (Thomas et al., 2000). It is in the Series 2 that shallow-subtropical marine biota exhibit the greatest diversity of the Cambrian; a defining characteristic of which is the widespread development of endemic species (Álvaro et al., 2003). This palaeobiological trait is accentuated by the palaeogeographic distribution of shallow marine carbonate and mixed carbonate-siliciclastic platforms, which, in the Series 2, harboured diverse and often isolated archaeocyathan reef communities, including early trilobites (Zhuravlev, 2001; Zhuravlev and Riding, 2001; Álvaro et al., 2003). The provincial nature of endemic trilobite faunas can be constrained to two main clusters: one consisting of Avalonian, Morrocan and Spanish (Ossa-Morena) assemblages; the other to British, French (Montage Noire), Spanish (central Iberia, Cantabrian), Sardinian and Baltic faunas (Álvaro et al., 2003). The isolation of trilobite faunas in Series 2 fostered geographic (i.e. allopatric) speciation of endemic faunas, promoted in part by ease of reproductive

communication between the two clustered regions, but also by the geographic distance between clusters (Álvaro et al., 2003). It is plausible that these geographically distinct communities were the precursors to Palmer's (1965) biomeres. Rooted in the rapid diversification of the Cambrian Series 2, Palaeozoic arthropod faunas exhibited an upward trajectory with increasingly complex characteristics through the Cambrian, reaching a much higher maximum diversity in the Ordovician (Briggs, 2015). However, during this spectacular radiation of the arthropod Phylum, and the trilobite Class, at the Series 2 – Series 3 boundary, trilobite faunas display a significant change in distribution patterns. Endemic faunas were replaced by much more homogenous assemblages, displaying open connectivity between regions and implying increased rates of trilobite immigration (Álvaro, 2003), essentially marking the first examples of biomere boundary turnover (e.g. Palmer, 1965). Whilst the macro-evolutionary propagation of the Cambrian Explosion often takes centre stage in defining the Cambrian, it is essential to consider the context of biotic crises and instability in Cambrian geochemical systems (e.g. globally reproducible $\delta^{13}C$ excursions) within the broader Cambrian system. As discussed in Chapter 1, the first major extinction event of the Phanerozoic occurs in the upper Series 2, known as the Botomian – Toyonian Extinction (BTE). The BTE heralded the extinction of the archaeocyathan sponges, as well as other reef-associated faunas such as hyoliths, molluscs, calcareous metaphytes (Brasier, 1996) and has been linked to the coupled transgression-regression of the Sinsk Event (shoaling anoxia during transgression) and the Hawke Bay Regression Event (HBRE; Zhuravlev and Wood, 1996). These phenomena preferentially affected sessile, fixed, and reef-associated faunas, which were inherently susceptible to the loss of habitable shallow marine shelves during shoaling anoxia and transgression, and the ensuing sea-level fall and regression (Brasier, 1996; Rowland and Hicks, 2004). During the BTE some olenellid trilobites were affected on all Cambrian continents except Laurentia, but ultimately, they survived beyond this until the Series 2 – Series 3 boundary (the top of the *Bonnia-Olenellus* trilobite biozone; Brasier, 1996; Palmer, 1998). This thesis contributes the first study to directly constrain the positions of the extinction of the olenellid trilobites; the Series 2 – Series 3

boundary; and the ROECE event within a single section (Chapter 3). Previously, correlation was based on a close temporal coincidence and there existed a discrepancy between the timing of ROECE, the extinction of the olenellids at the top of the *Olenellus* biozone, and its relative timing to the extinction of the archaeocyaths (e.g. Peng et al., 2012). Early studies long noted the biotic crisis of the BTE and coincident trilobite losses (e.g. Brasier 1996; Zhuravlev and Wood, 1996) and effectively considered these two as the same event, which has persisted in the literature (e.g. Zhang et al., 2015). However, this thesis contextualises the extinction of the olenellid trilobites as a temporally distinct event to the BTE.

There is no observed decline in diversity or abundance in trilobite faunas directly below the Series 2 – Series 3 boundary, and their disappearance transects any lithological boundaries (e.g. Combined Metals Member – C-Shale Member boundary of the Pioche Formation). This is analogous to later Cambrian trilobite faunal turnover associated with biomere boundaries during third or fourth-order sea-level changes, where new faunas replace older faunas within the transgressive systems tract (e.g. Palmer and Taylor, 1981; Peng et al, 2012). In the Furongian, two biomere boundaries mark rapid trilobite turnover at the top of the Marjumid and Pterocephalid biomeres (Brasier, 1996; Zhu et al., 2006; Gill et al., 2011; Gerhardt et al., 2016). The cause of this turnover has been ascribed to the replacement of endemic, shallow-water shelf faunas with pandemic, cool-water trilobites following rapid sea-level rise, upwelling and a fall in dissolved oxygen concentrations (Brasier, 1996; Gill et al., 2011; Gerhardt et al., 2016). Based on the position of the olenellid extinction within the transgressive systems tract (Chang et al., 2017; Faggetter et al., 2017), and the lack of evidence for a severe anoxic event on Laurentia, the nature of extinction at the Series 2 – Series 3 boundary is closely comparable to that of trilobite turnover at biomere boundaries in the Furongian (Brasier, 1996).

Dissociating the BTE and olenellid trilobite extinction is important in that it separates the severe environmental change during the Sinsk Event and the HBRE, and the ensuing faunal turnover at Series 2 – Series 3 boundary. End Series 2 strata exhibit successive extinction events first relating to the disappearance of microbial-archaeocyathan reef build-ups

during regressive sea-level fall (BTE), then signalling the extinction of endemic, inner platform trilobite faunas and the in-shore immigration of pandemic faunas in the Series 3 during transgression (olenellid extinction). This characterises the Series 2 – Series 3 extinction as part of a long-term palaeobiological event, succeeding an abrupt worldwide biotic crisis in the late Series 2 (BTE), then leading to a diachronous global diversity decline and extinction (olenellid extinction) and the initiation of repetitive turnover of endemic faunas and their replacements by homogeneous, pandemic faunas during episodes widespread sea-level rise (transgression). While there is little evidence that the kill mechanisms behind the BTE (i.e. ocean anoxia and regression) are globally persistent at the Series 2 – Series 3, this overall assessment of extinction at this time characterises a long-term global, extinction event resulting in clear and repetitive faunal turnover (e.g. biomere boundaries; Debrenne, 1991; Zhuravlev, 1996; Brasier, 1996; Álvaro et al., 2003).

Trilobite extinction, ROECE and facies changes at the Cambrian Series 2 – Series 3 boundary reflect dynamic abiotic changes throughout the Cambrian, inherently linked to sea-level variation, continental arrangement and weathering regimes.

Dynamic continental amalgamation, re-arrangement, uplift and erosion created pre-requisite geochemical and environmental conditions which would foster the biotic radiation of the Cambrian Explosion (Squire et al., 2006; Peters and Gaines, 2012). Across the Proterozoic – Phanerozoic boundary, continental denudation and subsequent erosion formed the Great Unconformity, saturating Cambrian oceans with dissolved weathering products proving essential to newly biomineralising animals (Porter, 2004, 2007; Squire et al., 2006; Peters and Gaines, 2012). Following periods of widespread continental amalgamation and the formation of Gondwana, the resultant orogenesis created vast interior mountain chains known as the Transgondwanan Supermountain (TGSM; Squire et al., 2006). As the Gondwanan landmass drifted into tropical latitudes during the late Proterozoic and Cambrian Terreneuvian, the TGSM was subjected to intensive tropical weathering which accentuated the transport of weathering

products to the oceans, resulting in the deposition of the massive Gondwana Super-fan system (TGSF) throughout the Cambrian Terreneuvian and Series 2 (Squire et al., 2006). Wide swathes of quartz rich sedimentary units formed broad quartz-rich continental shelves, which would harbour shallow-marine environments ideal for the proliferation of benthic biota, reef communities and endemic shallow-marine faunas (e.g. James and Gravestock, 1990; Zhuravlev and Riding, 2001). At the same time, subsidence along the north-western Laurentian passive margin created accommodation space allowing the deposition of second and third-order cycles of the Sauk Sequence (Keller et al., 2012; Peters and Gaines, 2012). As with the deposition of the TGSF, the deposition of broad clastic shelves during early Sauk transgression created habitable shallow-marine environments across extensive swathes of Laurentia that would harbour the evolution of abundant endemic faunas, often dominated by archaeocyath reefs and trilobite biomeres (e.g. Palmer, 1965; Rowland and Gangloff, 1988). As both the Laurentian and Gondwanan continents were positioned across tropical latitudes, conditions favoured the precipitation of thick carbonate belts on top of clastic shelves (Keller et al., 2012; Southgate and Shergold, 1991; Schmid, 2017). This created the sedimentary architecture that enabled the growth and proliferation of archaeocyath reefs within a thick carbonate belt, and abundant trilobite faunas in an outer detrital belt (Palmer and Halley, 1979; Rowland and Gangloff, 1988; Peters and Gaines, 2012). Lithological climate indicators (e.g. carbonates and evaporites) indicate that the Series 2 – Series 3 boundary interval was characterised by greenhouse conditions, a shift to evaporitic conditions, and that many faunas inhabited widespread epeiric seas encroaching onto the Gondwanan continent (Álvaro et al., 2003; Schmid, 2017). An ocean saturated with weathering products, climate favouring carbonate precipitation, and widespread transgression during the Series 2 allowed the global proliferation of the first metazoan reefs, which nurtured reef and off-reef communities, contributing to a global diversity increase in the run up to the Botomian-Toyonian Extinction (BTE; Zhuravlev and Wood, 1996; Debrenne, 2007). Where archaeocyaths and trilobites had thrived during habitat expansion during transgression, a coupled transgression-regression anoxic event halted this dramatic

diversification during the Botomian – Toyonian Extinction (Zhuravlev and Wood, 1996).

Following the BTE, at the Cambrian Series 2 – Series 3 boundary interval, endemic shallow marine trilobite faunas (e.g. olenellids and redlichiids) underwent widespread extinction on both the Laurentian and Gondwanan continents (e.g. Palmer, 1998; Zhu et al., 2004, 2006). On both continents, this coincides with sea-level change and transgression. On Laurentia, the Sauk 1/Sauk II sequence boundary precedes the olenellid extinction which occurs during a transgressive deepening cycle (Faggetter et al., 2016, 2017). On Gondwana, the redlichiid trilobites did not survive the base of Series 3, which is deposited during a transgressive cycle (Southgate and Shergold, 1991). As discussed before, sea-level change exhibits a broad control on biotic regimes in the Cambrian, especially concerning trilobites; from the basal Series 3 to the Furongian new pandemic species replace endemic species at biomere boundaries coincident with transgression (Palmer, 1965, 1998; Brasier, 1996; Saltzman et al., 2000: Gill et al., 2011; Gerhardt et al., 2016). This replacement has been linked to two functions of sea-level rise; the increased connectivity of ocean basins and thus the break-down of distinct faunal provinces (Álvaro et al., 2003); and, the reduction of shallow marine eco-space favouring the proliferation of cosmopolitan trilobite species during transgressive deepening (Brasier, 1996).

Sea-level change through the Cambrian (particularly Terreneuvian and Series 2) has also been implied as a control on globally synchronous, large-amplitude, high frequency $\delta^{13}C$ excursions, which some argue are inherently linked to changing productivity rates and organic carbon burial fluxes due to the changing size of marine basins during transgression and regression (Brasier and Lindsay, 2001). Their hypothesis argues that periods of high sediment accumulation (e.g. Cambrian Terreneuvian and Stage 2, TGSF and Sauk I) must have been characterised by high rates of organic carbon oxidation in order account for the first order fall in $\delta^{13}C_{carb}$ values across the Proterozoic – Phanerozoic transition. As for the high frequency second order $\delta^{13}C$ excursions in the Cambrian (e.g. during the Terreneuvian and Stage 2), Brasier and Lindsay (2001) suggest that this is due to

changing rates of organic burial and oxidation, modulated by subsidence and sea level change. Their hypothesis therefore sets out that positive δ^{13}C excursions record an increase in the burial flux of organic matter during transgression, and, negative δ^{13}C excursions record reduced rates of carbon burial and an increase in organic carbon oxidation rates during periods of regression. This appears to be at odds with the position of ROECE as observed within transgressive facies (e.g. Guo et al., 2010, 2014; Zhang et al., 2015; Chang et al., 2017; Faggetter et al., 2016, 2017; Ren et al., 2017). However, following the global diversity decline observed from the upper Series 2 until the Series 2 – Series 3 boundary (i.e. BTE to olenellid extinction), it is likely that the globally synchronous trend of decreasing δ^{13}C values of seawater, characterised as ROECE, reflect the culmination of a long-term biomass decline and subsequent reduction of the burial flux of organic matter (Guo et al., 2010, 2014; Zhang et al., 2015; Chang et al., 2017; Ren et al, 2017; Schmid, 2017). The position of ROECE within transgression implies that the shoaling of oxygen depleted bottom waters may have contributed toward a negative shift in δ^{13}C values as it did earlier in Series 2 (e.g. Feng et al., 2017; Jin et al., 2017), regional evidence for this is supported by Creveling et al. (2014), Zhang et al. (2015) and Schmid (2017). Creveling et al. (2014) and Schmid (2017) frame geochemical redox proxies (P and Fe speciation, carbonate mineralogy) within a sequence stratigraphic framework that depict second-order transgressive cycles deposited under a spectrum of anoxic conditions, including euxinic and ferruginous intervals. Zhang et al. (2015) note a sharp increase in the abundance and spatial distribution of microbial oncoidal carbonates at the Series 2 – Series 3 boundary in China. Although they do not report in-situ δ^{13}C values, they note the temporal association of this microbial resurgence with the Series 2 – Series 3 boundary interval (and they extrapolate to ROECE) and suggest a link to ocean anoxia. They show that thick (1-3m) beds display spherical to sub-spherical oncoids with alternating light – dark cortical laminae containing variable amounts of organic matter Zhang et al., 2015), and indicate that this interval is dominated by microbial, not metazoan, communities. Within their facies framework they deduce that oncoids formed within shallow-marine setting coincident with high-alkalinity

and bacterial sulfate reduction, invoking pyrite framboid size-distribution and heterotrophic bacterial as an indicator that these deposits accumulated under anoxic/dysoxic conditions. Thus, although within the sections studied in this thesis, evidence for severe anoxia is scarce, globally, there is evidence for severely oxygen depleted environments, microbial resurgence and anoxic waters flooding shallow continental seas during the Cambrian Series 2 – Series 3 boundary.

The Kalkarindji Large Igneous Province (LIP) was emplaced during the interval of the ROECE event and olenellid trilobite extinctions, thus implying the first Phanerozoic LIP-extinction event.

　　　　LIP-mass extinction links are well known from the Phanerozoic (e.g. Wignall, 2001) and increasingly, temporal links imply that there may yet be further examples of which that have not yet been thoroughly investigated (e.g. Gong et al., 2017; Jones et al., 2017). The BTE and ensuing trilobite extinction has long been recognised as a severe biotic crisis (Brasier, 1996; Zhuravlev and Wood, 1996), and, after the initial discovery of a suite of geochemically related basaltic deposits in northern and western Australia (Hanley and Wingate, 2000), an emerging temporal association was established (Glass and Phillips, 2006; Evins et al., 2009; Jourdan et al., 2014). The coincident timing between LIP emplacement age (or LIP related proxy evidence) and extinction is a fundamental pre-requisite in initiating an investigation into the causal-mechanisms between such phenomena. To date, Jourdan et al. (2014) provide the strongest evidence of temporal coincidence between their calculated age for the Kalkarindji LIP, 510.7 ± 0.6 Ma, and heightened extinction rates during the upper Cambrian Series 2 and Series 2 – Series 3 boundary. Currently the unratified age for the Series 2 – Series 3 boundary is 509 Ma (Ogg et al., 2016), which stands just outside of the error of calculated U-Pb zircon age from Jourdan et al. (2014), but still displays a strong correlation for proposed Stage 4 – Stage 5 (equivalent to the Series – Series 3) boundary ages of 509.11 ± 0.77 Ma (Harvey et al., 2011) and 511 ± 1 Ma (Landing et al., 1998). Therefore, the case that the Kalkarindji was emplaced within the period of observed extinction (BTE and trilobite) is fairly robust, but this is far from a mechanistic relationship

between extinction and the Kalkarindji LIP. It is also important to note that mass extinctions are generally defined as geologically brief intervals (~1 Ma) during which extinctions rates are elevated considerably beyond background rates, and during which diverse taxa from a broad range of habitats are affected worldwide (Hallam and Wignall, 1997). Certainly, the BTE fits this description (estimated minimum 45% generic loss; Sepkoski, 1996), though redlichiid-olenellid extinction at the Series 2 – Series 3 boundary is ascribed to a lesser extinction event following faunal turnover and a shift to dominantly agnostic trilobite faunas (Babcock et al., 2017) rather than a true mass extinction in the sense of the Phanerozoic "big five" events (Hallam and Wignall, 1997).

Further tertiary evidence for coincidental emplacement of the Kalkarindji LIP and the BTE and/or redlichiid-olenellid extinction is elucidated by $\delta^{34}S$ values and sulphate concentrations in francolite-bound sulphate from Series 2 – Series 3 boundary carbonates in Australia (Hough et al., 2006). Hough et al., (2006) find that $\delta^{34}S$ rise sharply across the Series 2 – Series 3 boundary interval and ascribe this to a significant increase in pyrite burial fluxes as a possible result of increased pyrite formation within the water column and the spread of anoxia. Hough et al. (2006) reconcile the abrupt nature of this $\delta^{34}S$ rise as inherently linked to the shoaling of deep, anoxic waters over continental shelves and carbonate platforms during transgression at this time. As previously discussed, this hypothesis is also consistent with the interpretation that the ROECE event records the shoaling of oxygen-depleted bottom waters onto shallow marine shelves following a protracted period of biomass decline in the upper Series 2. Hough et al. (2006) posit on the root cause of their data by implying expanding ocean anoxia- and remark that extended intervals of marine anoxia are often associated with warmer ocean temperatures (due to the diminished capacity for warmer water to store dissolved O_2). They attribute this to the potential of episodic emissions of vast CO_2 from the apparently coincident Kalkarindji LIP (Hanley and Wingate, 2000; Glass and Phillips, 2006; Evins et al., 2009; Jourdan et al., 2010), and the capacity of LIPs to drive global warming through large volcanic degassing events as observed throughout the Phanerozoic (e.g. Wignall, 2001). Hough et al. (2006) then hypothesise that

during this period of potential global warming (independent lithological climate indicators evidence warming through deposition of extensive carbonate and evaporite deposits, e.g. Keller et al., 2012; Schmid, 2017) the spread of ocean anoxia would have rendered shallow marine environments potentially vulnerable to CH_4 and/or H^2S poisoning during transgression, and maintain this as a plausible kill mechanism tied to global diversity loss in the upper Series 2 and at the Series 2 – Series 3 boundary, however, the biological effect of this remains speculative. While their evidence and hypothesis fit other examples of LIP driven extinction during the Phanerozoic, what remained elusive is the potential for their data to distinguish between the BTE and trilobite extinction, and to provide evidence that this scenario occurred within strata recording extinction.

Fluctuating $^{87}Sr/^{86}Sr$ seawater values have long alluded to major secular ocean chemical variations in the Cambrian, during which the highest $^{87}Sr/^{86}Sr$ values of the past 900 myr are recorded close to the Series 2 – Series 3 boundary (Montañez et al., 1996, 2000; Peters and Gaines, 2012). Peters and Gaines (2012) recognised the long-term rise in seawater $^{87}Sr/^{86}Sr$ during the Neoproterozoic and attributed this trend to the long-term erosion and exposure of ^{87}Sr rich granitic rocks during the formation of the Great Unconformity. In the late Proterozoic and up to the Cambrian Series 2 – Series 3 boundary, Squire et al. (2006) ascertains that increasing seawater $^{87}Sr/^{86}Sr$ values are accentuated by the uplift and erosion of the TGSM. A complex $^{87}Sr/^{86}Sr$ history is discussed in Chapter 1 (1.5.3), and depicts a long-term (~350 myr) rise culminating in a high in the Cambrian Terreneuvian, punctuated by an abrupt fall at the Cambrian Series 2 – Series 3 boundary, and returning to rising values in the late Series 3 and Furongian (Montañez et al., 1996, 2000). This abrupt, short-term (~4 myr) downturn close to the Series 2 – Series 3 boundary was ascribed by Montañez et al. (2000) as the plausible result of increased weathering fluxes of young, mafic-derived mantle rocks and speculatively attributed to an increase in hydrothermal Sr fluxes due to continental rifting in the latest Series 2. Crucially, Montañez et al. (2000) reveal the timing of decreasing $^{87}Sr/^{86}Sr$ seawater values as strongly corresponding to the current age framework for the Kalkarindji (e.g. Glass and Phillips, 2006; Evins et al.,

2009; Jourdan et al., 2010) and the position of ROECE at the Series 2 – Series 3 boundary. This then raises the possibility that the source driving the abrupt downturn of ^{87}Sr/^{86}Sr seawater values at the Series 2 – Series 3 is the weathering of newly emplaced basalts of the Kalkarindji LIP, and although Montañez (2000) provide a relatively low-resolution framework, this displays a strong temporal coincidence to the BTE and redlichiid-olenellid extinction.

Independently, these lines of evidence support the essential pre-requisite that the Kalkarindji LIP was emplaced during the broader interval of biotic crisis. However, proposed environmental repercussions and suggested kill mechanisms remain speculative, and although they are supported by their respective data-sets, they do not establish a specific link to either the BTE or the olenellid-redlichiid extinction, and do not present any in situ evidence of these phenomena in the same section. As previously discussed, the application of Hg as a tracer for volcanism is becoming increasingly popular and in a number of instances successful in showing a link between volcanism, ocean anoxia, climate change and extinction (e.g. Sanei et al., 2012; Percival et al., 2015, 2016, 2017; Thibodeau et al., 2016; Font et al., 2016; Grasby et al., 2016; Gong et al., 2017). This thesis reports varied success in the use of the Hg proxy, records from Laurentia reveal an inconsistent trend between Hg chemostratigraphies and extinction, whilst the Gondwanan record (effectively a "regional" signal of volcanism) shows more potential, but remains to be developed. Hg remains a valuable proxy and the potential for it to reveal a "smoking gun" between periods of increased volcanism and extinction is significant. However, for this instance in the Cambrian, it has not provided irrefutable evidence for the first Phanerozoic LIP-extinction link, and as such further work (discussed in 6.7) is essential.

6.6. Conclusions:

To synthesise the main conclusions of this thesis: new inorganic carbon isotope data are reported from 6 locations spanning the Cambrian Series 2 – Series 3 boundary. On Laurentia (Scottish and USA field sites; Fig. 6.1) the presence of a large ~-4‰ δ^{13}C shift is interpreted to be ROECE coinciding with the Series 2 – Series 3 boundary. In the USA, this co-occurs

with the olenellid extinction (in the Pioche Formation) and the last appearance of the olenellids as delineated by the *Olenellus-Eokochaspis nodosa* biozones boundary (Carrara Formation; Fig. 6.1). Whilst a coupled extinction-carbon isotope excursion marks the Cambrian Series 2 – Series 3 boundary in the SW USA, in Scotland ROECE coincides with the boundary but a lack of trilobite fossils prevents precise correlation with the extinction. For Laurentian sections, new analysis shows that the extinction horizon corresponds with variable evidence for anoxia; the most severe indication of anoxia is derived from euxinic framboid size distribution at Ruin Wash in the SW USA. However, elsewhere in the USA and Scotland, there is evidence only for periodic dysoxia- this new data does not support early interpretations (e.g. Montañez et al, 2000) that severe anoxia drove the olenellid extinction. Facies analysis reveals that ROECE and extinction occurred during the transgressive phase of the Sauk II supersequence, and evidence for dysoxia/euxinia correspond to theories that oxygen limited deep water periodically encroached upon shallow marine shelves during transgression. In the USA, we report mixed siliciclastic-carbonate facies; bioclastic packstone and grainstone event beds punctuate deeper water mid-shelf marl and silty marl- with ROECE and the olenellid extinction recorded in the latter. In Scotland, more shallow facies are present, with evidence for periodic emergence. Here, the Series 2 – Series 3 boundary is present at the formational boundary between the shallow, cross bedded, *Skolithos* bioturbated quartz arenite (An t-Sròn Formation) and the pyritic, dysoxic dolomicrite (basal Ghrudaidh Formation). Eroding into this dysoxic, restricted lagoonal facies is the amalgamated ravinement/sequence boundary marking the transition from the Sauk I to Sauk II supersequence.

To investigate the relationship between the Kalkarindji LIP eruptions, the Series 2 – Series 3 boundary and extinction, this thesis presents the first Hg chemostratigraphy for the Cambrian and assess the evidence for volcanic activity during extinction. New data show an inconsistent signal between Series 2 – Series 3 boundary sections, extinction and sedimentary Hg enrichment from the SW USA, and suggest further study to constrain the nature of these data and the timing of the Kalkarindji LIP. Chapter 5 is preliminary work on the chemostratigraphy and facies of Australian Series 2

– Series 3 boundary strata, that reports the discovery of Hg enrichment in the Thorntonia and Arthur Creek formations straddling the boundary interval. These Hg data show similar trends to volcanic signals from other Hg studies (e.g. pulsed enrichments occurring independently of facies changes), and as such this establishes a potential site for further investigating a sedimentary trace for LIP volcanism.

6.7. Suggestions for future work:

The findings of this thesis present several derivative lines of interest and pose unique further research questions to be explored with further work. Chapter 5 is presented as a work in progress, and thus before further projects are considered it would be beneficial to progress this chapter with the creation of a robust correlation framework for the Series 2 – Series 3 boundary interval. Biostratigraphic studies are hindered by a lack of shared fauna between Gondwanan and Laurentian fauna and correlation therefore requires additional chemostratigraphic studies, however, ongoing collaboration aims to create a correlative biostratigraphic framework. To test for evidence of redox variation, Fe speciation analysis is in progress following the Poulton and Canfield (2005) methodology.

Aside from the completion of Chapter 5, several gaps remain in the current understanding of the Cambrian system and the application of new the Hg proxy, which become apparent when summarising the findings of this thesis. Addressing the following suggested research questions will contribute to a more holistic understanding of the Cambrian, and address current inadequacies in new proxies.

1) Stable isotope variation throughout the Cambrian. Whilst the research focus this thesis targeted the Cambrian Series 2 – Series 3 boundary and associated ROECE excursion, the Cambrian period is defined by highly variable, globally synchronous and often reproducible stable isotope values, as exemplified by ~10 $^{13}C_{carb}$ excursions (e.g. Zhu et al., 2006). The root causes of the observed ^{13}C variation has remained elusive for decades despite novel new models and hypotheses being suggested. Generally synchronous $\delta^{13}C_{carb}$ oscillations, with a periodicity of ~1-2 Myr (and less)

and magnitude changes varying between ~2‰ - ~7‰, depict a carbon cycle reflexing to changes derived from a number of possible factors. Current understanding has not yet reached an unambiguous consensus for a single control behind this variability. Suggested mechanisms describe temporal changes to the amount of organic and inorganic carbon burial (e.g. Kump and Arthur, 1999); evolving isotopic composition of input fluxes and fractionation between carbonate and organic carbon (e.g. Maloof et al., 2010); interplay between true polar wander events and release of methane clathrates (e.g. Kirschvink and Raub, 2003); and periods of intensified volcanic outgassing and injection of isotopically light carbon (Maloof et al., 2010). While these scenarios all carry weight, it is becoming increasingly clear that changes to carbonate stable isotope chemostratigraphic records (e.g. δ^{13}C, δ^{34}S, δ^{44}Ca, δ^{26}Mg, δ^{18}O) through time do not necessarily track temporal shifts in global isotope mass balances. Rather, high frequency stable isotope fluctuations can be attributed to the lateral migration of facies reflecting changing local or regional conditions, as controlled by the mineralogical and diagenetic history of carbonate sediments in varying depositional settings (e.g. Higgins et al., 2018). Higgins et al. (2018) demonstrate that paired measurements of δ^{44}Ca and δ^{26}Mg illustrates the composition of carbonate minerals, and the style and extent of early diagenesis, as either controlled by the chemistry of the ambient fluid (fluid-buffered) or the precursor sediment (sediment-buffered). When coupled with variations in carbonate mineralogy (δ^{26}Mg values, e.g. aragonite, calcite, dolomite formation), early-marine diagenetic conditions play a fundamental role in determining the regional and global expressions of geochemical proxies (Higgins et al., 2018). This calls into question the validity of assuming that large perturbations to geochemical cycles (e.g. δ^{13}C) reflect globally synchronous, secular shifts in paleoenvironmental conditions and seawater chemistry. While these new insights do not preclude the use of stable isotope chemostratigraphies, they do necessitate renewed scrutiny when interpreting geochemical records. The control of locally varying conditions in the modern (and mirrored in deep geological time e.g. Present et al., 2015; Pasquier et al., 2017; Silva-Tamayo et al., 2018) and the potential of diagenesis to drive drastic stable isotope excursions illustrates

the importance of closely interrogating local sedimentary, mineralogical and diagenetic factors when interpreting the mechanisms behind geochemical perturbations. Integrating detailed sedimentological and chemostratigraphic studies, firmly grounded in a geologic and sequence stratigraphic framework, can provide a mechanistic explanation of the driving conditions behind such geochemical excursions, the role of diagenesis, and how they relate to biotic trends. To further elucidate the mechanisms behind δ^{13}C excursions it is necessary to apply this methodology addressing recent insights into stable isotope variability and map high resolution proxy records in the early Cambrian onto carbonate facies that are tightly constrained in a spatial shelf-to-basin framework.

A limiting factor in taking this approach is the prerequisite geological context where successions are mapped in detail (it's possible to construct an on-shore to off-shore transect); there is demonstrated variability in chemostratigraphic signals (e.g. δ^{34}S and/or δ^{13}C excursions); and there are thick carbonate successions with biostratigraphic temporal control. Problematically, no such study exists for the ROECE interval. However, the Cambrian Terreneuvian and Series 2 remains at the forefront of continuing efforts to establish causal mechanisms behind variations in marine geochemical cycles. Dramatic perturbations to the isotope composition of δ^{13}C during the Cambrian Terreneuvian are observed to show significant temporal and spatial heterogeneity. A suggested target is the early Cambrian carbonate rich deposits of the Bayangol and Salaagol Formations the Zavkhan terrane of southwestern Mongolia. These formations are described within an integrated sequence stratigraphic, δ^{13}C chemostratigraphic and palaeontological framework detailed in Smith et al., (2016). Facies associations are constrained within a slope to shore-face structure and it is therefore possible to investigate lateral heterogeneity of geochemical signals (Fig. 1, Table 1). These successions illustrate wide variability of δ^{13}C values both in time and spatially; because of a rigorous framework, they are selected as an ideal location to test whether chemostratigraphic proxies represent inherently local heterogeneous conditions varying laterally, or, global secular environmental changes through time.

This approach will *1) map high resolution δ¹³C stable isotopes onto lithofacies within a tightly constrained lithological, sequence stratigraphic, and spatial (shelf-to-basin transect) framework*. Mirroring approaches in the modern, δ^{44}Ca and δ^{26}Mg compositions will be tested to elucidate any variation in isotope trends controlled by different mineralogical, diagenetic and sedimentary processes between depositional environments. Once a robust assessment of the diagenetic and mineralogical history (δ^{44}Ca and δ^{26}Mg) is established, it is then possible to further interrogate the nature of observed isotope excursions. Isotope variability is common throughout the Cambrian Terreneuvian, could all observed variability be explained by locally changing mechanisms? If this is the case, how are isotope excursions generally reproducible? Following the results of the first aim, this project will then *2) test evidence that isotope excursions reflect only local mechanisms driving isotope heterogeneity (i.e. facies map); or that local mechanisms are widespread and occurring synchronously (i.e. "globally local") during the Cambrian Terreneuvian*. Only after these mechanisms are understood is it possible to carefully interrogate the spatial variations of δ^{34}S and δ^{13}C; model the extent to which variability represents secular environmental conditions; and evaluate isotope excursions as reflecting local, regional or widespread paleoredox conditions. It also stands to reason that this methodology can be applied to other δ^{13}C excursions in the Cambrian that fit within a robust geologic framework.

2) Hg in the geologic record, insights from sedimentary Hg concentrations and stable isotopes. There are significant questions that hinder a detailed understanding of Hg behaviour necessary to interrogate whether Hg enrichments could be caused by processes other than volcanism. These questions are not limited to the Cambrian, but are pertinent to the application of Hg in this study and continued use of Hg as a robust volcanic proxy. Potential results are applicable through wide swathes of geologic time and essential to progressing a robust use of sedimentary Hg as an environmental tracer of volcanism. Broadening the remit of the Hg proxy may help elucidate more traits of its behaviour; for example, it necessary to ask: *1) are there processes other than volcanism that can account for Hg*

spikes in the sedimentary record? 2) do changing sediment accumulation rates lead to greater Hg concentrations throughout a stratigraphic section? 3) can changes to ocean chemistry or redox states affect Hg drawdown into sediments? 4) Can diagenesis mobilise Hg into specific stratigraphic horizons and therefore alter the primary Hg signal? In order to take this approach, it is necessary to investigate long term geologic records. A theoretical candidate for such a record could be the Mochras Core; a 1.3 km long core, representing a 27 myr sedimentary archive from the Early Jurassic. An existing core from Mochras records an open-marine hemipelagic environment in a well-mixed basin with relatively low TOC concentrations, several $\delta^{13}C$ excursions that are correlated with Hg/TOC and Os isotope anomalies (Hesselbo et al., 2013; Percival et al., 2016). Investigating this sedimentary record, it is plausible to examine the following:

1) A "background" Hg record, comparing steady state Hg deposition with periods of intense volcanic Hg loading. Hg studies in geologic time are becoming increasingly prevalent, however, efforts are focussed on intervals of time with contemporaneous volcanism (mostly LIP volcanism). There are very few Hg studies that lack LIP association (e.g. Gong et al., 2017; Jones et al., 2017), by systematically investigating broad scale (e.g. 10's myrs) Hg records in the absence of volcanism, it is possible to decipher how Hg behaviour differs between periods of known volcanism and in the clear absence of volcanism

2) Hg and changing sedimentation regimes. Within the Mochras succession, sedimentation rates vary by a factor of ~2 (Ruhl et al., 2016), establishing it as a potential section in which to investigate the correlation between Hg and Hg/TOC variation with changing sedimentation rates, allowing an insight into Hg accumulation and burial.

3) Hg and changing ocean chemistry. Mimicking studies in the modern (e.g. Emili et al., 2011), investigating Hg behaviour during periods of known redox and ocean chemistry variation in conjunction with other chemical proxies (e.g. Fe speciation and redox sensitive trace metals such as Mo/Al) could shed light on how Hg behaves with changing ocean redox states.

4) Hg behaviour during diagenesis. It is also imperative to decipher between primary and diagenetic signals when interpreting Hg records. It would therefore be important to compare coeval records with similar depositional environments (e.g. Mochras mid- Pliensbachian succession compared to the coeval Cleveland Basin, Yorkshire, Ironstone Shale Member) and investigate how different diagenetic pathways (e.g. calcite cementation and pyrite precipitation in Mochas vs siderite cementation in the Ironstone Shale Member) and assess how any difference in the Hg record between sites relates to possible diagenetic processes acting upon Hg.

Aside from Hg and Hg/TOC concentrations, new insights from Hg isotopes render stable isotope analysis an important new avenue for investigating the behaviour of the proxy and determining depositional pathways and sources. Fractionation patterns of Hg stable isotopes have been demonstrated as tracers for various environmental pathways as Hg enters the sedimentary archive (e.g. Blum et al., 2014). There are significant challenges in terms of definitively identifying sedimentary Hg as volcanogenic based solely on isotopic data, as processes involved during eruption, transportation and deposition may lead to fractionation. However, as research progresses, applying these techniques to the geological record in future studies may aid in establishing the source of Hg, and unravel its potential for tracing volcanism, photic zone euxinia and diagenetic processes.

3) *How severe did environmental change (e.g. anoxia) have to be to drive extinction in the Cambrian?* Palmer (1984) noted the rapid and successive turnover of trilobite assemblages in the Cambrian, and, an earlier extinction of archaeocyathan reefs has been linked to widespread anoxia (Zhuravlev and Wood, 1996). Anoxia has long been implicated in driving these events (e.g. Gill et al., 2011) but no high-resolution geochemical studies seek to target these extinction events and reveal the role of varying redox conditions. This gap necessitates the question: *Did marine anoxia drive the first mass extinction of complex animal life?* This question requires is a multi-disciplinary investigation into the timing and effect of marine anoxia during the first Phanerozoic mass extinction; the Botomian - Toyonian extinction

(BTE). Previous studies of the BTE provide sedimentary observations that the onset is marked by the widespread de-oxygenation of shallow continental marine platforms; a phenomenon known as the Sinsk Event. This was followed in quick succession by the rapid disappearance of Earth's first reef builders (archaeocyaths) and a diversity of fauna associated with these habitats - the Tommotian fauna. This extinction period is bracketed by a final extinction pulse coinciding with a dramatic sea level fall named the Hawke Bay Regression Event (HBRE). The BTE is as severe (45% genera loss; Sepkoski, 1996) as the other mass extinctions during the Phanerozoic, yet no high resolution geochemical, sedimentological or paleoenvironmental studies exist spanning this event. This work proposes the first coupled geochemical and geobiological study through the BTE, tests the hypothesis that *marine anoxia drove extinction* and that *sessile or fixed organisms were worst affected during the BTE*. The aims are to *investigate the extinction of the archaeocyaths during the Botomian – Toyonian extinction (BTE) and reconstruct ocean redox conditions* through the Cambrian Series 2 within a robust shelf-to-basin sequence stratigraphic framework. Tentatively it is proposed that sections on the Siberian craton (e.g. Anabar- Sinsk region) constitute an ideal field locality with which to collect material in the required geologic framework. This will test the hypothesis that *marine anoxia halted the Cambrian Explosion, driving the first mass extinction* of the Phanerozoic; the BTE. This should be conducted through a collaborative multi-proxy approach utilising stable isotope analysis (C, U), carbonate sedimentology, field geology and paleontology. The following aims and research questions are imperative to testing the main hypothesis that anoxia caused extinction during the Cambrian Explosion.

Firstly: *Establish a fine scale Uranium isotope ($\delta^{238}U$) profile through the last appearance of archaeocyathan reef assemblages and their overlying strata.* Due to the long ocean residence time of U (ca. 400k.y. > ocean circulation time), oceanic mass balance results in a well-mixed, uniform marine U isotope signature. Due to its redox sensitive character, the abundance and isotopic composition of U can be used to reconstruct the redox evolution of marine U sinks (Anderson et al., 2017). $\delta^{238}U$ fractionation patterns provide a high resolution, fine scale line of evidence with which to

test the hypothesis that the last appearance of the archaeocyaths coincided with marine anoxia. This is crucial in assessing evidence that anoxia directly coincided with the extinction of archaeocyaths during the BTE. This research aim asks the specific questions: *1) Does the seawater isotopic profile of $\delta^{238}U$ reveal fractionation patterns associated with anoxic conditions in rocks preserving the last appearance of archaeocyaths? 2) If U isotope profiles exhibit anoxic fractionation patterns, how do archaeocyaths and reef faunas respond?*

Secondly: *Assess abundance and diversity change in archaeocyathan reefs and associated reef fauna through the BTE interval.* Palaeobiological and palaeoecological assessment of the archaeocyathan reefs and the Tommotian fauna in the run up to their demise is essential in quantitating the severity of the BTE. Understanding which biota succumb to diversity loss will identify susceptibility to environmental change, elucidate patterns of extinction selectivity and test the hypothesis that anoxia severely affected sessile faunas. This aims asks: *1) Does peak diversity loss occur in line with evidence for anoxic conditions? 2) What are the lasting ecological changes driven by the BTE? 3) Do these patterns fit with the hypothesis of extinction driven by encroaching anoxia?*

Thirdly, this study will: *Compile a record of Hg concentrations and isotope profiles through the BTE to test for a coincident sedimentary imprint of volcanism during extinction.* Volcanism is the dominant source of Hg to the sedimentary archive and the enrichment of Hg concentrations has been linked to increased environmental loading due to volcanic activity such as LIP eruptions (e.g. Percival et al., 2017). Additionally, Hg isotope compositions have been shown to exhibit characteristic fractionation patterns representative of a volcanic source, they can therefore be used as a sedimentary tracer for volcanism (e.g. Thibodeau et al., 2016) within rocks recording the last appearance of archaeocyaths. This is essential in testing the hypothesis that LIP volcanism occurred during the BTE. The presence of a sedimentary trace of volcanism in rocks recording the BTE strengthens the hypothesis that volcanism played a part in driving environmental change and extinction. The link between volcanism and extinction has been widely suggested but never tested, therefore this aim is the first attempt to establish

a temporal connection between volcanism and extinction for the BTE. This aim asks*: 1) Is there evidence for increased concentrations of sedimentary Hg in the run up to and during the BTE? 2) If so, do sedimentary Hg enrichments support a hypothesis of increased environmental Hg loading? 3) Do Hg fractionation patterns support the hypothesis that sedimentary Hg is derived from a volcanogenic source?*

Finally, it is essential to: *Generate a Carbon (C) isotope chemostratigraphy of Cambrian seawater throughout the BTE.* When compared to the global $\delta^{13}C$ isotope curve, this data will serve as a chemostratigraphic framework with which to constrain the age of our study sections and elucidate the timing of extinction. $\delta^{13}C$ chemostratigraphy is regarded as a robust way to correlate geographically distal sections throughout geological time; this is therefore essential in enabling the temporal correlation of my field sections with other time equivalent sections worldwide. This therefore posed the questions: *1) Is the BTE marked by an excursion in the $\delta^{13}C$ isotope profile of seawater? If so, how does this relate to marine productivity and the carbon cycle during the BTE? 2) How does the regional $\delta^{13}C$ signal reflect the global record of carbon cycling through the BTE? 3) What is the relationship between the evolution of the seawater $\delta^{13}C$ signal, carbon cycling, productivity and extinction during the BTE?*

This project would constitute the first high resolution study of redox variation during the first mass extinction of the Phanerozoic, pairing paleobiologic and paleoecological assessment with innovative geochemical proxies to reveal the role of varying redox conditions during the BTE. In highlighting the persistence of marine anoxia in the early Cambrian, this proposal is a provocative reassessment of the early Cambrian as a period defined not exclusively by rapid and expansive biological radiation, but by severe environmental instability and mass extinction.

6.8. References:

Adams, R. D. (1995). Sequence-stratigraphy of Early-Middle Cambrian Grand Cycles in the Carrara Formation, southwest basin and range, California and Nevada. In *Sequence stratigraphy and depositional*

response to eustatic, tectonic and climatic forcing (pp. 277-328). Springer Netherlands.

Álvaro, J. J., Vennin, E., Moreno-Eiris, E., Perejón, A., Bechstädt, T. (2000). Sedimentary patterns across the Lower–Middle Cambrian transition in the Esla nappe (Cantabrian Mountains, northern Spain). *Sedimentary Geology*, *137*(1), 43-61.

Álvaro, J. J., Elicki, O., Geyer, G., Rushton, A. W., Shergold, J. H. (2003). Palaeogeographical controls on the Cambrian trilobite immigration and evolutionary patterns reported in the western Gondwana margin. *Palaeogeography, Palaeoclimatology, Palaeoecology*, *195*(1-2), 5-35.

Andersen, M. B., Stirling, C. H., Weyer, S. (2017). Uranium isotope fractionation. *Reviews in Mineralogy and Geochemistry*, *82*(1), 799-850.

Babcock, L. E., Peng, S., Ahlberg, P. (2017). Cambrian trilobite biostratigraphy and its role in developing an integrated history of the Earth system. *Lethaia*, *50*(3), 381-399.

Brasier, M. D. (1996). The basal Cambrian transition and Cambrian bio-events (from terminal Proterozoic extinctions to Cambrian biomeres). In *Global events and event stratigraphy in the Phanerozoic* (pp. 113-138). Springer, Berlin, Heidelberg.

Brasier, M. D., Lindsay, J. F. (2001). Did supercontinental amalgamation trigger the "Cambrian Explosion". *The Ecology of the Cambrian Radiation. Columbia University Press, New York*, 69-89.

Blum, J. D., Sherman, L. S., Johnson, M. W. (2014). Mercury isotopes in earth and environmental sciences. *Annual Review of Earth and Planetary Sciences*, *42*, 249-269.

Briggs, D. E. (2015). The Cambrian Explosion. *Current Biology*, *25*(19), R864- R868.

Chang, C., Hu, W., Wang, X., Yu, H., Yang, A., Cao, J., Yao, S. (2017). Carbon isotope stratigraphy of the lower to middle Cambrian on the eastern Yangtze   Platform, South China. *Palaeogeography, Palaeoclimatology, Palaeoecology*, *479*, 90-101.

Creveling, J. R., Johnston, D. T., Poulton, S. W., Kotrc, B., März, C., Schrag, D. P., Knoll, A. H. (2014). Phosphorus sources for phosphatic Cambrian carbonates. *Geological Society of America Bulletin*, *126*(1-2), 145-163.

Debrenne, F. (1991). Extinction of the Archaeocyatha. *Historical Biology*, *5*(2-4), 95-106.

Debrenne, F. (2007). Lower Cambrian archaeocyathan bioconstructions. *Comptes Rendus Palevol*, *6*(1-2), 5-19.

Emili, A., Koron, N., Covelli, S., Faganeli, J., Acquavita, A., Predonzani, S., De Vittor, C. (2011). Does anoxia affect mercury cycling at the sediment–water interface in the Gulf of Trieste (northern Adriatic Sea)? Incubation experiments using benthic flux chambers. *Applied geochemistry*, *26*(2), 194-204.

Evins, L. Z., Jourdan, F., Phillips, D. (2009). The Cambrian Kalkarindji Large Igneous Province: extent and characteristics based on new 40 Ar/39 Ar and geochemical data. *Lithos*, *110*(1), 294-304.

Faggetter, L.E., Wignall, P.B., Pruss, S.B., Sun, Y., Raine, R.J., Newton, R.J., Widdowson, M., Joachimski, M.M., Smith, P.M. (2016). Sequence   stratigraphy, chemostratigraphy and facies analysis of Cambrian Series 2 - Series 3 boundary strata in northwest Scotland. *Geological Magazine*, pp. 1-   13

Faggetter, L.E., Wignall, P. B., Pruss, S. B., Newton, R. J., Sun, Y., Crowley, S. F. (2017). Trilobite extinctions, facies changes and the ROECE carbon isotope excursion at the Cambrian Series 2–3 boundary, Great Basin, western   USA. *Palaeogeography, Palaeoclimatology, Palaeoecology*, *478*, 53-66.

Fedo, C. M., Cooper, J. D. (2001). Sedimentology and sequence stratigraphy of Neoproterozoic and Cambrian units across a craton-margin hinge zone, southeastern California, and implications for the early evolution of the Cordilleran margin. *Sedimentary Geology*, *141*, 501-522.

Fan, R., Deng, S., Zhang, X. (2011). Significant carbon isotope excursions in the Cambrian and their implications for global correlations. *Science China Earth   Sciences*, *54*(11), 1686-1695.

Feng, L., Li, C., Huang, J., Chang, H., Chu, X. (2014). A sulfate control on marine mid-depth euxinia on the early Cambrian (ca. 529–521 Ma) Yangtze platform, South China. *Precambrian Research*, *246*, 123-133.

Font, E., Adatte, T., Sial, A. N., de Lacerda, L. D., Keller, G., Punekar, J. (2016). Mercury anomaly, Deccan volcanism, and the end-Cretaceous mass extinction. *Geology*, *44*(2), 171-174.

Gerhardt, A. M., Gill, B. C. (2016). Elucidating the relationship between the later Cambrian end-Marjuman extinctions and SPICE Event. *Palaeogeography, palaeoclimatology, palaeoecology*, *461*, 362-373.

Geyer, G., Peel, J. S. (2011). The Henson Gletscher Formation, North Greenland, and its bearing on the global Cambrian Series 2–Series 3 boundary. *Bulletin   of Geosciences*, *86*(3), 465-534.

Geyer, G. (2015). Exotic trilobites from the Lower–Middle Cambrian boundary interval in Morocco and their bearing on the Cambrian Series 3 lower boundary. *Paläontologische Zeitschrift*, *89*(4), 749-781.

Geyer, G., Peel, J. S. (2017). Middle Cambrian trilobites from the Ekspedition Bræ Formation of North Greenland, with a reappraisal of the genus Elrathina. *Journal of Paleontology*, *91*(2), 265-293.

Gill, B. C., Lyons, T. W., Young, S. A., Kump, L. R., Knoll, A. H., Saltzman, M. R. (2011). Geochemical evidence for widespread euxinia in the Later Cambrian ocean. *Nature*, *469*(7328), 80-83.

Glass, L. M., Phillips, D. (2006). The Kalkarindji continental flood basalt province: A new Cambrian large igneous province in Australia with possible links to faunal extinctions. *Geology*, *34*(6), 461-464.

Gong, Q., Wang, X., Zhao, L., Grasby, S. E., Chen, Z. Q., Zhang, L., Li, Z. (2017). Mercury spikes suggest volcanic driver of the Ordovician-Silurian mass extinction. *Scientific Reports*, *7*.

Grasby, S.E., Beauchamp, B., Bond, D.P.G., Wignall, P.B., Sanei, H. (2016). Mercury anomalies associated with three extinction events (Capitanian crisis, l atest Permian extinction and the Smithian/Spathian extinction) in NW Pangea. Geological Magazine 153, 285-297. doi:10.1017/S0016756815000436

Guo, Q., Strauss, H., Liu, C., Zhao, Y., Yang, X., Peng, J., Yang, H. (2010). A negative carbon isotope excursion defines the boundary from Cambrian Series 2 to Cambrian Series 3 on the Yangtze Platform, South China. *Palaeogeography, Palaeoclimatology, Palaeoecology*, *285*(3-4), 143-151.

Guo, Q., Strauss, H., Zhao, Y., Yang, X., Peng, J., Yang, Y., Deng, Y. (2014). Reconstructing marine redox conditions for the transition between Cambrian Series 2 and Cambrian Series 3, Kaili area, Yangtze Platform: Evidence from biogenic sulfur and degree of pyritization. *Palaeogeography, Palaeoclimatology, Palaeoecology*, *398*, 144-153.

Hallam, A., Wignall, P. B. (1997). *Mass extinctions and their aftermath*. Oxford University Press, UK.

Hanley, L. M., Wingate, M. T. D. (2000). SHRIMP zircon age for an Early Cambrian dolerite dyke: an intrusive phase of the Antrim Plateau Volcanics of northern Australia. *Australian Journal of Earth Sciences*, *47*(6), 1029-1040.

Harvey, T. H., Williams, M., Condon, D. J., Wilby, P. R., Siveter, D. J., Rushton, A. W., Gabbott, S. E. (2011). A refined chronology for the Cambrian succession of southern Britain. *Journal of the Geological Society*, *168*(3), 705-716.

Hesselbo, S. P., Bjerrum, C. J., Hinnov, L. A., MacNiocaill, C., Miller, K. G., Riding, J. B., Van de Schootbrugge, B. (2013). Mochras borehole revisited: a new global standard for Early Jurassic earth history.

Higgins, J. A., Blättler, C. L., Lundstrom, E. A., Santiago-Ramos, D. P., Akhtar, A. A., Ahm, A. C., Swart, P. K. (2018). Mineralogy, early marine diagenesis, and the chemistry of shallow-water carbonate sediments. *Geochimica et Cosmochimica Acta*, *220*, 512-534.

Hough, M. L., Shields, G. A., Evins, L. Z., Strauss, H., Henderson, R. A., Mackenzie, S. (2006). A major sulphur isotope event at c. 510 Ma: a possible anoxia–extinction–volcanism connection during the Early–Middle Cambrian transition?. *Terra Nova*, *18*(4), 257-263.

Howley, R. A., Rees, M. N., Jiang, G. (2006). Significance of Middle
Cambrian mixed carbonate-siliciclastic units for global correlation:
southern Nevada, USA. *Palaeoworld*, *15*(3), 360-366.

Huselbee, M. Y., Thomas, A. T. (1998). Olenellus and conodonts from the
Durness Group, NW Scotland, and the correlation of the Durness
succession. *Scottish Journal of Geology*, *34*(1), 83-88.

James, N. P., Gravestock, D. I. (1990). Lower Cambrian shelf and shelf
margin buildups, Flinders Ranges, South
Australia. *Sedimentology*, *37*(3), 455-480.

Jin, C., Li, C., Algeo, T. J., Planavsky, N. J., Cui, H., Yang, X., Xie, S.
(2016). A highly redox-heterogeneous ocean in South China during
the early Cambrian (~ 529–514 Ma): Implications for biota-
environment co-evolution. *Earth and Planetary Science Letters*, *441*,
38-51.

Jones, D. S., Martini, A. M., Fike, D. A. Kaiho, K. (2017). A volcanic trigger
for the Late Ordovician mass extinction? Mercury data from south
China and Laurentia. *Geology*, *45*(7), 631-634.

Jourdan, F., Hodges, K., Sell, B., Schaltegger, U., Wingate, M. T. D., Evins,
L. Z., Blenkinsop, T. (2014). High-precision dating of the Kalkarindji
large igneous province, Australia, and synchrony with the Early–
Middle Cambrian (Stage 4–5) extinction. *Geology*, *42*(6), 543-546.

Keller, M., Cooper, J. D., Lehnert, O. (2012). Sauk megasequence
supersequences, southern Great Basin: second-order
accommodation events on the southwestern Cordilleran margin
platform.

Kirschvink, J. L., Raub, T. D. (2003). A methane fuse for the Cambrian
explosion: carbon cycles and true polar wander. *Comptes   Rendus
Geoscience*, *335*(1), 65-78.

Kump, L. R., Arthur, M. A. (1999). Interpreting carbon-isotope excursions:
carbonates and organic   matter. *Chemical Geology*, *161*(1-3), 181-
198.

Landing, E., Bowring, S. A., Davidek, K. L., Westrop, S. R., Geyer, G.,
Heldmaier, W. (1998). Duration of the Early Cambrian: U-Pb ages of

volcanic ashes from Avalon and Gondwana. *Canadian Journal of Earth Sciences*, *35*(4), 329-338.

Li, Z. (2017). Mercury spikes suggest volcanic driver of the Ordovician-Silurian mass extinction. *Scientific Reports*, *7*.

Lieberman, B. S. (2003). A new soft-bodied fauna: the Pioche Formation of Nevada. *Journal of Paleontology*, *77*(4), 674-690.

Maloof, A. C., Ramezani, J., Bowring, S. A., Fike, D. A., Porter, S. M., Mazouad, M. (2010). Constraints on early Cambrian carbon cycling from the duration of the Nemakit-Daldynian–Tommotian boundary δ13C shift, Morocco. *Geology*, *38*(7), 623-626.

Montañez, I. P., Banner, J. L., Osleger, D. A., Borg, L. E., Bosserman, P. J. (1996). Integrated Sr isotope variations and sea-level history of Middle to Upper Cambrian platform carbonates: Implications for the evolution of Cambrian seawater 87Sr/86Sr. *Geology*, *24*(10), 917-920.

Montañez, I. P., Osleger, D. A., Banner, J. L., Mack, L. E., Musgrove, M. (2000). Evolution of the Sr and C isotope composition of Cambrian oceans. *GSA today*, *10*(5), 1-7.

Morgan, W.A., 2012. Sequence stratigraphy of the great American carbonate bank. In: Derby, J.R., Fritz, R.D., Longacre, S.A., Morgan, W.A., Sternbach, C.A. (Eds.), The Great American Carbonate Bank: the Geology and Economic Resources of the Cambrian-Ordovician Sauk Megasequences of Laurentia: Association of American Petroleum Geologists Memoir 98, pp. 37–79.

Ogg, J. G., Ogg, G., Gradstein, F. M. (2016). *A Concise Geologic Time Scale: 2016*. Elsevier.

Pagès, A., Schmid, S. (2016). Euxinia linked to the Cambrian Drumian carbon isotope excursion (DICE) in Australia: Geochemical and chemostratigraphic evidence. *Palaeogeography, Palaeoclimatology, Palaeoecology*, *461*, 65-76.

Palmer, A. R. (1965). Biomere: A new kind of biostratigraphic unit. *Journal of Paleontology*, 149-153.

Palmer, A. R., Taylor, M. E. (1981). Subdivision of the Sauk sequence. In *Short Papers for the Second International Symposium on the*

Cambrian System: US Geological Survey, Open-File Report (pp. 81-743).

Palmer, A. R. (1984). The biomere problem: evolution of an idea. *Journal of Paleontology*, 599-611.

Palmer, A. R. (1998). Terminal early Cambrian extinction of the Olenellina: documentation from the Pioche Formation, Nevada. *Journal of Paleontology*, *72*(04), 650-672.

Palmer, A. R., Halley, R. B. (1979). *Physical stratigraphy and trilobite biostratigraphy of the Carrara Formation (Lower and Middle Cambrian) in the southern Great Basin* (No. 1047). US Govt. Print. Off..

Pasquier, V., Sansjofre, P., Rabineau, M., Revillon, S., Houghton, J., Fike, D. A. (2017). Pyrite sulfur isotopes reveal glacial− interglacial environmental changes. *Proceedings of the National Academy of Sciences*, *114*(23), 5941-5945.

Peng, S., Babcock, L. E., Cooper, R. A. (2012). The Cambrian Period. In *The geologic time scale* (pp. 437-488).

Percival, L.M.E., Witt, M.L.I., Mather, T.A., Hermoso, M., Jenkyns, H.C., Hesselbo, S.P., Al-Suwaidi, A.H., Storm, M.S., Xu, W., Ruhl, M. (2015). Globally enhanced mercury deposition during the end-Pliensbachian extinction and Toarcian OAE: A link to the Karoo-Ferrar Large Igneous Province. *Earth and Planetary Science Letters 428*, 267-280.

Percival, L. M., Cohen, A. S., Davies, M. K., Dickson, A. J., Hesselbo, S. P., Jenkyns, H. C., Xu, W. (2016). Osmium isotope evidence for two pulses of increased continental weathering linked to Early Jurassic volcanism and climate change. *Geology*, *44*(9), 759-762.

Percival, L. M., Ruhl, M., Hesselbo, S. P., Jenkyns, H. C., Mather, T. A., Whiteside, J. H. (2017). Mercury evidence for pulsed volcanism during the end-Triassic mass extinction. *Proceedings of the National Academy of Sciences*, *114*(30), 7929-7934.

Peters, S. E., Gaines, R. R. (2012). Formation of the 'Great Unconformity as a trigger for the Cambrian explosion. *Nature*, *484*(7394), 363.

Porter, S. M. (2004). Closing the phosphatization window: testing for the influence of taphonomic megabias on the pattern of small shelly fossil decline. *Palaios*, *19*(2), 178-183.

Porter, S. M. (2007). Seawater chemistry and early carbonate biomineralization. *Science*, *316*(5829), 1302-1302.

Prave, A. R. (1992). Depositional and sequence stratigraphic framework of the Lower Cambrian Zabriskie Quartzite: implications for regional correlations and the Early Cambrian paleogeography of the Death Valley region of California and Nevada. *Geological Society of America Bulletin*, *104*(5), 505-515.

Present, T. M., Paris, G., Burke, A., Fischer, W. W., Adkins, J. F. (2015). Large carbonate associated sulfate isotopic variability between brachiopods, micrite, and other sedimentary components in Late Ordovician strata. *Earth and Planetary Science Letters*, *432*, 187-198.

Raine, R. J., Smith, M. P. (2012). Sequence stratigraphy of the Scottish Laurentian margin and recognition of the Sauk Megasequence. In *The Great American Carbonate Bank: The Geology and Economic Resources of the Cambrian–Ordovician Sauk Megasequence of Laurentia* (eds J. R. Derby, R. D. Fritz, S. A. Longacre, W. A. Morgan & C. A. Sternbach), pp. 575–98. American Association of Petroleum Geologists Memoir 98.

Ren, Y., Zhong, D., Gao, C., Liang, T., Sun, H., Wu, D., Zheng, X. (2017). High-resolution carbon isotope records and correlations of the lower Cambrian Longwangmiao formation (stage 4, Toyonian) in Chongqing, South China. *Palaeogeography, Palaeoclimatology, Palaeoecology*.

Rowland, S. M., Gangloff, R. A. (1988). Structure and paleoecology of Lower Cambrian reefs. *Palaios*, 111-135.

Rowland, S. M., Hicks, M. (2004). The early Cambrian experiment in reef-building by metazoans. *The Paleontological Society Papers*, *10*, 107-130.

Ruhl, M., Hesselbo, S. P., Hinnov, L., Jenkyns, H. C., Xu, W., Riding, J. B., Leng, M. J. (2016). Astronomical constraints on the duration of the

Early Jurassic Pliensbachian Stage and global climatic fluctuations. *Earth and Planetary Science Letters*, *455*, 149-165.

Saltzman, M. R., Ripperdan, R. L., Brasier, M. D., Lohmann, K. C., Robison, R. A., Chang, W. T., Runnegar, B. (2000). A global carbon isotope excursion (SPICE) during the Late Cambrian: relation to trilobite extinctions, organic-matter burial and sea level. *Palaeogeography, Palaeoclimatology, Palaeoecology*, *162*(3-4), 211-223.

Sanei, H., Grasby, S., Beauchamp, B. (2012). Latest Permian mercury anomalies. *Geology 40*, 63–66.

Schmid, S. (2017). Chemostratigraphy and palaeo-environmental characterisation of the Cambrian stratigraphy in the Amadeus Basin, Australia. *Chemical Geology*, *451*, 169-182.

Sepkoski, J. J. (1996). Patterns of Phanerozoic extinction: a perspective from global data bases. In *Global events and event stratigraphy in the Phanerozoic* (pp. 35-51). Springer, Berlin, Heidelberg.

Silva-Tamayo, J. C., Lau, K. V., Jost, A. B., Payne, J. L., Wignall, P. B., Newton, R. J., Lehrmann, D. J. (2018). Global perturbation of the marine calcium cycle during the Permian-Triassic transition. *Geological Society of America Bulletin*.

Sloss, L. L. (1963). Sequences in the cratonic interior of North America. *Geological Society of America Bulletin*, *74*(2), 93-114.

Smith, T., Kelman, A. P., Nicoll, R., Edwards, D., Hall, L., Laurie, J., Carr, L. (2013). An updated stratigraphic framework for the Georgina Basin, NT and Queensland. *The APPEA Journal*, *53*(2), 487-487.

Smith, E. F., Macdonald, F. A., Petach, T. A., Bold, U., Schrag, D. P. (2016). Integrated stratigraphic, geochemical, and paleontological late Ediacaran to early Cambrian records from southwestern Mongolia. *Bulletin*, *128*(3-4), 442-468.

Southgate, P. N., Shergold, J. H. (1991). Application of sequence stratigraphic concepts to Middle Cambrian phosphogenesis, Georgina Basin, Australia. *Journal of Australian Geology and Geophysics*, *12*, 119-144.

Squire, R. J., Campbell, I. H., Allen, C. M., Wilson, C. J. (2006). Did the Transgondwanan Supermountain trigger the explosive radiation of

animals on Earth?. *Earth and Planetary Science Letters*, *250*(1-2), 116-133.

Sundberg, F. A., McCollum, L. B. (2000). Ptychopariid trilobites of the lower-middle Cambrian boundary interval, Pioche Shale, southeastern Nevada. *Journal of Paleontology*, *74*(4), 604-630.

Thibodeau, A.M., Ritterbush, K., Yager, J.A., West, A.J., Ibarra, Y., Bottjer, D.J., Berelson, W.M., Bergquist, B.A., Corsetti, F.A. (2016). Mercury anomalies and the timing of biotic recovery following the end-Triassic mass extinction. Nature   Communications 7:11147, doi: 19.1038/ncomms11147

Thomas, R. D. K., Shearman, R. M., Stewart, G. W. (2000). Evolutionary exploitation of design options by the first animals with hard skeletons. *Science*, *288*(5469), 1239-1242.

Zhang, W., Shi, X., Jiang, G., Tang, D., Wang, X. (2015). Mass-occurrence of oncoids at the Cambrian Series 2–Series 3 transition: Implications for microbial resurgence following an Early Cambrian extinction. *Gondwana Research*, *28*(1), 432-450.

Zhu, M. Y., Zhang, J. M., Li, G. X., Yang, A. H. (2004). Evolution of C isotopes in the Cambrian of China: implications for Cambrian subdivision and trilobite mass extinctions. *Geobios*, *37*(2), 287-301.

Zhu, M. Y., Babcock, L. E., Peng, S. C. (2006). Advances in Cambrian stratigraphy and paleontology: integrating correlation techniques, paleobiology, taphonomy and paleoenvironmental reconstruction. *Palaeoworld*, *15*(3), 217-222.

Wang, X., Hu, W., Yao, S., Chen, Q., Xie, X. (2011). Carbon and strontium isotopes and global correlation of Cambrian Series 2-Series 3 carbonate rocks in the Keping area of the northwestern Tarim Basin, NW China. *Marine and Petroleum Geology*, *28*(5), 992-1002.

Webster, M., Gaines, R. R., Hughes, N. C. (2008). Microstratigraphy, trilobite biostratinomy, and depositional environment of the "Lower Cambrian" Ruin Wash Lagerstätte, Pioche Formation, Nevada. *Palaeogeography, Palaeoclimatology, Palaeoecology*, *264*(1), 100-122.

Wignall, P. B. (2001). Large igneous provinces and mass extinctions. *Earth-science reviews*, *53*(1), 1-33.

Wotte, T., Strauss, H., Fugmann, A., Garbe-Schönberg, D. (2012). Paired δ 34 S data from carbonate-associated sulfate and chromium-reducible sulfur across the traditional Lower–Middle Cambrian boundary of W-Gondwana. *Geochimica et Cosmochimica Acta*, *85*, 228-253.

Zhang, W., Shi, X., Jiang, G., Tang, D., Wang, X. (2015). Mass-occurrence of oncoids at the Cambrian Series 2–Series 3 transition: implications for microbial resurgence following an early Cambrian extinction. *Gondwana Research*, *28*(1), 432-450.

Zhuravlev, A. Y. (1996). Reef ecosytem recovery after the Early Cambrian extinction. *Geological Society, London, Special Publications*, *102*(1), 79-96.

Zhuravlev, A. Y. (2001). Paleoecology of Cambrian reef ecosystems. In *The history and sedimentology of ancient reef systems* (pp. 121-157). Springer, Boston, MA.

Zhuravlev, A. I., Riding, R. (Eds.). (2001). *The ecology of the Cambrian radiation*. Columbia University Press.

Zhuravlev, A. Y., Wood, R. A. (1996). Anoxia as the cause of the mid-Early Cambrian (Botomian) extinction event. *Geology*, *24*(4), 311-314.

Appendix A: Supplementary material from Chapter 3. Stratigraphic log of the Pioche Formation at Ruin Wash, Chief Range, Nevada. See Fig. 3.2 for key.

PIOCHE FM,
RUIN WASH,
NV

KEY

← *e* Framboids- euxinic
← *d* Framboids- dysoxic

Silty marl
Muddy/silty Limestone
Limestone
Dolomicrite
Fine marl
Marl
Silty/sandy clastics
Ooids
Oncoids
Nodular fabric

e — Olenellid
e — extinction

C-SHALE

COMBINED METALS

30

20

(m)

10

0

Facies

MWPG
CSFMC
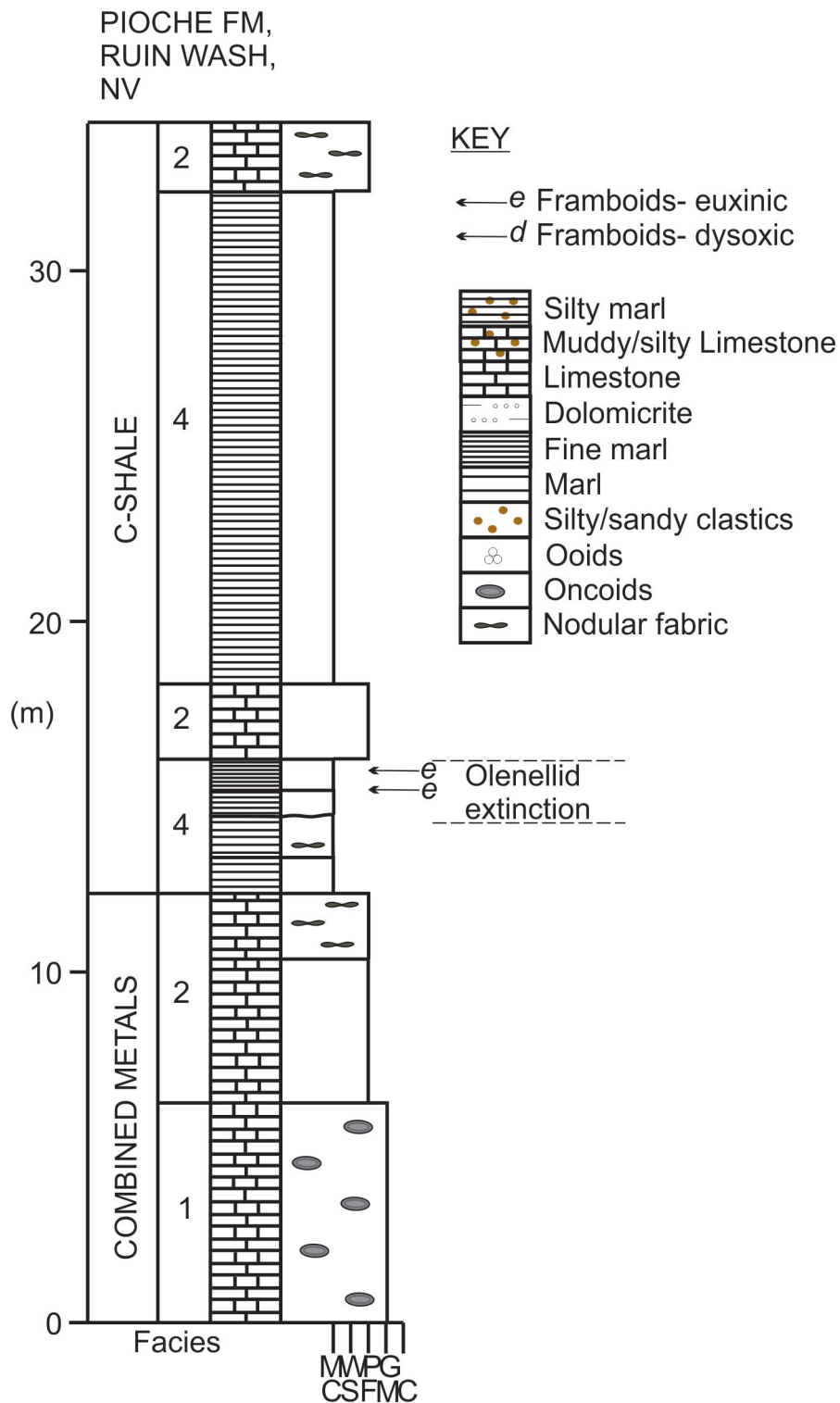
Appendix B: Supplementary material from Chapter 3. Cross-plots of isotope data from the Carrara and Pioche formations.

2 CarraraFormation

3 Pioche Formation

4 Carrara Formation

5 Pioche Formation

6 Pioche Formation
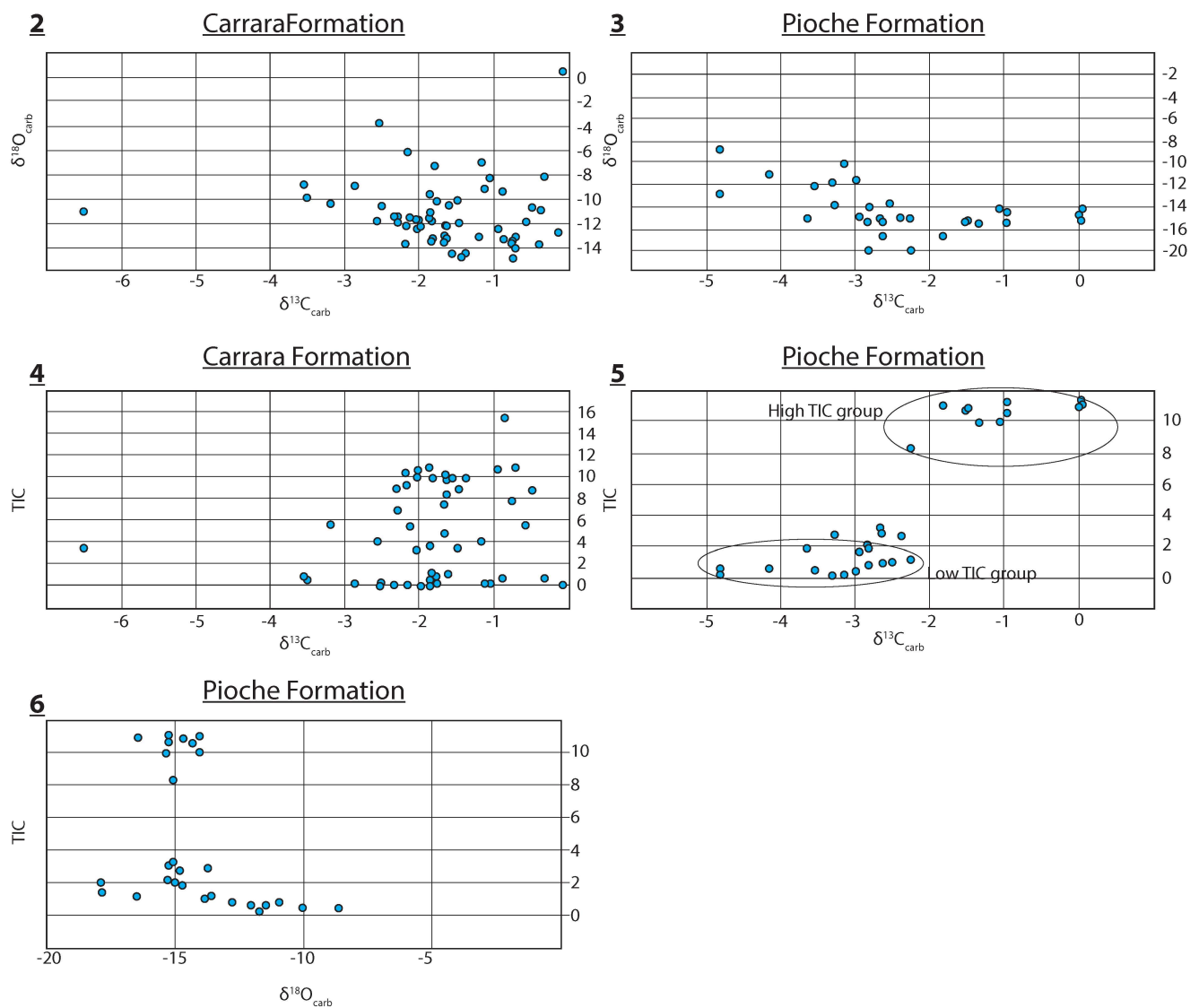
Table 2. 1: Geochemical data from both Loch Eriboll and Ardvreck Castle locations. Height is measured from the base of logged sections (Fig. 2. 2).

	Original ID	Lithology	Height (m)	δ13Ccarb mean ‰ (V-PDB)	δ18Ocarb mean ‰ (VPDB)	δ13Corg ‰ (VPDB)	wt% S	wt% Total	TOC wt%	TIC wt%
	LOCH ERIBOLL									
SALTERELLA GRIT	AS36	Sstone	0.1			-25.16	0.096	0.088	0.08	0.006
	AS37	Sstone	0.5			-25.29	0.166	0.083	0.09	-0.010
	AS38	Sstone	1			-23.84	0.229	0.844	0.03	0.815
	AS39	Sstone	1.75			-25.70	0.063	0.059	0.01	0.051
	AS40	Sstone	3.7			-25.64	0.060	0.051	0.01	0.045
	AS41	Sstone	3.8			-25.79	0.054	0.114	0.08	0.031
	AS42	Sstone	4.5			-26.40	0.324	0.030	0.02	0.015
	AS43	Sstone	5.75			-25.95	0.040	0.036	0.01	0.026
	AS44	Sstone	7.5			-24.61	0.138	1.841	0.02	1.824
	AS45	Sstone	8.25			-24.46	0.354	6.644	0.10	6.539
	AS46	Sstone	8.8	-2.98	-10.93	-22.89	0.515	4.829	0.09	4.734
	AS47	Sstone	9.15			-23.81	0.377	4.353	0.23	4.119
GHRUDAIDH FORMATION	AS48	Carbonate	9.75	-2.84	-11.43	-23.75	0.734	3.985	0.20	3.786
	AS49	Carbonate	10.1			-24.76	0.066	9.741	0.45	9.296
	AS50	Carbonate	10.75	-1.85	-8.52	-24.73	-0.002	8.819	0.11	8.709
	AS51	Carbonate	10.95			-25.04	-0.001	10.393	0.12	10.270
	AS52	Carbonate	11.05	-1.77	-8.99	-24.50	-0.001	8.182	0.31	7.877
	AS53	Carbonate	11.4	-1.65	-8.84	-25.64	-0.001	11.057	0.55	10.508
	AS54	Carbonate	11.8	-1.37	-8.65	-22.61	-0.001	12.71	0.68	12.031
	AS55	Carbonate	12.25			-23.36	-0.002	13.128		
	AS56	Carbonate	13	-1.17	-7.83	-24.91	-0.001	13.009		
	AS57	Carbonate	13.5			-24.71	0.000	12.876	0.23	12.648
	AS58	Carbonate	14.55	-0.86	-6.82	-23.23	0.027	13.166	0.88	12.290
	AS59	Carbonate	15.6	-0.97	-6.77	-21.34	0.000	12.513	0.18	12.330
	AS60	Carbonate	17.1	-1.06	-6.65	-24.34	-0.002	13.592	0.67	12.923
	AS61	Carbonate	18			-24.80	-0.001	13.326	0.72	12.606
	AS62	Carbonate	18.5	-0.38	-7.01	-23.47	-0.001	12.93	0.44	12.490
	AS63	Carbonate	20			-25.65	0.026	13.557	0.84	12.717
	AS64	Carbonate	20.55	-1.45	-6.36	-27.86	-0.002	14.057	0.91	13.149
	AS65	Carbonate	22.25	-1.36	-6.20	-25.84	0.006	13.516	1.61	11.908
	AS66	Carbonate	22.25	-1.11	-6.54	-26.87	0.003	14.281	2.58	11.705
	AS67	Carbonate	26.5	-0.81	-7.12	-24.53	0.002	13.68	4.17	9.514
	AS32	Carbonate	28.55	-0.96	-7.55		0.004	14.043	0.00	14.041
	AS33	Carbonate	28.55	-1.48	-6.67		0.014	13.937	5.16	8.780
	AS34	Carbonate	31.35	-1.60	-5.82		-0.003	13.889	4.08	9.812
	AS35	Carbonate	31.35	-1.41	-6.28	-23.07	0.019	13.171	0.58	12.588
	AS1	Carbonate	33.9	-1.49	-5.91	-27.05	-0.001	13.863	1.58	12.280
	AS2	Carbonate	34.5	-1.36	-6.50		0.007	13.92	0.00	13.918
	AS3	Carbonate	34.9	-1.60	-5.81	-25.67	-0.008	14.043	0.81	13.236
	AS4	Carbonate	35.5	-1.60	-5.28	-24.63	0.004	13.342	0.96	12.378
	AS5	Carbonate	36.1	-1.87	-5.86	-23.37	0.010	13.473	1.37	12.108
	AS6	Carbonate	36.1	-1.66	-5.90		0.013	13.513	0.00	13.512
	AS7	Carbonate	36.75	-1.27	-5.70	-26.17	0.011	12.828	1.53	11.299
	AS8	Carbonate	37.05			-25.67	0.012	12.13	0.95	11.180
	AS9.1	Carbonate	37.2	-1.48	-5.71	-26.72	-0.002	12.906	2.39	10.521
	AS11	Carbonate	37.4			-25.98	-0.001	13.093	1.42	11.673
	AS12	Carbonate	37.8	-1.77	-6.76	-25.75	-0.009	12.49	1.05	11.442
	AS13	Carbonate	38.5			-22.82	0.005	13.284	1.35	11.931
	AS14	Carbonate	38.85	-1.61	-6.17	-23.87	0.010	13.644	1.18	12.469
	AS15	Carbonate	39.1	-1.78	-7.22	-22.20	-0.001	13.405	2.08	11.321
	AS16	Carbonate	39.55			-21.92	-0.006	13.869	1.60	12.274
	AS17	Carbonate	40	-1.63	-6.40	-20.15	-0.002	13.859	2.17	11.693
	AS18	Carbonate	40.95				-0.001	13.875		
	AS19	Carbonate	41.75	-1.57	-6.60	-20.72	-0.002	13.767	5.19	8.577
	AS20	Carbonate	42.2			-24.31	0.000	13.85	0.62	13.226
	AS21	Carbonate	42.6	-1.22	-6.17	-25.47	0.000	13.679	0.72	12.959
	AS22	Carbonate	43.5			-25.63	0.005	13.802	0.11	13.693
	AS23	Carbonate	44	-0.91	-6.60	-25.00	0.002	13.925	0.12	13.804
	AS24	Carbonate	45.5	-0.62	-6.39	-25.57	-0.002	13.599	0.29	13.311
	AS25	Carbonate	47			-22.53	0.003	13.774	1.15	12.621
	AS26	Carbonate	48	-0.78	-6.63	-20.93	-0.001	13.972	0.23	13.742
	AS27	Carbonate	49.2			-22.21	0.004	13.974	0.51	13.462
	AS29	Carbonate	51.2	-1.63	-6.63		-0.002	13.544	3.91	9.634
	AS30	Carbonate	52.2			-24.97	-0.003	13.385	0.83	12.554

Table 3.1: Facies of the Carrara and Pioche formations.

Facies	Sub-facies	Description	Occurrence
1. Grainstone	1. Ooidal grainstone (Fig 6. D)	Ooidal grainstone composed of ooids, trilobite and hyolith hash with minor quartz silt (Fig. 4 A). This facies forms prominent ledges. Some beds contain rip-up intraclasts and inclined stacked shell material in a chevron arrangement (Fig 4. D), with prod and skip marks at bed bases. Some bioclasts are extensively overgrown by orange/brown iron oxides. Ooids are often micritised, obscuring any original concentric structure.	Emigrant Pass, Eagle Mountain Shale and Pyramid Shale members.
	2. Peloidal grainstone (Fig 6. C)	Millimetre-sized micritic pellets with fine quartz sand grains in a fine sparite matrix. Minor bioclastic components, dominated by trilobite fragments and rounded silty micrite lithoclasts up to 1cm in size (Fig. 6 C). Abundant oxidised pyrite cubes.	Emigrant Pass, Eagle Mountain Shale. Oak Springs Summit, Combined Metals Member.
	3. Bioclastic grainstone (Fig 5. D)	Predominantly an orange-brown bioclastic grainstone. Skeletal material is dominated by disarticulated and often abraded trilobite carapaces and trilobite spines alongside abundant hyolith remains and rarer echinoderm plates. Chlorite is present both as well rounded detrital grains and also replacing shell fragments. The matrix ranges from fine to coarse sparite cement. Trilobite, echinoderm and hyolith remains are frequently micritised and replaced by iron oxide. Locally they form oolitic deposits (Fig 6. D). These beds occur ubiquitously at Emigrant Pass, though they becoming less frequent in the upper 40m, and are discontinuous lenses.	Emigrant Pass, Eagle Mountain Shale, Echo Shale, Pyramid Shale members.
2. Packstone	4. Oncolitic packstone (Fig 4. B, 5. C)	Oncolitic grainstone beds form prominent ledges at Emigrant Pass (Fig. 4 B). Oncoid nuclei are well-rounded bioclasts, typically echinoderm plates. Oncoids are generally 5mm in diameter and occur within a matrix composed of abraded and fragmented trilobite, echinoderm and hyolith hash. Some shelly fragments are micritised and exhibit coatings of, and replacement by, dark brown and orange iron-oxides.	Emigrant Pass, Gold Ace, Pyramid Shale, Red Pass Limestone members. Oak Springs Summit, Combined Metals Member.
	5. Bioclastic packstone	Grey, intensely bioturbated (II4) bioclastic packstone containing abundant trilobite and rare echinoderm fragments and micro-oncoids. Bioclasts are broken and abraded, shell fragments have micrite envelopes.	Oak Springs Summit, Combined Metals Member.
	6. Silty bioclastic packstone (Fig 5. B)	This facies forms prominent ribs and is a well-bioturbated (II5) bioclastic packstone with abundant quartz silt. Trilobite carapaces and other shelly fragments (hyoliths, echinoderm plates) occur within a muddy micrite matrix. Abundant within the matrix is chlorite, chamosite and oxidised iron. Stylolites are lined with iron oxides.	Emigrant Pass, Eagle Mountain Shale, Echo Shale, Gold Ace Limestone members.

3. Silty marl	7. Silty marl (Fig 4. E, F; 5. A)	Rubbly and recessive weathering, grey to grey-green, fissile, calcareous siltstone. The silt grains include well-rounded detrital chlorite grains (Fig. 6 A, E), well-sorted fine quartz silt grains and rounded sand-grains of chlorite and clinochlore. This facies alternates between fissile and bioturbated. Bioturbation is commonly ~1cm in depth and not abundant enough to destroy lamination (Fig. 4 G, H). *Thalassinoides* trace fossils along with *Planolites* (Fig. 4 C) occur. The most intense bioturbation forms grey-orange couplets (5-10cm scale) with vertical and horizontal burrows (II5) and trilobite fragments. This facies has a minor chlorite fraction in the matrix. Rare hyolith and echinoderm are present, sometimes overgrown by iron oxide (Fig 6. F). Minor constituents within the matrix are rare, well rounded, fine feldspar grains; iron oxide replacing cubic pyrite, and chlorite (Fig. 5 A).	Emigrant Pass, Eagle Mountain Shale, Gold Ace and Pyramid Shale members. Oak Springs Summit- Combined Metals, C-Shale members.
4. Marl	8. Marl (Fig. 6 B)	This is the most abundant facies in the sections. The grey-green marls vary from fissile to mildy bioturbated, the most common form of bioturbation is vertical burrows. Trilobite fragments and other shell remains are recrystallised by orange/brown iron oxide needles (Fig. 6 B). Minor constituents are well rounded detrital chlorite grains and as flecks within the matrix. This facies occasionally displays weak microbial laminations. At Oak Spring Summit, this facies is a red weathering (grey-green when fresh) massive, very fine, mudstone displaying indistinct nodular fabrics at outcrop.	Emigrant Pass, Eagle Mountain Shale, Gold Ace Limestone, Pyramid Shale, Red Pass Limestone members. Oak Springs Summit- Combined Metals, C- Shale members.
	9. Laminated pyritic dolomicrite	Red-purple laminated mudstone (Fig. 4 F) is comprised of medium to fine dolomite rhombs amongst a pyritic micrite matrix. Laminations are accentuated by the horizontal accumulation of very small mica flakes. Some rare larger trilobite fragments are present and are replaced by iron oxide minerals..	Emigrant Pass, Eagle Mountain, Echo Shale members.

217

Table 3.2: Geochemical and framboid measurements for the Carrara and Pioche formations at Emigrant Pass (EP) and Oak Springs Summit (OSS) and framboid data from the Pioche Formation at Ruin Wash (RW).

					EMIGRANT PASS							
Sample	height (m)	$\delta1^3C^{crb}$ ‰	δ1Ocarb ‰	δ13Ccarb ‰	$\delta1^{O}c^{arb}$ ‰	wt.% S	wt.% C	wt. % TOC	wt.% TIC	eq. wt.% calcite	$10^3\delta^{13}C$ VPDB	$10^3\delta^{18}O$ VPDB
EP1	0.3					0.00	0.04	0.05	0.00	0.00		
EP2	1.35			-2.16	-6.10	0.00	0.21	0.02	0.19	1.57	-2.16	-6.10
EP3	1.65					0.00	0.04	0.03	0.02	0.14		
EP4	2.25			-3.56	-8.77	0.03	0.92	0.02	0.90	7.51	-3.56	-8.77
EP5	2.5					0.00	0.00	0.03	0.00	0.00		
EP6	3.85					0.00	0.03	0.02	0.01	0.09		
EP7	5.35					0.00	0.00	0.03	0.00	0.00		
EP8	7.05					0.02	0.00	0.04	0.00	0.00		
EP9	8.25					0.01	0.00	0.02	0.00	0.00		
EP11	9.5					0.00	0.08	0.03	0.05	0.39		
EP10	10.05			-3.20	-10.31	0.00	5.71	0.08	5.63	46.95	-3.20	-10.31
EP12	11.25			-1.18	-6.98	0.01	4.07	0.06	4.01	33.39	-1.18	-6.98
EP13	11.6					0.01	0.11	0.02	0.09	0.73		
EP15	11.85			-0.50	-10.62	0.00	8.88	0.06	8.81	73.44	-0.50	-10.62
EP14	13.45					0.00	0.01	0.02	0.00	0.00		
EP17	15.85	-6.46	-10.93	-6.52	-11.01	0.00	3.47	0.03	3.44	28.65	-6.49	-10.97
EP16	16.15					0.00	0.00	0.03	0.00	0.00		
EP18	17					0.00	0.06	0.04	0.02	0.18		
EP19	20.65	-1.80	-7.27			0.01	0.88	0.02	0.86	7.19	-1.80	-7.27
EP20	21.45					0.00	0.04	0.04	0.00	0.00		
EP21	22.6	-0.33	-8.09			0.00	0.62	0.04	0.58	4.87	-0.33	-8.09
EP22	24.05					0.00	0.03	0.02	0.01	0.07		
EP23	25.15	-2.40	-11.58	-2.22	-11.41	0.03	9.01	0.08	8.93	74.43	-2.31	-11.50
EP24	27.25					0.00	0.05	0.02	0.03	0.25		
EP25	28.05	-2.12	-11.88	-2.14	-11.02	0.00	5.53	0.04	5.49	45.75	-2.13	-11.45
EP26	29.75					0.00	0.07	0.02	0.05	0.44		
EP27	31.5					0.00	11.15	0.01	11.14	92.85		
EP28	32.8			-2.56	-11.73	0.00	4.14	0.01	4.13	34.40	-2.56	-11.73
EP29	33.45	-1.49	-14.69	-1.66	-14.17	0.00	9.97	0.05	9.92	82.70	-1.57	-14.43
EP30	33.55			-1.38	-14.38	0.00	10.15	0.13	10.02	83.51	-1.38	-14.38
EP31	35.45	-1.97	-10.66	-2.10	-12.67	0.01	10.22	0.20	10.02	83.47	-2.03	-11.66
EP33	37.8			-1.77	-10.10	0.00	0.22	0.04	0.18	1.52	-1.77	-10.10
EP32	39.65	-1.66	-12.17	-1.63	-12.12	0.00	8.48	0.06	8.42	70.19	-1.65	-12.15
EP34	40.65			-1.62	-10.41	0.00	1.11	0.04	1.07	8.94	-1.62	-10.41
EP35	41.7	-1.67	-13.62	-1.62	-12.46	0.00	10.37	0.60	9.77	81.40	-1.64	-13.04
EP36	43.75	-2.12	-12.25	-2.23	-12.04	0.00	9.49	0.22	9.26	77.21	-2.18	-12.14
EP37	44.7					0.00	0.08	0.05	0.04	0.30		
EP38	46.9	-1.99	-12.19			0.00	0.45	0.41	0.04	0.33	-1.99	-12.19
EP39	48.5			-2.05	-11.64	0.00	3.31	0.03	3.28	27.31	-2.05	-11.64
EP40	50.3					0.01	0.05	0.03	0.01	0.11		
EP41	50.65	-2.23	-13.72	-2.15	-13.52	0.01	10.50	0.11	10.39	86.58	-2.19	-13.62
EP42	51.1			-1.84	-11.76	0.00	1.24	0.05	1.19	9.91	-1.84	-11.76
EP43	52.9	-2.12	-12.19	-1.94	-12.56	0.01	10.91	0.23	10.68	89.00	-2.03	-12.38
EP44	53.9			-1.67	-12.92	0.00	4.89	0.07	4.82	40.17	-1.67	-12.92
EP45	54.85	-1.87	-11.48			0.00	10.99	0.14	10.85	90.40	-1.87	-11.48
EP46	56	-0.78	-13.62	-0.76	-13.47	0.00	8.10	0.24	7.86	65.50	-0.77	-13.54
EP47	57.1			-0.95	-12.36	0.01	11.03	0.29	10.74	89.52	-0.95	-12.36
EP48	60.05	-0.78	-13.50	-0.97	-12.94	0.00	16.24	0.70	15.54	129.51	-0.87	-13.22
EP49	63			-0.57	-11.83	0.00	10.83	5.17	5.66	47.19	-0.57	-11.83
EP50	65	-0.72	-14.02			0.00	11.04	0.14	10.91	90.88	-0.72	-14.02
EP51	67	-0.90	-9.37			0.01	0.82	0.06	0.76	6.37	-0.90	-9.37
EP52	68			-1.87	-9.59	0.00	3.77	0.05	3.72	31.02	-1.87	-9.59
EP53	69.55			-0.09	0.49	0.00	0.17	0.06	0.11	0.94	-0.09	0.49
EP54	71			-1.86	-11.06	0.00	0.06	0.03	0.03	0.28	-1.86	-11.06
EP55	72.5	-1.14	-9.09	-1.86	-11.06	0.00	3.60	0.03	3.56	29.69	-1.50	-10.07
EP56	74.65	-1.89	-13.78	-1.76	-12.60	0.00	10.10	0.11	9.98	83.17	-1.82	-13.19

Sample	height (m)	$10^3\delta^{13}C$ VPDB	$10^3\delta^{18}O$ VPDB	$10^3\delta^{13}C$ VPDB	$10^3\delta^{18}O$ VPDB	wt% S	wt% C	wt. % TOC	wt.% TIC	eq. wt.% calcite	$10^3\delta^{13}C$ VPDB	$10^3\delta^{18}O$ VPDB
EP57	75.85	-1.68	-13.49			0.00	7.65	0.09	7.56	62.97	-1.68	-13.49
EP58	80.55			-1.14	-9.15	0.00	0.33	0.04	0.29	2.44	-1.14	-9.15
EP59	83.2	-2.30	-12.97	-2.29	-10.68	0.00	6.95	0.00	6.95	57.88	-2.30	-11.82
EP60	84.2	-1.73	-13.07	-1.58	-11.11	0.01	10.45	0.17	10.27	85.62	-1.66	-12.09
EP61	58.3			-1.06	-8.27	0.00	0.31	0.03	0.28	2.33	-1.06	-8.27
EP62	86.3	-1.99	-11.73	-2.07	-11.58	0.00	10.71	0.12	10.59	88.27	-2.03	-11.66
EP63	88.4					0.00	0.00	0.03	0.00	0.00		
EP64	90.4					0.00	0.00	0.01	0.00	0.00		
EP65	92.4					0.00	0.07	0.01	0.06	0.46		
EP66	94.4					0.00	0.04	0.02	0.03	0.24		
EP67	99.65					0.00	0.11	0.01	0.09	0.79		
EP68	101.5			-2.87	-8.81	0.00	0.28	0.03	0.26	2.13	-2.87	-8.81
EP69	103.1			-2.53	-3.71	0.00	0.15	0.03	0.13	1.06	-2.53	-3.71
EP70	105	-3.52	-9.9			0.01	0.62	0.00	0.62	5.20	-3.52	-9.90
EP71	109.15	-2.51	-10.47			0.00	0.30	0.01	0.29	2.38	-2.51	-10.47
EP72	112			-1.85	-13.40	0.09	0.57	0.01	0.56	4.67	-1.85	-13.40
EP73	113.3					0.00	0.01	0.07	0.00	0.00		
EP74	117.3					0.00	0.00	0.03	0.00	0.00		
EP75	123.45					0.03	0.00	0.02	0.00	0.00		
EP76	128.5					0.01	0.05	0.02	0.03	0.27		
EP77	135.8			-2.34	-11.39	0.02	0.22	0.04	0.18	1.47	-2.34	-11.39
EP78	137					0.02	0.06	0.04	0.02	0.18		
EP79	139.7	-1.24	-10.97	-1.72	-12.81	0.00	8.95	0.03	8.92	74.33	-1.48	-11.89
SBP 1	143.25	-0.76	-14.78								-0.76	-14.78
SBP 2	145.2	-1.45	-14.70								-1.45	-14.70
SBP 3	146.51	-0.39	-10.83								-0.39	-10.83
SBP 4	152.2	-0.41	-13.65								-0.41	-13.65
SBP 5	153.12	-0.76	-13.32								-0.76	-13.32
SBP 6	158.17	-0.71	-12.98								-0.71	-12.98
SBP 7	158.47	-0.15	-12.65								-0.15	-12.65
SBP 8	166.77	-1.21	-13.02								-1.21	-13.02
OAK SPRINGS SUMMIT												58.00
OSS1	0.1			-4.83	-12.75	0.00	0.76	0.07	0.69	5.76	-4.83	-12.75
OSS2	1.6					0.00	0.32	0.02	0.29	2.45		
OSS3	2.6					0.00	0.10	0.03	0.07	0.57		
OSS4	3.53			-2.83	-17.88	0.00	2.01	0.02	1.99	16.57	-2.83	-17.88
OSS5	4.18			-1.84	-16.44	0.00	11.35	0.34	11.00	91.70	-1.84	-16.44
OSS6	5.53			-2.65	-15.22	0.00	2.98	0.02	2.96	24.69	-2.65	-15.22
OSS7	6.78			-3.29	-13.72	0.00	2.86	0.04	2.82	23.49	-3.29	-13.72
OSS8	7.78			-2.96	-14.74	0.00	1.82	0.07	1.75	14.58	-2.96	-14.74
OSS9	8.78			-2.82	-13.80	0.00	0.94	0.03	0.91	7.55	-2.82	-13.80
OSS10	9.73			-2.85	-15.27	0.00	2.17	0.07	2.10	17.51	-2.85	-15.27
OSS11	11			-2.68	-15.08	0.01	3.21	0.01	3.20	26.70	-2.68	-15.08
OSS12	12.48			-2.26	-17.82	0.00	1.34	0.03	1.31	10.93	-2.26	-17.82
OSS13	13.23			-2.64	-16.50	0.00	1.03	0.00	1.02	8.53	-2.64	-16.50
OSS14	13.92			-0.99	-14.34	0.00	11.10	0.48	10.62	88.51	-0.99	-14.34
OSS15	15.01			-1.36	-15.34	0.01	10.11	0.13	9.97	83.09	-1.36	-15.34
OSS16	16.01			-1.08	-14.06	0.01	12.68	2.69	9.99	83.25	-1.08	-14.06
OSS17	17.91			-0.98	-15.27	0.00	11.63	0.38	11.24	93.70	-0.98	-15.27
OSS18	18.81			-2.55	-13.54	0.00	1.10	0.06	1.04	8.67	-2.55	-13.54
OSS19	20.71			-1.53	-15.26	0.00	10.94	0.17	10.77	89.74	-1.53	-15.26
OSS20	22.01			-1.50	-15.19	0.00	10.93	0.04	10.89	90.77	-1.50	-15.19
OSS21	22.76			-2.40	-14.86	0.00	2.73	0.04	2.69	22.45	-2.40	-14.86
OSS22	23.96			-3.32	-11.68	0.00	0.26	0.06	0.20	1.67	-3.32	-11.68
OSS23	25.06			-4.17	-10.96	0.01	0.73	0.03	0.70	5.82	-4.17	-10.96
OSS24	26.06			-3.00	-11.43	0.00	0.53	0.03	0.50	4.14	-3.00	-11.43

Sample	N	mean	sd	Skewness	Kurtosis	min.	max.	10	25	50	75	90
OSS25	27.06			-3.15	-10.03	0.00	0.36	0.06	0.30	2.52	-3.15	-10.03
OSS26	27.71			-3.55	-12.04	0.00	0.57	0.03	0.55	4.55	-3.55	-12.04
OSS27	28.11			-3.66	-15.00	0.00	2.03	0.03	2.00	16.68	-3.66	-15.00
OSS28	28.41					0.00	0.04	0.03	0.02	0.13		
OSS29	28.86			-2.27	-15.02	0.00	8.33	0.02	8.31	69.22	-2.27	-15.02
OSS30	29.36								0.00	0.00		
OSS31	30.36					0.00	0.00	0.02	0.00	0.00		
OSS32	31.36			-4.82	-8.68	0.00	0.26	0.02	0.24	1.99	-4.82	-8.68
OSS33	32.36					0.01	0.00	0.04	0.00	0.00		
OSS34	33.36					0.01	0.00	0.02	0.00	0.00		
OSS35	34.36					0.00	0.06	0.04	0.02	0.13		
OSS36	35.36					0.02	0.00	0.03	0.00	0.00		
OSS37	36.96					0.00	0.00	0.02	0.00	0.00		
OSS38	37.96					0.00	0.41	0.01	0.40	3.36		
OSS39	38.96					0.00	0.00	0.01	0.00	0.00		
OSS40	40.01					0.00	0.04	0.02	0.02	0.15		
OSS41	41					0.00	0.00	0.01	0.00	0.00		
OSS42	42					0.00	0.00	0.02	0.00	0.00		
OSS43	43					0.00	0.00	0.00	0.00	0.00		
OSS44	44					0.00	0.00	0.00	0.00	0.00		
OSS45	45					0.00	0.00	0.01	0.00	0.00		
OSS46	46					0.04	0.00	0.01	0.00	0.00		
OSS47	47					0.00	0.00	0.01	0.00	0.00		
OSS48	48								0.00	0.00		
OSS49	49					0.00	0.04	0.03	0.01	0.11		
OSS50	50					0.00	0.04	0.05	0.00	0.00		
OSS51	50.4			-0.02	-14.63	0.03	11.24	0.28	10.96	91.33	-0.02	-14.63
OSS52	51.41			0.01	-15.19	0.00	11.37	0.13	11.24	93.64	0.01	-15.19
OSS53	53.26			0.03	-14.10	0.00	11.36	0.25	11.11	92.56	0.03	-14.10

				FRAMBOID DATA								
										Percentile		
Sample	N	mean	sd	Skewness	Kurtosis	min.	max.	10	25	50	75	90
Combined	55	7.17	2.73	0.98	0.34	3	17.5	4.25	5.05	3.25	8.81	10.25
Combined	57	7.58	4.02	1.62	2.71	2	42	3.59	4.91	6.06	8.88	12.65
Wash 1	50	4.97	1.98	0.47	-0.17	4	50	2.20	3.25	4.58	5.81	8.00
Wash 2	42	4.40	1.88	1.04	0.35	2	20	2.28	3.06	4.07	5.08	7.90
Combined	14	5.39	0.92	0.11	0.73	1.5	24	4.20	4.65	5.00	5.63	6.65
C-Shale	20	6.63	2.59	2.18	6.80	2	21	4.00	4.75	6.50	7.00	9.00
Combined	12	7.46	3.90	4.03	0.15	4	16.5	3.80	5.00	5.50	10.50	12.40

Table 4.1: Table containing stratigraphic and geochemical data. Rows coloured in grey indicate samples excluded due to low TOC (< 0.01 wt% TOC). Rows coloured in orange indicate the extinction horizon at Oak Springs Summit and Ruin Wash.

				Carrara Formation, Emigrant Pass			
Sample	Height (m)	δ13C	wt% C	TOC wt %	TIC wt%	Hg (p.p.b.)	Hg/TOC
EP1	0.3		0.04	0.05	-0.02	2.8	51.38
EP2	1.35	-2.16	0.21	0.02	0.19	54.7	2435.44
EP3	1.65		0.04	0.03	0.02	6.1	233.73
EP4	2.25	-3.56	0.92	0.02	0.90	44.5	2339.84
EP5	2.5		-0.09	0.03	-0.11	2.4	84.00
EP6	3.85		0.03	0.02	0.01	6.6	291.18
EP7	5.35		-0.06	0.03	-0.08	6.8	247.82
EP8	7.05		-0.01	0.04	-0.05	24.0	557.90
EP9	8.25		-0.05	0.02	-0.08	17.7	712.55
EP11	9.5		0.08	0.03	0.05	8.6	264.18
EP10	10.05	-3.20	5.71	0.08	5.63	270.0	3354.81
EP12	11.25	-1.18	4.07	0.06	4.01	120.7	2064.02
EP13	11.6		0.11	0.02	0.09	16.0	836.62
EP15	11.85	-0.50	8.88	0.06	8.81	65.4	1050.25
EP14	13.45		0.01	0.02	-0.02	19.0	872.98
EP17	15.85		3.47	0.03	3.44	186.4	6665.64
EP16	16.15		-0.07	0.03	-0.10	48.4	1891.47
EP18	17		0.06	0.04	0.02	20.2	546.95
EP19	20.65	-1.80	0.88	0.02	0.86	22.8	1466.79
EP20	21.45		0.04	0.04	-0.01	3.9	95.39
EP21	22.6	-0.33	0.62	0.04	0.58	14.1	372.13
EP22	24.05		0.03	0.02	0.01	27.6	1565.53
EP23	25.15	-2.31	9.01	0.08	8.93	85.1	1117.45
EP24	27.25		0.05	0.02	0.03	7.3	459.39
EP25	28.05	-2.13	5.53	0.04	5.49	13.6	314.92
EP26	29.75		0.07	0.02	0.05	4.2	242.60
EP27	31.5		11.15	0.01	11.14	27.2	4897.58
EP28	32.8	-2.56	4.14	0.01	4.13	16.7	1981.34
EP29	33.45	-1.57	9.97	0.05	9.92	17.2	353.01
EP30	33.55	-1.38	10.15	0.13	10.02	15.6	122.78
EP31	35.45	-2.03	10.22	0.20	10.02	13.6	68.05
EP33	37.8	-1.77	0.22	0.04	0.18	5.9	160.33
EP32	39.65	-1.65	8.48	0.06	8.42	35.0	570.09
EP34	40.65	-1.62	1.11	0.04	1.07	7.0	197.76
EP35	41.7	-1.64	10.37	0.60	9.77	33.7	55.97
EP36	43.75	-2.18	9.49	0.22	9.26	157.5	710.40
EP37	44.7		0.08	0.05	0.04	5.3	109.51
EP38	46.9	-1.99	0.45	0.41	0.04	14.7	36.06
EP39	48.5	-2.05	3.31	0.03	3.28	34.7	1038.99
EP40	50.3		0.05	0.03	0.01	3.1	91.29
EP41	50.65	-2.19	10.50	0.11	10.39	53.0	478.43
EP42	51.1	-1.84	1.24	0.05	1.19	35.1	710.71
EP43	52.9	-2.03	10.91	0.23	10.68	28.5	123.57
EP44	53.9	-1.67	4.89	0.07	4.82	40.1	575.39
EP45	54.85	-1.87	10.99	0.14	10.85	28.5	208.63

EP46	56	-0.77	8.10	0.24	7.86	42.3	177.25
EP47	57.1	-0.95	11.03	0.29	10.74	34.3	117.87
EP48	60.05	-0.87	16.24	0.70	15.54	16.9	24.29
EP49	63	-0.57	10.83	5.17	5.66	28.9	5.58
EP50	65	-0.72	11.04	0.14	10.91	25.4	186.64
EP51	67	-0.90	0.82	0.06	0.76	10.1	166.06
EP52	68	-1.87	3.77	0.05	3.72	16.5	313.76
EP53	69.55	-0.09	0.17	0.06	0.11	15.3	273.43
EP54	71	-1.86	0.06	0.03	0.03	10.0	386.99
EP55	72.5	-1.50	3.60	0.03	3.56	101.0	2968.45
EP56	74.65	-1.82	10.10	0.11	9.98	75.3	662.08
EP57	75.85	-1.68	7.65	0.09	7.56	55.4	589.01
EP58	80.55	-1.14	0.33	0.04	0.29	9.6	272.03
EP59	83.2	-2.30	6.95	0.00	6.95	13.4	6041.76
EP60	84.2	-1.66	10.45	0.17	10.27	53.4	307.48
EP61	85.3	-1.06	0.31	0.03	0.28	8.5	282.83
EP62	86.3	-2.03	10.71	0.12	10.59	50.9	438.27
EP63	88.4		-0.02	0.03	-0.06	6.6	188.65
EP64	90.4		-0.02	0.01	-0.03	4.4	518.05
EP65	92.4		0.07	0.01	0.06	3.6	311.42
EP66	94.4		0.04	0.02	0.03	3.1	199.72
EP67	99.65		0.11	0.01	0.09	2.4	198.06
EP68	101.5	-2.87	0.28	0.03	0.26	2.4	83.78
EP69	103.1	-2.53	0.15	0.03	0.13	1.6	60.98
EP70	105	-3.52	0.62	0.00	0.62	1.2	2557.79
EP71	109.15	-2.51	0.30	0.01	0.29	6.6	509.99
EP72	112	-1.85	0.57	0.01	0.56	1.6	220.63
EP73	113.3		0.01	0.07	-0.06		0
EP74	117.3		-0.04	0.03	-0.07	1.7	57.79
EP75	123.45		-0.04	0.02	-0.06	1.2	59.36
EP76	128.5		0.05	0.02	0.03	2.1	93.18
EP77	135.8	-2.34	0.22	0.04	0.18	3.2	78.21
EP78	137		0.06	0.04	0.02	4.0	110.60
EP79	139.7	-1.48	8.95	0.03	8.92	22.9	718.71
			Pioche Formation, Ruin Wash				
Sample	Height (m)	δ13C VPDB		wt % TOC		Hg (p.p.b.)	Hg/TOC
RW1	0.20			0.07		204.20	2857.89
RW2	0.76	-2.26		0.19		501.82	2612.33
RW3	4.23			0.05		19.64	364.05
RW4	4.63	-0.50		0.28		53.29	192.81
RW5	5.86	-0.87		0.39		226.57	587.56
RW6	7.96	-1.43		0.37		8.91	23.92
RW7	8.66	-1.46		0.38		23.65	62.79
RW8	10.46	-1.79		0.09		6.04	67.36
RW9	11.06	-1.98		0.16		4.59	28.70
RW10	11.76	-1.53		0.12		11.26	94.48
RW11	12.66			0.08		9.81	118.85

Sample	Height (m)	$10^3\delta^{13}C$	wt% C	TOC wt %	TIC wt%	Hg (p.p.b.)	Hg/TOC
RW12	13.26	-1.66		0.33		8.09	24.20
RW13	13.71			0.08		9.09	116.56
RW14	14.34			0.10		10.04	104.22
RW15	14.59			0.08		5.58	74.19
RW16	15.09			0.09		7.79	83.29
RW17	15.64			0.08		6.17	79.29
RW18	16.05			0.08		13.88	181.86
RW19	18.14			0.07		3.92	53.25
RW20	19.84			0.09		3.94	43.43
RW21	20.84			0.10		3.34	33.37
RW22	22.24			0.08		1.85	24.33
RW23	23.64			0.07		2.49	35.51
RW24	26.84			0.08		5.01	65.58
RW25	28.34			0.09		4.59	52.75
RW26	29.84			0.08		2.52	32.54
RW27	30.84			0.09		4.23	48.39
RW28	31.94			0.09		2.20	25.24
RW29	33.44			0.06		5.97	101.95
RW30	33.84	-0.51		0.16		1.53	9.36
RW31	34.50	0.64		0.24		2.32	9.66
Pioche Formation, Oak Springs Summit							
Sample	Height (m)	$10^3\delta^{13}C$	wt% C	TOC wt %	TIC wt%	Hg (p.p.b.)	Hg/TOC
OSS1	0.1	-4.83	0.76	0.07	0.69	-	-
OSS2	1.6		0.32	0.02	0.29	13.02	581.55
OSS3	2.6		0.10	0.03	0.07	-	-
OSS4	3.53	-2.83	2.01	0.02	1.99	-	-
OSS5	4.18	-1.84	11.35	0.34	11.00	-	-
OSS6	5.53	-2.65	2.98	0.02	2.96	-	-
OSS7	6.78	-3.29	2.86	0.04	2.82	4.20	105.54
OSS8	7.78	-2.96	1.82	0.07	1.75	0.00	0.00
OSS9	8.78	-2.82	0.94	0.03	0.91	0.00	0.00
OSS10	9.73	-2.85	2.17	0.07	2.10	-	-
OSS11	11	-2.68	3.21	0.01	3.20		0.00
OSS12	12.48	-2.26	1.34	0.03	1.31	46.00	1696.20
OSS13	13.23	-2.64	1.03	0.00	1.02	0.00	0.00
OSS14	13.92	-0.99	11.10	0.48	10.62	0.00	0.00
OSS15	15.01	-1.36	10.11	0.13	9.97	-	-
OSS16	16.01	-1.08	12.68	2.69	9.99	5.94	2.21
OSS17	17.91	-0.98	11.63	0.38	11.24	7.33	19.09
OSS18	18.81	-2.55	1.10	0.06	1.04	5.00	90.04
OSS19	20.71	-1.53	10.94	0.17	10.77	-	-
OSS20	22.01	-1.50	10.93	0.04	10.89	-	-
OSS21	22.76	-2.40	2.73	0.04	2.69	-	-
OSS22	23.96	-3.32	0.26	0.06	0.20	0.00	0.00
OSS23	25.06	-4.17	0.73	0.03	0.70	8.59	277.81
OSS24	26.06	-3.00	0.53	0.03	0.50	0.00	0.00
OSS25	27.06	-3.15	0.36	0.06	0.30	-	-

OSS26	27.71	-3.55	0.57	0.03	0.55	-	-
OSS27	28.11	-3.66	2.03	0.03	2.00	9.61	301.38
OSS28	28.41		0.04	0.03	0.02	-	-
OSS29	28.86	-2.27	8.33	0.02	8.31	-	-
OSS30	29.36				0.00	-	-
OSS31	30.36		-0.05	0.02	-0.07	31.44	1265.85
OSS32	31.36	-4.82	0.26	0.02	0.24	15.28	802.16
OSS33	32.36		-0.05	0.04	-0.09	0.00	0.00
OSS34	33.36		-0.07	0.02	-0.09	5.36	336.23
OSS35	34.36		0.06	0.04	0.02		-
OSS36	35.36		0.00	0.03	-0.03	5.25	184.32
OSS37	36.96		-0.07	0.02	-0.08	17.05	917.09
OSS38	37.96		0.41	0.01	0.40	0.00	0.00
OSS39	38.96		-0.07	0.01	-0.08	6.82	633.70
OSS40	40.01		0.04	0.02	0.02		-
OSS41	41		-0.09	0.01	-0.10	4.13	522.31
OSS42	42		-0.07	0.02	-0.09	0.00	0.00
OSS43	43		-0.08	0.00	-0.08	0.00	0.00
OSS44	44		-0.08	0.00	-0.08	0.00	0.00
OSS45	45		-0.06	0.01	-0.07	0.00	0.00
OSS46	46		-0.08	0.01	-0.08	0.00	0.00
OSS47	47		-0.07	0.01	-0.09	0.00	0.00
OSS48	48				0.00	-	-
OSS49	49		0.04	0.03	0.01	-	-
OSS50	50		0.04	0.05	-0.01	-	-
OSS51	50.4	-0.02	11.24	0.28	10.96	0.00	0.00
OSS52	51.41	0.01	11.37	0.13	11.24	-	-
OSS53	53.26	0.03	11.36	0.25	11.11	-	-

Table 5.1: Table containing stratigraphic and geochemical data for cores CKAD001, NTGS Huc 1 and Baldwin 1.

			CKAD001				
Sample Name	Depth (m)	Formation	wt% TOC	δ13C ‰	δ18O ‰	Hg/TOC	Conc [ng/g]
CKAD1	498.02		1.27	2.10	-9.02	10.64	13.49
CKAD2	499.60		1.47	1.50	-8.18	2.46	3.62
CKAD03	501.00		1.57	1.95	-9.60	10.18	15.99
CKAD04	501.65		1.09	2.23	-9.14	19.90	21.61
CKAD05	502.43		1.31			14.17	18.51
CKAD06	503.47		1.05	1.95	-9.16	6.21	6.55
CKAD07	504.45						
CKAD08	505.50		1.90			13.79	26.19
CKAD09	507.00		1.37			21.92	29.96
CKAD10	508.90		2.35	1.09	-8.63	14.50	34.10
CKAD11			2.95			11.92	35.20
CKAD12	512.57		0.99	0.19	-9.12	31.52	31.28
CKAD13	513.65		0.61	-1.57	-6.98	20.62	12.67
CKAD14	515.05		0.76	-1.36	-9.38	34.67	26.26
CKAD15	517.85		1.56	-2.58	-10.50	34.24	53.53
CKAD16	518.25		1.44	-2.52	-10.42	24.94	35.98
CKAD17	521.10		1.24	-2.91	-10.17	34.18	42.50
CKAD18	522.35		1.75			74.73	130.69
CKAD19	523.65	Arthur	3.50	-5.52	-10.05	12.06	42.21
CKAD20	526.00	Creek		-7.92	-12.71		25.62
CKAD21	528.50	Formation	3.50			42.27	147.83
CKAD22	529.95		3.86			58.89	227.36
CKAD23	532.10		5.63			27.24	153.45
CKAD24	532.44		10.94	-10.19	-11.00	4.17	45.61
CKAD25	534.50		10.57	-7.72	-13.37	2.89	30.50
CKAD26	536.05						161.24
CKAD27	537.30		6.83			26.54	181.38
CKAD28	538.85		8.21			13.83	113.51
CKAD29	540.50		13.19			24.59	324.40
CKAD30	541.20		14.32			28.64	410.02
CKAD31	541.50		5.19	-1.45	-7.23	25.26	131.13
CKAD32	543.30		2.56	-0.40	-8.27	2.15	5.50
CKAD33	546.10		3.47	-0.43	-8.43	0.59	2.04
CKAD34	548.00			-0.45	-9.17		0.99
CKAD35	549.00			-0.46	-9.00		0.91
CKAD36	550.00		9.69	-0.40	-9.84	0.09	0.88
CKAD37	551.00		6.95	-0.41	-9.01	0.15	1.02
CKAD38	552.00		5.23	-0.41	-9.27	0.66	3.47
CKAD39	555.15		5.69	-0.54	-10.70	0.88	5.01
CKAD40	557.00		12.60	-0.28	-10.35	0.07	0.90
CKAD41	558.50		4.07	-0.46	-10.15	1.14	4.63
CKAD42	561.00		10.01	-0.39	-9.52	0.12	1.16
CKAD43	563.20		6.46	-0.33	-10.08	0.53	3.41

Sample Name	Depth (m)	Formation	wt% TOC	δ13C ‰	δ18O ‰		
CKAD44	565.00		24.27	-0.26	-10.31	0.04	0.93
CKAD45	567.00		22.77	0.02	-9.54	0.05	1.17
CKAD46	570.00		20.24	-0.32	-7.52	0.03	0.67
CKAD47	571.00		9.85	-0.11	-10.22	0.18	1.81
CKAD48	573.70		27.86			0.22	6.11
CKAD49	574.00	Thorntonia	36.59			0.64	23.45
CKAD50	575.80	Limestone	14.61	-0.01	-10.46	0.18	2.63
CKAD51	577.00		0.17			73.50	12.18
CKAD52	577.90		0.80			3.28	2.63
CKAD53	579.90		0.09	0.51	-6.39	24.50	2.12
CKAD54	582.10		0.12	-0.94	-7.81	339.07	39.59
CKAD55	583.10						
CKAD56	585.00		0.14			47.95	6.89
CKAD57	586.28		0.14	-0.13	-6.59	53.62	7.53
CKAD58	587.93		0.10	0.47	-7.07	73.44	7.63
CKAD59	589.58		0.07			28.61	2.06
CKAD60	592.50			-0.51	-10.79		0.42
CKAD61	594.00			-0.76	-10.37		0.35
CKAD62	597.70	Red Heart	0.05			8.69	0.47
CKAD63	599.00	Dolostone					0.32
CKAD64	601.00		0.08			7.41	0.58
CKAD65	603.00		0.06	-1.78	-9.79	7.24	0.40

NTGS Huc 1

Sample Name	Depth (m)	Formation	wt% TOC	δ13C ‰	δ18O ‰		
Huc1	47.70			-0.83	-10.37		
Huc2	49.73			-1.36	-9.85		
Huc3	52.10						
Huc4	55.08			-1.02	-9.92		
Huc5	56.86						
Huc6	58.73						
Huc7	61.75						
Huc8	67.11			-1.00	-9.86		
Huc9	70.07			-0.55	-9.72		
Huc10	73.06						
Huc11	76.80						
Huc12	79.70			-0.46	-9.78		
Huc13	81.65						
Huc14	83.95						
Huc15	87.62						
Huc16	90.30			0.26	-8.22		
Huc17	91.70			-0.08	-8.81		
Huc18	93.90			-0.54	-11.07		
Huc19	95.23						
Huc20	97.75			-0.33	-10.26		

Huc21	100.70					
Huc22	102.90					
Huc23	105.43			0.10	-8.23	
Huc24	106.73			-1.49	-7.39	
Huc25	109.60			0.41	-7.41	
Huc26	116.13					
Huc27	118.75			0.33	-8.58	
Huc28	122.25			1.47	-8.24	
Huc29	124.75			1.41	-8.32	
Huc30	128.05			1.00	-8.14	
Huc31	130.35			0.31	-9.34	
Huc32	133.50	Arthur				
Huc33	136.30	Creek		1.52	-8.17	
Huc34	137.85	Formation		1.63	-7.90	
Huc35	139.60			1.70	-8.25	
Huc36	140.28			0.00	-8.91	
Huc37	143.20			1.21	-9.36	
Huc38	146.70			0.88	-7.81	
Huc39	149.70			0.94	-7.93	
Huc40	152.20					
Huc41	154.90			1.07	-8.15	
Huc42	156.75			1.66	-8.23	
Huc43	159.60			2.07	-8.54	
Huc44	163.60			1.50	-8.11	
Huc45	166.65			1.84	-9.09	
Huc46	169.34			2.14	-9.08	
Huc47	173.18			0.96	-9.79	
Huc48	176.03			2.40	-9.22	
Huc49	180.10			2.05	-9.96	
Huc50	186.20			2.51	-9.54	
Huc51	189.90			2.25	-9.26	
Huc52	192.81			2.17	-9.31	
Huc53	196.05			2.10	-9.67	
Huc54	200.10			2.33	-9.23	
Huc55	202.75			1.83	-9.08	
Huc56	209.10			1.74	-10.00	
Huc57	212.15			1.50	-10.39	
Huc58	216.80			1.41	-10.18	
Huc59	220.70			0.21	-8.68	
Huc60	225.00			-0.98	-9.14	
Huc61	229.80			-0.68	-9.33	
Huc62	233.25			0.28	-7.67	
Huc63	236.20			-0.94	-6.74	
Huc64	240.50			-3.96	-7.13	
Huc65	242.35			-5.66	-8.08	

Sample Name	Depth (m)	Formation	wt% TOC	δ13C ‰	δ18O ‰		
Huc66	244.20			0.31	-8.35		
Huc67	251.00			0.66	-9.56		
Huc68	254.92			0.65	-9.20		
Huc69	257.26			0.98	-7.62		
Huc70	260.82			0.54	-8.82		
Huc71	266.03	Errarra Formation					
Huc72	270.27						
Huc73	273.98						
Huc74	277.70						
Huc75	283.70						
Huc76	286.65						
Huc77	289.80						
Huc78	292.30						
			Baldwin 1				
Sample Name	Depth (m)	Formation	wt% TOC	δ13C ‰	δ18O ‰		
B1	968.50						
B2	968.20			-0.67	-4.90		
B3	966.60	Red Heart Dolostone		-0.22	-6.71		
B4	966.00			-0.28	-9.59		
B5	961.30			0.09	-6.12		
B6	959.30			0.88	-5.77		
B7	956.60			0.27	-6.44		
B8	945.50			0.14	-9.39		
B9	936.20			0.68	-4.81		
B10	929.00			1.20	-9.96		
B11	919.00			0.27	-6.46		
B12	911.30	Thorntonia Limestone		0.27	-7.76		
B13	899.50			1.50	-8.04		
B14	899.30			1.43	-8.68		
B15	898.80			1.18	-8.44		
B16	894.20			0.94	-6.30		
B17	890.00			-4.30	-9.60		
B18	889.50			0.26	-9.27		
B19	889.20			-2.21	-6.61		
B20	888.40						
B21	888.00			-6.37	-7.15		
B22	885.00						
B23	883.30						
B24	881.20						
B25	878.00			-5.98	-7.23		
B26	874.60						
B27	868.30			1.13	-8.19		
B28	866.90			1.72	-10.24		
B29	865.00			2.38	-10.48		

228

B30	859.50			3.09	-10.04	
B31	840.70			3.31	-9.05	
B32	824.20			2.83	-8.11	
B33	805.50	Arthur		2.74	-9.21	
B34	782.70	Creek		2.59	-9.54	
B35	767.80	Formation		2.22	-8.79	
B36	735.50			0.70	-8.84	
B37	724.10			1.24	-8.36	
B38	700.00					
B39	678.50			0.83	-10.44	
B40	654.20			1.01	-7.98	
B41	631.35			1.08	-8.92	
B42	613.70					
B43	594.80			0.30	-9.42	
B44	577.50			-0.31	-9.89	
B45	561.50			-0.48	-9.21	
B46	543.70			-0.09	-8.80	
B47	522.80					
B48	486.40			0.15	-11.50	
B49	470.50			0.09	-11.98	
B50						
B51						
B52						
B53		Arrunthrung				
B54		a Formation				
B55						
B56						
B57						